UNIVERSITY OF CALIFORNIA
Los Angeles

Advances in Quasilinear Gyrokinetic Modeling of Turbulent Transport

A dissertation submitted in partial satisfaction
of the requirements for the degree
Doctor of Philosophy in Physics

by

Cole Darin Stephens

2021

ABSTRACT OF THE DISSERTATION

Advances in Quasilinear Gyrokinetic Modeling of Turbulent Transport

by

Cole Darin Stephens
Doctor of Philosophy in Physics
University of California, Los Angeles, 2021
Professor Frank Jenko, Co-Chair
Professor Troy A. Carter, Co-Chair

The quest to harness fusion energy requires the successful modeling of plasma turbulence and transport in magnetic confinement devices. For such modeling, the requisite length and time scales span many orders of magnitude. Integrated modeling approaches are constructed to account for the wide range of physics involved in turbulent transport by coupling separate physical models together. The primary physical models used in this work are kinetic and designed to simulate microturbulence on the smallest scales associated with turbulent transport. However, high precision nonlinear kinetic simulations often cannot be easily coupled to integrated modeling suites due to the extreme computational costs that would be involved. Model reduction which drastically reduces the computational complexity of the problem is therefore necessary. One must of course ensure that the reduced model does not severely diminish the accuracy of the calculation; the model reduction itself must be founded on more exact computational approaches as well as fundamental theoretical principles.

One of the most successful approaches in model reduction is quasilinear gyrokinetics. There are two fundamental assumptions for the quasilinear model examined in this work. First, the three

adiabatic invariants (the magnetic moment, the longitudinal invariant, and the poloidal flux) must be appropriately conserved and their associated single charged particle motions (the gyromotion, the bounce-transit motion, and the toroidal drift motion) must be characterized accurately. Second, the quasilinear approximation must hold such that the coherent linear response is adequate enough to compute the quasilinear fluxes without full calculation of the nonlinear physics. The particular model used, QuaLiKiz, has been proven successful in reproducing local gyrokinetic fluxes in the tokamak core while remaining computationally tractable.

There are three primary goals of this dissertation project. The first is to examine the fundamental physics underlying gyrokinetic and reduced model approaches at the single charged particle scale. To achieve this goal, we examine the assumption of magnetic moment invariance in a wide variety of electromagnetic fields. We successfully identify the dimensionless parameters that determine magnetic moment conservation in each scenario and then proceed to quantify the degree to which magnetic moment conservation is broken. In doing so, we confirm that the magnetic moment is sufficiently conserved for a wide range of regimes relevant to tokamak plasmas. In addition, we derive new analytic formulas for quantities associated with bounce-transit motion in circular tokamak fields. We compare these new, more exact calculations to approximations commonly used in reduced models (including QuaLiKiz) and determine the conditions such that the approximations break down. We then also confirm that the approximations are valid in the tokamak core for conventional, large aspect ratio devices.

The second goal of this dissertation project is to rederive and compile the model equations for QuaLiKiz from first principles. Over the years of QuaLiKiz's development, there has never been a complete manuscript that sketches the derivation of QuaLiKiz from start to finish. The lack of such a document makes it difficult to extend the physics of QuaLiKiz to new parameter regimes of interest. Various possible extensions such as including electromagnetic effects or more realistic tokamak geometries require the adjustment of several different assumptions that would affect the derivation in key ways. As such, correct implementations of new physics would require an existing derivation as a reference point lest the implementation be handled in an incoherent fashion. In

addition, a step-by-step outline of how each assumption of QuaLiKiz affects the derivation can be helpful in determining which assumptions can be relaxed for a more accurate model. The successful completion of this derivation, included in this dissertation, will be immensely useful for future QuaLiKiz improvement and validation.

With the derivation in hand, we proceed to the third goal of this project: improving the collisional model of QuaLiKiz. Collisions play an essential role in characterizing the transport associated with trapped electron modes. It has become evident in recent studies that the collisional model in QuaLiKiz requires improvement; in integrated modeling, the imprecise treatment of collisional trapped electron modes leads to incorrect density profile predictions near the tokamak core for highly collisional regimes. We revisit the collision model implemented in QuaLiKiz and use the more exact gyrokinetic code GENE (Gyrokinetic Electromagnetic Numerical Experiment) to make improvements to QuaLiKiz's collision operator. We then use the new version of QuaLiKiz in integrated modeling to compare density profiles predicted by the old and new collision operators. We confirm that the new collision operator leads to density profiles that more accurately match the experimental profiles.

The dissertation of Cole Darin Stephens is approved.

Marco C. M. Velli

Warren B. Mori

Troy A. Carter, Committee Co-Chair

Frank Jenko, Committee Co-Chair

University of California, Los Angeles

2021

To my wife, Renee Chen Sima

TABLE OF CONTENTS

LIST OF FIGURES

LIST OF TABLES

ACKNOWLEDGMENTS

I owe my success and accomplishments in my physics studies to many people who supported me throughout my life. Without these people, I would have never been able to develop a passion for learning or an eye towards critical thinking, and it is through their emotional support that I was able to overcome the many trials and tribulations to ultimately achieve the publication of this dissertation. Although is impossible for me to express my gratitude to my friends, family, mentors, and colleagues in such few words, I shall attempt to do so.

Firstly, I thank my parents, Trent and Kimi Stephens. Without their sacrifices or support for my education, I may have never left Washington State for my studies. I also thank my aunts and uncles as well as my grandparents, in particular Henry and Thelma Kaihara, for all their emotional support from when I was growing up to the present day. I also thank my younger siblings, Carson, Emmerson, and Chase Stephens, for bringing joy into my life.

I next thank my first and only love and newlywed wife, Renee Sima. I know without a doubt that without her support and help I would have never made it through graduate school. Thank you for your patience during some of the most stressful times of my life, for keeping the light when things were most dark, and for helping me edit my dissertation. I also thank her parents, Hong Sima and Qing Jiang, as well as her brother, Richard Sima. I also especially thank our family pets, Kitkat and Rushell, for being such wonderful companions and for also being very cute.

The completion of my dissertation would not have been possible without my advisor and mentor, Frank Jenko. I thank you for giving me the opportunity to experience living in Germany, for your continuous oversight and support for my work, and for giving me the confidence to succeed in plasma physics. I also thank Jonathan Citrin and Clarisse Bourdelle for all your support and guidance; my interactions with you were some of the most fulfilling and productive weeks of my time in Europe. I also thank Xavier Garbet for his physical insights and for always answering my theoretical questions, no matter how simple.

I owe my curiosity to all the educators throughout my life. My love for physics is first and foremost a love for learning itself, and without these educators I would never have been able to achieve my academic success. I cannot possibly name them all, but I shall list a few that left a deep impact on my life: Casey Jones, Diane Hunt, Alex Koerger, Hiroe Une, Robert Scotlan, Joseph Lovejoy, Leon Phillips, Joseph Wolfson, Ahmed Jebari, Catherine Holden, Kayoko Tazawa, Kent McConnell, James Dicarlo, Eimer Page, Jeffrey Ibbotson, Simon Billinge, Andrew Cole, Michael Mauel, William Bailey, Michael Makowski, Troy Carter, Eric D'Hoker, Joseph Teran, and George Morales. I must of course give thanks to my mother again, as she was my first educator.

Throughout my education at Charles Wright Academy, Phillips Exeter Academy, and Columbia University, I formed bonds with a great many people. It was with these people that I went through it all, thick and thin. I give special thanks to Alex Paczek and William Ang for always having my back and never failing me with their humor, wit, and loyalty. I thank Isaiah Everin, who, as a sort of philosophical life partner, always challenges me to grow emotionally and intellectually. I also thank Miguel Escobar, Miles and Nicholas Rohan, and Myles Jackson for all their love and support as well as their shenanigans in Dungeons and Dragons.

When I first started at UCLA, I did not know what to expect beyond hard work and good weather. Luckily, many of the students quickly became some of my closest friends, as well as nice study partners! Shoutout to David Hamilton, Lance Hildebrand, Helen Kim, Gurleen Bal, Matteo Vicino, John Gardiner, Masha Sargeeva, Patrick Astfalk, and Daniel Grošelj for all the fun and joint insights. I also thank Stephanie Krilov and David Saltzberg for their immense emotional support through some of the most difficult periods at UCLA. I also would like to thank my defense committee for their patience and feedback, especially given my stay abroad.

Moving to Munich to start work at IPP was of course its own challenge. I thank the friends and colleagues that defeated the isolation that would otherwise have plagued me while in a foreign country. I give special thanks to "The Squid Squad", Robert Brzozowski and Paul Crandall[†], for the American solidarity during my first few months in Munich. I also thank Nathan de Oliveira Lopes, Karl Stimmel, Franscisco Matos, Daniel Told, William McCorkindale, Dan Schäfer, Liza

Sytova, Rohan Ramasamy, Tobias Görler, Colin Benz, and Xin Wang for all their emotional and intellectual support. I also thank the friends I met at DIFFER in Eindhoven who made every one of my trips to the Netherlands a blast, especially Karel van de Plassche, Aaron Ho, and Michele Marin.

Last but not least, I would like to thank the crazy online community that kept me sane through the past few years, especially during the pandemic. You are some of the most goofy, amazing, magnanimous, marvelous, uplifting, splendid people I have ever met.

Chapter 3 is a reproduction of (C. D. Stephens, R. W. Brzozowski III, and F. Jenko, "On the limitations of gyrokinetics: Magnetic moment conservation," Physics of Plasmas **24**, 102517 (2017), DOI: 10.1063/1.4998968), for which R. W. Brzozowski III performed the numerical simulations and F. Jenko was the PI. Chapter 4 is a reproduction of (C. D. Stephens, X. Garbet, and F. Jenko. "Analytic guiding center formulas for bounce-transit motion in a concentric circular, finite inverse aspect ratio tokamak geometry," Physics of Plasmas **27**, 052504 (2020), DOI: 10.1063/5.0004811), for which X. Garbet offered key theoretical insights and F. Jenko was the PI. Chapter 5 is a reproduction of (C. D. Stephens, X. Garbet, J. Citrin, C. Bourdelle, K. van de Plassche, and F. Jenko. "Quasilinear gyrokinetic theory: A derivation of QuaLiKiz," in preparation to be submitted to Journal of Plasma Physics (2021)), for which X. Garbet laid the groundwork for the derivation, J. Citrin and C. Bourdelle offered key support in constructing the derivation, K. van de Plassche helped implement the numerical changes to QuaLiKiz, and F. Jenko was the PI. Chapter 6 is a reproduction of (C. D. Stephens, J. Citrin, K. van de Plassche, C. Bourdelle, T. Tala, A. Salmi, and F Jenko. "Quasilinear modeling of collisional trapped electron modes," in preparation to be submitted to Nuclear Fusion (2021)), for which J. Citrin, K. van de Plassche, and C. Bourdelle offered critical support for QuaLiKiz, T. Tala and A. Salmi motivated the collisionality scans, and F. Jenko was the PI and provided critical support for GENE.

I acknowledge the following works for allowing the reproduction of their figures:

1. C. E. Rolfs and W. S. Rodeny, *Cauldrons in the Cosmos: Nuclear Astrophysics* (Univ. of

Chicago Press, Chicago, 1998).

2. J. Wesson. *Tokamaks* (Oxford University Press, Oxford, 2012).

3. W. M. Stacey. *Fusion Plasma Physics* (Wiley-VCH, Weinheim, 2012)

4. J. A. Bittencourt. *Fundamentals of Plasma Physics*. (Springer, New York, 2007).

VITA

2011	High School Diploma (Phillips Exeter Academy, Exeter, NH)
2014	Summer Undergraduate Student Researcher (General Atomics, San Diego, CA)
2015	Bachelor of Science in Applied Physics (Columbia University, New York, NY)
2016	Master of Science in Physics (University of California, Los Angeles, Los Angeles, CA)
2017–2020	Visiting Scientist (Max Planck Institute for Plasma Physics, Tokamak Theory Division, Munich, Germany)

PUBLICATIONS

C. D. Stephens, R. W. Brzozowski III, and F. Jenko, "On the limitations of gyrokinetics: Magnetic moment conservation," Physics of Plasmas **24**, 102517 (2017), DOI: 10.1063/1.4998968.

C. D. Stephens, X. Garbet, and F. Jenko. "Analytic guiding center formulas for bounce-transit motion in a concentric circular, finite inverse aspect ratio tokamak geometry," Physics of Plasmas **27**, 052504 (2020), DOI: 10.1063/5.0004811.

X. Yang, P. Manas, C. Bourdelle, [et al., including C. D. Stephens]. "Core tungsten transport in WEST long pulse L-mode plasmas," Nuclear Fusion **60**, 086012 (2020), DOI: 10.1088/1741-4326/ab9669.

CHAPTER 1

Introduction

1.1 Fusion power

Meeting the world's growing demand for energy continues to be one of the most pressing tasks of the 21st century. According to the International Energy Agency (IEA), the world consumed approximately 116 petawatt hours of energy in 2018 and will continue to consume more every year.[1] Meanwhile, a 2013 report from the U.S. Energy Information Administration (EIA) projects that the primary energy use of countries within the Organization of Cooperation and Development (OECD) will grow by 0.5% per year from 2010 through 2040, while energy consumption in non-OECD countries is projected to grow by 2.2% per year in the same time frame.[2] Thus, while some of the change in energy consumption will come from population growth in wealthy countries, most of the increase will be due to population growth and rising living standards in developing countries. Meanwhile, fossil fuels, which include coal, oil, and natural gas, account for over 81% of energy produced to meet current energy demand.[3] The world must decrease worldwide dependence on fossil fuels for the sake of sustainability, environmental conservation, and minimization of the negative effects of climate change. Moreover, even after the world achieves net zero carbon emissions, any new energy production and distribution technologies must be sustainable to maintain carbon neutrality. Humanity thus faces the dual responsibility of satisfying rising global energy demands to lift the global poor out of poverty and ensuring a sustainable existence that limits damage to the environment and future generations.

Because the challenge is inherently global in scope, development must be pursued in all aspects

of energy production. Any particular advancement may not be uniformly useful to all countries in the world, and certain innovations are not guaranteed to transpire. For instance, the significant reduction of cost in producing solar panels and wind turbines in recent years will greatly contribute to decarbonization across the world.[4] International investment and global efforts have been increasing the availability of hydroelectric power in developing countries.[5] Renewable energy, however, does not on its own necessarily constitute a panacea due to various trade-offs. Renewable energy production often competes with agriculture in terms of land use. One must also consider geography and climate in determining the efficacy of any given renewable energy source; diversification in energy supply is necessary to fortify energy security in the face of natural disasters and changes in the environment. Overreliance on one energy source can render these energy systems extremely susceptible to the environment. For instance, many nations in eastern and southeastern Africa derive the vast majority of their energy from hydropower.[6] Rainfall variability and climate change itself can threaten the energy security of these nations. Even in diversified systems, seasonal and stochastic variation in renewable energy generation necessitates a combination of baseload energy sources as well as significant expansions in energy storage.[7] While further innovation in renewable energy could in principle mitigate these concerns, it is wise to develop technologies that complement renewable sources.

Fusion power is one such proposed technology currently being researched.[8] Fusion power is generated through fusion reactions in which multiple atomic nuclei bind together, thus fusing into heavier nuclei. This reaction only occurs when the nuclei overcome electrostatic repulsion via a close enough proximity for a long enough time such that the attractive strong nuclear force dominates. The nuclear binding energy, defined as the minimum energy to disassemble a given nucleus, partially characterizes such reactions. Figure 1.1 demonstrates that the elements with the most tightly bound nuclei per nucleon are clustered around nickel-62 and iron-56 in terms of atomic weight. According to Einstein's mass-energy equivalence, this manifests as a mass defect where tightly bound nuclei have a lower rest mass than the sum of their constituent nucleons' rest masses. Therefore, fusion reactions that involve nuclei much lighter than iron are exothermic,

thereby releasing energy. Meanwhile, especially heavy elements such as uranium release energy through nuclear fission, whereby atomic nuclei split into lighter nuclei.

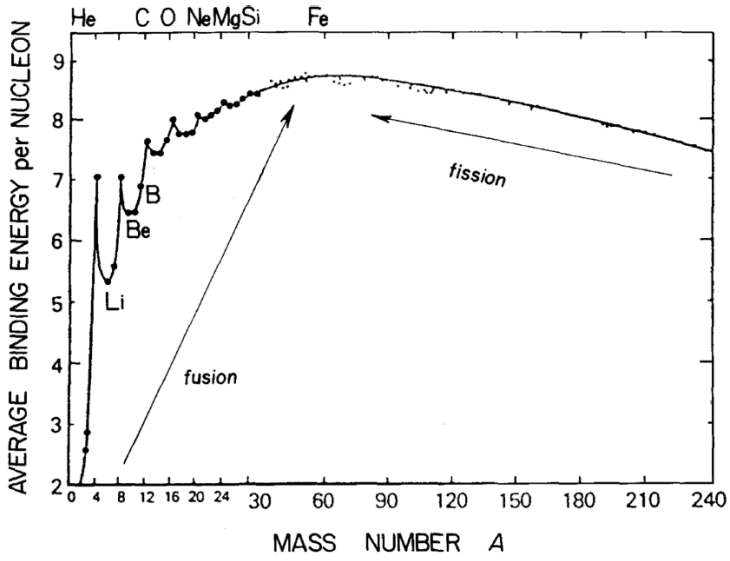

Figure 1.1: Average nuclear binding energy in MeV per nucleon as a function of atomic mass number A. Source: Ref. 9.

To undergo nuclear fusion, the reactant nucleons must achieve a high enough kinetic energy to overcome the electrostatic Coulomb barrier. Such conditions naturally occur in stars where massive gravitational forces pressurize the nuclear fuel to a high density and temperature state, leading to nucleosynthesis and thus heat generation.[9] However, the specific fusion processes in the Sun, such as the proton-proton chain reaction, are too slow to be of interest in the construction of a fusion power plant. Figure 1.2 plots the fusion reaction rates of those most relevant to fusion power, with the fastest being the deuterium-tritium (D-T) reaction:

$$\mathrm{D} + \mathrm{T} = {}^{2}_{1}\mathrm{H} + {}^{3}_{1}\mathrm{H} \longrightarrow {}^{4}_{2}\mathrm{He} + \mathrm{n} + 17.6\,\mathrm{MeV}. \tag{1.1}$$

Here, three major advantages of fusion energy can already be seen. Firstly, a single fusion reaction can generate energy on the order of 10 MeV, while a typical chemical reaction generates on the order of 1 eV of energy. Thus, only a relatively small amount of fuel is necessary to sustain a fusion

power plant. Secondly, the fuel is composed of deuterium and tritium. Deuterium accounts for 0.02% of hydrogen in the ocean, and is thus effectively infinite in abundance for human purposes. Although tritium does not occur naturally, it can be produced by using lithium-6 in the following reaction:

$$^{6}_{3}\mathrm{Li} + ^{1}_{0}\mathrm{n} \longrightarrow ^{4}_{2}\mathrm{He} + \mathrm{T} + 4.8\,\mathrm{MeV}. \tag{1.2}$$

Although lithium-6 is naturally occurring, it would require enrichment of the far more common isotope lithium-7. Identified land-based reserves for lithium-7 in 2020 are estimated to be 17 million metric tons worldwide.[10] Given the amount of energy released in a fusion reaction, these reserves can produce enough tritium to alone satisfy worldwide energy demands for centuries. The fuel necessary for fusion power is thus readily abundant. Thirdly, fusion reactions do not produce greenhouse gases, an important criterion for any long-term power source.

Beyond being sustainable, fusion power could prove to complement renewables. Fusion power plants could be built in locations where environmentally dependent sources of energy are not viable because fusion energy would be generated via reactors. Moreover, a fusion power plant can be operated through all hours of the day on a continuous basis. It could thus function as a reliable baseload source to offset the inherent variations of renewable energy generation. In addition, the external costs borne by the construction and operation of a fusion power plant (including land use, pollution due to construction of materials, and waste disposal) are projected to be comparable to that of renewables.[11] All the advantages of fusion power discussed so far, however, are shared by nuclear fission power. Given the mature status of fission energy production, fusion power must offer clear advantages over fission power if it is to be a worthwhile pursuit.

The primary advantage of fusion power in comparison to fission power is safety on both local and global scales. The plainest tail risk in the operation of a fission power plant is a potential reactor meltdown releasing radioactive materials into the environment. Although rare, nuclear accidents constitute enough of a danger such that entire populations must be evacuated in response. Such accidents have also triggered public and political backlash against nuclear energy, thereby undermining its role in sustainable energy production. Fortunately, fusion power plants would not

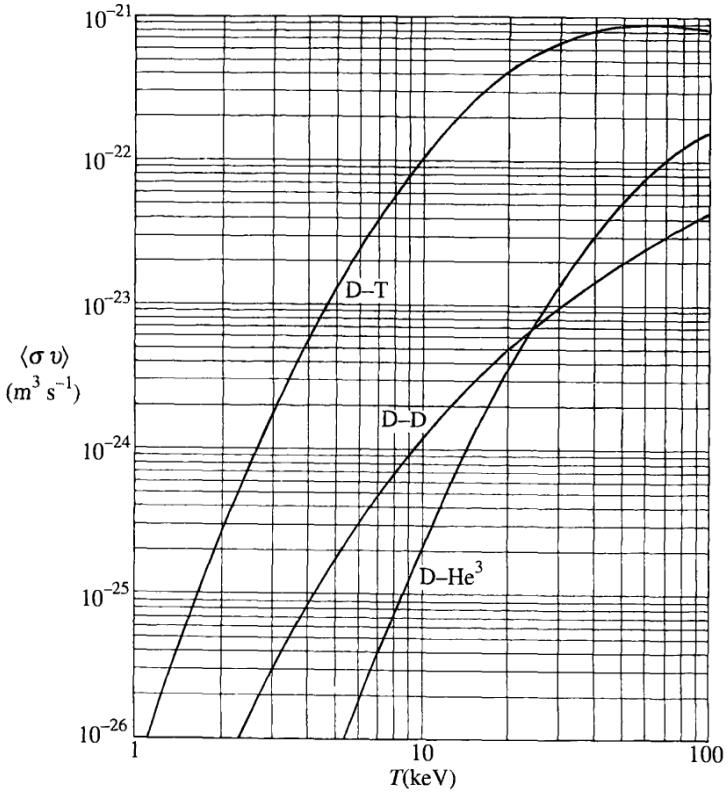

Figure 1.2: Reaction rate $\langle\sigma v\rangle$ measured in m^3s^{-1} as a function of temperature T measured in keV. Source: Ref. 8.

allow for such a catastrophic accident. Unlike fission reactions, fusion reactions are inherently unstable and require active maintenance to continue the process. Any accident or loss of control would lead to heat dissipation and cease the fusion process without causing a runaway nuclear reaction. In addition, fusion energy does not entail the same sort of nuclear waste production. Although the majority of fission waste is radioactive for a relatively short period of time, high-level radioactive waste must be stored for at least thousands of years and in some cases millions of years. Such waste must be shielded and protected from accidents during that entire time period. Fusion involves two main sources of waste: tritium production and neutron activation of plant components. Although tritium is radioactive, it has a half-life of 12.3 years and decays into stable helium-3. Meanwhile, the use of specially engineered materials would lead to the potential recycling of

irradiated components over the span of centuries and would prevent the creation any high-level waste.[12]

Perhaps the most important consideration with regards to the safety of nuclear power is proliferation of nuclear weapons material and technology. Needless to say, the unsanctioned manufacture or presence of nuclear weapons would assuredly manifest as a source of regional instability and increase the global threat of nuclear war. Any sovereign state capable of using nuclear fuel cycle technologies for the purpose of nuclear fission could in principle create fissile materials for the use of nuclear weapons. For instance, centrifuge isotropic separation is required to create enriched uranium, a critical component for nuclear power generation. The technology and resulting enriched uranium, however, are also crucial in the development of nuclear weapons. Moreover, a state that uses nuclear fission plants could also construct facilities to extract plutonium-239 from spent nuclear fuel to aid in the manufacture of nuclear weapons. Under the current Treaty on the Non-Proliferation of Nuclear Weapons (NPT), there is no prohibition of the development of such technologies for peaceful purposes. While such fissile materials are mandated to be safeguarded by the International Atomic Energy Agency (IAEA), there exists risk of nuclear breakout whereby a state produces enough weapons-grade material for a nuclear weapon before diplomatic or military intervention. State actors could also sell components and fuel for nuclear weapons, worsening proliferation. In the worst-case scenario, malicious state actors or violent non-state actors could potentially acquire nuclear weapons and spark a global crisis. As a result, there are severe international apprehensions in developing nuclear fission energy on a global scale and not all states can safely and economically pursue fission power.[13]

In contrast, fusion power presents minimal risks of nuclear proliferation. For instance, the operation of a fusion power plant does not require the production or use of fissile material whatsoever. Although a fusion reactor could be modified to produce weapons-grade fissile material through the use of fertile material, such a process would be far from clandestine given adequate IAEA safeguards. Without the presence of already-produced fissile material, it would be extremely unlikely for a state to assemble a nuclear weapons prior to detection. The world would then have weeks

to respond with diplomatic or military means between detection and final production, ample time compared to potential breakout using nuclear fission technologies. Moreover, hybrid systems that combine fission and fusion can be used to process plutonium and other transuranic elements, thus further reducing the risk of proliferation if implemented in secure states. Thus, fusion power is far more preferable to fission power with regards to nuclear proliferation and could in the long-term be developed in states that would otherwise be deemed unsuitable for hosting nuclear fission plants.[14]

This is not to say that fusion power is a panacea to the world's energy problems. Intense engineering efforts are required to create components that can withstand large amounts of radiation and extremely high temperatures. The waste created in manufacturing and operation must be taken into account in determining fusion power's exact role in sustainable energy. The economics of fusion power are also crucial; depending on the capital costs and required safety regulations, it may be uneconomical to derive a substantial amount of the world's energy from fusion power. It is also clear that the timescale for developing fusion power is too far in the future to substantially aid in mitigating climate change. According to the Paris Agreement, efforts to limit global warming to 1.5 °C compared to pre-industrial levels require net zero greenhouse gas emissions worldwide by 2050.[15] Meanwhile, the largest fusion experiment is currently being built in southern France. The device, called ITER ("The Way" in Latin), is scheduled to commence experiments in 2025, with D-T fusion reaction experiments scheduled for 2035. As of 2018, a proposed prototype nuclear fusion power station called the DEMOnstration Power Station (DEMO) is planned for construction in 2040. While this prototype could open the way for commercial nuclear fusion, it would most likely begin operations in 2050 or beyond, far later than when the bulk of climate change mitigation needs to occur.[16] However, even after carbon neutrality has been achieved, further developments in sustainable energy will be required to satisfy the world's energy demand in the long term. To achieve energy diversification, newly developed sources of energy must also be safe and minimize risk of harm. If successfully developed, fusion power could be one of the many tools humanity uses to ensure a sustainable future due its myriad advantages and features that complement renewables and fission power.

1.2 Magnetic confinement

The fundamental difficulty of fusion power is confinement. As seen in Figure 1.2, the energies required to achieve significant fusion reaction rates are on the order of 10 keV to 100 keV, corresponding to temperatures of 10^8 K to 10^9 K. This is much hotter than the thermonuclear solar core, which possesses a temperature on the order of 10^7 K. These temperatures are high enough to strip the light atoms of their orbital electrons, thus creating an ionized gas called a plasma. To achieve ignition, we must confine the plasma for a long enough time at a high enough temperature such that the power generated by fusion exceeds any losses so that the external power can be switched off.[17]

A simple estimate for the requirements, dubbed the Lawson criterion, can be constructed from rudimentary power balance considerations.[18] We first note that the internal energy density of the plasma is given by

$$\mathcal{E}_{\text{in}} = \frac{3}{2}\left(n_e T_e + \sum_i n_i T_i\right), \tag{1.3}$$

where T is the temperature measured in units of energy, n is the number density, the subscript "e" denotes electrons, and the subscript "i" denotes ions. To simplify the calculation, we assume that the electron and ion temperatures are equal. Moreover, we also assume a charge neutral plasma where all electrons are stripped from initially neutral atoms, leading to

$$n \equiv n_e = \sum_i n_i. \tag{1.4}$$

Thus, the energy density is simply

$$\mathcal{E}_{\text{in}} = 3nT. \tag{1.5}$$

The number of fusion reactions per unit volume per unit time of two ion species, meanwhile, is given by

$$f_{\text{re}} = n_1 n_2 \langle \sigma v \rangle_{\text{re}}, \tag{1.6}$$

where $\langle \sigma v \rangle$ is the reaction rate. For D-T fusion, we assume $n_D = n_T$. Given the energy of each fusion reaction $E_{\text{D-T}}$, the power produced per unit volume is then

$$\mathcal{P}_{\text{D-T}} = \frac{1}{4} n^2 \langle \sigma v \rangle_{\text{D-T}} E_{\text{D-T}}. \tag{1.7}$$

To achieve a steady state, we require that the power produced must exceed the power lost. We characterize the power lost per unit volume as

$$\mathcal{P}_{\text{loss}} = \mathcal{E}_{\text{in}}/\tau_E, \tag{1.8}$$

where τ_E is the confinement time. Here, τ_E denotes the amount of time it takes for the plasma to dissipate all of its internal energy into the environment. For ignition, we require

$$\mathcal{P}_{\text{D-T}} > \mathcal{P}_{\text{loss}}, \tag{1.9}$$

leading to Lawson's criterion for D-T fusion:

$$nT\tau_E > \frac{12T^2}{\langle\sigma v\rangle_{\text{D-T}} E_{\text{D-T}}}. \tag{1.10}$$

The minimum of this triple product occurs near $T = 14$ keV; in this region, the right-hand side can be approximated as a constant, leading to

$$nT\tau_E > 3 \cdot 10^{21} \text{ keV s m}^{-1}. \tag{1.11}$$

A confinement time satisfying the Lawson criterion has so far not been achieved and will likely remain out of reach until the operation of ITER. A less stringent requirement known as scientific breakeven, where external sources of power to maintain the fusion reaction is at least equal to the power generated from fusion, has also never been achieved but is projected to be easily accomplished by ITER.[16]

The main difficulty of fusion power is that no solid material can confine a plasma at these thermonuclear temperatures without being vaporized or destroyed, thereby quenching the plasma. Instead, cleverer means must be used to confine the plasma such that the Lawson criterion is satisfied. In stellar nucleosynthesis, gravity provides the means of pressurizing the core of a star. Since gravitational confinement is infeasible for constructing a reactor, two additional approaches have been pursued. The first is known as inertial confinement, whereby a small D-T pellet is compressed to extremely high densities and then heated via external beams. In this scenario, the confinement time would be on the order of 10 ns to 100 ns and the Lawson criterion would

be satisfied via sufficiently high densities and temperatures. The second approach is magnetic confinement, the main topic of this work. With magnetic confinement, the plasma would be trapped via a strong magnetic field using the property that charged particles spiral about magnetic field lines. An appropriate magnetic geometry would be able to confine the plasma inside the device, with the goal being a confinement time on the order of 0.1 s to 10 s.[17]

The most popular and well developed device for magnetic confinement is the tokamak, the term being a Russian acronym for *toroidal chamber with an axial magnetic field*.[19] A diagram for a typical tokamak can be seen in Fig. 1.3. The toroidal component of the magnetic field guides the electrons and ions about the center of the tokamak and is generated by external coils. This alone, however, would not sufficiently confine the plasma. The inherent inhomogeneities in the magnetic field, namely the spatially dependent strength and the curvature of the magnetic field, would naturally cause the charged particles to drift away from the field line. These magnetic drifts are charge dependent and thus would lead to charge separation and the creation of an electric field. The combination of this electric field and the background magnetic field would give rise to another drift velocity called the E-cross-B drift, which would lead to charged particles drifting out of the device and therefore confinement failure.

The solution is to introduce a twist to the magnetic field lines through the inclusion of a poloidal magnetic field smaller than the toroidal field; the resulting magnetic field lines would then have a helical structure. This helical structure results in periodic particle motion in the poloidal plane since the guiding center of the particle follows the field line to lowest order. Ignoring collisions, the particle returns to initial position in the poloidal plane after one period despite the magnetic drifts. This prevents the disastrous development of an electric field and thus allows for better confinement of the plasma. To generate these poloidal fields, a tokamak incorporates coils in the center of the device that induce a changing magnetic flux through the plasma. Through Faraday's law, this changing magnetic flux thus induces an electric field that drives a toroidal plasma current, in turn generating a poloidal magnetic field. The winding of this magnetic field is characterized by the spatially dependent safety factor q, denoting the number of toroidal rotations per poloidal rotation

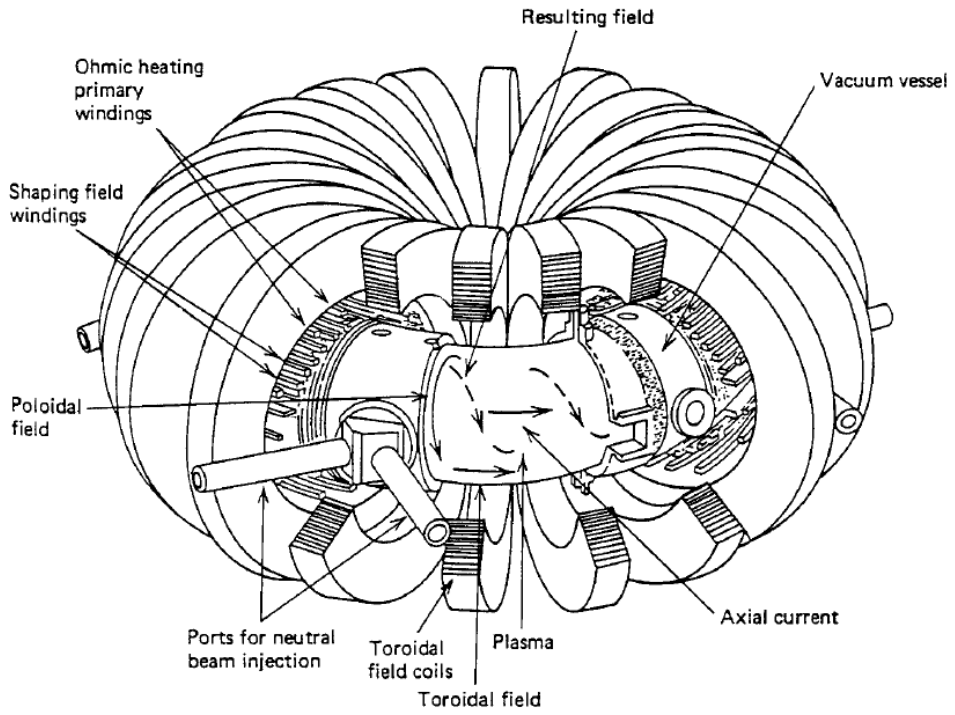

Figure 1.3: Schematic of a tokamak. Source: Ref. 17.

of the magnetic field line. The plasma is then heated via external electromagnetic waves, neutral-beam injections, and ohmic heating from the generated currents. Although this basic configuration makes magnetic confinement tenable, there are numerous instabilities to grapple with as a result of ordinary fluid turbulence as well as the turbulent effects due to a plasma's electromagnetic properties.[12] These instabilities can lead to the transport of particles and heat radially out of the tokamak, thereby breaking confinement of the plasma. Understanding and controlling tokamak transport is thus of paramount importance in confining a plasma.

1.3 Tokamak transport

Understanding tokamak transport requires consideration of irreducible transport caused by collisions. Basic flux processes follow Fick's laws of diffusion. For instance, the particle flux $\mathbf{\Gamma}$ is

given by

$$\mathbf{\Gamma} = -D\boldsymbol{\nabla} n, \tag{1.12}$$

where D is the diffusivity or diffusion coefficient. A naive estimate for the diffusivity can be formulated from a cylindrical magnetic geometry with no curvature. Diffusion processes within such a geometry fall under the category of classical transport. In such a simple geometry, we treat individual particles as undergoing a random walk in the radial direction across the magnetic field lines. The random walk is itself caused by collisions; the step size of the walk is characterized by the cyclotron radius ρ_c (also known as the Larmor radius and the gyroradius). The time between each step is the characteristic collision time τ_C, which describes the time for a particle to scatter a full 90 degrees. The classical radial diffusion coefficient is then

$$D_{\text{class}} \sim \frac{(\Delta x)^2}{\Delta t} = \frac{\rho_c^2}{\tau_C}. \tag{1.13}$$

The classical diffusivity rate for ions and electrons are equivalent, resulting in ambipolar diffusion. To see this, note that the ion cyclotron radius is equal to the electron cyclotron radius multiplied by a factor of the mass ratio $\sqrt{m_e/m_i}$, where m is the mass, assuming thermal electrons and ions at the same temperature. Meanwhile, collisions between unlike particles produce net particle diffusion and the characteristic ion-electron collision time goes like electron-ion collision frequency multiplied the ratio m_e/m_i. Here, σ-σ' collisions refer to particles of species σ scattering off of particles of species σ'. Thus,

$$\frac{\rho_i^2}{\tau_{ie}} = \frac{\frac{m_e}{m_i}\rho_e^2}{\frac{m_e}{m_i}\tau_{ei}} = \frac{\rho_e^2}{\tau_{ei}}. \tag{1.14}$$

Although this provides a simple and intuitive picture, classical transport analysis greatly underestimates experimentally measured diffusion by several orders of magnitude. The key problem with this analysis is that we completely neglected the effects of magnetic curvature by assuming a cylindrical geometry. Essentially, the inhomogeneities of the magnetic field in a tokamak result in qualitatively different orbits than those in straight magnetic fields. Models that incorporate non-trivial magnetic geometry are called neoclassical.[20] One key effect is due to the mirror force

parallel to the magnetic field, $F_{d\parallel}$, given to lowest order in the gyroradius by

$$F_{d\parallel} = -(\mu \nabla B) \cdot \hat{\mathbf{b}}, \tag{1.15}$$

where $\mu = W_\perp / B$ is the magnetic moment, $W_\perp$ is the perpendicular kinetic energy, B is the magnetic field strength, and $\hat{\mathbf{b}}$ is the unit vector parallel to the magnetic field. The source of this force comes from the gyrating motion of the charged particle; in a strong magnetic field, the charged particle is akin to a small magnet with magnetization μ, thus leading to a diamagnetic force. This ultimately arises from the adiabatic invariance of μ. An important parameter is the pitch angle of the particle, typically defined to be the angle between the particle's velocity vector and the local magnetic field. Particles with pitch angle close to 90 degrees at the outer midplane are slowed down by this mirror force until the motion along the field line halts and then reverses direction. Because these particles are effectively trapped by a potential well μB, they are dubbed trapped particles and bounce between mirror points. Particles with pitch angle close to 0 degrees at the outer midplane instead pass through the potential well and continue along the magnetic field line and are thus called passing particles.[21]

The bounce orbits of trapped particles are periodic and characterized by the thermal bounce frequency ω_b; moreover, a finite radial excursion from the magnetic field line arises when higher-order effects are taken into account. The shape of these orbits take on a banana shape, hence the name "banana orbit." In the collisional regime where trapped particles can complete multiple bounce orbits before a significant collision event, it is these banana orbits that dominate the diffusion process. This is called the banana regime, and the diffusion coefficient is given by

$$D_{\text{ban}} \sim f_t \frac{\delta_b^2}{\tau_{\text{eff}}}. \tag{1.16}$$

Here, δ_b is the thermal banana excursion width, while τ_{eff} is the effective collision time for trapped particles. In contrast to before, we modify the treatment of collisions by realizing that trapped particles only need to scatter at angles much lower than 90 degrees to leave the trapped particle population. Moreover, we multiply this random walk estimate by the fraction of trapped particles

f_t to account for the fact that not all the particles in the system are trapped. This can be simplified further using elementary calculations of these various quantities, resulting in

$$D_{\text{ban}} \sim \frac{q^2 \rho_c^2}{\epsilon^{3/2} \tau_C}, \tag{1.17}$$

where $\epsilon = r/R_0$ is the ratio of the minor radius r of the particle to the major radius of the device R_0 and is commonly referred to as the inverse aspect ratio. These considerations account for much of the difference between classical and measured transport given that for most conventional tokamaks $\epsilon \ll 1$ in the tokamak core.

In the strongly collisional limit, a trapped particle will instead undergo many collisions before completing a single bounce orbit. Since the majority of particles that contribute to the diffusion process are instead passing, the typical radial step is instead given by the characteristic magnetic drift velocity $v_{D,B}$ multiplied by the thermal transit time τ_t, which is the characteristic time for a particle to complete one full poloidal turn. In this limit, collisions are frequent enough such that even a passing particle will undergo many collisions before completing a full transit. This is called the Pfirsch-Schlüter regime. Since conventional collisions dominate, we obtain the estimate

$$D_{\text{P-S}} \sim \frac{v_{D,B} \tau_t}{\tau_C} = \frac{q^2 \rho_c^2}{\tau_C}, \tag{1.18}$$

where we have again included estimates for the various quantities involved. Here, trapped particles do not play any role, and it is clear that the introduction of strong collisionality quenches much of the neoclassical transport.

To characterize collisionality regimes, it is common to define a dimensionless collisional frequency ν^* as

$$\nu^* = (\omega_b \tau_{\text{eff}})^{-1} = \frac{\epsilon}{\omega_b \tau_C} \approx \frac{\nu_C q R_0}{\epsilon^{3/2} v_T}, \tag{1.19}$$

where v_T is the thermal velocity of the particle and $\nu_C = \tau_C^{-1}$. We also introduce the characteristic neoclassical diffusive coefficient $D_0 = q \rho_c^2 v_T / R_0$. We then find that

$$D_{\text{ban}} \sim \nu^* D_0, \tag{1.20}$$

$$D_{\text{P-S}} \sim \epsilon^{3/2} \nu^* D_0. \tag{1.21}$$

The differing ϵ dependence implies an intermediate regime where these two estimates coincide. This regime, called the plateau regime, lies in the range $1 < \nu^* < \epsilon^{-3/2}$ and is given by

$$D_{\text{plat}} \sim D_0. \tag{1.22}$$

In this regime, the diffusion coefficient is in fact independent of collisionality, hence the name. Physically, this corresponds to the case where a non-zero fraction of trapped particles bounce several times before becoming detrapped. These three regimes characterize collisional neoclassical transport in a tokamak.[22]

In practice, the measured transport in a tokamak can even be larger than that predicted by neoclassical theory. The additional transport is referred to as anomalous and is thought to arise from plasma turbulence driven by instabilities.[23] Turbulence in general is quite difficult to characterize since turbulent plasma is not in thermal equilibrium, has many dynamical degrees of freedom, and is highly nonlinear. The perpendicular wavelengths of these unstable modes are comparable to the gyroradius and are thus microscopic in scale. The presence of these microinstabilities arise from the fusion plasma being far away from thermodynamic equilibrium, thus resulting in a large pressure gradient across the entire plasma. The temperature and density gradients linked to the pressure gradient provide a source of free energy for the plasma to destabilize, thereby resulting in profile and electromagnetic fluctuations. These fluctuations saturate into a quasi-stationary state through nonlinear mode coupling. In particular, the electromagnetic perturbations create a perturbed E-cross-B drift that then gives rise to turbulent fluxes.

1.4 Dissertation scope and outline

Studying these microinstabilities requires the use of numerical models designed to probe the microscopic kinetic physics. Due to the highly nonlinear and complex nature of the problem, computational methods must be used to complement analytical models and physical experiments. Naively, one would simply conduct direct numerical simulations of the necessary kinetic physics that could then be coupled into macroscopic fluid codes through integrated modeling; the requisite

kinetic physics would be calculated separately and then used in tandem with the fluid physics as well as other considerations such radiation, impurities, edge effects, and so on. However, the cost of such simulations is prohibitive. Although the essential kinetic physics in a strong magnetic field can be reduced to the gyrokinetic equation, nonlinear gyrokinetic simulations require $\sim 10^4$ CPUh to calculate the relevant fluxes for any given radial point when considering only a single time scale and a background Maxwellian distribution. Furthermore, the electron-ion mass ratio leads to ion dynamics operating at different time scales than electron dynamics; proper multiscale simulations would be even more expensive. Moreover, the time scale associated with any given kinetic flux calculation is small compared to the time scale of plasma confinement; thousands of flux evaluations are required just to simulate a plasma on the order of seconds.

To use kinetic physics in tandem with simulations of the entire tokamak plasma, model reduction is essential. Such reduced models must be constructed with speed in mind while also preserving a measure of accuracy. To ensure this, these reduced models must be validated against more fundamental approaches and analytical methods. We utilize the quasilinear approximation whereby the nonlinear evolution of the equilibrium background is approximated by the underlying linear physics. The full nonlinear response would normally involve the coupling of all the linear modes; the quasilinear approximation only considers the linear coherent response of any given mode. Such an approach has been successful in the context of turbulence modeling over a wide range of parameters. The main advantage of the quasilinear approach is the large reduction in computational complexity. QuaLiKiz, the gyrokinetic quasilinear code that is the primary focus of this work, takes advantage of simplifications that introduces a 10^6 speedup when compared to nonlinear gyrokinetic codes.[24]

There are three main goals of this dissertation. The first is to use analytic methods to test various assumptions underlying kinetic models. Many fusion models, QuaLiKiz included, rely on the adiabatic invariance of certain quantities to reduce the complexity of the problem for the sake of computational tractability. These adiabatic invariants are often calculated approximately before being implemented in a reduced model. Verifying the approximate invariance of these

quantities and numerically quantifying the exactness of common approximations are both vital to ensuring that they are used correctly within their limits of applicability. The second goal is to explicitly derive the model equations of QuaLiKiz using these adiabatic invariants, both to serve as a guide for how to improve the model and to demonstrate how a reduced model can be in principle constructed. The third goal of this thesis is to then improve QuaLiKiz with a more accurate treatment of collisional physics, as collisional effects are essential to calculate the turbulent fluxes. The rest of this subsection will outline the remainder of this thesis.

In Chapter 2, we describe the theoretical framework informing the rest of this work. Namely, we present descriptions of single charged particle motion, tokamak geometry, and the plasma kinetic equation. Then, we formulate the key adiabatic invariants relevant to this work and describe their applications in quasilinear kinetic physics.

Chapter 3 is devoted to the analysis of one of these adiabatic invariants, the magnetic moment μ. Gyrokinetics, a popular approach to study low-frequency phenomena, is only applicable when μ is conserved. To investigate the limitations of gyrokinetics, we calculate the maximum non-conservation of this magnetic moment in various elementary combinations of electromagnetic fields. This allows us to discuss the limitations of gyrokinetics on a quantifiable basis.

In Chapter 4, we study the bounce-transit motion and the longitudinal adiabatic invariant $J_{\parallel}$. Approximate formulas for bounce-transit motion in concentric circular magnetic geometry are usually derived assuming that the inverse aspect ratio, ϵ, of the tokamak is small. We show that this approximation is not necessary by deriving new analytical formulas that are more accurate. Moreover, we use these formulas to demonstrate that the approximation is robust for $\epsilon \leqslant 0.3$.

A line-by-line derivation of the quasilinear code known as QuaLiKiz is presented in Chapter 5. The goal of this derivation is to provide a self-contained and complete description of the underlying physics and mathematics of QuaLiKiz from first principles. This work serves both as a comprehensive overview of QuaLiKiz specifically as well as an illustration for deriving quasilinear models in general.

Having presented a full description of QuaLiKiz, we then improve its collisional model in Chapter 6. The previous treatment of collisions in QuaLiKiz produced incorrect density profile behavior in the tokamak core when paired with integrated modeling suites. It is suspected that the incorrect calculation of the trapped electron mode (TEM) in the presence of collisions is the likely cause of these incorrect density profiles. We use the Gyrokinetic Electromagnetic Numerical Experiment (GENE) code to investigate the role of collisions in TEMs and construct a reduced model to characterize collsional TEMs via linear GENE simulations. We then compare QuaLiKiz and GENE simulations to tune the free parameters of QuaLiKiz's collisional model to the more exact calculations produced by GENE. We then confirm the improvements made to QuaLiKiz by comparing the density profiles predicted in integrated modeling by the new collisional model to the old collisional model.

Finally, conclusions are given in Chapter 7 along with an outlook of future work to extend the applicability and accuracy of QuaLiKiz.

CHAPTER 2

Theoretical framework

2.1 Introduction

In this chapter, we establish a theoretical framework for tokamak fusion physics that will be used throughout the rest of this work. We begin with the fundamentals by describing single charged particle motion in Sec. 2.2. A particle in a strong magnetic field will spiral around the magnetic field line and drift perpendicular to the magnetic field line. This motivates the decoupling of the fast cyclotron motion and the slow drift motion. This leads to the development of the guiding center equations of motion, which can then be extended to the gyrocenter equations of motion. Both rely on the adiabatic invariance of the magnetic moment, an essential conservation law in magnetized plasmas. Next, we devote Sec. 2.3 to describing tokamak magnetic geometry where the axisymmetric equilibrium magnetic field can be decomposed into toroidal and poloidal components. We then classify particle orbits within such a magnetic field as either trapped, where the particle is trapped by the effective potential well created by the inhomogeneous magnetic field strength, or passing, where the particle passes through the potential well and continues to follow the magnetic field line without reversing direction. Furthermore, we characterize deviations from the magnetic field line. We then use the guiding center framework to prove that the motion is integrable and bounded. This allows us to characterize the motion via the action-angle formalism in Sec. 2.4; in essence, we can construct three adiabatic invariants as well as conjugate angles that together form a canonical coordinate system. Each invariant is linked to one of three different motions: the cyclotron motion, the bounce-transit motion, and the drift motion. This decomposition of the total particle motion forms a hierarchy in the characteristic time scales of the motion and can be used to

perform a perturbative analysis when perturbations in the electromagnetic fields are introduced.

Having sufficiently characterized single charged particle motion in a tokamak, we then discuss kinetic theory in Sec. 2.5. We use the framework of single charged particle motion to develop the appropriate kinetic equations to describe the whole plasma. We first derive the Klimontovich equation, which describes the evolution of all point charges in the plasma. From there, we make use of an averaging procedure to acquire the distribution function, a scalar function that quantifies the probability of measuring particles to be located at specific points in space with specific velocities. The evolution of this distribution function is described by the Boltzmann equation and requires knowledge of the single charged particle behavior as well as collisions; neglecting collisions leads us to the Vlasov equation. The kinetic equation is then reduced to the gyrokinetic equation via magnetic moment conservation. Further reductions are made via the quasilinear approximation within the action-angle variable formalism. We then present a brief description of electrostatic microinstabilities that arise from the plasma kinetics. Finally, a summary of this chapter is given in Sec. 2.6.

2.2 Single charged particle motion

To characterize single charged particle motion, we follow Goldston and Rutherford via Ref. 25. Before discussing the case of general electromagnetic fields, it is illustrative to discuss the case of homogeneous and static magnetic fields. The equation of motion given by the non-relativistic Lorentz force is

$$m\ddot{\mathbf{x}}(t) = e\mathbf{v}(t) \times \mathbf{B}, \tag{2.1}$$

where m and e are the mass and charge of the particle, respectively, $\mathbf{x}$ is the particle position, $\mathbf{v}$ is the particle velocity, and $\mathbf{B}$ is the magnetic field. Taking the magnetic field to be pointing in the $\hat{\mathbf{z}}$

direction, the equation of motion simplifies to

$$\dot{v}_x = \frac{e v_y B}{m}, \tag{2.2}$$

$$\dot{v}_y = -\frac{e v_x B}{m}, \tag{2.3}$$

$$\dot{v}_z = 0. \tag{2.4}$$

Without loss of generality, we define the initial conditions to be

$$\mathbf{x}(0) = \frac{eB}{m} v_{x0} \hat{\mathbf{y}}, \tag{2.5}$$

$$\mathbf{v}(0) = v_{x0} \hat{\mathbf{x}} + v_{z0} \hat{\mathbf{z}} \tag{2.6}$$

From here, it can be easily derived that the solutions to the velocity of the particle are

$$v_x(t) = v_{x0} \cos(\Omega_c t), \tag{2.7}$$

$$v_y(t) = -v_{x0} \sin(\Omega_c t), \tag{2.8}$$

$$v_z(t) = v_{z0}, \tag{2.9}$$

where we define the cyclotron frequency Ω to be

$$\Omega_c \equiv \frac{eB}{m}. \tag{2.10}$$

The cyclotron frequency is also known as the gyrofrequency and the Larmor frequency. The position of the particle can then be integrated from these solutions:

$$\mathbf{x}(t) = \rho_c (\sin(\Omega_c t) \hat{\mathbf{x}} + \cos(\Omega_c t) \hat{\mathbf{y}}) + v_{z0} t. \tag{2.11}$$

Here, we define the gyroradius (also known as the gyroradius or Larmor radius) to be

$$\rho_c \equiv \frac{v_\perp}{\Omega_c} = \frac{m v_{x0}}{eB}, \tag{2.12}$$

where $v_\perp$ is the speed perpendicular to the magnetic field. This rudimentary analysis reveals that the particle follows the magnetic field line in a helical pattern denoted as the cyclotron motion or gyromotion. We then obtain

$$\mathbf{x}(t) = \boldsymbol{\rho}_c(t) + \mathbf{x}_{\mathrm{GC}}(t), \tag{2.13}$$

where we have decomposed the solution into the gyromotion $\boldsymbol{\rho}_c$ and the guiding center motion $\mathbf{x}_{\mathrm{GC}}$. In this simple case, the guiding center velocity is given by

$$\mathbf{v}_{\mathrm{GC}}(t) = v_{z0}\hat{\mathbf{z}} = v_{\parallel}\hat{\mathbf{b}}, \tag{2.14}$$

where $v_{\parallel}$ and $\hat{\mathbf{b}}$ are the velocity and unit vector parallel to the magnetic field, respectively. Fig. 2.1 presents a useful picture of this basic motion. Given a strong magnetic field, this is the dominant motion of the charged particle. It is clear then how strong closed magnetic fields can be used to confine a plasma; the zeroth-order motion simply corresponds to a gyration about the field line while the guiding center moves along the magnetic field line.

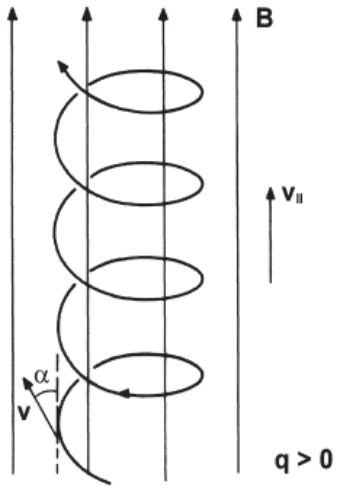

Figure 2.1: Helical orbit in a uniform and static magnetic field for a particle with positive charge q. Note that a negatively charged particle would gyrate with opposite handedness with respect to the magnetic field direction. Source: Ref. 21.

We now consider generalizations of the system by considering perturbations to the equations of motion. The simplest case is to introduce a static force $\mathbf{F}_0$:

$$m\ddot{\mathbf{x}}(t) = e\mathbf{v}(t) \times \mathbf{B} + \mathbf{F}_0. \tag{2.15}$$

A simple transformation $\mathbf{u} = \mathbf{v} - (\mathbf{F}_0 \times \mathbf{B})/B^2$ can be utilized to simplify the equations of motion. We find that the solution can be decomposed to be identical to Eq. (2.13), where the only change lies in the guiding center velocity,

$$\mathbf{v}_{\mathrm{GC}}(t) = v_{\parallel}(t)\hat{\mathbf{b}} + \mathbf{v}_D, \tag{2.16}$$

where

$$\dot{v}_{\parallel} = \mathbf{F}_0 \cdot \hat{\mathbf{b}}, \tag{2.17}$$

$$\mathbf{v}_D = \frac{\mathbf{F}_0 \times \mathbf{B}}{B^2}. \tag{2.18}$$

The only change to the parallel motion is due to the inclusion of the force $\mathbf{F}_0$ in a typical way. Motion perpendicular to the magnetic field, however, now includes a drift $\mathbf{v}_D$ generated by the dual effect of $\mathbf{F}_0$ and $\mathbf{B}$ on the particle. Essentially, the additional force accelerates and decelerates the particle throughout the cyclotron orbit. The result is the radius of curvature of the motion varies throughout the orbit, thus manifesting as a net drift perpendicular to both $\mathbf{F}_0$ and $\mathbf{B}$. Although rudimentary, this reveals the fundamental reason charged particles possess guiding center drifts.

An important, more general case concerns a static electric field $\mathbf{E}$ in tandem with a static inhomogeneous magnetic field. Given that tokamaks are explicitly designed with strong background magnetic fields, the length scale of the inhomogeneities are taken to be much larger than the gyroradius. Moreover, the electric field in a tokamak is typically much weaker than the magnetic field. We can therefore treat these additional complexities as perturbations to the base gyromotion. This allows us to expand the velocity vector as $\mathbf{v} = \mathbf{v}_0 + \mathbf{v}_1 + \ldots$ and so on. To zeroth-order, the equation of motion in the perpendicular direction is simply

$$m\dot{\mathbf{v}}_0 = e\mathbf{v}_0 \times \mathbf{B}_{\mathrm{GC}}, \tag{2.19}$$

which corresponds to the gyromotion. Here, the magnetic field is evaluated at the guiding center of the particle according to the Taylor expansion

$$\mathbf{B} = \mathbf{B}_{\mathrm{GC}} + (\mathbf{x}_0 - \boldsymbol{\rho}_c) \cdot \nabla \mathbf{B}_{\mathrm{GC}} = \mathbf{B}_{\mathrm{GC}} - \left(\frac{\mathbf{v}_0 \times \hat{\mathbf{b}}}{\Omega_c}\right) \cdot \nabla \mathbf{B}_{\mathrm{GC}}. \tag{2.20}$$

This allows us to construct a first-order magnetic field for the first-order equation of motion. Meanwhile, given that we assumed a small electric field, there are no zeroth-order forces in the parallel direction or zeroth-order drifts. Therefore, the zeroth-order velocity is

$$\mathbf{v}_0 = v_{\parallel 0}\hat{\mathbf{b}} + \dot{\boldsymbol{\rho}}_c = v_{\parallel 0}\hat{\mathbf{b}} + v_\perp \cos(\Omega_c t)\hat{\mathbf{e}}_\perp + v_\perp \sin(\Omega_c t)\left(\hat{\mathbf{b}} \times \hat{\mathbf{e}}_\perp\right), \tag{2.21}$$

where $\hat{\mathbf{e}}_\perp$ is an arbitrary local unit vector perpendicular to the magnetic field. By iterating, we then write the first-order equation of motion after performing a cyclotron average, noting that

$$\langle \dot{\boldsymbol{\rho}}_c \rangle = \langle \boldsymbol{\rho}_c \rangle = \mathbf{0}, \tag{2.22}$$

$$\langle \mathbf{v}_0 \rangle = \mathbf{v}_{\parallel 0}\hat{\mathbf{b}}, \tag{2.23}$$

$$\langle \mathbf{v}_0 \mathbf{v}_0 \rangle = v_{\parallel 0}^2 \hat{\mathbf{b}}\hat{\mathbf{b}} + \frac{v_{\perp 0}^2}{2}\left(\hat{\mathbf{e}}_\perp \hat{\mathbf{e}}_\perp + \left(\hat{\mathbf{b}} \times \hat{\mathbf{e}}_\perp\right)\left(\hat{\mathbf{b}} \times \hat{\mathbf{e}}_\perp\right)\right), \tag{2.24}$$

where we have introduced conventional dyadic notation. Thus, after time averaging over the cyclotron period, we can then write the first-order equation of motion as

$$m\left\langle \frac{d}{dt}(\mathbf{v}_0)\right\rangle = e\mathbf{E} + e\,\langle \mathbf{v}_1 \rangle \times \mathbf{B} - \frac{e}{B}\left\langle \left(\mathbf{v}_0 \times \left[\left(\mathbf{v}_0 \times \hat{\mathbf{b}}\right) \cdot \nabla \mathbf{B}\right]\right)\right\rangle, \tag{2.25}$$

where we have introduced the electric field, the magnetic force due to the first-order velocity and zeroth-order magnetic field, and the magnetic force due to the zeroth-order velocity and first-order magnetic field. The first-order drift is given by $\mathbf{v}_D = \langle \mathbf{v}_1 \rangle$. The time derivative term can be expanded for static fields using

$$\left\langle \frac{d}{dt}(\mathbf{v}_0)\right\rangle = \left\langle \frac{d}{dt}\left(\mathbf{v}_{0\parallel}\hat{\mathbf{b}}\right)\right\rangle = \dot{v}_{0\parallel}\hat{\mathbf{b}} + v_{0\parallel}\left\langle \frac{d\hat{\mathbf{b}}}{dt}\right\rangle = \dot{v}_{0\parallel}\hat{\mathbf{b}} + v_{0\parallel}\left(v_{0\parallel}\hat{\mathbf{b}} \cdot \nabla\hat{\mathbf{b}}\right). \tag{2.26}$$

We then note that

$$\hat{\mathbf{b}} \cdot \nabla\hat{\mathbf{b}} = \frac{1}{2}\nabla\left(\hat{\mathbf{b}}^2\right) - \hat{\mathbf{b}} \times \left(\nabla \hat{\mathbf{b}}\right) = -\hat{\mathbf{b}} \times \left(\nabla \hat{\mathbf{b}}\right) \tag{2.27}$$

and compute via the aid of Eq. (2.22) that

$$\left\langle \left(\mathbf{v}_0 \times \left[\left(\mathbf{v}_0 \times \hat{\mathbf{b}}\right) \cdot \nabla \mathbf{B}\right]\right)\right\rangle = \frac{v_{0\perp}^2}{2}\nabla B. \tag{2.28}$$

The parallel component of Eq. (2.25) then reads

$$m\frac{dv_{0\parallel}}{dt} = \hat{\mathbf{b}} \cdot \left(e\mathbf{E} - \frac{mv_{0\perp}^2}{2B}\nabla B \right). \tag{2.29}$$

Meanwhile, taking the cross product of Eq. (2.25) and $\hat{\mathbf{b}}$ reveals that

$$\mathbf{v}_D = \frac{\mathbf{E}\times\mathbf{B}}{B^2} + \frac{\mathbf{B}\times(\mu\nabla B)}{eB^2} + \frac{\mathbf{B}\times\left(mv_{0\parallel}^2\boldsymbol{\kappa}\right)}{eB^2} = \mathbf{v}_E + \mathbf{v}_{\nabla B} + \mathbf{v}_{R_c}, \tag{2.30}$$

where we have defined the magnetic moment μ and the curvature vector $\boldsymbol{\kappa}$ such that

$$\mu \equiv \frac{mv_\perp^2}{2B} = \frac{W_\perp}{B}, \tag{2.31}$$

$$\boldsymbol{\kappa} \equiv \hat{\mathbf{b}} \cdot \nabla\hat{\mathbf{b}}. \tag{2.32}$$

These are the classical guiding center drifts quoted in many introductory textbooks: the E-cross-B drift $\mathbf{v}_E$, the grad-B drift $\mathbf{v}_{\nabla B}$, and the curvature drift $\mathbf{v}_{R_c}$. The E-cross-B drift arises from the electric field; because the electric force is charge dependent, the net drift is charge independent, leading to ions and electrons drifting in the same direction with the same speed. The electric force also appears in the parallel equation of motion in the usual way. The grad-B drift ultimately arises from the inhomogeneities of the magnetic field leading to differentiations in the radius of curvature in the cyclotron motion. This effectively leads to a description where the charged particle motions can be interpreted as a current ring with a dipole moment μ with a diamagnetic mirror force corresponding to

$$\mathbf{F}_d = -\mu\nabla B. \tag{2.33}$$

This is identical to the force on a magnetic dipole with dipole moment $-\mu\hat{\mathbf{b}}$, hence why it is referred to as diamagnetic. Lastly, the curvature drift arises from the curvature of the magnetic field. For the particle to follow the field line closely, it must accelerate due to the field line's curvature. This acceleration can be framed as a centrifugal force:

$$\mathbf{F}_C = -mv_{0\parallel}^2\boldsymbol{\kappa}. \tag{2.34}$$

Since this centrifugal force is perpendicular to $\hat{\mathbf{b}}$ and therefore the parallel motion, it does not to lowest-order contribute to the parallel equation of motion.

The significance of the magnetic moment μ is that it is an adiabatic invariant, leading to lowest-order that

$$\frac{d\mu}{dt} = 0. \tag{2.35}$$

A rigorous way of demonstrating is provided by in Kruskal in Ref. 26. It is important to note that the adiabatic invariance of μ can be proven through geometrical arguments without presupposing a cyclotron motion and cyclotron average. This more rigorous method also leads to what is called the guiding center equations of motion by decoupling the gyromotion from the drift motion. Once magnetic moment invariance is on rigorous footing, the basic sketch to acquiring the guiding center equations of motion is as follows: we first note that the Lagrangian for a charged particle in an electromagnetic field is

$$L = \frac{1}{2}mv^2 + e\mathbf{v}\cdot\mathbf{A} - q\Phi, \tag{2.36}$$

where $\mathbf{A}$ is the magnetic vector potential and Φ is the electrostatic potential such that

$$\mathbf{E} = -\nabla\Phi - \frac{\partial\mathbf{A}}{\partial t}, \tag{2.37}$$

$$\mathbf{B} = \nabla\times\mathbf{A}. \tag{2.38}$$

Meanwhile, the Hamiltonian is

$$H = \frac{1}{2m}(\mathbf{p} - e\mathbf{A})^2 + e\Phi, \tag{2.39}$$

where the canonical momentum is $\mathbf{p} = m\mathbf{v}+e\mathbf{A}$. Both the Lagrangian and Hamiltonian are functions of seven coordinates. The Lagrangian is explicitly dependent on the coordinate space variables $(\mathbf{x}, \mathbf{v})$ as well as time t, while the Hamiltonian is dependent on the phase space variables $(\mathbf{x}, \mathbf{p})$ and time t. The advantage of the Lagrangian formulation is that it yields the Euler-Lagrange equations for coordinate space, whereas the Hamiltonian formulation yields Hamilton's equations of motion for canonical coordinates. However, it would be most advantageous to use general coordinates; the phase space Lagrangian allows for such an approach. The single particle phase space Lagrangian

is

$$\mathcal{L}(\mathbf{x}, \dot{\mathbf{x}}, \mathbf{p}, \dot{\mathbf{p}}, t) = \mathbf{p} \cdot \dot{\mathbf{x}} - H(\mathbf{q}, \mathbf{p}, t). \tag{2.40}$$

Unlike the ordinary Lagrangian or the Hamiltonian, the phase space Lagrangian is a function of thirteen coordinates (including time), and the following Euler-Lagrange equations reproduce Hamilton's equations of motion:

$$\frac{d}{dt}\left(\frac{\partial \mathcal{L}}{\partial \dot{\mathbf{x}}}\right) = \frac{\partial \mathcal{L}}{\partial \mathbf{x}}, \tag{2.41}$$

$$\frac{d}{dt}\left(\frac{\partial \mathcal{L}}{\partial \dot{\mathbf{p}}}\right) = \frac{\partial \mathcal{L}}{\partial \mathbf{p}}. \tag{2.42}$$

This phase space Lagrangian can be transformed with a spatial coordinate transformation from $\mathbf{x}$ to $\mathbf{z}$. Although this transformation is in general non-canonical, the Euler-Lagrange equations reproduce the correct equations of motion. In these new coordinates $\mathbf{z}$, the phase space Lagrangian is

$$\mathcal{L} = \left(\mathbf{p} \cdot \frac{\partial \mathbf{x}}{\partial \mathbf{z}}\right) \cdot \dot{\mathbf{z}} + H - \mathbf{p} \cdot \frac{\partial \mathbf{x}}{\partial t}. \tag{2.43}$$

Through an ordering argument for small inhomogeneities and small electric field, Littlejohn in Refs. 27 and 28 showed that the phase space Lagrangian in terms of the guiding center position $\mathbf{X}$ is

$$\mathcal{L}(\mathbf{X}, \dot{\mathbf{X}}, v_\parallel, \mu, \alpha, \dot{v}_\parallel, \dot{\mu}, \dot{\alpha}) = \left(e\mathbf{A} + mv_\parallel \hat{\mathbf{b}}\right) \cdot \dot{\mathbf{X}} + \frac{m\mu}{e}\dot{\alpha} - \frac{1}{2}mv_\parallel^2 - \mu B - e\Phi. \tag{2.44}$$

The new variable α is known as the gyrophase. The first few Euler-Lagrange equations result in

$$\dot{\alpha} = \frac{eB}{m} = \Omega_c, \tag{2.45}$$

$$\dot{\mu} = 0, \tag{2.46}$$

$$v_\parallel = \mathbf{X} \cdot \hat{\mathbf{b}}. \tag{2.47}$$

The first equation states that the time derivative of the gyrophase is the cyclotron frequency, as expected. The second equation confirms that the magnetic moment is indeed an adiabatic invariant. We again emphasize that this is not a proof that μ is conserved, as the guiding center construction requires a proof of μ conservation beforehand. The third equation is simply the constraint that the

parallel particle velocity corresponds to the parallel guiding center velocity. After some massaging of the remaining Euler-Lagrange equations, we also obtain

$$B_{\parallel}^{*}\frac{d\mathbf{X}}{dt} = v_{\parallel}\mathbf{B}^{*} + \frac{\mathbf{B}}{eB}\times(\mu\nabla B - e\mathbf{E}^{*}), \tag{2.48}$$

$$B_{\parallel}^{*}m\frac{dv_{\parallel}}{dt} = \mathbf{B}^{*}\cdot(e\mathbf{E}^{*} - \mu\nabla B). \tag{2.49}$$

where we define the modified electromagnetic quantities as

$$\mathbf{A}^{*} = \mathbf{A} + \frac{mv_{\parallel}}{e}\hat{\mathbf{b}}, \tag{2.50}$$

$$\mathbf{B}^{*} = \nabla\times\mathbf{A}^{*} = \mathbf{B} + \frac{mv_{\parallel}}{e}\nabla\times\hat{\mathbf{b}}, \tag{2.51}$$

$$\mathbf{E}^{*} = -\nabla\Phi - \frac{\partial\mathbf{A}^{*}}{\partial t} = \mathbf{E} - \frac{mv_{\parallel}}{e}\frac{\partial\hat{\mathbf{b}}}{\partial t}, \tag{2.52}$$

$$\mathbf{B}_{\parallel}^{*} = \mathbf{B}^{*}\cdot\hat{\mathbf{b}} = B + \frac{mv_{\parallel}}{e}\hat{\mathbf{b}}\cdot\left(\nabla\times\hat{\mathbf{b}}\right). \tag{2.53}$$

After some manipulation, we also find that

$$\frac{\mathbf{B}^{*}}{B_{\parallel}^{*}} = \hat{\mathbf{b}} + \frac{mv_{\parallel}}{eB_{\parallel}^{*}}\hat{\mathbf{b}}\times\boldsymbol{\kappa}, \tag{2.54}$$

thereby introducing the curvature term. The guiding center equations of motion then simplify to

$$\frac{d\mathbf{X}}{dt} = v_{\parallel}\hat{\mathbf{b}} + \frac{\mathbf{E}\times\mathbf{B}}{B_{\parallel}^{*}B} + \frac{\mathbf{B}\times\left(mv_{\parallel}^{2}\boldsymbol{\kappa} + \mu\nabla B\right)}{eB_{\parallel}^{*}B} + \frac{mv_{\parallel}}{eB_{\parallel}^{*}B}\mathbf{B}\times\frac{\partial\hat{\mathbf{b}}}{\partial t}, \tag{2.55}$$

$$m\frac{dv_{\parallel}}{dt} = \left(\hat{\mathbf{b}} + \frac{mv_{\parallel}}{eB_{\parallel}^{*}}\hat{\mathbf{b}}\times\boldsymbol{\kappa}\right)\cdot\left(e\mathbf{E} - \mu\nabla B - mv_{\parallel}\frac{\partial\hat{\mathbf{b}}}{\partial t}\right), \tag{2.56}$$

where all fields are explicitly evaluated at the guiding center. We have thus acquired modified guiding center drifts as well as the inclusion of terms that correspond to the time dependence of the electromagnetic fields. By assuming a sufficiently small gyroradius and static fields, we obtain the classical equations,

$$\frac{d\mathbf{X}}{dt} \approx v_{\parallel}\hat{\mathbf{b}} + \frac{\mathbf{E}\times\mathbf{B}}{B^{2}} + \frac{\mathbf{B}\times(\mu\nabla B)}{eB^{2}} + \frac{\mathbf{B}\times\left(mv_{0\parallel}^{2}\boldsymbol{\kappa}\right)}{eB^{2}}, \tag{2.57}$$

$$m\frac{dv_{\parallel}}{dt} \approx \hat{\mathbf{b}}\cdot(e\mathbf{E} - \mu\nabla B). \tag{2.58}$$

Two additional conservation laws aside from μ conservation can be obtained from the guiding center equations of motion. We first define the energy of the guiding center particle as

$$E \equiv \frac{1}{2} m v_{\parallel}^2 + \mu B + e\Phi. \tag{2.59}$$

This is simply the sum of the kinetic energy and the electrostatic potential where the perpendicular kinetic energy is μB. Using the equations of motion, we find that

$$\frac{dE}{dt} = (e\mathbf{E}^* - \mu \nabla B) \cdot \frac{d\mathbf{X}}{dt} + \mu \left(\frac{\partial B}{\partial t} + \frac{d\mathbf{X}}{dt} \cdot \nabla B \right) + e \frac{d\Phi}{dt}. \tag{2.60}$$

Here, we utilized the fact that since all fields are evaluated at the guiding center, the total time derivative can be written as

$$\frac{d}{dt} = \frac{\partial}{\partial t} + \frac{d\mathbf{X}}{dt} \cdot \nabla. \tag{2.61}$$

This then simplifies to

$$\frac{dE}{dt} = -\left(\frac{\partial \mathbf{A}}{\partial t} + m v_{\parallel} \frac{\partial \hat{\mathbf{b}}}{\partial t} \right) \cdot \frac{d\mathbf{X}}{dt} + \mu \frac{\partial B}{\partial t} + e \frac{\partial \Phi}{\partial t}. \tag{2.62}$$

In a quasistatic scenario, the background electromagnetic field is in equilibrium and thus not explicitly time dependent. This immediately leads us to energy conservation:

$$\frac{dE}{dt} = 0. \tag{2.63}$$

Next, we note that in a tokamak equilibrium, the electromagnetic fields are axisymmetric. Although the presence of a magnetic ripple in practice breaks the toroidal symmetry, the effect is small enough for our purposes. For this part of the derivation, it is easiest to work in orthonormal cylindrical coordinates (R, z, φ). Here, R is the perpendicular distance from the major axis of the tokamak, z is the height along the center axis, and φ is the geometric toroidal coordinate. We take these to be our guiding center variables. The guiding center position can then be written as

$$\mathbf{X} = R\hat{\mathbf{R}} + z\hat{\mathbf{z}}, \tag{2.64}$$

where

$$\frac{\partial \hat{\mathbf{R}}}{\partial \varphi} = \hat{\boldsymbol{\varphi}}, \tag{2.65}$$

$$\frac{\partial \hat{\mathbf{z}}}{\partial \varphi} = \mathbf{0}. \tag{2.66}$$

Meanwhile, the guiding center velocity is

$$\frac{d\mathbf{X}}{dt} = \frac{\partial \mathbf{X}}{\partial R}\dot{R} + \frac{\partial \mathbf{X}}{\partial Z}\dot{Z} + \frac{\partial \mathbf{X}}{\partial \varphi}\dot{\varphi}, \tag{2.67}$$

leading to

$$\frac{\partial}{\partial \dot{\varphi}}\left(\frac{d\mathbf{X}}{dt}\right) = \frac{\partial \mathbf{X}}{\partial \varphi} = R\hat{\boldsymbol{\varphi}}. \tag{2.68}$$

If the electromagnetic fields are axisymmetric, then φ is an ignorable coordinate. This means that under an appropriate choice in gauge for the vector and scalar potentials, $\mathcal{L}$ has no explicit φ dependence. We define that canonical toroidal momentum as

$$P_\varphi \equiv \frac{\partial \mathcal{L}}{\partial \dot{\varphi}}, \tag{2.69}$$

and then obtain from the Euler-Lagrange equations that

$$\frac{dP_\varphi}{dt} = \frac{d}{dt}\left(\frac{\partial \mathcal{L}}{\partial \dot{\varphi}}\right) = \frac{\partial \mathcal{L}}{\partial \varphi} = 0. \tag{2.70}$$

The canonical toroidal momentum can be computed directly as

$$P_\varphi = \frac{\partial}{\partial \dot{\varphi}}\left(e\mathbf{A}\cdot\frac{\mathbf{X}}{dt} + mv_\parallel \hat{\mathbf{b}}\cdot\frac{\mathbf{X}}{dt}\right) = eR\mathbf{A}\cdot\hat{\boldsymbol{\varphi}} + mRv_\parallel\hat{\mathbf{b}}\cdot\hat{\boldsymbol{\varphi}} = eA_\varphi R + \frac{mRv_\parallel B_\varphi}{B}. \tag{2.71}$$

The canonical toroidal momentum is commonly written as

$$P_\varphi = -e\psi + \frac{mRv_\parallel B_\varphi}{B}, \tag{2.72}$$

where ψ is minus the poloidal flux normalized by 2π; a more explicit definition of ψ as well as its significance will be discussed in Sec. 2.3.

In summary, from guiding center theory we obtain equations of motion that correspond to the guiding center drifts as well the following invariants of motion:

$$\frac{d\mu}{dt} = 0, \tag{2.73}$$

$$\frac{dE}{dt} = 0, \tag{2.74}$$

$$\frac{dP_\varphi}{dt} = 0. \tag{2.75}$$

It is difficult to overstate the significance of obtaining three invariants of motion from guiding center theory. The guiding center equations of motion correspond to three degrees of freedom. The use of the phase space Lagrangian guarantees that we are ultimately working in a Hamiltonian system (albeit in non-canonical coordinates) that is ultimately integrable. Moreover, powerful theorems such as the Liouville-Arnold theorem can be applied; this is the subject of Sec. 2.4. Finally, it should be noted that the guiding center equations of motion are alone of little applicability when concerning quickly varying electromagnetic perturbations; an extension of this theory will be discussed in Sec. 2.5 within the context of gyrokinetics.

2.3 Tokamak geometry

We next summarize important properties of magnetic field geometry in tokamaks. In this section, we closely follow D'haeseller in Ref. 29. The first task is to construct an appropriate coordinate system. There are two popular choices in orthonormal coordinate systems, the toroidal coordinate system (r, θ, φ) and the cylindrical coordinate system (R, z, φ). Note that we take the convention that $\hat{\mathbf{r}} \times \hat{\boldsymbol{\theta}} = \hat{\boldsymbol{\varphi}}$ and $\hat{\mathbf{R}} \times \hat{\mathbf{z}} = \hat{\boldsymbol{\varphi}}$ so that we do not have to define two different toroidal coordinates for the sake of right-handedness. Both coordinate systems offer the advantage of a simplified geometry, leading to orthonormal basis vectors as well as manifestly physical interpretations of each coordinate. Fig. 2.2 presents a useful diagram of these coordinate systems. However, these coordinate systems are often inconvenient in practice; although the these coordinate systems involve simple geometries, magnetic tokamak geometries are in general quite complicated. For analytical calculations, it is often more convenient to work in more natural coordinate systems that take into account the complex magnetic geometry. In such a coordinate system, the complexities are taken into account by the transformation equations between coordinate systems. In this work, we will primarily use coordinate systems that are closely related to the mundane toroidal coordinate system.

In a tokamak, magnetic field lines lie on surfaces known as magnetic flux surfaces. From ideal

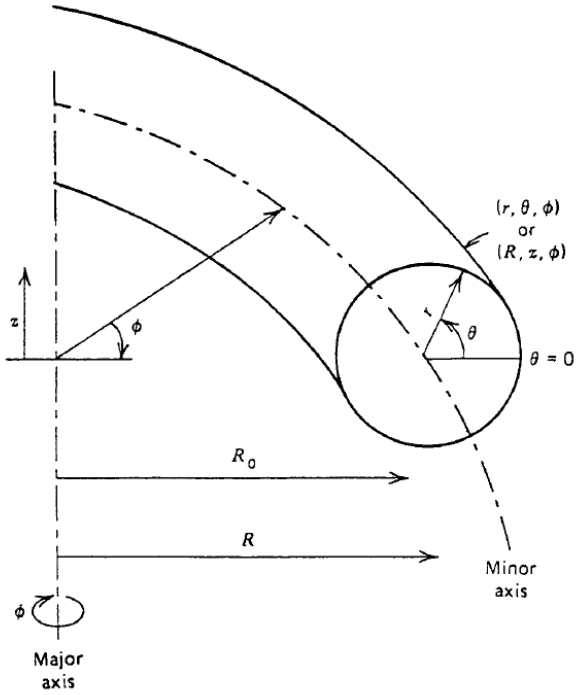

Figure 2.2: Toroidal coordinates and cylindrical coordinates for a tokamak. Source: Ref. 17.

magnetohydrodynamic (MHD) theory it can be shown that these surfaces are isobaric surfaces with constant pressure p. In an asymmetric device such as a tokamak, these flux surfaces are guaranteed to exist. Although perturbations away from axisymmetry can in principle complicate the picture, for the purposes of this work we treat these perturbations as small enough such that we presuppose the existence of nested toroidal flux surfaces. Thus, we ignore the effects of magnetic islands and consider only one unique magnetic axis, the flux surface corresponding to zero volume. We note that the magnetic axis in general does not coincide with the minor axis of the tokamak. We can then label these magnetic with a flux coordinate Ψ with the requirement that

$$\mathbf{B} \cdot \nabla \Psi = 0. \tag{2.76}$$

Functions that are dependent only Ψ are known as flux functions. The particular flux label we

choose to use is minus the poloidal flux normalized by 2π and defined to be

$$\psi \equiv -\frac{1}{2\pi}\int\int \mathbf{B}\cdot \mathrm{d}\mathbf{S}_\theta\,, \tag{2.77}$$

where the surface is defined to be the disk tangent to the flux surface everywhere. For the remaining coordinates, we use (χ, φ) where φ is the typical geometric toroidal angle and χ is chosen such that (χ, φ) are straight field line coordinates such that magnetic field lines are straight in (χ, φ). We can then write the axisymmetric magnetic field as

$$\mathbf{B} = I(\psi)\nabla\varphi + \nabla\varphi \times \nabla\psi, \tag{2.78}$$

or equivalently in Clebsch form

$$\mathbf{B} = \nabla(\varphi - q(\psi)\chi) \times \nabla\psi, \tag{2.79}$$

where I and q are flux functions (that is, only functions of ψ). The toroidal field is $\mathbf{B}_T = I(\psi)\nabla\varphi$ whereas the smaller poloidal field is $\mathbf{B}_P = \nabla\varphi \times \nabla\psi$. Since $|\nabla\varphi| = 1/R$, the total field strength decreases inversely with the major radius R in accordance with a magnetic field from a toroidal solenoid. It is important to note that this curvilinear system is not orthonormal or even orthogonal. Moreover, our definition of the poloidal flux ψ increases radially outward from the magnetic axis, thus making (ψ, χ, φ) a right-handed coordinate system. We can then write the vector potential $\mathbf{A}$ as

$$\mathbf{A} = \Phi_t(\psi)\nabla\chi - \psi\nabla\varphi, \tag{2.80}$$

where Φ_t is the toroidal flux normalized by 2π. Therefore, the physical toroidal component of $\mathbf{A}$ is such that

$$RA_\varphi = R\mathbf{A}\cdot(R\nabla\varphi) = -\psi, \tag{2.81}$$

thus confirming the relation between the poloidal flux and the vector potential. Here, we used the fact that these coordinates satisfy the relations

$$\nabla\varphi\cdot\nabla\psi = \nabla\varphi\cdot\nabla\chi = 0. \tag{2.82}$$

The flux function q is known as the safety factor and is defined as

$$q(\psi) \equiv \frac{\mathbf{B} \cdot \nabla \varphi}{\mathbf{B} \cdot \nabla \chi} = \frac{d\varphi}{d\chi}. \tag{2.83}$$

The safety factor quantities the number of times a magnetic field line wraps around toroidally per poloidal turn. Flux surfaces where the magnetic field line wraps back into itself are known as rational flux surfaces where q is a rational number. In a circular geometry, the safety factor can be approximated as

$$q \approx \frac{rB_T}{R_0 B_P}. \tag{2.84}$$

Moreover, it can be shown that

$$q = \frac{d\Phi_t}{d\psi}. \tag{2.85}$$

The relation between I and q can be seen from taking a dot product of $\mathbf{B}$ with $\nabla\varphi$, leading to

$$I|\nabla\varphi|^2 = q\nabla\varphi \cdot (\nabla\psi \times \nabla\chi). \tag{2.86}$$

We then obtain

$$\frac{I}{JR^2} = q, \tag{2.87}$$

where J is the Jacobian of the transformation from Cartesian coordinates to (ψ, χ, φ) and is defined as

$$J \equiv \frac{1}{\nabla\varphi \cdot (\nabla\psi \times \nabla\chi)}. \tag{2.88}$$

Moreover, we can construct the straight field line coordinate χ directly from the poloidal angle θ. The angle θ is typically measured with respect to either the magnetic axis or the center of the flux surface rather than the minor axis of the tokamak. Whatever the choice, the construction requires that the poloidal angle θ satisfy

$$\nabla\varphi \cdot \nabla\theta = 0. \tag{2.89}$$

The straight field line angle can then be calculated as

$$\chi = \frac{1}{q}\int_0^\theta \mathrm{d}\theta' \, \frac{\mathbf{B} \cdot \nabla\varphi}{\mathbf{B} \cdot \nabla\theta'} \frac{1}{q} \int_0^\theta \mathrm{d}\theta' \, \frac{I}{R^2} \frac{1}{\nabla\varphi \cdot (\nabla\psi \times \nabla\theta)}. \tag{2.90}$$

Likewise, the safety factor q can also be calculated via a similar method,

$$q = \frac{1}{2\pi}\int_0^{2\pi} \mathrm{d}\theta \, \frac{\mathbf{B} \cdot \nabla\varphi}{\mathbf{B} \cdot \nabla\theta} = \frac{1}{2\pi}\int_0^{2\pi} \mathrm{d}\theta \, \frac{I}{R^2} \frac{1}{\nabla\varphi \cdot (\nabla\psi \times \nabla\theta)}. \tag{2.91}$$

2.3.1 Guiding center motion in a tokamak

Now that we have characterized tokamak geometry, we analyze charged particle motion in a tokamak magnetic field. As explained in Sec. 2.2, the charged particle gyrates about magnetic field lines and is subject to magnetic drifts. Taking our variables to be guiding center variables, we obtain the guiding center equations of motion,

$$\frac{d\psi}{dt} = \mathbf{v} \cdot \nabla\psi, \tag{2.92}$$

$$\frac{d\chi}{dt} = \mathbf{v} \cdot \nabla\chi, \tag{2.93}$$

$$\frac{d\varphi}{dt} = \mathbf{v} \cdot \nabla\varphi, \tag{2.94}$$

with the velocity being $\mathbf{v} = v_\parallel \hat{\mathbf{b}} + \mathbf{v}_D$. Rather than solving these equations exactly, we analyze them in successive orders of the gyroradius. To lowest-order, the guiding center particle follows the field line exactly and does not stray from the flux surface. This leads to the constraints

$$\frac{d\psi}{dt} = 0, \tag{2.95}$$

$$\frac{d}{dt}(\varphi - q\chi) = 0. \tag{2.96}$$

Therefore, the lowest-order guiding center equations of motion are

$$\frac{d\psi}{dt} = 0, \tag{2.97}$$

$$\frac{d\chi}{dt} = v_\parallel \hat{\mathbf{b}} \cdot \nabla\chi, \tag{2.98}$$

$$\frac{d\varphi}{dt} = q v_\parallel \hat{\mathbf{b}} \cdot \nabla\chi. \tag{2.99}$$

Due to toroidal symmetry, it suffices to analyze $\dot{\chi}$. Essentially, our constraints have turned a 3-dimensional problem into a 1-dimensional problem. We then write

$$\frac{d\chi}{dt} = \Omega_\chi, \tag{2.100}$$

where

$$\Omega_\chi \equiv v_\parallel \frac{\mathbf{B} \cdot \nabla\chi}{B} = \frac{v_\parallel}{JB} = \frac{I v_\parallel}{qR^2 B}. \tag{2.101}$$

We then utilize conservation of the magnetic moment and the energy to find

$$v_{\parallel} = \epsilon_{\parallel}\sqrt{\frac{2}{m}}\sqrt{E - \mu B}, \tag{2.102}$$

where we define $\epsilon_{\parallel}$ to be the sign of $v_{\parallel}$. Here, we have neglected any electrostatic potential since we assume a small electric field. We then find that

$$\left|\frac{d\chi}{dt}\right| = \sqrt{\frac{2E}{m}}\sqrt{1 - \lambda b}\frac{I}{qR^2B}, \tag{2.103}$$

where we define λ and b such that

$$\lambda \equiv \frac{\mu B_{\min}}{E}, \tag{2.104}$$

$$b(\psi, \chi) \equiv \frac{B}{B_{\min}}, \tag{2.105}$$

$$B_{\min}(\psi) \equiv B(\psi, \chi = 0). \tag{2.106}$$

Here, $\chi = 0$ corresponds to the outermost point of the flux surface. It is there that the magnetic field strength it at its minimum on the flux surface, and thus it is also known as the low field side. Meanwhile, $B_{\max} = B(\psi, \chi = \pi)$ corresponds to the innermost, high field side side. Thus, we take $-\pi \leq \chi \leq \pi$. The distinction between the low field side and high field side originates from the $1/R$ dependence of the magnetic field strength. According to our constraints and reductions, E, λ, and ψ are all constant. The reduced equation of motion therefore only depends on χ itself and is thus completely integrable. Moreover, the motion is periodic because the magnetic field strength is 2π periodic in χ, where in this reduced system we stitch together any solutions outside of the domain $-\pi \leq \chi \leq \pi$. Since we are considering motion on a flux surface, we will ignore any ψ dependence for the time being.

The specific nature of the motion depends on the value λ. For a large enough value of λ, the speed of the guiding center particle along the field line vanishes to zero eventually due to the mirror force. A small enough value of λ, meanwhile, will lead to a particle that never reaches zero speed. Thus, the magnetic field effectively creates a periodic potential well where particles that cannot overcome the well are trapped, while particles that can overcome the well simply pass through

while following the magnetic field line. We therefore call the former particles trapped particles and the latter particles passing particles. Trapped particles periodically bounce between points of the magnetic field; in an up-down symmetric equilibrium, the flux surface is symmetric across the $\theta = 0$ line, leading to a magnetic field strength that is an even function of both θ and χ. In this equilibrium, we can then define a bounce point $\chi_b > 0$ where $-\chi_b \leq \chi(t) \leq \chi_b$. The requirement is

$$1 - \lambda b(\chi_b) = 0. \tag{2.107}$$

Meanwhile, passing particles will contain no such bounce point regardless of the value of χ. Thus, the conditions that determine whether a particle is trapped or passing are

$$\begin{aligned} \frac{B_{\min}}{B_{\max}} < \lambda \leq \frac{1}{b}, &\qquad \text{trapped,} \\ 0 \leq \lambda < \frac{B_{\min}}{B_{\max}}, &\qquad \text{passing,} \end{aligned} \tag{2.108}$$

where $0 \leq \lambda \leq 1/b$. We note from the definition of λ that

$$\lambda = \frac{v_\perp^2}{v^2}\frac{1}{b} = \frac{v_\perp^2(\chi = 0)}{v^2(\chi = 0)}. \tag{2.109}$$

where $v_\perp$ is the perpendicular velocity associated with the cyclotron motion along the field line. Thus, λ is representative of the pitch angle of the velocity with respect to the magnetic field and we call it the pitch angle parameter. The case where $\lambda = 1$ corresponds to a purely trapped particle with no parallel velocity, whereas $\lambda = 0$ corresponds to a purely passing particle such that $\mu = 0$.

In velocity space, we can construct a a boundary between trapped particles and passing particles, defined by the relation

$$v_\parallel^2 = v_\perp^2 \frac{B_{\max} - B}{B}. \tag{2.110}$$

If we imagine a spherical volume of velocity space, the relation above is simply the intersection of two lines spherically revolved around the $v_\parallel$ axis. Assuming the velocity of particles at any given point on the flux surface is isotropic, we can then use simple spherical geometry to find that the

fraction of trapped particles f_t and the fraction of passing particles f_p are

$$f_t = \sqrt{1 - \frac{B}{B_{\max}}}, \tag{2.111}$$

$$f_p = 1 - \sqrt{1 - \frac{B}{B_{\max}}}. \tag{2.112}$$

It is important to note that the trapped and passing particle fractions are dependent on the angle χ (and thus the poloidal angle). Justification for this can be seen in the following limiting case. If we consider the point on the flux surface $\chi = \pi$, corresponding to the high field side, $f_t(\chi = \pi) = 0$ while $f_p(\chi = \pi) = 1$. This simply because any trapped particle that reaches the high field side must have bounce angle $\chi_b = \pi$ or else be a passing particle. Since the proportion of particles with bounce angle $\chi_b = \pi$ is of measure zero, $f_t(\chi = \pi) = 0$. This is also the same reason why the bounds of λ are dependent on χ. For instance, because particles with $\lambda = 1$ are bound to the low field side of the flux surface due to having 0 parallel velocity, no particles with $\lambda = 1$ can be found on the high field side.

For the trapped and passing particle fraction, we can take into account this discrepancy by averaging over the flux surface. Consider the background density of particles $n(\psi, \chi)$; to compute a flux surface average, we need to count the number of particles per unit length that are either trapped or passing on any given part of the flux surface and divide by the total number of particles per unit length on the flux surface. The flux surface averaged trapped fraction and passing fraction are then

$$\langle f_t \rangle = \frac{\int \mathrm{d}S\, n f_t}{\int \mathrm{d}S\, n} = \frac{\int_{-\pi}^{\pi} \mathrm{d}\chi\, J n f_t}{\int_{-\pi}^{\pi} \mathrm{d}\chi\, J n}, \tag{2.113}$$

$$\langle f_p \rangle = \frac{\int \mathrm{d}S\, n f_p}{\int \mathrm{d}S\, n} = \frac{\int_{-\pi}^{\pi} \mathrm{d}\chi\, J n f_t}{\int_{-\pi}^{\pi} \mathrm{d}\chi\, J n}, \tag{2.114}$$

where in integrating over the flux surface we take advantage of toroidal symmetry and recall that J is the Jacobian for coordinates (ψ, χ, φ). In the case where the density is a flux function, the

expressions simplify to

$$\langle f_t \rangle = \frac{\int_{-\pi}^{\pi} \mathrm{d}\chi \, J f_t}{\int_{-\pi}^{\pi} \mathrm{d}\chi \, J}, \tag{2.115}$$

$$\left\langle f_p \right\rangle = \frac{\int_{-\pi}^{\pi} \mathrm{d}\chi \, J f_t}{\int_{-\pi}^{\pi} \mathrm{d}\chi \, J}. \tag{2.116}$$

It is instructive to consider an approximate magnetic geometry. For small inverse aspect ratio $\epsilon = r/R_0$, the magnetic field strength of a tokamak is often approximated as

$$B \propto \frac{1}{1 + \epsilon \cos(\theta)} \approx 1 - \epsilon \cos(\theta). \tag{2.117}$$

To lowest-order in ϵ, we find that $\theta \approx \chi$. Therefore, the trapped and passing fractions can be approximated as

$$f_t \approx \sqrt{\epsilon(1 + \cos(\theta))}, \tag{2.118}$$

$$f_p \approx 1 - \sqrt{\epsilon(1 + \cos(\theta))}. \tag{2.119}$$

Via substitution of $\theta = 0$, we obtain the familiar formula $f_t(\theta = 0) \approx \sqrt{2\epsilon}$. The well known flux surface averages of these quantities can be computed as

$$\langle f_t \rangle \approx \frac{2}{\pi}\sqrt{2\epsilon}, \tag{2.120}$$

$$\left\langle f_p \right\rangle \approx 1 - \frac{2}{\pi}\sqrt{2\epsilon}. \tag{2.121}$$

Thus, the trapped particle fraction scales with $\sqrt{\epsilon}$.

As mentioned earlier, the bounce-transit motion is periodic. We can thus characterize the timescale of this motion by computing the period T,

$$T = \oint \frac{\mathrm{d}\chi \, qR^2 B}{\sqrt{2E/m}\sqrt{1 - \lambda b}}, \tag{2.122}$$

where we integrate over an entire bounce-transit orbit. One complete orbit for a trapped particle corresponds to a bounce from $-\chi_b$ to χ_b and then back to $-\chi_b$; therefore the bounce period T_b is simply twice the half-period and can be computed as

$$T_b = \int_{-\chi_b}^{\chi_b} \frac{2\,\mathrm{d}\chi \, qR^2 B}{\sqrt{2E/m}\sqrt{1 - \lambda b}}. \tag{2.123}$$

Meanwhile, a full transit orbit corresponds to the particle completing one poloidal turn from $-\pi$ to π, leading to

$$T_t = \int_{-\pi}^{\pi} \frac{\mathrm{d}\chi \, qR^2 B}{\sqrt{2E/m}\sqrt{1-\lambda b}}. \tag{2.124}$$

We then define the bounce frequency ω_b and the transit frequency ω_t such that

$$\omega_b = \frac{2\pi}{T_b}, \tag{2.125}$$

$$\omega_t = \frac{2\pi}{T_t}. \tag{2.126}$$

In the small inverse aspect ratio limit, these integrals can be compute relatively easily with the aid of elliptic integrals. There are two sets of formulas often given for the bounce-transit frequency. One set[30] is given by

$$\omega_b \approx \frac{\pi\omega_0}{2K(\kappa_1)}, \tag{2.127}$$

$$\omega_t \approx \frac{\pi\omega_0\kappa_1}{K\left(\kappa_1^{-1}\right)}, \tag{2.128}$$

where the K is the complete elliptic integral of the first kind and the characteristic bounce-transit frequency is given by

$$\omega_0 \approx \frac{\sqrt{E/m}\sqrt{\epsilon}}{qR_0}. \tag{2.129}$$

Importantly, qR_0 is known as the connection length; it is the characteristic length scale for a full poloidal turn. We also make use of a trapping parameter κ, to be defined momentarily. The other commonly cited set of formulas[31] are

$$\omega_b \approx \frac{\pi\omega_0\sqrt{\lambda}}{2K(\kappa_2)} \approx \frac{\pi\omega_0}{2K(\kappa_2)} \tag{2.130}$$

$$\omega_t \approx \frac{\pi\omega_0\sqrt{\lambda}\kappa_2}{K\left(\kappa_2^{-1}\right)}. \tag{2.131}$$

The difference in the equations comes from the definition of the trapping parameter κ. For a circular magnetic geometry, κ can be defined exactly such that

$$\kappa \equiv \sin(\theta_b/2), \tag{2.132}$$

where θ_b is the poloidal bounce angle. However, depending on how the small ϵ approximation is specifically carried out, the approximate form of κ in terms of the pitch angle parameter λ. The two sets of equations use the following definitions,

$$\kappa_1^2 = \frac{1-\lambda}{2\epsilon}, \tag{2.133}$$

$$\kappa_2^2 = \frac{1-\lambda(1-2\epsilon)}{2\epsilon\lambda}. \tag{2.134}$$

In both cases, $0 \leq \kappa < 1$ corresponds to trapped particles while $1 < \kappa < \infty$ corresponds to passing particles. Although the first set of equation is simpler and more compact, the passing frequency diverges as $\kappa \to \infty$. However, a purely passing particle with finite energy is akin to a pendulum with a high enough speed to make poloidal transits while barely slowing down. More concretely, in the limit that $\kappa \to \infty$ we expect $\mu \to 0$ and $\lambda \to 0$, which corresponds to no magnetic well at all. Thus, the passing frequency in that limit should simply be the velocity of the particle divided by the length of the orbit, leading to

$$\lim_{\lambda\to 0} \omega_t = \frac{\left|v_\parallel\right|}{qR_0} \tag{2.135}$$

In the small ϵ and small λ limit, $\sqrt{2\epsilon\lambda} \approx \kappa_2^{-1}$, leading to

$$\lim_{\lambda\to 0} \frac{\pi\omega_0\sqrt{\lambda}\kappa_2}{K\left(\kappa_2^{-1}\right)} = \frac{\pi\omega_0\sqrt{2\epsilon}}{K(0)} = \lim_{v_\perp\to 0} \frac{\sqrt{2E/m}}{qR_0} = \frac{\left|v_\parallel\right|}{qR_0}. \tag{2.136}$$

Therefore, the second set of equations predict the correct limiting behavior in the extreme passing limit.

We next consider guiding center motion that deviates from magnetic field lines. Recall that the invariant canonical toroidal momentum is given by

$$P_\varphi = -e\psi + \frac{mRv_\parallel B_\varphi}{B} = -e\psi + \frac{mv_\parallel I}{B}. \tag{2.137}$$

We note that motion strictly along a field line does not conserve P_φ since the particle would be bound to the magnetic surface. This can be easily verified by considering that ψ and I are flux functions and thus would be invariant during this motion. Moreover, $v_\parallel/B$ is certainly not invariant

as that would violate energy and magnetic moment conservation. Therefore, any guiding center motion that enforces P_φ conservation requires excursions from the magnetic surface. The deviation from the flux surface can be found by noting that

$$\Delta P_\varphi = P_\varphi(\psi_0, \chi_0) - P_\varphi(\psi_1, \chi_1) = 0 \tag{2.138}$$

along the actual guiding center orbit. For a trapped particle, we simply choose ψ_0 to be a reference flux surface such that $\chi_0 = \chi_b$ corresponds to the bounce angle and $\chi_1 = 0$. Such an orbit is called a banana orbit due to the resemblance of the orbit shape to a banana, as can be seen in Fig. 2.3. The angle χ_b is a banana tip such that $v_\parallel(\psi_0, \chi_b) = 0$. We then presuppose that the excursion is small by evaluating $v_\parallel$, I, and B at ψ_0 instead of ψ_1. Using energy conservation, we can write the excursion from the flux surface for trapped particles as

$$|\Delta\psi| \approx \frac{I\sqrt{2Em}}{eB_{\min}}\sqrt{1 - \frac{\mu B_{\min}}{E}} = \frac{I}{\Omega_c}\sqrt{\frac{2E}{m}}\sqrt{1-\lambda} = I\rho_c\sqrt{\lambda}\sqrt{1-\lambda}. \tag{2.139}$$

where the cyclotron frequency Ω_c and the gyroradius $\rho_c = v_\perp/\Omega_c$ are evaluated at the low field side. In the small ϵ limit, we note that

$$\frac{d\psi}{dr} \approx \frac{I\epsilon}{q}, \tag{2.140}$$

leading to the radial excursion

$$|\Delta r| \approx \frac{q\rho_c}{\epsilon}\sqrt{\lambda}\sqrt{1-\lambda}. \tag{2.141}$$

For deeply trapped particles such that $\lambda = 1$, the radial excursion therefore vanishes. Meanwhile, for particles that are marginally trapped such that the banana tip is at $\theta_b = \pi$ (leading to $\lambda \approx 1 - 2\epsilon$), we obtain

$$|\Delta r| \approx \frac{q\rho_c}{\epsilon}\sqrt{1-2\epsilon}2\epsilon = \frac{\sqrt{2}q\rho_c}{\sqrt{\epsilon}}. \tag{2.142}$$

This leads us to conclude that the banana orbits have a characteristic banana width

$$\delta_b \sim \frac{q\rho_c}{\sqrt{\epsilon}}, \tag{2.143}$$

which approximately corresponds to the radial width at $\theta_b = \frac{\pi}{4}$; this itself corresponds to $\lambda \approx 1 - \epsilon$. For passing particles, we can perform a similar analysis. However, there is no longer any angle χ

where the parallel velocity vanishes, resulting in

$$|\Delta\psi| \approx \left| \frac{Iv_\parallel}{eB} - \frac{Iv_\parallel(\chi = 0)}{eB_{\min}} \right|, \tag{2.144}$$

where we evaluate $v_\parallel/B$ at the angle corresponding to the reference flux surface. If we take the reference flux surface to be that of the high field side and consider a purely passing particle such that $v_\parallel$ is a constant, then we obtain

$$|\Delta r| \approx \frac{qv_\parallel}{\epsilon\Omega_c}|\Delta R| \approx \frac{2qv_\parallel}{\Omega_c}. \tag{2.145}$$

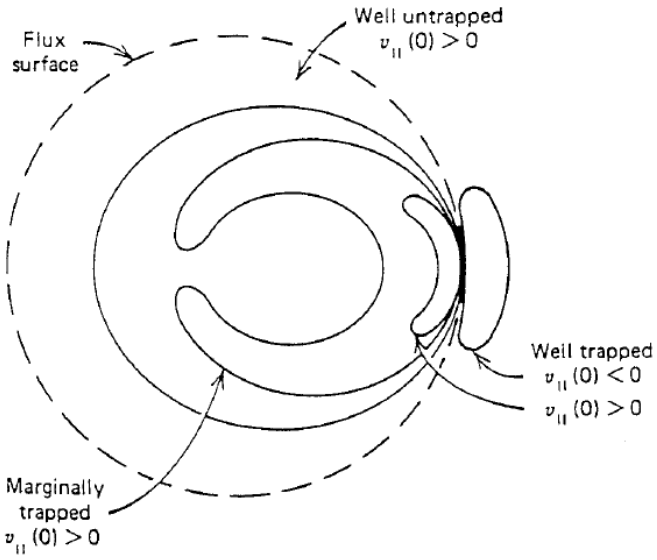

Figure 2.3: Guiding center orbits projected into the poloidal plane. Source: Ref. 17.

For both trapped and passing particles, the radial excursion from the flux surface is proportional to the gyroradius and therefore quite small compared to the size of the tokamak. This suggests that the motion of the guiding center particle can then decomposed further into the fast bounce-transit motion and the slow drift motion. The next step is to expand the guiding center equations of motion about the reference flux surface ψ_0. Formally, we write

$$\psi = \psi_0 + \psi_1. \tag{2.146}$$

We choose ψ_0 such that $\psi_0 = P_\varphi$, leading to

$$\psi_1 = \frac{m v_\parallel I}{eB}, \tag{2.147}$$

where we evaluate the right-hand side at ψ_0. We then expand the equations of motion such that

$$\frac{d\psi}{dt} = \frac{d\psi_1}{dt} = \mathbf{v} \cdot \nabla \psi_1, \tag{2.148}$$

$$\frac{d\chi}{dt} = \Omega_\chi + \frac{\partial \Omega_\chi}{\partial \psi} \psi_1 + \mathbf{v} \cdot \nabla \chi, \tag{2.149}$$

$$\frac{d\varphi}{dt} = q\Omega_\chi + \frac{\partial}{\partial \psi}\big(q\Omega_\chi\big)\psi_1 + \mathbf{v} \cdot \nabla \varphi, \tag{2.150}$$

where q, Ω_χ, their derivatives, and the guiding center drift terms are evaluated at $\psi = \psi_0$. The inclusion of derivatives with respect to ψ take into account excursions from the magnetic surface due to P_φ conservation; including only the drift terms would neglect this effect. Although a closed form solution to the instantaneous guiding center position is still out of reach, we can proceed further in our analysis by using the fact that the drift motion is slow compared to the bounce-transit motion. Through substitution, we note that

$$\frac{d\varphi}{dt} = \frac{dq}{d\psi}\Omega_\chi \psi_1 + \mathbf{v}_D \cdot \nabla \varphi - q\mathbf{v}_D \cdot \nabla \chi + q\frac{d\chi}{dt}. \tag{2.151}$$

Our expression for $\frac{d\varphi}{dt}$ is only dependent on χ due to toroidal symmetry and the expansion in ψ. Because the drift motion is slow and the magnetic drift excursion is small, we can decompose the motion in φ into the bounce-transit motion and the drift motion. To do this, we define a time average over the bounce-transit motion. For the bounce motion, we find

$$\big\langle F\big(\epsilon_\parallel, \chi\big)\big\rangle \equiv \frac{1}{T_b}\int_0^{T_b} \mathrm{d}t\, F\big(\epsilon_\parallel, \chi\big) + F\big(-\epsilon_\parallel, \chi\big) = \frac{\omega_b}{2\pi}\int_{-\chi_b}^{\chi_b} \frac{\mathrm{d}\chi}{\Omega_\chi}\big(F\big(\epsilon_\parallel, \chi\big) + F\big(-\epsilon_\parallel, \chi\big)\big), \tag{2.152}$$

where $\epsilon_\parallel$ allows us to keep track of the back and forth motion in the bounce orbit. Meanwhile, the transit average is

$$\big\langle F\big(\epsilon_\parallel, \chi\big)\big\rangle \equiv \frac{1}{T_t}\int_0^{T_t} \mathrm{d}t\, F\big(\epsilon_\parallel, \chi\big) = \frac{\omega_t}{2\pi}\int_{-\pi}^{\pi} \frac{\mathrm{d}\chi}{\Omega_\chi} F\big(\epsilon_\parallel, \chi\big). \tag{2.153}$$

Note that there is no sum for the transit average since the parallel velocity never changes. We then use this to compute the time average, finding that

$$\langle \dot{\varphi} \rangle = \langle \omega_d \rangle + \bar{\epsilon}\big(\epsilon_{\parallel} q \omega_t\big), \tag{2.154}$$

where $\bar{\epsilon} = 0$ for trapped particle and $\bar{\epsilon} = 1$ for passing particles and we define

$$\omega_d \equiv \frac{dq}{d\psi}\Omega_\chi \psi_1 + \mathbf{v}_D \cdot \nabla\varphi - q\mathbf{v}_D \cdot \nabla\chi. \tag{2.155}$$

For trapped particles, the time average of $\dot{\chi}$ vanishes due to the back and forth motion. For passing particles, this calculation effectively takes into account how full poloidal transits will result in a change in the toroidal angle. Separated from that motion, $\langle \omega_d \rangle$ is purely due to the drifts and P_φ conservation. In particular, recall that

$$\mathbf{B} \cdot \nabla(\varphi - q\chi) = 0. \tag{2.156}$$

The quantity $\varphi - q\chi$ can be seen then as parameterizing any individual field line while holding the flux ψ constant. Thus, the drifts in φ and χ cause the guiding center particle to deviate from the field line on the magnetic surface. Meanwhile, the magnetic shear term $\frac{dq}{d\psi}$ is due to excursions from the magnetic field line. Thus, we call $\langle \omega_d \rangle$ the toroidal precession frequency. In calculating the toroidal precession frequency, it is useful to use the lowest-order MHD equilibrium condition as well as Ampere's law,

$$\nabla p = \mathbf{j} \times \mathbf{B}, \tag{2.157}$$

$$\nabla \times \mathbf{B} = \mu_0 \mathbf{j}, \tag{2.158}$$

where $\mathbf{j}$ is the current density and μ_0 is the vacuum permeability. This simplifies the classical curvature drift to

$$\mathbf{v}_{R_c} = \frac{m v_\parallel^2}{eB}\left(\frac{\mathbf{B} \times \nabla B}{B^2} + \frac{\beta}{2p}\frac{\mathbf{B} \times \nabla p}{B}\right), \tag{2.159}$$

where we have introduced the fundamental plasma parameter β which relates the plasma pressure to the energy density of the magnetic field:

$$\beta \equiv \frac{p}{B^2/(2\mu_0)}. \tag{2.160}$$

We therefore find that the total magnetic drift to lowest-order is

$$\mathbf{v}_D \approx \left(\frac{mv_\parallel^2 + \mu B}{eB^2}\right)\hat{\mathbf{b}} \times \nabla B + \frac{mv_\parallel^2}{eB}\frac{\beta}{2p}\hat{\mathbf{b}} \times \nabla p. \tag{2.161}$$

The qualitative behavior of $\langle \omega_d \rangle$ can be examined by considering a purely toroidal magnetic field with no electrostatic field and assuming the poloidal field will contribute only small corrections to the drifts in φ and χ for small ϵ. If we consider the magnetic field

$$\mathbf{B} = \frac{B}{R}\hat{\boldsymbol{\varphi}}, \tag{2.162}$$

we note that $\nabla \times \mathbf{B} = 0$. In the curvature drift, $\mathbf{B} \times \boldsymbol{\kappa} = \hat{\mathbf{b}} \times \nabla B$ for magnetic fields with no curl. To lowest-order in the gyroradius and assuming small pressure gradients, the magnetic drift can then be written as

$$\mathbf{v}_D \approx \left(\frac{mv_\parallel^2 + \mu B}{eB^2}\right)\hat{\mathbf{b}} \times \nabla B, \tag{2.163}$$

where $\nabla B \approx (B/R)\hat{\mathbf{R}}$. Meanwhile, in a circular geometry we define the magnetic shear s as

$$s = \frac{q}{r}\frac{dq}{dr}. \tag{2.164}$$

Noting that that $\frac{d\psi}{dr} \approx rB_0/q$ in a circular geometry and that $\chi \approx \theta$, we then find to lowest-order in ϵ that

$$\omega_d \approx \frac{q}{r}\frac{E}{eB_0R_0}\left((2 - \lambda b)\cos(\theta) + \frac{2s}{\epsilon}(1 - \lambda b)\right). \tag{2.165}$$

We then identify the characteristic magnetic drift frequency

$$\omega_{d,0} = \frac{Eq}{eB_0rR} \approx \frac{\omega_0^2 q^3}{\Omega_c \epsilon}, \tag{2.166}$$

confirming that the characteristic magnetic drift frequency is much smaller than the characteristic bounce-transit frequency. The full expression for the toroidal precession frequency is

$$\langle \omega_d \rangle \approx \begin{cases} \omega_{d,0}\left(\dfrac{(2+4s)E(\kappa_1) - \left(1 + 4s\left(1 - \kappa_1^2\right)\right)K(\kappa_1)}{K(\kappa_1)}\right) & \text{if } 0 \le \kappa_1 < 1 \text{ (trapped)}, \\ \omega_{d,0}\left(\dfrac{2\kappa_1^2(1+2s)E\left(\kappa_1^{-1}\right) - \left(2\kappa_1^2 - 1\right)K\left(\kappa_1^{-1}\right)}{K\left(\kappa_1^{-1}\right)}\right) & \text{if } 1 < \kappa_1 < \infty \text{ (passing)}, \end{cases} \tag{2.167}$$

where we make use of the simpler convention using κ_1. The more complex convention using κ_2 can be computed by simply multiplying the right-hand side of the above expression by a factor of λ, leading to

$$\langle \omega_d \rangle \approx \begin{cases} \omega_{d,0}\lambda\left(\dfrac{(2+4s)E(\kappa_2) - \left(1+4s\left(1-\kappa_2^2\right)\right)K(\kappa_2)}{K(\kappa_2)}\right) & \text{if } 0 \le \kappa_2 < 1 \text{ (trapped)}, \\ \omega_{d,0}\lambda\left(\dfrac{2\kappa_2^2(1+2s)E\left(\kappa_2^{-1}\right) - \left(2\kappa_2^2-1\right)K\left(\kappa_2^{-1}\right)}{K\left(\kappa_2^{-1}\right)}\right) & \text{if } 1 < \kappa_2 < \infty \text{ (passing)}. \end{cases} \tag{2.168}$$

where as before $\lambda \approx 1$ for trapped particles.

Finally, it is important to note that small electric fields provide only a small correction to the bounce-transit frequency. Meanwhile, the toroidal drift frequency is easily modified by including E-cross-B drift. Having sufficiently characterized guiding center motion in a tokamak, we are now in a position to describe the action-angle formalism, a key theoretical framework for this work.

2.4 Action-angle variables

As a preliminary example, we begin with an analysis of a harmonic oscillator with a time dependent frequency $\omega(t)$ demonstrated by Goldstein in Ref. 32. The Hamiltonian is given by

$$H = \frac{1}{2m}\left(p^2 + m^2\omega(t)^2 q^2\right), \tag{2.169}$$

which satisfies Hamilton's equations of motion

$$\dot{q} = \frac{\partial H}{\partial p} = \frac{p}{m}, \tag{2.170}$$

$$\dot{p} = -\frac{\partial H}{\partial q} = -m\omega(t)^2 q, \tag{2.171}$$

where (q, p) are canonical coordinates. Due to the time dependence of the oscillator frequency, the Hamiltonian is not conserved. The time derivative of the Hamiltonian can be explicitly computed as

$$\frac{dH}{dt} = \frac{\partial H}{\partial t} + \{H, H\} = \frac{\partial H}{\partial t} = m\dot{\omega}\omega x^2. \tag{2.172}$$

Although obtaining a full solution to the problem relies on the precise nature of $\omega(t)$, we consider the situation where $\omega(t)$ slowly varies in time compared to the natural frequency of motion. Thus, we require that

$$\left|\frac{\dot{\omega}}{\omega}\right| \ll |\omega|. \tag{2.173}$$

To be precise, we define a small parameter ϵ_ω such that

$$\epsilon_\omega \equiv \left|\frac{\dot{\omega}}{\omega}\right| \ll 1. \tag{2.174}$$

This allows us to analyze the problem perturbatively and separate the fast oscillatory motion from the additional orbit complexities due to $\dot{\omega}$. We define the action J as

$$J \equiv \frac{1}{2\pi} \oint p \, \mathrm{d}q \,, \tag{2.175}$$

where we integrate the momentum p over a closed orbit along q. This is equivalent to the area in phase space (x, p) of a particular orbit normalized to 2π. It can then be shown that

$$\frac{1}{J}\frac{dJ}{dt} = O(\epsilon_\omega). \tag{2.176}$$

This alone is not particularly noteworthy given that the time derivatives of the Hamiltonian and the frequency are both also proportional to ϵ_ω. The importance of J becomes apparent when examining the long the secular change. It can be shown that by taking a time average of $\dot{J}$ that

$$\left\langle \frac{dJ}{dt} \right\rangle = O\left(\epsilon_\omega^2\right). \tag{2.177}$$

That is, the ϵ_ω dependence in J is oscillatory. Over a period of motion, the relative change in J is then

$$\frac{\Delta J}{J} = O\left(\epsilon_\omega^2\right). \tag{2.178}$$

The result is that even in cases where the energy and frequency increase without bound at a rate ϵ_ω, the long-term secular evolution of J will be proportional to ϵ_ω^2, a much stronger result.[33] We thus call J an adiabatic invariant. In the case of the harmonic oscillator, the adiabatic invariant is easily calculated. Consider that in the time independent case, we can write p as

$$p = \sqrt{2Em - m^2\omega^2 q^2}. \tag{2.179}$$

We then integrate this over an orbit where the endpoints $\pm x_0$ can be determined by solving $p = 0$ (notice the similarities in integrating over the bounce-transit orbit), resulting in the integral

$$J = \frac{1}{2\pi} \int_{-\sqrt{\frac{2E}{m\omega^2}}}^{\sqrt{\frac{2E}{m\omega^2}}} 2\sqrt{2Em - m^2\omega^2 q^2}\, \mathrm{d}q = \frac{E}{\omega}. \tag{2.180}$$

Thus, even if E and ω both grow without bound at a rate proportional to ϵ_ω, their ratio will at most grow without bound at a rate proportional to ϵ_ω^2. We then write

$$J = \frac{E(t=0)}{\omega(t=0)} \approx \frac{E(t)}{\omega(t)}. \tag{2.181}$$

In general, the quantity J is also referred to as an action variable. Consider the time independent system where we can write

$$H(q, p) = E, \tag{2.182}$$

where E is the constant energy. We can then invert to find $p = p(q, E)$, just like in the harmonic oscillator example. The adiabatic invariant J is then

$$J \equiv \frac{1}{2\pi} \oint p(q, E)\, \mathrm{d}q\,. \tag{2.183}$$

Due to the integration, J is purely a function of E. It follows then that the Hamiltonian itself can be written as a function of J, leading to $H = H(J)$. We can then construct a conjugate variable α such that

$$\frac{d\alpha}{dt} = \frac{\partial H}{\partial J} = \omega, \tag{2.184}$$

$$\frac{dJ}{dt} = -\frac{\partial H}{\partial \alpha} = 0. \tag{2.185}$$

where ω is the frequency of the motion in question. Thus, the coordinates (α, J) form a set of canonical variables that greatly simplify Hamilton's equations of motion. The action variable J takes the form of a conserved canonical momentum while α is an angular variable that changes at a constant pace. For a Harmonic oscillator, we found that $H = J\omega$, leading to

$$\alpha = \omega t + \alpha_0, \tag{2.186}$$

$$J = \frac{E}{\omega}. \tag{2.187}$$

Thus, adiabatic invariants and action coordinates are equivalent for a time independent Hamiltonian. We can extend the analysis to multiple dimensions. If a system with $2n$ degrees of freedom is integrable and completely separable, we can write a set of n action angles and n adiabatic invariants such that,

$$J_i = \oint p_i \, \mathrm{d}q_i \,, \tag{2.188}$$

$$\frac{d\alpha_i}{dt} = \frac{\partial H}{\partial J_i} = \Omega_i, \tag{2.189}$$

$$\frac{dJ_i}{dt} = -\frac{\partial H}{\partial \alpha_i} = 0. \tag{2.190}$$

Here, (q_i, p_i) pairs define either closed orbits or periodic functions of q_i, and Ω_i is a constant frequency associated with the motion. Formally constructing this action-angle variable formalism requires the use of Hamilton's characteristic function and other methods of Hamiltonian mechanics. We leave that aside here and point the reader to Ref. 32 for a more comprehensive discussion.

Due to the multiply periodic nature of the motion with respect to the action angles, we can expand any position q_i and momentum p_i as Fourier series in the action angles. This means that any function of the separable variable pairs (q_i, p_i) will be multiply periodic and thus can be written as a Fourier series. For concreteness, we restrict ourselves to six degrees of freedom and define the vectors $\boldsymbol{\alpha} = (\alpha_1, \alpha_2, \alpha_3)$ and $\mathbf{J} = (J_1, J_2, J_3)$. Then, a general function f can be written as

$$f(\mathbf{q}, \mathbf{p}) = \sum_{\mathbf{n}} f_{\mathbf{n}}(\mathbf{J}) e^{i\mathbf{n}\cdot\boldsymbol{\alpha}}, \tag{2.191}$$

where we sum over all integer triads $\mathbf{n} = (n_1, n_2, n_3)$ and the Fourier coefficients can be computed as

$$f_{\mathbf{n}}(\mathbf{J}) = \frac{1}{(2\pi)^3} \int \mathrm{d}^3\alpha \, f(\mathbf{q}, \mathbf{p}) e^{-i\mathbf{n}\cdot\boldsymbol{\alpha}}, \tag{2.192}$$

where we integrate each action angle from 0 to 2π. The advantage of this Fourier series becomes clear when we apply perturbation theory. Consider the equilibrium Hamiltonian $H_0(\mathbf{J})$ where the action-angle variables are known. If we apply a perturbation δh, the total Hamiltonian is

$$H(\boldsymbol{\alpha}, \mathbf{J}, t) = H_0(\mathbf{J}) + \delta h(\boldsymbol{\alpha}, \mathbf{J}, t), \tag{2.193}$$

where the perturbation can in principle depend on the action-angle variables as well as time. Hamilton's equations still hold in this system, and they become

$$\dot{\boldsymbol{\alpha}} = \frac{\partial H}{\partial \mathbf{J}} = \boldsymbol{\Omega} + \frac{\partial \delta h}{\partial \mathbf{J}}, \tag{2.194}$$

$$\dot{\mathbf{J}} = -\frac{\partial H}{\partial \boldsymbol{\alpha}} = -\frac{\partial \delta h}{\partial \boldsymbol{\alpha}}. \tag{2.195}$$

Therefore, the adiabatic invariants $\mathbf{J}$ only vary according to the perturbed field, as expected. This variation can computed through the use of the Fourier series, leading to

$$\dot{\mathbf{J}} = -\sum_{\mathbf{n}} i\mathbf{n} h_{\mathbf{n}}(\mathbf{J}, t) e^{i\mathbf{n}\cdot\boldsymbol{\alpha}}. \tag{2.196}$$

We will see later that this representation simplifies a great deal of analysis in the context of kinetic models.

We now seek to apply the action-angle formalism to charged particle orbits in an equilibrium tokamak geometry. The Liouville-Arnold theorem states that we can perform a canonical transformation for an integrable Hamiltonian system using action-angle variables if the energy level set is compact.[34] Compactness of energy level sets is equivalent to orbits being bounded for this system. Moreover, the Kolmogorov-Arnold-Moser theorem states that if a small perturbation is applied to the Hamiltonian, most orbits remain quasiperiodic for a sufficiently small perturbation.[35] With no perturbation, the motion is automatically quasiperiodic. These conditions can all be safely applied to tokamak guiding center motion as there exist no singularities and the motion is smooth (for ease of analysis, we assume that the guiding center particle will not follow an open magnetic field line into the separatrix).

To show integrability, we formally we need to provide three first integrables of motion that Poisson commute since a charged particle possesses three degrees of freedom. For the axisymmetric guiding center system, these correspond to $\left(\mu, E, P_\varphi\right)$. We can actually show that the system is integrable and that the motion is bounded directly through rudimentary means. First, note that the guiding center system of equations is 4-dimensional. By moving into the guiding center framework, we removed two degrees of freedom and parameterized the remaining equations of motion via μ,

an independent parameter in the guiding center framework. Energy conservation allows us to write

$$v_{\parallel}(\psi, \chi) = \epsilon_{\parallel}\sqrt{\frac{2}{m}}\sqrt{E - \mu B}. \tag{2.197}$$

We recall that $\epsilon_{\parallel}$ keeps track of the sign of $v_{\parallel}$. We also note that throughout this analysis φ is an ignorable coordinate. For trapped particles, the sign of $\epsilon_{\parallel}$ switches when the particle reaches a bounce angle such that $\mu B(\psi_b, \chi_b) = E$. For passing particles, $\epsilon_{\parallel}$ is invariant. This removes one equation of motion. Next, we consider the canonical toroidal momentum, which is

$$P_{\varphi}\big(\psi, \chi, v_{\parallel}\big) = -e\psi + \frac{m v_{\parallel} I}{B} = -e\psi + \frac{mI}{B}\epsilon_{\parallel}\sqrt{\frac{2}{m}}\sqrt{E - \mu B}. \tag{2.198}$$

The level sets of P_{φ} correspond to closed curves in the poloidal plane. For trapped particles, this corresponds to a banana orbit where two smooth curves join at the banana tips and encircle the low field side; these two smooth curves correspond to different signs of $\epsilon_{\parallel}$. For passing particles, there is one smooth curve that encompasses the magnetic axis and fully goes through the high field side. This allows us to parameterize ψ in terms of χ. We then note that

$$\frac{d\chi}{dt} = \frac{d\chi}{dt}\big(\psi, \chi, v_{\parallel}\big). \tag{2.199}$$

Using the constants of motion, various substitutions, and the inclusion of $\epsilon_{\parallel}$, we can parameterize $v_{\parallel}$ and ψ in terms of χ, leading to

$$\frac{d\chi}{dt} = \frac{d\chi}{dt}\big(\psi(\chi), \chi, v_{\parallel}(\chi)\big) = \frac{d\chi}{dt}(\chi). \tag{2.200}$$

This can then be solved through the usual method of quadratures. For trapped particles, we consider the signs of $\epsilon_{\parallel}$ separately and stitch the solutions together, whereas for passing particles no such consideration is required. It is clear then that the motion in the poloidal plane is integrable and also bounded to the closed curves mentioned previously. The only complexity concerns particles that are exactly at the trapped-passing boundary. However, such a situation is unstable and any perturbation or collision would knock the particle into either the trapped or passing part of velocity space. Lastly, to take into account the motion in φ, one simply needs to note that

$$\frac{d\varphi}{dt} = \frac{d\varphi}{dt}\big(\psi(\chi), \chi, v_{\parallel}(\chi)\big) = \frac{d\varphi}{dt}(\chi). \tag{2.201}$$

This can be pictured by imagining the closed curve in the poloidal plane revolved around the major axis of the tokamak into a toroidal surface. The guiding center particle is perfectly confined to this surface. Moreover, the specific curve on this surface that corresponds to the particle's orbit can be found via

$$\frac{d\varphi}{d\chi}(\chi) = \frac{\frac{d\varphi}{dt}}{\frac{d\chi}{dt}}. \tag{2.202}$$

This can be in principle integrated to find $\varphi(\chi)$ such that

$$\varphi(\chi + 2\pi) = \varphi(\chi) + c, \tag{2.203}$$

where c is a constant and representative of the toroidal winding number of the orbit (compare this analysis to that of a magnetic field line with safety factor q). If c is rational, then the guiding center orbit will close on itself and the motion is thus strictly periodic. If c is irrational, the more likely case, then the guiding center orbit will densely fill the toroidal surface and the motion is quasiperiodic. Note that although we neglected the inclusion of an equilibrium electric field, all our above arguments would still hold as long as the electric field is axisymmetric. We note that this analysis explicitly does not include collisions between guiding center particles.

Now that we have proven that the Liouville-Arnold theorem can be used for guiding center orbits, the task remains to construct the action-angle variables. Notice that we decomposed guiding center motion into three different time scales: the gyromotion, the bounce-transit motion, and the toroidal precession. A direct demonstration of the adiabatic invariance of the quantities associated with these three motions can be found in Ref. 36. We first start with the gyromotion. We know that for ignorable coordinates q_i, the conjugate momenta p_i produce actions $J_i = p_i$. The guiding center formulation thus suggests

$$J_1 = P_\alpha = \frac{\partial \mathcal{L}}{\partial \dot{\alpha}} = \frac{m}{e}\mu. \tag{2.204}$$

This corresponds to the angular variable α_1 and frequency Ω_1 such that

$$\alpha_1 = \alpha, \tag{2.205}$$

$$\Omega_1 = \Omega_c, \tag{2.206}$$

where we recall that α is the gyrophase. This, however, would be too hasty. The phase space Lagrangian for the guiding center framework presupposes the adiabatic invariance of μ. It is the magnetic moment invariance itself that allows us to expand in terms of the gyroradius and transform the single particle equations of motion into the guiding center equations of motion. For a sense as to why the magnetic moment is conserved, consider a charged particle in a time dependent magnetic field that is straight and homogeneous,

$$\mathbf{B} = B(t)\hat{\mathbf{z}}. \tag{2.207}$$

The vector potential for such a field is

$$\mathbf{A} = \frac{1}{2}B(t)(x\hat{\mathbf{y}} - y\hat{\mathbf{x}}). \tag{2.208}$$

The time dependence of the vector potential automatically includes an induced electric field. This can be rewritten in cylindrical coordinates (ρ, φ, z),

$$\mathbf{A} = \frac{1}{2}B(t)\rho\hat{\boldsymbol{\varphi}}. \tag{2.209}$$

The resulting Hamiltonian is then

$$H = \frac{1}{2m}\left(p_r^2 + \left(\frac{p_\varphi}{\rho} - \frac{e}{2}B(t)\rho\right)^2 + p_z^2\right). \tag{2.210}$$

There are no forces in the z direction, thus we ignore that motion. Because the Hamiltonian is cyclic in φ, the canonical momentum p_φ is conserved. Evidently, we can then write

$$J_1 = -p_\varphi. \tag{2.211}$$

(we include the minus sign out of convention). We then note that in the static limit where $B = B_0$ that

$$p_\varphi = -m\rho^2\dot{\varphi} - \frac{eB_0\rho^2}{2} = m\rho_c^2\Omega_c - \frac{m\rho_c^2}{2} = -\frac{e}{m}\mu. \tag{2.212}$$

Interestingly, we can also compute

$$\frac{1}{2\pi}\oint p_r\,\mathrm{d}r = \oint \sqrt{2mW_\perp - \left(\frac{p_\varphi}{r} - \frac{m\Omega_c r}{2}\right)}\,\mathrm{d}r = \min\left(\frac{e}{m}\mu, \frac{e}{m}\mu + p_\phi\right), \tag{2.213}$$

which again reduces to the magnetic moment after accounting for the exact invariant p_φ. In either case, we find

$$J_1 = \frac{e}{m}\mu. \tag{2.214}$$

It is also clear from this description that the magnetic moment corresponds the magnetic flux through the cyclotron orbit.

Next, we describe the procedure for the bounce-transit motion. First, we wish to compute

$$J_2 = \frac{1}{2\pi}\oint P_\chi d\chi = \frac{1}{2\pi}\oint \left(e\mathbf{A} + mv_\parallel \hat{\mathbf{b}}\right)\cdot\frac{\partial \mathbf{X}}{\partial \chi}\,\mathrm{d}\chi\,. \tag{2.215}$$

To proceed, we separate out the vector potential term and the parallel velocity term. The vector potential term is

$$\frac{1}{2\pi}\oint e\mathbf{A}\cdot\frac{\partial \mathbf{X}}{\partial \chi}\,\mathrm{d}\chi = \frac{1}{2\pi}\oint e(\psi\nabla\varphi + \Phi_t\nabla\chi)\cdot\frac{\partial \mathbf{X}}{\partial \chi}\,\mathrm{d}\chi = \frac{1}{2\pi}\oint e\Phi_t\,\mathrm{d}\chi\,. \tag{2.216}$$

We note that Φ_t is a flux function. As mentioned earlier, this orbit is closed in the poloidal plane even when accounting for excursions from the magnetic surface. However, this fact means that ψ is parameterized by χ and other constants of motion due to P_φ invariance. To account for this, we perform the Taylor expansion

$$\Phi_t(\psi) \approx \Phi_t(\psi_0) + \psi_1\frac{d\Phi_t}{d\psi}(\psi_0), \tag{2.217}$$

where we recall

$$\psi_0 = -\frac{P_\varphi}{e}, \tag{2.218}$$

$$\psi_1 = \frac{mv_\parallel I}{B}, \tag{2.219}$$

$$\frac{d\Phi_t}{d\psi} = q. \tag{2.220}$$

Evaluating all remaining functions of ψ at $\psi = \psi_0$, we then find that

$$\frac{1}{2\pi}\oint e\Phi_t\,\mathrm{d}\chi = \bar{\epsilon}e\Phi_t(\psi_0) + \frac{1}{2\pi}\oint\frac{mv_\parallel Iq}{B}\,\mathrm{d}\chi = \bar{\epsilon}e\Phi_t(\psi_0) + \frac{1}{2\pi}\oint\frac{mv_\parallel J|\mathbf{B}_T|^2}{B}, \tag{2.221}$$

where the Jacobian is $J = qBR^2/I$, the toroidal field strength is $|\mathbf{B}_T| = I/R$, and $\bar{\epsilon}$ is zero for trapped particles and unity for passing particles. This factor of $\bar{\epsilon}$ takes into account the closed loop integral; for trapped particles with no excursions from the magnetic surface, the flux enclosed by the path is zero. Meanwhile, it can be shown that

$$\mathbf{B} \cdot \frac{\partial \mathbf{X}}{\partial \chi} = \frac{J|\nabla\psi|^2}{R^2} = J|\mathbf{B}_P|^2, \tag{2.222}$$

where we make use of the poloidal field strength instead. We then find that

$$\frac{1}{2\pi} \oint m v_\parallel \hat{\mathbf{b}} \cdot \frac{\partial v b X}{\partial \chi} \, \mathrm{d}\chi = \frac{1}{2\pi} \oint \frac{m v_\parallel J |\mathbf{B}_P|^2}{B}, \tag{2.223}$$

where we again evaluate all functions at $\psi = \psi_0$. We then find that the adiabatic invariant J_2 is

$$J_2 = \bar{\epsilon} e \Phi_t(\psi_0) + \frac{1}{2\pi} \oint \frac{m v_\parallel J |\mathbf{B}_T|^2 + |\mathbf{B}_P|^2}{B} = \bar{\epsilon} e \Phi_t(\psi_0) + \frac{1}{2\pi} \oint m v_\parallel B J \, \mathrm{d}\chi \, . \tag{2.224}$$

Lastly, we make use of the fact that the equation for a field line can be written as $\mathrm{d}l \, / B = J \, \mathrm{d}\chi$ where l is the arc length along the field line. Finally, we find that

$$J_2 = \bar{\epsilon} e \Phi_t(\psi_0) + \frac{1}{2\pi} \oint m v_\parallel \, \mathrm{d}l \, . \tag{2.225}$$

This is also known as the longitudinal invariant or parallel adiabatic invariant. The frequency associated with this action variable is simply the bounce-transit frequency, which can be verified directly by taking the of J_2 with respect to the energy E while holding μ and ψ_0 fixed:

$$\Omega_2 = \frac{\partial H}{\partial J_2} = \left(\frac{\partial J_2}{\partial E} \right)^{-1} = \begin{cases} \omega_b, & \text{if trapped,} \\ \epsilon_\parallel \omega_t & \text{if passing.} \end{cases} \tag{2.226}$$

The action angle for the bounce-transit motion can be computed by considering the equation of motion on a field line:

$$\frac{d\chi}{dt} = \frac{d\chi}{d\alpha_2} \frac{d\alpha_2}{dt} = \frac{d\chi}{d\alpha_2} \Omega_2 = \Omega_\chi . \tag{2.227}$$

Thus, we find that

$$\alpha_2 = \Omega_2 \int_0^\chi \frac{\mathrm{d}\chi'}{\Omega_\chi} . \tag{2.228}$$

Here, we take the convention that $\alpha_2(\chi = 0) = 0$; for the case of trapped particles, we stitch together solutions to take into account the bounce motion as usual. For a circular cross section, the formulas for the action J_2 is

$$J_2 \approx \begin{cases} \dfrac{8m\omega_0 q^2 R_0^2}{\pi}\Big(E(\kappa_1) - (1-\kappa_1)^2 K(\kappa_1)\Big) & \text{if } 0 \le \kappa_1 < 1 \text{ (trapped)}, \\ \bar{\epsilon} e \Phi_t + \dfrac{4m\omega_0 q^2 R_0^2}{\pi}\kappa_1 E(\kappa_1) & \text{if } 1 < \kappa_1 < \infty \text{ (passing)}, \end{cases} \tag{2.229}$$

where we use the κ_1 convention. For the κ_2 convention, we obtain

$$J_2 \approx \begin{cases} \dfrac{8m\omega_0 q^2 R_0^2}{\pi}\lambda\Big(E(\kappa_2) - (1-\kappa_2)^2 K(\kappa_2)\Big) & \text{if } 0 \le \kappa_2 < 1 \text{ (trapped)}, \\ \bar{\epsilon} e \Phi_t + \dfrac{4m\omega_0 q^2 R_0^2}{\pi}\lambda\kappa_2 E(\kappa_2) & \text{if } 1 < \kappa_2 < \infty \text{ (passing)}, \end{cases} \tag{2.230}$$

Meanwhile, the expression for the action angle α_2 is identical regardless of convention:

$$\sin(\theta/2) \approx \begin{cases} \kappa \,\mathrm{sn}\left(\dfrac{2\alpha}{\pi}K(\kappa), \kappa\right) & \text{if } 0 \le \kappa < 1 \text{ (trapped)}, \\ \mathrm{sn}\left(\dfrac{\alpha}{\pi}K\Big(\kappa^{-1}\Big), \kappa^{-1}\right) & \text{if } 1 < \kappa < \infty \text{ (passing)}, \end{cases} \tag{2.231}$$

where sn is a Jacobi elliptic function and we define α_2 in terms of the poloidal angle $\theta \approx \chi$. We emphasize that although E is an exact invariant in the time independent system, J_2 is the action variable and thus the adiabatic invariant. Time dependent perturbations to the Hamiltonian system will not guarantee that the energy is conserved, while J_2 will be adiabatically conserved.

Finally, we arrive at the toroidal drift motion. Because P_φ is invariant, we find that

$$J_3 = \frac{1}{2\pi}\oint P_\varphi \,\mathrm{d}\varphi = P_\varphi = -e\psi + \frac{m v_\parallel I}{B}. \tag{2.232}$$

For a tokamak plasma, the term proportional to $v_\parallel$ is quite small compared to the flux term. Thus, J_3 is typically approximated as

$$J_3 \approx -e\psi. \tag{2.233}$$

More accurately, in accordance with the analysis above, we can simply identify the third adiabatic invariant with the reference flux surface,

$$J_3 = -e\psi_0. \tag{2.234}$$

The frequency associated with this motion is simply the bounce-transit average of $\dot{\varphi}$. This can be shown by considering that the action-angle variables are canonical, implying that the canonical momenta Poisson commute. This implies

$$\left(\frac{\partial J_2}{\partial J_3}\right)_{J_1,J_3} = 0, \tag{2.235}$$

where here we emphasize which variables are being held constant for the partial derivative. Using the chain rule, this can be expanded as

$$\left(\frac{\partial J_2}{\partial J_3}\right)_{J_1,J_3} = \left(\frac{\partial J_2}{\partial E}\right)_{J_1,J_3}\left(\frac{\partial E}{\partial J_3}\right)_{J_1,J_2} + \left(\frac{\partial J_2}{\partial J_3}\right)_{J_1,E}\left(\frac{\partial J_3}{\partial J_3}\right)_{J_1,J_2} = \frac{\Omega_2}{\Omega_3} + \left(\frac{\partial J_2}{\partial J_3}\right)_{J_1,E} = 0. \tag{2.236}$$

Thus, we obtain

$$\Omega_3 = -\Omega_2\left(\frac{\partial J_2}{\partial J_3}\right)_{J_1,E} = \frac{\Omega_2}{e}\left(\frac{\partial J_2}{\partial \psi_0}\right). \tag{2.237}$$

It can then be shown that

$$\frac{\Omega_2}{e}\left(\frac{\partial J_2}{\partial \psi_0}\right) = \langle \omega_d \rangle + \epsilon_{\parallel} q \Omega_2. \tag{2.238}$$

To construct the angle α_3 is not so straightforward. First, we note that the Ω_3 was computed via a bounce-transit average. Moreover, the equations for $\dot{\varphi}$ are only functions of χ and the invariants (μ, E, ψ_0), while χ itself can be parameterized in terms of α_2. This suggests that we should first split $\dot{\varphi}$ into equilibrium and fluctuation components relative to the bounce-transit motion:

$$\dot{\varphi} = \Omega_3 + \frac{dq}{d\psi}\Omega_\chi \psi_1 + \mathbf{v}_D \cdot \nabla\varphi - q\mathbf{v} \cdot \nabla\chi + q\frac{d\chi}{dt} - \Omega_d - \bar{\epsilon} q \Omega_2. \tag{2.239}$$

The first term in the sum is clearly $\dot{\alpha}_3$. Meanwhile, the latter terms are functions of α_2. We can then integrate this equation of motion in terms of α_2 and α_3, leading to

$$\varphi = \alpha_3 - \bar{\epsilon} q \alpha_2 + \int_0^{\alpha_2} \frac{\mathrm{d}\alpha_2'}{\Omega_2}\left(\mathbf{v}_D \cdot \nabla\varphi - q\mathbf{v} \cdot \nabla\chi + q\frac{d\chi}{dt} - \Omega_d\right). \tag{2.240}$$

We have now specified explicit constructions of $(\boldsymbol{\alpha}, \mathbf{J}, \boldsymbol{\Omega})$ in terms of guiding center variables. The strength of this approach is that it is applicable to not just the single particle system but also a system consisting of many particles. To apply this formalism in full, we must first discuss kinetic models.

2.5 Kinetic models

Kinetic models of plasmas ultimately stem from microscopic dynamics. There are two approaches to derive kinetic physics from the microscopic dynamics. One approach uses the Klimontovich equation and while the other uses the Liouville equation. We present a description of the Klimontovich approach following Nicholson in Ref. 37. We first provide an exact description of the microscopic dynamics by considering the phase space density of the system. The phase space density of a species s constituted by N_0 discrete particles is given by

$$N_s(\mathbf{x}, \mathbf{v}, t) \equiv \sum_{i=1}^{N_0} \delta(\mathbf{x} - \mathbf{X}_i(t))\delta(\mathbf{v} - \mathbf{V}_i(t)), \tag{2.241}$$

where δ is the Dirac delta function, $(\mathbf{x}, \mathbf{v})$ are the Eulerian coordinates of the entire phase space, $(\mathbf{X}, \mathbf{V})$ are the Lagrangian coordinates of any individual particle, and t denotes time. Neglecting the gravitational force, the equations of motion for each particle is given by Newton's laws of motion and the Lorentz force,

$$\frac{d\mathbf{X}_i}{dt}(t) = \mathbf{V}_i(t), \tag{2.242}$$

$$\frac{d\mathbf{V}_i}{dt}(t) = \frac{e_s}{m_s}(\mathbf{E}_m(\mathbf{X}_i(t), t) + \mathbf{V}_i(t) \times \mathbf{B}_m(\mathbf{X}_i(t), t)), \tag{2.243}$$

where e and m are the electric charge and mass of the species in question and $\mathbf{E}_m$ and $\mathbf{B}_m$ denote the microscopic electric and magnetic fields of the system. Here, it is understood that these electromagnetic fields omit the self-field generated by the individual particle in question. The microscopic fields obey Maxwell's equations:

$$\begin{aligned} \nabla \cdot \mathbf{E}_m(\mathbf{x}, t) &= \frac{\rho_m(\mathbf{x}, t)}{\epsilon_0}, & \nabla \times \mathbf{E}_m(\mathbf{x}, t) &= -\frac{\partial \mathbf{B}_m}{\partial t}(\mathbf{x}, t), \\ \nabla \cdot \mathbf{B}_m(\mathbf{x}, t) &= 0, & \nabla \times \mathbf{B}_m(\mathbf{x}, t) &= \mu_0 \mathbf{j}_m(\mathbf{x}, t) + \frac{1}{c^2}\frac{\partial \mathbf{E}_m}{\partial t}(\mathbf{x}, t). \end{aligned} \tag{2.244}$$

Here, ϵ_0 and μ_0 are respectively the vacuum permittivity and permeability, c is the speed of light, and the microscopic charge density ρ_m and microscopic current density $\mathbf{j}_m$ are given by

$$\rho_m(\mathbf{x}, t) = \sum_s e_s \int \mathrm{d}^3 v \, N_s(\mathbf{x}, \mathbf{v}, t), \tag{2.245}$$

$$\mathbf{j}_m(\mathbf{x}, t) = \sum_s e_s \int \mathrm{d}^3 v \, \mathbf{v} N_s(\mathbf{x}, \mathbf{v}, t). \tag{2.246}$$

We implicitly exclude the self-field generated by any given particle when determining the Lorentz force. By utilizing properties of the Dirac delta function, one can obtain the time evolution of N_s to be

$$\frac{\partial N_s}{\partial t} + \mathbf{v} \cdot \frac{\partial N_s}{\partial \mathbf{x}} + \frac{e_s}{m_s}(\mathbf{E}_m + \mathbf{v} \times \mathbf{B}_m) \cdot \frac{\partial N_s}{\partial \mathbf{v}} = 0. \tag{2.247}$$

This is the Klimontovich equation. Together with Maxwell's equations and the expressions for the charge and current densities, the Klimontovich equation exactly describes the microscopic dynamics of the system.

This formulation is of little practical use, since solving the exact dynamics is insurmountable for a system of many particles. To proceed, we ensemble average the Klimontovich equation and define a new function f such that

$$f_s(\mathbf{x}, \mathbf{v}, t) \equiv \langle N_s(\mathbf{x}, \mathbf{v}, t) \rangle \, . \tag{2.248}$$

This function is called the distribution function and measures the probability of measuring a particle of species s around an infinitesimal phase space volume of size $\mathrm{d}^3x \, \mathrm{d}^3v$. We then obtain the plasma kinetic equation,

$$\frac{\partial f_s}{\partial t} + \mathbf{v} \cdot \frac{\partial f_s}{\partial \mathbf{x}} + \frac{e_s}{m_s}(\mathbf{E} + \mathbf{v} \times \mathbf{B}) \cdot \frac{\partial f_s}{\partial \mathbf{v}} = -\frac{e_s}{m_s} \left\langle (\delta\mathbf{E} + \mathbf{v} \times \delta\mathbf{B}) \cdot \frac{\partial (\delta N_s)}{\partial \mathbf{v}} \right\rangle, \tag{2.249}$$

where $\mathbf{E}$ and $\mathbf{B}$ are the averaged electromagnetic fields and δN_s, $\delta\mathbf{E}$, and $\delta\mathbf{B}$ are the perturbed quantities. The macroscopic fields obey the usual Maxwell equations, where the averaged charged and current densities used to determine the electromagnetic fields are

$$\rho = \sum_s e_s \int \mathrm{d}^3 v \, f_s, \tag{2.250}$$

$$\mathbf{j} = \sum_s e_s \int \mathrm{d}^3 v \, \mathbf{v} f_s. \tag{2.251}$$

This averaging process can be formalized via the BBGKY hierarchy (named for Bogoliubov, Born, Green, Kirkwood, and Yvon); we sketch the contours of the idea here. Essentially, the right-hand side of the kinetic equation represents cross-fluctuations of microscopic quantities. To determine this exactly would require solving a chain of coupled differential equations of difficulty equal to solving the Klimontovich equation. These spikey quantities are representative of the microscopic and discrete interactions between individual particles, giving rise to collisional effects. The importance of these collisional effects depends on macroscopic parameters of the plasma; it is typical to only include two-particle Coulomb collisions, essentially cutting the hierarchy of equations short. There are two length scales one must consider when evaluating the importance of higher-order collisional effects. One is the Debye length, defined as

$$\lambda_D \equiv \sqrt{\frac{\epsilon_0 T}{ne^2}}, \tag{2.252}$$

where n is the number density and T is the temperature given in units of energy. The Debye length is the length scale of Debye screening, where microscopic electric fields are spatially damped due to the collective motion of the surrounding charged particles in response to the microscopic field. Meanwhile, given a static Coulomb potential for like particles, the distance of closest approach of thermal one particle to another is given by

$$r_C = \frac{e^2}{4\pi\epsilon_0 T}. \tag{2.253}$$

The ratio of these two quantities is known as the plasma parameter,

$$\Lambda \equiv \frac{\lambda_D}{r_C} = \frac{4\pi\epsilon_0^{3/2}}{e^3}\frac{T^{3/2}}{n^{1/2}} = 4\pi n\lambda_D^3. \tag{2.254}$$

When Λ is large the dominant influence on charged particle motion will be the collective electrostatic fields rather than spikey Coulomb collisions. This condition necessitates that the typical kinetic energies of the constituent particles are greater than the interaction potential energies; plasmas that obey this condition are thus called weakly coupled. The opposite limit, when Λ is small, is called strongly coupled since the typical particle motion is dominated by many Coulomb collisions.

We then proceed as follows. A weakly coupled plasma requires that

$$\Lambda \gg 1 \tag{2.255}$$

In this case, we then rewrite the kinetic equation as the Boltzmann equation, given by

$$\frac{\partial f_s}{\partial t} + \mathbf{v} \cdot \frac{\partial f_s}{\partial \mathbf{x}} + \frac{e_s}{m_s}(\mathbf{E} + \mathbf{v} \times \mathbf{B}) \cdot \frac{\partial f_s}{\partial \mathbf{v}} = \left(\frac{\partial f_s}{\partial t}\right)_{\text{coll}}, \tag{2.256}$$

where

$$\left(\frac{\partial f_s}{\partial t}\right)_{\text{coll}} = C_s = \sum_{s'} C_{ss'}(f_s, f_{s'}). \tag{2.257}$$

Here, the collision term considers only two-particle Coulomb collisions and considers the distribution functions of all interacting species in the system, hence the sum. Given that tokamak plasmas have extremely large plasma parameters (on the order of 10^8), this approach is perfectly valid for fusion plasmas.

The Vlasov equation neglects collisions entirely and is written as

$$\frac{\partial f_s}{\partial t} + \mathbf{v} \cdot \frac{\partial f_s}{\partial \mathbf{x}} + \frac{e_s}{m_s}(\mathbf{E} + \mathbf{v} \times \mathbf{B}) \cdot \frac{\partial f_s}{\partial \mathbf{v}} = 0. \tag{2.258}$$

This equation can be put into Liouville form,

$$\frac{df_s}{dt} = \frac{\partial f_s}{\partial t} + \{f_s, H_s\} = 0, \tag{2.259}$$

where H_s is the single charged particle Hamiltonian and the Poisson bracket $\{\cdot, \cdot\}$ is defined as

$$\{f, g\} = \sum_{i=1}^{3} \left(\frac{\partial f}{\partial q_i}\frac{\partial g}{\partial p_i} - \frac{\partial g}{\partial p_i}\frac{\partial f}{\partial q_i}\right), \tag{2.260}$$

where $(\mathbf{q}, \mathbf{p})$ are canonical coordinates that satisfy Hamilton's equations of motion. This form of the Vlasov equation makes apparent that there are many equilibrium solutions f_{0s} such that

$$\frac{\partial f_{0s}}{\partial t} = \frac{df_{0s}}{dt} = 0. \tag{2.261}$$

In particular, a distribution that is only a function of constants of motion in the single particle system is itself an equilibrium solution of the Vlasov equation. For instance, if we take the Hamiltonian to be time independent, then it can be easily verified that

$$\frac{d}{dt}(f_{0s}(H_s)) = 0. \tag{2.262}$$

Moreover, it can be shown that the entropy density, defined as

$$s_s = -\int \mathrm{d}^3 v \ln(f_s) f_s, \tag{2.263}$$

is conserved under evolution of the Vlasov equation. This indicates that entropy production under this kinetic framework is driven by collisions. According to the H-theorem, the entropy is either constant or increases under the Boltzmann equation, leading to

$$\frac{ds_s}{dt} = \int (1 + \ln(f_s)) \left(\frac{\partial f_s}{\partial t}\right)_{\text{coll}} \geq 0. \tag{2.264}$$

The entropy density is in fact bounded from above. For a system with no interacting forces other than collisions, the distribution function that maximizes the entropy density is known as the Maxwell-Boltzmann distribution and is given by

$$f_M = n\left(\frac{m}{2\pi T}\right)^{\frac{3}{2}} e^{-\frac{m(\mathbf{v}-\mathbf{V})^2}{2T}}, \tag{2.265}$$

where $\mathbf{V}$ is the average bulk motion of the particles. Thus, collisions drive distribution functions to an equilibrium state characterized by Maxwellians. We can compute moments of the distribution function to verify that

$$n = \int \mathrm{d}^3 v \, f_M, \tag{2.266}$$

$$n\mathbf{V} = \int \mathrm{d}^3 v \, \mathbf{v} f_M, \tag{2.267}$$

$$\frac{3}{2} nT = \int \mathrm{d}^3 v \, \frac{1}{2} m(\mathbf{v} - \mathbf{V})^2 f_M. \tag{2.268}$$

Macroscopic quantities such as this are defined not just in the context of Maxwellian distributions, but also generic distribution functions that are close to a local Maxwellian. Indeed, fluid theory can be directly derived from the Boltzmann equation, resulting in partial differential equations that are only dependent on space and time. The strategy is to take moments of the Boltzmann equation by multiplying the equation by dyadic terms proportional to the velocity vector ($1, \mathbf{v}, \mathbf{vv}$, etc.) and integrating over all of velocity space. The result of this process is an infinite hierarchy of coupled partial differential equations generated by taking moments of $\mathbf{v}$; this is the price of

reducing a 6-dimensional phase space partial differential equation to a set of 3-dimensional partial differential equations all in terms of macroscopic variables. These equations are truncated by enforcing a fluid closure relating one of the higher-order moments to some condition or in terms of lower-order moments. Although these fluid equations are in principle far more tractable than the Boltzmann equation, the averaging procedure implicitly neglects kinetic effects and thus ignores microinstabilities. Since the phase space of the Boltzmann equation is often too large to solve computationally (even in the collisionless limit), it is necessary reduce the kinetic model without neglecting essential kinetic effects.

2.5.1 Gyrokinetics

To simplify the model, one must realize that the Vlasov equation can be used with equations of motion that approximately model a single charged particle. Due to the strong adiabatic invariance of the magnetic moment, a natural choice would be to use the guiding center equations of motion. However, the guiding center equations of motion are only valid if the time and length scales of any perturbations are small compared to the gyrofrequency and gyroradius. Perturbations with characteristic perpendicular length scales such that $k_\perp \rho_s \sim 1$ are often considered, where $k_\perp$ is the perpendicular wavenumber and ρ_s is the gyroradius of the dominant ion species. Thus, the formalism must be modified in a consistent manner that retains adiabatic invariance of μ. The full gyrokinetic ordering[38] can be summarized as follows with the small quantities ϵ_B, ϵ_ω, and ϵ_δ:

$$\frac{\rho}{L_B} \sim \epsilon_B \ll 1, \tag{2.269}$$

$$\frac{\omega}{\Omega_c} \sim \epsilon_\omega \ll 1, \tag{2.270}$$

$$\frac{\delta g}{\bar{G}} \sim \epsilon_\delta \ll 1, \tag{2.271}$$

$$k_\perp \rho \sim \epsilon_\perp \sim O\left(1\right), \tag{2.272}$$

$$\frac{k_\parallel}{k_\perp} \sim \frac{\epsilon_\omega}{\epsilon_\perp} \ll 1. \tag{2.273}$$

Here, L_B is the length scale of magnetic field gradients, ω is the mode frequency, δg represents any fluctuating quantity while G is the corresponding equilibrium quantity, and $k_\parallel$ and $k_\perp$ are respectively the parallel and perpendicular wavenumbers with respect to the magnetic field direction. To derive the proper phase space Lagrangian, a Lie perturbation approach is typically employed,[39] leading to

$$\mathcal{L} = \left(e\mathbf{A}_0 + e\bar{\mathbf{A}}_\parallel + mv_\parallel\right) \cdot \frac{d\mathbf{X}}{dt} + \frac{\mu m}{e}\dot{\alpha} - \frac{1}{2}mv_\parallel^2 - e\bar{\phi} - \mu\left(B_0 + \bar{B}_\parallel\right), \tag{2.274}$$

where $\mathbf{X}$ is the guiding center and $\boldsymbol{\rho}$ is the gyroradius. Essentially, we introduce the perturbed electrostatic potential ϕ, perturbed parallel magnetic field strength $\mathbf{B}_\parallel$, and perturbed parallel vector potential $\mathbf{A}_\parallel$ that are perturbations from the equilibrium fields $\mathbf{A}_0$ and $\mathbf{B}_0$ and where $\hat{\mathbf{b}} = \mathbf{B}_0/B_0$. The overbar signifies that the quantity is gyroaveraged, which we define via

$$\bar{f}(\mathbf{X}) \equiv \frac{1}{2\pi}\int_0^{2\pi} \mathrm{d}\alpha\, f(\mathbf{X} + \boldsymbol{\rho}). \tag{2.275}$$

The essential idea is that the perpendicular perturbations in the fields are treated via a gyroaverage of the phase space Lagrangian to remove any gyrophase dependence. The gyroaverage is often represented in terms of a Bessel function, which can be shown via a Fourier transform:

$$f(\mathbf{X} + \boldsymbol{\rho}) = \int \frac{\mathrm{d}^3k}{(2\pi)^3}\hat{f}(\mathbf{k})e^{i\mathbf{k}\cdot(\mathbf{X}+\boldsymbol{\rho})}, \tag{2.276}$$

where the hat signifies a Fourier transformed quantity. We note that

$$e^{i\mathbf{k}\cdot\boldsymbol{\rho}} = e^{ik_\perp\rho\cos(\alpha)}. \tag{2.277}$$

The gyroaverage is then

$$\langle f\rangle = \int \frac{\mathrm{d}^3k}{(2\pi)^3}\hat{f}(\mathbf{k})e^{i\mathbf{k}\cdot\mathbf{X}}\int_0^{2\pi}\frac{\mathrm{d}\alpha}{2\pi}e^{ik_\perp\rho\cos(\alpha)} = \int \frac{\mathrm{d}^3k}{(2\pi)^3}\hat{f}(\mathbf{k})e^{i\mathbf{k}\cdot\mathbf{X}}J_0(k_\perp\rho), \tag{2.278}$$

where J_0 is the zeroth-order Bessel function of the first kind. Thus, in Fourier space, the gyroaverage corresponds to including the gyroradius dependence via a Bessel function. The inclusion of such effects explicitly is known as including finite Larmor radius (FLR) effects. This allows us to write

the modified equations of motion,

$$\frac{d\mathbf{X}}{dt} = v_{\parallel}\hat{\mathbf{b}} + \mathbf{v}_{\delta} + \mathbf{v}_{\nabla B} + \mathbf{v}_{R_c}, \tag{2.279}$$

$$m\frac{dv_{\parallel}}{dt} = \left(\hat{\mathbf{b}} + \frac{mv_{\parallel}}{eB^*_{0\parallel}}\hat{\mathbf{b}} \times \boldsymbol{\kappa}\right) \cdot \left(-e\nabla\bar{\phi} + e\frac{\partial \bar{A}_{\parallel}}{\partial t}\hat{\mathbf{b}} - \mu\nabla B_0 - \mu\nabla\bar{B}_{\parallel}\right), \tag{2.280}$$

where terms such as $\mathbf{v}_{\nabla B}, \mathbf{v}_{R_c}, \boldsymbol{\kappa}$, and so on are defined in terms of the equilibrium magnetic field in accordance with the full guiding center equations of motion. Meanwhile, we introduce a new drift corresponding to the perturbed quantities

$$\mathbf{v}_{\delta} \equiv \frac{\mathbf{B}}{B^*_{0\parallel}B_0} \times \left(\nabla\bar{\phi} - v_{\parallel}\bar{A}_{\parallel} + \frac{\mu}{e}\bar{B}_{\parallel}\right). \tag{2.281}$$

With this new transformation in hand, we can apply it to the Vlasov equation. This approach is known as gyrokinetics; the collisionless gyrokinetic equation is then

$$\frac{\partial f}{\partial t} + \frac{d\mathbf{X}}{dt} \cdot \frac{\partial f}{\partial \mathbf{X}} + \frac{dv_{\parallel}}{dt}\frac{\partial f}{\partial v_{\parallel}} = 0. \tag{2.282}$$

We see here that the Vlasov equation has been greatly simplified, in part due to ignoring collisions. Instead of depending on six variables in phase space, the distribution function now only depends on four due to magnetic moment invariance as well as independence of the gyrophase due to the gryoaverage. From here, we can couple this to Maxwell's equations and solve the gyrokinetic equation given an equilibrium magnetic field. As an additional note, it is important to recognize that the field equations require taking moments of the distribution while also reversing the transformation of the distribution function back from gyrocenter coordinates to guiding center coordinates. This requires the use of what is known as a pullback operator. Meanwhile, the original transformation we used involved a pushforward operator. The result is a double gyroaverage, which can be defined via

$$\left\langle \bar{f} \right\rangle \equiv \frac{1}{4\pi^2}\int_0^{2\pi} \mathrm{d}\alpha \int \mathrm{d}^3X\, \delta(\mathbf{X} + \boldsymbol{\rho}(\alpha) - \mathbf{x}) \int_0^{2\pi} \mathrm{d}\alpha'\, f(\mathbf{X} + \boldsymbol{\rho}(\alpha')). \tag{2.283}$$

2.5.2 Quasilinear approximation

Although the gyrokinetic equation has been studied and used extensively to investigate a wide variety of kinetic phenomena, there are limits to the approach. Nonlinear simulations can be

prohibitively costly if one wishes to search throughout a wide range in parameter space. Even though the gyrokinetic equation can be linearized, the amount of grid points necessary to resolve the system precisely is computationally expensive. We can, however, take inspiration from the approach to reduce the system even further. Recall that the gyrokinetic formulation relies on the adiabatic invariance of μ, allowing one to decouple the time evolution of the distribution function from the gyrophase. A similar approach can be taken using the other adiabatic invariants found in the action-angle formalism. We introduce this formalism briefly; the full derivation of the approach as well as numerous reductions for the sake of numerical feasibility can be found in Chapter 5. Consider a Hamiltonian that is perturbed in the following way:

$$H = H_0(\mathbf{J}) + \delta h(\boldsymbol{\alpha}, \mathbf{J}, t) = H_0 + e\phi, \tag{2.284}$$

where ϕ is an electrostatic perturbation. We assume that the equilibrium Hamiltonian takes the form

$$H_0 = \frac{1}{2m}(\mathbf{p} - e\mathbf{A}_0)^2 + e\Phi, \tag{2.285}$$

where $\mathbf{A}_0$ is an equilibrium vector potential and Φ is an equilibrium electrostatic potential. Thus, for now, we do not consider perturbations in the magnetic field. In this system, the coordinates $(\boldsymbol{\alpha}, \mathbf{J})$ are canonical, leading to the simplified equations of motion

$$\frac{\boldsymbol{\alpha}}{dt} = \frac{\partial H}{\partial \mathbf{J}} = \boldsymbol{\Omega} + e\frac{\partial \phi}{\partial \mathbf{J}}, \tag{2.286}$$

$$\frac{d\mathbf{J}}{dt} = -\frac{\partial H}{\partial \boldsymbol{\alpha}} = -e\frac{\partial \phi}{\partial \mathbf{J}}. \tag{2.287}$$

In exchange for characterizing the motion in the equilibrium Hamiltonian completely, we have acquired reduced equations of motion. We then use these coordinates for the Vlasov equation, leading to

$$\frac{df}{dt} = \frac{\partial f}{\partial t} + \frac{d\boldsymbol{\alpha}}{dt} \cdot \frac{\partial f}{\partial \boldsymbol{\alpha}} + \frac{d\mathbf{J}}{dt} \cdot \frac{\partial f}{\partial \mathbf{J}} = 0. \tag{2.288}$$

We now invoke the quasilinear approximation. We assume that the distribution function f can be separated into an equilibrium solution f_0 and a perturbation δf; this piece is known as the δf

approximation. The equilibrium solution is found using the equilibrium Hamiltonian, and thus satisfies

$$\frac{df_0}{dt} = \mathbf{\Omega} \cdot \frac{\partial f_0}{\partial \boldsymbol{\alpha}} = 0, \tag{2.289}$$

leading to $f_0 = f_0(\mathbf{J})$. More precisely, we assume that although in the equilibrium system f_0 is stationary, in the nonlinear system f_0 slowly varies on a time scale longer than any oscillations associated with the linear perturbations. Thus, quasilinear theory takes a mean-field theory approach. We then find that

$$\frac{\partial \delta f}{\partial t} + \mathbf{\Omega} \cdot \frac{\partial \delta f}{\partial \boldsymbol{\alpha}} - e\frac{\partial \phi}{\partial \mathbf{J}} \cdot \frac{\partial f_0}{\partial \mathbf{J}} = -e\frac{\partial \phi}{\partial \mathbf{J}} \cdot \frac{\partial \delta f}{\partial \boldsymbol{\alpha}} + e\frac{\partial \phi}{\partial \boldsymbol{\alpha}} \cdot \frac{\partial \delta f}{\partial \mathbf{J}}. \tag{2.290}$$

The terms on the left-hand side are linear with the perturbed quantities, whereas the terms on the right-hand side are nonlinear. We assume the perturbations are small and thus neglect terms on the right-hand side in the linear limit. Moreover, the action-angle formalism allows us to write

$$\phi = \sum_{\mathbf{n}} \phi_{\mathbf{n}} e^{i\mathbf{n}\cdot\boldsymbol{\alpha} - i\omega t}, \tag{2.291}$$

$$\delta f = \sum_{\mathbf{n}} f_{\mathbf{n}} e^{i\mathbf{n}\cdot\boldsymbol{\alpha} - i\omega t}, \tag{2.292}$$

where ω is the frequency of oscillation of any individual mode. We assume that ω is a complex number and write

$$\omega = \omega_r + i\gamma. \tag{2.293}$$

Thus, the mode will have a real oscillation frequency ω_r as well as a growth rate γ. If the growth rate is positive, then the mode is said to be unstable; the perturbed mode will grow exponentially in time. If nonlinear physics were properly included, the mode would saturate and eventually cease exponential growth. As a result of this linearization, we find

$$f_{\mathbf{n}} = e\phi_{\mathbf{n}} \frac{\mathbf{n} \cdot \frac{\partial f_0}{\partial \mathbf{J}}}{\mathbf{n} \cdot \mathbf{\Omega} - \omega}. \tag{2.294}$$

We see that this relation does not depend on $\boldsymbol{\alpha}$ at all, only $\mathbf{J}$. Thus, we have successfully reduced the dimensionality of the kinetic equation to three phase space variables. This then can be coupled

to Poisson's equation, linking together all species. An important assumption for tokamak plasmas is quasineutrality, which can be written as

$$\sum_s n_s = 0. \tag{2.295}$$

This essentially arises from Debye screening; we are interested in length scales longer than the Debye length, thus we expect the Laplacian of the electrostatic potential to be negligible due to Debye screening. Moreover, due to the canonical choice in variables, various integrals necessary in the computation of the dispersion relation can be simplified since

$$\mathrm{d}^3x\,\mathrm{d}^3p = \mathrm{d}^3\alpha\,\mathrm{d}^3J\,. \tag{2.296}$$

Once the problem is solved linearly, we can then analyze the quasilinear behavior of the system by attaching a slow time dependence to the equilibrium distribution, $f_0 = f_0(\mathbf{J}, t)$. We then perform a time average over the Vlasov equation in order to analyze the long-term behavior (equivalent to averaging over the action angles $\boldsymbol{\alpha}$). We find that the only surviving terms are the slow evolution of the equilibrium distribution and the nonlinear terms, resulting in

$$\frac{\partial f_0}{\partial t} = \left\langle -e\frac{\partial \phi}{\partial \mathbf{J}} \cdot \frac{\partial \delta f}{\partial \boldsymbol{\alpha}} + e\frac{\partial \phi}{\partial \boldsymbol{\alpha}} \cdot \frac{\partial \delta f}{\partial \mathbf{J}} \right\rangle. \tag{2.297}$$

In accordance with the quasilinear approximation, we substitute the linear response into the quasilinear equation. Essentially, the linear solution informs the first-order nonlinear behavior. We then arrive at a quasilinear diffusion process described by

$$\frac{\partial f_0}{\partial t} = \frac{\partial}{\partial \mathbf{J}} \cdot \boldsymbol{D} \cdot \frac{\partial f_0}{\partial \mathbf{J}}, \tag{2.298}$$

where $\boldsymbol{D}$ is a quasilinear diffusion tensor. This is defined as

$$\boldsymbol{D} = -\frac{1}{2}\,\mathrm{Re}\left(\sum_{\mathbf{n}} ie^2 \mathbf{nn} \frac{\phi_{\mathbf{n}}\phi^*_{\mathbf{n}}}{\mathbf{n}\cdot\boldsymbol{\Omega} - \omega}\right). \tag{2.299}$$

We note that taking the real part and the factor of $\frac{1}{2}$ come from taking the time average of fluctuation quantities multiplied together. From here, quasilinear transport fluxes can be determined by taking

moments of this equation. For instance, the radial particle flux can be derived by considering

$$\frac{\partial n}{\partial t} + \frac{d\Gamma}{dr} = 0, \tag{2.300}$$

where

$$\frac{\partial n}{\partial t} = \int \mathrm{d}^3 v \, \frac{\partial f_0}{\partial t}. \tag{2.301}$$

Thus, the quasilinear transport term can be used to construct the fluxes. Importantly, quasilinear physics is not enough to tell us the magnitude of the fluxes; this can be seen from the fact that the linear response is projected to evolve exponentially in time if it is unstable. The magnitude of the flux is thus set by the saturation of the linear perturbations, which can only be resolved via nonlinear physics. Thus, quasilinear models require information from fuller nonlinear physics (such as nonlinear gyrokinetic simulations) in order to truly predict the quasilinear transport.

Finally, we note that to account for electromagnetic effects, one only needs to write

$$H = H_0 + \delta h, \tag{2.302}$$

$$H_0 = \frac{(\mathbf{p} - e\mathbf{A}_0)^2}{2m} + e\Phi, \tag{2.303}$$

$$\delta h = e\phi - e\mathbf{v}\cdot\mathbf{A}_1 + \frac{e}{2m}|\mathbf{A}_1|^2 \approx e\phi - e\mathbf{v}\cdot\mathbf{A}_1, \tag{2.304}$$

where $\mathbf{A}_0$ is the equilibrium vector potential and $\mathbf{A}_1$ is the fluctuating vector potential. A similar derivation can be done where the action-angle variables still form a canonical coordinate system. Some subtleties as to the interpretation of the action-angle variables in this formulation are addressed in Ref. 40.

2.5.3 Electrostatic drift wave instabilities

One of the primary goals of kinetic models is to identify and study microinstabilities that are responsible for anomalous transport. In this work, we focus on the existence of electrostatic drift wave instabilities. These particular instabilities are driven by gradients in the equilibrium profiles that are perpendicular to the flux surface, as they are sources of free energy; the most

important gradients are the temperature gradient and the density gradient. Moreover, they only require the existence of electrostatic perturbations to exist. There are other microinstabilities that are electromagnetic, but they will not be considered in this work. A more complete description of microinstabilities can be found in Refs. 41 and 42.

Unlike MHD instabilities that can become violently unstable and disrupt the plasma, these electrostatic microinstabilities saturate at small amplitudes on the order of 1% to 10% due to nonlinear effects. Moreover, these modes are highly anisotropic such that the parallel wavelength is much longer than the perpendicular wavelength (with the local magnetic field line serving as a reference direction); this flute-like nature is ultimately due to the fast parallel motion of the particle compared to the slow perpendicular drift motion. Moreover, while the typical frequencies of these instabilities are much smaller than the gyrofrequency (thus preserving magnetic moment invariance), the perpendicular wavelengths are on the order of the gyroradius. It is this particular characteristic that rendered the development of gyrokinetics necessary, as FLR effects are essential. To simulate these instabilities, one can either conduct a global simulation of the entire plasma or conduct a local, flux tube simulation in which the domain consists of a small domain around a reference flux surface. In a local simulation, the equilibrium quantities and the gradients of those quantities are held approximately constant to render the calculation tractable. One cost of the local approach, of course, is that one loses the global effects that comes with simulating the microturbulence in the presence of the entire magnetic field.

The main classes of electrostatic microinstabilities important for anomalous transport are the ion temperature gradient (ITG) mode, the trapped electron mode (TEM), and the electron temperature gradient (ETG) mode. As suggested by the name, ITG modes are primarily driven by ion temperature gradients. The perpendicular wavelength for ITG instabilities is of the order of the ion gyroradius. Moreover, one of the key mechanisms for the instability to manifest is the interaction between the temperature gradient and the ion drift direction. If the curvature of the magnetic field points in the direction of the pressure gradient, we say that this is a bad curvature region due to resulting instabilities that can arise as a result of the interplay between the pressure gradient and

the curvature drift; specifically, the direction of the curvature drift leads to a perturbed E-cross-B drift as a result of charge separation that enhances the instability in the bad curvature region. For normal profiles in a tokamak, the low field region consists of bad curvature while the high field region consists of good curvature.

TEMs, on the other hand, are destabilized in the presence of electron temperature and density gradients. For the collisionless trapped electron mode (CTEM), there exists a resonance between the toroidal precession frequency and the mode frequency as a result of the trapped electron bounce motion. For CTEMs, the electrons are able to complete many bounce motions before diffusing towards the passing part of velocity space due to collisions. Meanwhile, the presence of strong collisions leads to the dissipative trapped electron mode (DTEM). In DTEMs, collisions can prove to be a destabilizing effect by causing marginally passing electrons to diffuse into the trapped part of velocity space, thus contributing to the instability as TEMs in general are driven by the trapped electron fraction. For high collisionality, however, trapped particles can undergo many collisions before completing a single bounce orbit. In this scenario, collisions can stabilize the mode by virtue of interrupting the bounce orbits via diffusion into the passing part of velocity space. Their characteristic perpendicular wavelength is often taken to be on the order of the radial deviation from the magnetic surface. In practice, this leads to a significant overlap between ITG modes and TEMs as the perpendicular wavelength will then be of the order of the ion gyroradius due to the electron-ion mass ratio. There thus exists a significant coupling between ITG modes and TEMs such that assessing both ion and electron dynamics is necessary for an accurate calculation.

Finally, the ETG mode is naively analogous to the ITG mode; ETG modes are destabilized by electron temperature gradients and the perpendicular wavelength is of the order of the electron gyroradius. Due to the electron-ion mass ratio, the dynamics of the ions at this scale are approximately adiabatic and not kinetic. As a result of the electron-ion mass ratio, one might expect the resulting electron heat transport to be smaller than the ITG driven ion heat turbulence. In actuality, however, there is a non-trivial interplay between electron scales and ion scales that affect ETG turbulence. Capturing this interaction requires the use of multiscale simulations which do not

neglect ion dynamics despite the large difference in time scales.

2.6 Chapter summary

In this chapter, we have built up the fundamentals of plasma theory relevant to this work. First, we characterized single particle motion in a magnetic field by decomposing the magnetic drifts from the cyclotron motion. This allowed us to proceed to describing the guiding center equations of motion in full. From there, we then examined guiding center motion in a tokamak field and characterized its orbits via the action-angle formalism. Using single particle motion, we then developed kinetic theory to describe the evolution of a system with many particles. This allowed us to reduce the system of many individual particles to the evolution of a distribution function f. We then reduced the complexity of this system even further by relying on notions of adiabatic invariance as well as the action-angle formalism to construct a quasilinear approach to plasma kinetics. With these tools in hand, we can proceed to the primary work of this dissertation.

CHAPTER 3

On the limitations of gyrokinetics: Magnetic moment conservation

3.1 Introduction

Gyrokinetic theory[39] is a popular approach to investigate phenomena in magnetized natural or laboratory plasmas whose dynamics are subject to the so-called gyrokinetic ordering.[39] Originally developed for fusion applications, gyrokinetics has also been employed to study a wide range of problems in basic or space plasma physics, including magnetic field reconnection[43–47] and solar wind turbulence.[48–51] It nicely complements other kinetic approaches like fully kinetic models or hybrid kinetic-fluid models.[52]

Although gyrokinetics provides an efficient description of magnetized plasmas, it is somewhat challenging to characterize its range of validity beyond the general scalings implied by the gyrokinetic ordering. To make progress on this front, we therefore focus on one of the fundamental assumptions of gyrokinetic theory, namely, magnetic moment conservation. In the absence of strong electric fields, the magnetic moment μ of a charged particle in a magnetic field is an adiabatic invariant if the magnetic field changes slowly in time and space.[21] If this adiabatic invariant is not conserved appropriately, the validity of gyrokinetics comes into question. Here, we investigate the validity of gyrokinetics by explicitly calculating the perturbation of the magnetic moment of a single charged particle in several elementary combinations of prescribed electromagnetic fields. This will allow us to clearly quantify some of the limitations of gyrokinetics in transparent ways.

Historically, μ has been defined as the ratio of the transverse kinetic energy to the magnetic

field. We maintain that definition here:

$$\mu_1 = \frac{1}{2}\frac{m\mathbf{v}_\perp{}^2}{B}. \tag{3.1}$$

Here, m is the mass of the particle, $\mathbf{B} = B\hat{\mathbf{b}}$ is the magnetic field where $\hat{\mathbf{b}}$ is the unit vector denoting the direction of the magnetic field, $\mathbf{v}$ is the velocity of the particle, and the subscript $\perp$ denotes that we take the component that is perpendicular to the magnetic field. In addition, the subscript $\parallel$ will denote that we take the component parallel to the magnetic field. For the discrimination from alternative definitions, to be introduced below, we attach the '1' subscript. We note that this conception of μ does not take into consideration any drift-motion of the gyrocenter.

We propose further definitions of the magnetic moment, which account for the drift-motion of the guiding center in various ways. These definitions provide varying degrees of generality and conservation. Qin and Davidson have previously showed that there is an exact magnetic moment invariant for a homogeneous time-dependent magnetic field.[53] Our goal is to find an invariant that experiences strong conservation but is also not computationally costly.

In this work, we utilize a definition of the gyroradius, ρ, to account for the motion of the guiding center:

$$\mu_\rho = \frac{1}{2}\frac{m\left(\mathbf{v} - \mathbf{v}_{gc}\right)_\perp^2}{B}. \tag{3.2}$$

The meaning of $\mathbf{v}_{gc}$ becomes clear in the following:

$$\mathbf{r}_{gc} = \mathbf{r} - \boldsymbol{\rho} = \mathbf{r} + \frac{\mathbf{v}\times\hat{\mathbf{b}}}{\Omega}, \tag{3.3}$$

$$\mathbf{v}_{gc} = \dot{\mathbf{r}}_{gc}, \tag{3.4}$$

$$\Omega = \frac{qB}{mc}. \tag{3.5}$$

We define $\mathbf{r}$ as the instantaneous position of the particle q as the charge of the particle, c as the speed of light, and Ω as the cyclotron frequency. We suppose that this correction should lead to a more robust magnetic moment conservation. Furthermore, this definition requires no information about the perturbing electromagnetic fields other than the cyclotron frequency dominated by $\mathbf{B}$.

We also define a magnetic moment that has been corrected for the instantaneous $\mathbf{E} \times \mathbf{B}$ drift velocity, evaluated at the guiding center position:

$$\mu_E = \frac{1}{2} \frac{m \left(\mathbf{v}_\perp - \mathbf{v}_E \right)^2}{B}, \tag{3.6}$$

$$\mathbf{v}_E = \frac{\mathbf{E} \times c\mathbf{B}}{B^2}. \tag{3.7}$$

The vector $\mathbf{E}$ denotes the electric field of the system. Again, we suppose that this correction should lead to stronger μ conservation. In contrast to Eq. (3.2), this definition requires explicit information about a perturbing field. We also note that if $\mathbf{B}$ is constant and uniform and if $\mathbf{E}$ is not spatially dependent, then $\mu_\rho = \mu_E$.

Throughout this work, we will develop further definitions of the magnetic moment which take into consideration the drift velocities particular to certain field configurations. These definitions lose generality for the sake of μ conservation. We also define a characteristic scale for the magnetic moment,

$$\mu_0 = \frac{q}{2c} \Omega_0 \rho_0^2, \tag{3.8}$$

where $\Omega_0 = \frac{qB_0}{mc}$, ρ_0 refers to a length scale for the gyroradius, while B_0 and Ω_0 characterize the magnetic field and cyclotron frequency for the system in question. For convenience, we assume $B_0 > 0$ and $\rho_0 > 0$ throughout this work; thus, $\mu_0 > 0$

We also refer to four dimensionless parameters that characterize the breaking of μ conservation. These parameters are used in treatments of gyrokinetics such as in Refs. 39 and 54 to carry out the gyrokinetic ordering:

$$\epsilon_\omega = \left| \frac{\omega}{\Omega_0} \right|, \tag{3.9}$$

$$\epsilon_B = \left| \frac{\rho_{\text{th}}}{L_B} \right|, \tag{3.10}$$

$$\epsilon_\perp = \left| k_\perp \rho_{\text{th}} \right|, \tag{3.11}$$

$$\epsilon_\delta \sim \left| \frac{v_E}{v_{\text{th}}} \right| = \left| \frac{E_\perp c}{B_0 v_{\text{th}}} \right| = \epsilon_\perp \left| \frac{q\varphi}{T} \right|. \tag{3.12}$$

Here, ω is the characteristic frequency of explicitly time dependent fields, L_B is the length scale of magnetic field variations, ρ_{th} is the thermal Larmor radius, $k_\perp$ is the wavenumber of perpendicular electric field variations, v_{th} is the thermal velocity, and T is the temperature. $E_\perp$ refers to the fluctuating electric fields perpendicular to the magnetic field, while φ is the fluctuating electric potential.

When the charged particle is subject to a magnetic field of the form $\mathbf{B} = B(x, y, t)\hat{\mathbf{z}}$, we analyze the problem two-dimensionally and ignore all motion parallel to the magnetic field. The variables x, y, and z represent the standard Cartesian coordinates, while t represents the time. In addition, we take $\rho_{\text{th}} \sim \rho_0$ and $v_{\text{th}} \sim u = \rho_0\Omega_0$ when we subject the particle to initial conditions. Subsequent sections of this work analyze specific electromagnetic field configurations. We examine uniform time dependent magnetic fields in Sec. 3.2, and then we analyze spatially dependent magnetic fields in Sec. 3.3. Sec. 3.4 includes a time dependent electric field superimposed on top of a constant, uniform magnetic field. We then analyze a spatially dependent electric field together with a constant and uniform magnetic field in Sec. 3.5. Sec. 3.6 of this work then summarizes our results and relates them to the standard gyrokinetic theory. We also perform calculations that connect Littlejohn's guiding center theory to the work in this paper; they are contained within Appendix 3.A. We also note that we use Gaussian units in this work.

3.2 Time dependent magnetic field

We first consider the motion of a charged particle in a spatially uniform but time dependent magnetic field pointing in the $\hat{\mathbf{z}}$ direction. This system physically corresponds to that of an infinitely long solenoid with a time dependent current that changes quasi-statically. The magnetic field is assumed to satisfy

$$\left|\frac{1}{B}\frac{dB}{dt}\right| \ll |\Omega| \,. \tag{3.13}$$

The changing magnetic field creates an induced electric field which curls around the center of the solenoid, perpendicular to the magnetic field. We also assume that $|B(t)| > 0$ for all time. Then,

we can use the WKB approximation to obtain equations of motion for the charged particle. An introduction to the WKB approximation can be found in Ref. 55.

Using WKB theory, Kulsrud demonstrates in Ref. 56 that if the natural frequency of a harmonic oscillator is initially constant, varies, and then returns to constancy after some finite amount of time, then there is no overall change in the adiabatic invariant of this system before and after the variation. Kruskal extends the results of Kulsrud's work to the case of the magnetic moment of a charged particle in Ref. 26 using the fact that the motion of a gyrating particle and that of a harmonic oscillator are intrinsically linked. What Kulsrud and Kruskal do not consider, however, is how much the adiabatic invariant is perturbed from its initial value in the intermediate stage. Using WKB theory, we show explicitly that the magnetic moment returns to its initial value, and we also calculate a first-order expression to determine the maximum perturbation of the magnetic moment as the magnetic field is changing.

3.2.1 WKB approximation

The vector potential for this system is

$$\mathbf{A} = \frac{1}{2} B(t)\,(x\hat{\mathbf{y}} - y\hat{\mathbf{x}})\,, \tag{3.14}$$

where the origin of our coordinate system is at the center of the solenoid. This produces the following electromagnetic fields:

$$\mathbf{B} = \nabla \times \mathbf{A} = B(t)\hat{\mathbf{z}}, \tag{3.15}$$

$$\mathbf{E} = -\frac{1}{c}\frac{\partial \mathbf{A}}{\partial t} = -\frac{\dot{B}(t)}{2c}\,(x\hat{\mathbf{y}} - y\hat{\mathbf{x}})\,. \tag{3.16}$$

The two-dimensional Lagrangian for this system is

$$L = \frac{1}{2} m\mathbf{v}_\perp^2 + \frac{q}{c}\mathbf{v}_\perp \cdot \mathbf{A}, \tag{3.17}$$

where $\mathbf{v}_\perp = \dot{x}\hat{\mathbf{x}} + \dot{y}\hat{\mathbf{y}}$. From the Euler-Lagrange equations we obtain

$$\ddot{x} = \Omega\dot{y} + \frac{1}{2}\dot{\Omega}y, \tag{3.18}$$

$$\ddot{y} = -\Omega\dot{x} - \frac{1}{2}\dot{\Omega}x. \tag{3.19}$$

We decouple these ODEs by defining new variables u and v to be

$$u = x + iy, \qquad\qquad v = x - iy. \tag{3.20}$$

The decoupled equations are

$$\ddot{u} = -i\left(\Omega\dot{u} + \frac{1}{2}\dot{\Omega}u\right), \tag{3.21}$$

$$\ddot{v} = i\left(\Omega\dot{v} + \frac{1}{2}\dot{\Omega}v\right). \tag{3.22}$$

We cast these ODEs into normal form by defining the following transformations:

$$u(t) = f(t)\exp\left(\int^t -\frac{i}{2}\Omega(t')\,dt'\right), \tag{3.23}$$

$$v(t) = g(t)\exp\left(\int^t \frac{i}{2}\Omega(t')\,dt'\right). \tag{3.24}$$

Plugging these transformations into Eq. (3.22), we obtain

$$\ddot{f}(t) + \frac{1}{4}\Omega(t)^2 f(t) = 0, \qquad\qquad \ddot{g}(t) + \frac{1}{4}\Omega(t)^2 g(t) = 0. \tag{3.25}$$

Since Eq. (3.13) is satisfied, we can then apply the WKB approximation to Eq. (3.25). The WKB solutions are

$$f(t) = \frac{C_1\exp\left(\int^t \frac{i}{2}\Omega(t')\,dt'\right) + C_2\exp\left(\int^t -\frac{i}{2}\Omega(t')\,dt'\right)}{\sqrt{|\Omega(t)|}}, \tag{3.26}$$

$$g(t) = \frac{C_3\exp\left(\int^t \frac{i}{2}\Omega(t')\,dt'\right) + C_4\exp\left(\int^t -\frac{i}{2}\Omega(t')\,dt'\right)}{\sqrt{|\Omega(t)|}}, \tag{3.27}$$

where each C_i is a constant determined by the initial conditions. Finally, we invert our transformations and apply the following initial conditions:

$$x(t_0) = x_0, \qquad y(t_0) = y_0, \qquad \dot{x}(t_0) = v_{x0}, \qquad \dot{y}(t_0) = v_{y0}. \tag{3.28}$$

We also define $\Omega(t_0) = \Omega_0$. The equations of motion are then

$$x(t) = \sqrt{\frac{\Omega_0}{\Omega(t)}} \left(\frac{v_{x0}}{\Omega_0} \sin(\theta(t)) - \frac{v_{y0}}{\Omega_0} \cos(\theta(t)) + x_0 + \frac{v_{y0}}{\Omega_0} \right), \tag{3.29}$$

$$y(t) = \sqrt{\frac{\Omega_0}{\Omega(t)}} \left(\frac{v_{x0}}{\Omega_0} \cos(\theta(t)) + \frac{v_{y0}}{\Omega_0} \sin(\theta(t)) + y_0 - \frac{v_{x0}}{\Omega_0} \right), \tag{3.30}$$

where $\theta(t) = \int_{t_0}^{t} \Omega(t')\, dt'$ is the elapsed phase.

We now restrict the problem to the case where instantaneously at $t = t_0$, the particle is circling around a center point $\mathbf{R}_0 = R_{x0}\hat{\mathbf{x}} + R_{y0}\hat{\mathbf{y}}$ with radius ρ_0 and speed $|\Omega_0 \rho_0|$. To simplify the problem, without loss of generality, we set $v_{x0} = 0$. The equations of motion are then the following:

$$x(t) = \sqrt{\frac{\Omega_0}{\Omega(t)}} \left(\rho_0 \cos(\theta(t)) + R_{x0} \right), \tag{3.31}$$

$$y(t) = \sqrt{\frac{\Omega_0}{\Omega(t)}} \left(-\rho_0 \sin(\theta(t)) + R_{y0} \right). \tag{3.32}$$

3.2.2 Magnetic moment conservation

Before calculating the magnetic moment, we first calculate the $\mathbf{E} \times \mathbf{B}$ velocity:

$$\mathbf{v}_E(\mathbf{x}, t) = -\frac{\dot{B}}{2B} \left(x\hat{\mathbf{x}} + y\hat{\mathbf{y}} \right). \tag{3.33}$$

We next correct for the guiding center motion of the particle by evaluating $\mathbf{v}_E$ at the guiding center position $\mathbf{R}$. To calculate $\mathbf{R}$, we average the position of the particle over one gyration:

$$\mathbf{R} = \langle \mathbf{r}_\perp \rangle = \frac{1}{2\pi} \int_{-\pi}^{\pi} \mathbf{r}_\perp \, d\theta. \tag{3.34}$$

Here, $\mathbf{r}_\perp$ is the position of the particle in the xy-plane. We note that since the cyclotron frequency is a slowly varying function of time, we may simply treat it as constant during the averaging procedure.[57] Thus, the position of the guiding center is

$$\mathbf{R} = \sqrt{\frac{\Omega_0}{\Omega(t)}} \mathbf{R}_0. \tag{3.35}$$

With this in mind, we can easily compute the standard magnetic moment of the particle μ_1 using the approximate equations of motion. The expression is

$$\mu_1(t) = \mu_0 \left(1 + \frac{R_{x0}\sin(\theta(t)) + R_{y0}\cos(\theta(t))}{\rho_0}\frac{\dot{\Omega}}{\Omega^2} + \left(\frac{1}{4} + \frac{R_{x0}^2 + R_{y0}^2}{4\rho_0^2} + \frac{R_{x0}}{2\rho_0}\cos(\theta(t)) - \frac{R_{y0}}{2\rho_0}\sin(\theta(t))\right)\frac{\dot{\Omega}^2}{\Omega^4}\right). \tag{3.36}$$

We note that terms like $(R_0/\rho_0)(\dot{\Omega})/(\Omega^2)$ are characteristic of the $\mathbf{E}\times\mathbf{B}$ drift. Thus, the perturbation is $O(\epsilon_\delta)$ and is determined by ϵ_ω as well as the initial guiding center $\mathbf{R}_0$. If the particle's guiding center is initially far from the center of the solenoid, then it will experience a large drift velocity that will break μ conservation unless ϵ_ω is small enough to compensate. We also notice that after the magnetic field has stopped changing, μ_1 returns to its initial value.

We next evaluate the $\mathbf{E}\times\mathbf{B}$ velocity at this position and calculate μ_E to be

$$\mu_E(t) = \frac{m}{2B(t)}\left(\mathbf{v}(t) - \mathbf{v}_E(\mathbf{R}, t)\right)^2. \tag{3.37}$$

To simplify the calculation, we prescribe a magnetic field such that $\dot{B}(t = t_0) = 0$. Plugging in our equations of motion, we find that the corrected magnetic moment is

$$\mu_E(t) = \mu_0\left(1 + \frac{\dot{\Omega}^2}{4\Omega^4}\right). \tag{3.38}$$

We note that μ_E is predicted by Littlejohn's guiding center theory to be better conserved than μ_1. Furthermore, the maximum perturbation of the magnetic moment is small due to Eq. (3.13). For $\mathbf{R}_0 = 0$, $\mu_1 = \mu_E$. Thus, μ_E will be conserved to higher order than μ_1.

Next, we prescribe an example magnetic field and find the maximum perturbation. We define the magnetic field to be

$$B(t) = B_0\left(1 + \frac{\alpha_B}{1 + e^{-\omega t}}\right), \qquad B_0, \alpha_B, \omega > 0. \tag{3.39}$$

This magnetic field has an initial value of B_0, and slowly increases to a final value of $(1 + \alpha_B)B_0$ with a characteristic frequency ω. To satisfy Eq. (3.13), we require that

$$\left|\frac{\dot{\Omega}(t)}{\Omega(t)^2}\right| \ll 1. \tag{3.40}$$

For our specified magnetic field,

$$\max\left(\left|\frac{\dot{\Omega}(t)}{\Omega(t)^2}\right|\right) = \left|\frac{\omega}{\Omega_0}\right| \frac{\alpha_B}{4(1+\alpha_B)}. \tag{3.41}$$

Thus, we require

$$\frac{\epsilon_\omega \alpha_B}{4(1+\alpha_B)} \ll 1. \tag{3.42}$$

For our prescribed magnetic field, the condition in Eq. (3.42) is satisfied for even large values of α_B as long as ϵ_ω is small.

For this system, we define the maximum perturbation the corrected magnetic moment,

$$\Delta\mu_E = |\max(\mu_E) - \min(\mu_E)|\,. \tag{3.43}$$

To calculate this quantity, we maximize the function $\dot{B}(t)^2/B(t)^4$. We find that

$$\frac{\Delta\mu_E}{\mu_0} = \frac{\epsilon_\omega^2 \alpha_B^2}{64(1+\alpha_B)^2} \ll 1, \tag{3.44}$$

where the inequality is due to Eq. (3.42). We note here that as long as $\epsilon_\omega \ll 1$, the perturbation is small even for large values of α_B.

Finally, we present another way to calculate a corrected magnetic moment. We take $\mathbf{R}_0 = \mathbf{0}$ so that the particle is circling around the origin. We note that this is equivalent to first correcting for $\mathbf{v}_E(\mathbf{R}, t)$. We then calculate μ_B using the equations of motion to obtain

$$\mu_\rho(t) = \mu_0\left(1 + \frac{\dot{\Omega}^4}{4\Omega^8}\right). \tag{3.45}$$

Thus, we have gained higher order magnetic moment conservation because the perturbation now depends on even higher time derivatives than previously. Plugging in our defined magnetic field, we calculate that the maximum perturbation is

$$\frac{\Delta\mu_\rho}{\mu_0} = \frac{\epsilon_\omega^4 \alpha_B^4}{1024\,(1+\alpha_B)^4} \ll 1. \tag{3.46}$$

3.2.3 Adiabatic invariant

We now calculate the adiabatic invariant for this system by following a slightly modified approach to Taylor in Ref. 58. We define our adiabatic invariant to be

$$I = \oint p_r \, dr = 2 \int_{r_{\min}}^{r_{\max}} \sqrt{2mH_\perp - \left(\frac{p_\phi}{r} - \frac{m\Omega r}{2}\right)^2} \, dr, \tag{3.47}$$

where we integrate over the region where the integrand is real. Here, r is the perpendicular distance away from the cylindrical axis of symmetry, ϕ is the azimuthal angle, $H_\perp = mv_\perp^2/2$ is the two-dimensional Hamiltonian, $p_r = m\dot{r}$ is the canonical momentum associated with r, and $p_\phi = mr^2\dot{\phi} + (qBr^2)/(2c)$ is the canonical momentum associated with ϕ. We note that even when the magnetic field is changing in time, p_ϕ is an exact constant of motion due to the cylindrical symmetry of the system. The quantity $H_\perp$ is a constant of motion if the magnetic field is static. The integral can be computed exactly:

$$I = \pi \min\left(\frac{2mH_\perp}{\Omega}, \frac{2mH_\perp}{\Omega} + 2p_\phi\right). \tag{3.48}$$

We note that since p_ϕ is an exact constant of motion even in a time dependent magnetic field, the term $2\pi p_\phi$ can simply be subtracted to get a new adiabatic invariant. We can then write the magnetic moment based off of this invariant:

$$\mu_I = \frac{q}{mc}\frac{I}{2\pi} = \frac{H_\perp}{B} = \mu_1. \tag{3.49}$$

The adiabatic invariant for this system is simply the uncorrected magnetic moment μ_1, a well known result. As seen above, while μ_1 does fluctuate over time, its perturbation is proportional to ϵ_ω, as to be expected from an adiabatic invariant.

3.2.4 Summary

In summary, we used the WKB approximation for a slowly time varying magnetic field to show that all three of our defined magnetic moments return to their original value after the magnetic field has stopped changing. In addition, if the rate at which the magnetic field changes is small compared

to the cyclotron frequency, then the perturbation of the magnetic moment is small regardless of how much the magnetic field changes in magnitude. If the change of magnitude of the magnetic field is small, then naturally the perturbation will be even smaller. By correcting for the guiding center motion, we can attain higher order μ conservation. Finally, we note that the above use of the WKB approximation only applies for magnetic fields that do not become exactly zero or change sign. If the magnetic field does indeed change sign, then the use of Airy functions is required to properly apply the WKB approximation. We now examine magnetic moment conservation in spatially dependent magnetic fields without any electric fields.

3.3 Spatially dependent magnetic field

3.3.1 Straight magnetic field

The next system we consider is one already analyzed by Brizard in Ref. 59. We define our nonuniform magnetic field to be

$$\mathbf{B}(x) = B_0(1 - x/L_B)\hat{\mathbf{z}}, \qquad B_0, L_B > 0, \tag{3.50}$$

where L_B is the gradient length scale of the magnetic field. We also subject our particle to the following initial conditions:

$$\begin{aligned} x(0) &= \rho_0, \\ \dot{x}(0) &= 0, \\ y(0) &= 0, \\ \dot{y}(0) &= -\Omega_0\rho_0 = -u. \end{aligned} \tag{3.51}$$

Here, $\rho_0 \sim \rho_{\text{th}}$ is the characteristic length of the gyromotion while $u = \Omega_0\rho_0 \sim v_{\text{th}}$ is the characteristic velocity. We also assume that $\rho_0 > 0$.

3.3.1.1 Equations of motion

The ODEs for this system are

$$\ddot{x} = \Omega_0 \dot{y}\,(1 - x/L_B), \tag{3.52}$$

$$\ddot{y} = -\Omega_0 \dot{x}\,(1 - x/L_B). \tag{3.53}$$

As Brizard demonstrates, $x(t)$ is periodic and varies between ρ_0 and $-\rho_0$. In addition, because magnetic fields do no work, the kinetic energy is conserved.

We first follow Brizard's approach in reducing our ODEs from second-order to first-order. We note that the right-hand side of Eq. (3.53) is a total derivative, and thus we can integrate the equation to obtain

$$\dot{y} = \Omega_0 \left(\frac{1}{2L_B} \left(x^2 - \rho_0^2 \right) - x \right). \tag{3.54}$$

Here, we can explicitly see the grad-B drift term $-u\epsilon_B/2$. Next, we plug this into Eq. (3.52) and note that

$$\ddot{x}(2\dot{x}) = \frac{d}{dt}(\dot{x}^2). \tag{3.55}$$

We integrate the result and obtain

$$(\dot{x})^2 = \Omega_0^2 \left[-\epsilon_B \rho_0 (y - \rho_0) + \left(\frac{\epsilon_B^2}{2} - 1 \right) \left(y^2 - \rho_0^2 \right) + \frac{1}{L_B} \left(y^3 - \rho_0^3 \right) - \frac{1}{4L_B^2} (y^4 - \rho_0^4) \right]. \tag{3.56}$$

Brizard then uses these equations to finally obtain the equations of motion:

$$x(t) = \rho_0 \left(\frac{2}{\epsilon_B} - 1 - \frac{2}{\epsilon_B} \left(\frac{1 - \epsilon_B}{1 - \epsilon_B \,\mathrm{sn}^2(\Omega_0 t/2 | \epsilon_B^2)} \right) \right), \tag{3.57}$$

$$\begin{aligned} y(t) = \rho_0 \Bigg(& -\frac{\Omega_0 t}{\epsilon_B} \left(1 - \frac{E(\epsilon_B^2)}{K(\epsilon_B^2)} \right) + \frac{2}{\epsilon_B} Z \left(\mathrm{am}(\Omega_0 t/2 | \epsilon_B^2) | \epsilon_B^2 \right) \\ & - \frac{2\,\mathrm{sn}(\Omega_0 t/2 | \epsilon_B^2)\,\mathrm{cn}(\Omega_0 t/2 | \epsilon_B^2)\,\mathrm{dn}(\Omega_0 t/2 | \epsilon_B^2)}{1 - \epsilon_B \,\mathrm{sn}^2(\Omega_0 t/2 | \epsilon_B^2)} \Bigg). \end{aligned} \tag{3.58}$$

The solutions are expressed in terms of Jacobi elliptic functions sn, cn, and dn, complete elliptic integrals E and K, the Jacobi amplitude function am, and the Jacobi zeta function Z.

3.3.1.2 Magnetic moment conservation

We now calculate the magnetic moment as a function of x; one finds

$$\mu_1(x) = \frac{\mu_0}{1 - x/L_B}. \tag{3.59}$$

This function oscillates between a maximum at $x = \rho_0$ and a minimum at $x = -\rho_0$. Due to the oscillation, we define the magnetic moment deviation to be the difference between the maximum and minimum divided by 2. The deviation is then

$$\frac{\Delta\mu_1}{\mu_0} = \frac{\epsilon_B}{1 - \epsilon_B^2}. \tag{3.60}$$

For $\epsilon_B \ll 1$, the perturbation is $\epsilon_B + \epsilon_B^3 + O\left(\epsilon_B^5\right)$.

Next, we correct for the lowest-order grad-B drift velocity, which Brizard calculates to be,

$$\mathbf{v}_{\nabla B} = -\frac{u\epsilon_B}{2}\hat{\mathbf{y}}. \tag{3.61}$$

To do so, we define the corrected magnetic moment to be

$$\mu_{\nabla B} = \frac{1}{2}\frac{m(\mathbf{v} - \mathbf{v}_{\nabla B})^2}{B(x)}. \tag{3.62}$$

Carrying out the calculation by substituting in the equations for $\dot{x}^2$ and $\dot{y}$, we obtain $\mu_{\nabla B}$ as a function of x:

$$\mu_{\nabla B}(x) = \mu_0\left(\frac{1}{2L_B^2}\frac{x^2 - \rho_0^2/2}{1 - x/L_B} + 1\right). \tag{3.63}$$

We next find the extrema of this function within the domain $-\rho_0 \le x \le \rho_0$ and calculate the deviation. A local maximum exists at $x = -\rho_0$, a global maximum at $x = \rho_0$, and a global minimum at $x = L_B\left(1 - \sqrt{1 - \epsilon_B^2/2}\right)$. We calculate the deviation of the corrected magnetic moment using the global maximum:

$$\frac{\Delta\mu_{\nabla B}}{\mu_0} = \frac{\epsilon_B^2}{8(1 - \epsilon_B)} + \frac{1 - \sqrt{1 - \epsilon_B^2/2}}{2}. \tag{3.64}$$

For $\epsilon_B \ll 1$, this is equal to $\epsilon_B^2/4 + \epsilon_B^3/8 + O\left(\epsilon_B^4\right)$. Thus, by correcting for the lowest-order grad-B drift, we have gained an extra order in magnetic moment conservation. This is consistent with

Littlejohn's result, which predicts that a grad-B correction will lead to higher magnetic moment conservation.

Finally, from the equations of motion it is clear that the exact drift is

$$\mathbf{v}_D = -\frac{\rho_0 \Omega_0}{\epsilon_B}\left(1 - \frac{E\left(\epsilon_B^2\right)}{K\left(\epsilon_B^2\right)}\right)\hat{\mathbf{y}}. \tag{3.65}$$

We can then correct for this drift when calculating the magnetic moment:

$$\mu_D = \frac{1}{2}\frac{m\left(\mathbf{v}_\perp - \mathbf{v}_D\right)^2}{B_0(1 - x/L_B)}. \tag{3.66}$$

The maximum deviation of this magnetic moment is defined to be

$$\Delta\mu_D = \frac{1}{2}\left|\max(\mu_D) - \min(\mu_D)\right|. \tag{3.67}$$

This is done numerically, and the results are plotted in Fig. 3.1, with the deviation in magnetic moment scaled to μ_0. It is evident that correcting for the exact drift exhibits the same quadratic scaling as correcting for the lowest-order grad-B drift. The exact correction and the approximate correction agree to a high degree of accuracy for small ϵ_B. For example, for $\epsilon_B = 0.2$, $\Delta\mu_{\nabla B}$ is only 5.05% lower than $\Delta\mu_D$.

3.3.1.3 Adiabatic invariant

Finally, we calculate an adiabatic invariant for the system, following the approach in Ref. 58 more directly. First, we define our vector potential to be

$$\mathbf{A} = B_0\left(x - \frac{x^2}{2L_B}\right)\hat{\mathbf{y}}. \tag{3.68}$$

As long as parameters such as L_B change slowly in time compared to the cyclotron frequency, then the following quantity will be approximately conserved:

$$I = \oint p_x\, dx = 2\int_{-\rho_0}^{\rho_0} \sqrt{2mH_\perp - \left(p_y - m\Omega_0\left(x - \frac{x^2}{2L_B}\right)\right)^2}\, dx. \tag{3.69}$$

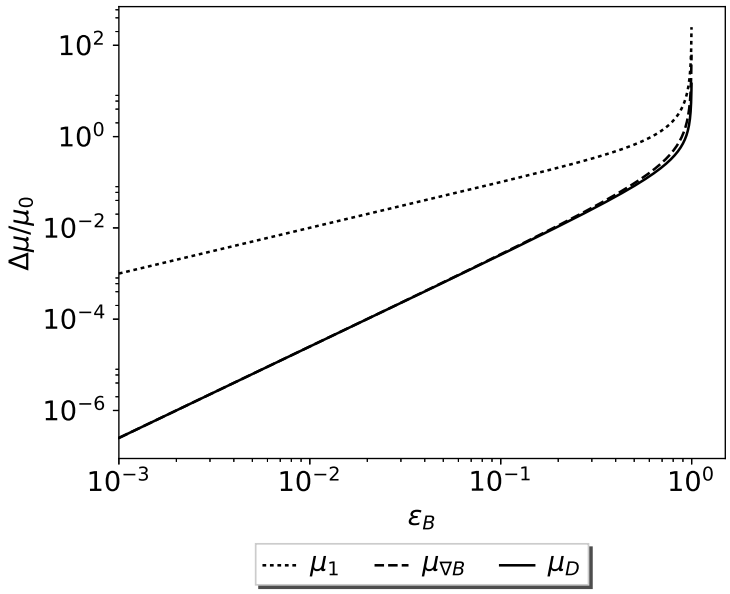

Figure 3.1: Plot of the deviation of magnetic moment normalized to μ_0 vs. ϵ_B. μ_1 exhibits linear scaling while both $\mu_{\nabla B}$ and μ_D exhibit quadratic scaling. Eventually, as $\epsilon_B \to 1$, the magnetic moment deviations diverge. This is consistent with the period of the motion diverging as well as $\epsilon_B \to 1$.

Here, $H_\perp = mv_\perp^2/2$ is the two-dimensional Hamiltonian, while $p_x = m\dot{x}$ and $p_y = m\dot{y} + qA_y/c$ are the canonical momenta. We note that H and p_y are constants of motion. Using a change of variables $s = x/\rho_0$, and using our initial conditions to plug in values for H and p_y, we simplify the integral:

$$\frac{I}{2m\Omega_0 L_B^2} = \int_{-\epsilon_B}^{\epsilon_B} \sqrt{\frac{1}{4}(s-\epsilon_B)(s+\epsilon_B-2)(s-\epsilon_B-2)(s+\epsilon_B)}\, ds. \tag{3.70}$$

We use Refs. 60–62 to transform the integral:

$$\frac{I}{16mL_B^2} = \epsilon_B^2(1-\epsilon_B^2)\int_0^{K(\epsilon_B)^2} \frac{\mathrm{sn}^2(u)\,\mathrm{cn}^2(u)\,\mathrm{dn}^2(u)}{\left(1-\epsilon_B\,\mathrm{sn}^2(u)\right)^4}\, du. \tag{3.71}$$

Byrd and Friedman demonstrate how this may be simplified further into complete elliptic integrals, which will not be included here for brevity. Taylor expanding the final result reveals that

$$\mu_I = \frac{q}{mc}\frac{I}{2\pi} = \mu_0\left(1 - \frac{\epsilon_B^2}{8} + O\left(\epsilon_B^4\right)\right). \tag{3.72}$$

We next calculate an approximate drift that would correspond to this magnetic moment.

$$\mu_I = \frac{1}{2}\frac{m\left(\mathbf{v}-\mathbf{v}_I\right)^2}{B_0(1-x/L_B)} \approx \mu_0 \frac{1-(v_I\dot{y})/(u^2)}{1-x/L_B} \tag{3.73}$$

Here, we have assumed that $v_I/(\rho_0\Omega_0)$ is small and can be neglected to attain an approximate drift. We obtain that

$$v_I \approx \frac{2u^2}{\dot{y}}\left(1-\frac{\mu_I}{\mu_0}\right)(1-x/L_B)\,. \tag{3.74}$$

We have analytically shown that requiring $\epsilon_B \ll 1$ for this magnetic field results in good magnetic moment conservation and that correcting for the grad-B drift results in even higher μ conservation. In addition, the exact drift and the grad-B drift do not appreciably differ in terms of magnetic moment conservation. To lowest-order in ϵ_B, the adiabatic invariant of this system corresponds to μ_1 evaluated at $x = 0$. Next, we examine magnetic moment conservation for the magnetic field of a wire, which has both a gradient and curvature.

3.3.2 Magnetic field of a wire

To study the coupled effects of the grad-B drift and the curvature drift, we consider the necessarily three-dimensional case of the magnetic field of an infinite wire. While single particle motion in arbitrary axisymmetric fields is well studied in the literature,[63] we restrict ourselves to the simplest case of the magnetic field of a wire. By choosing the magnetic field to have unit strength at a normalized distance, we have in cylindrical coordinates the following form for the magnetic field:

$$\mathbf{B} \sim \frac{1}{s}\hat{\boldsymbol{\phi}}. \tag{3.75}$$

Here, s is the perpendicular distance away from the wire, and ϕ is the azimuthal angle around the wire. We numerically integrate the motion of a charged particle the following initial conditions:

$$\begin{aligned} x_0 &= 1 + \epsilon_B, \\ y_0 &= 0, \\ z_0 &= 0, \\ v_{x0} &= 0, \\ v_{y0} &= \zeta, \\ v_{z0} &= \epsilon_B, \end{aligned} \tag{3.76}$$

where the parameters ϵ_B and ζ are given by

$$\epsilon_B \equiv \frac{\rho_0}{R_0}, \tag{3.77}$$

$$\zeta \equiv \frac{v_\parallel}{v_\perp}. \tag{3.78}$$

Here, R_0 is the initial radial distance of the guiding center from the wire. For convenience, we choose $R_0 = 1$. We do not consider cases in which ϵ_B or ζ exceed unity.

3.3.2.1 Further magnetic moment definitions

We are motivated to introduce definitions for the magnetic moment, akin to Eq. (3.6), that account for the guiding center drifts associated with spatially dependent magnetic fields.

To separate the effects of the grad-B and curvature drifts, we first define moments that are independently corrected:

$$\mu_{\nabla B} = \frac{1}{2}\frac{m(\mathbf{v}_\perp - \mathbf{v}_{\nabla B})^2}{B}, \tag{3.79}$$

$$\mathbf{v}_{\nabla B} = \frac{1}{2}\frac{m v_\perp^2}{qB}\frac{c\mathbf{B}\times\nabla B}{B^2}, \tag{3.80}$$

and

$$\mu_{R_c} = \frac{1}{2}\frac{m(\mathbf{v}_\perp - \mathbf{v}_{R_c})^2}{B}, \tag{3.81}$$

$$\mathbf{v}_{R_c} = \frac{mv_\parallel^2}{qB}\frac{\mathbf{R}_c \times c\mathbf{B}}{R_c^2 B}. \tag{3.82}$$

We note that due to the circular geometry of our magnetic field, the radius of curvature vector $\mathbf{R}_c$ of the magnetic field is equal to the radial position vector $\mathbf{s}$. We can combine these definitions to simultaneously account for both drifts:

$$\mu_{B(x)} = \frac{1}{2}\frac{m(\mathbf{v}_\perp - \mathbf{v}_{\nabla B} - \mathbf{v}_{R_c})^2}{B}. \tag{3.83}$$

We note that this is exactly the same expression one obtains for a corrected magnetic moment by following Littlejohn's guiding center theory. Thus, we expect higher magnetic moment conservation by correcting for the above drifts.

3.3.2.2 Magnetic moment conservation

We use the fourth-order Runge-Kutta method to numerically integrate our system of equations, scanning over the parameters ϵ_B and ζ to measure the maximum relative change of the magnetic moment. As expected, the traditional definition of the magnetic moment fails to conserve well. We find that $\mu_1 \sim \epsilon_B$ with a prefactor of order unity. This is the case for all relevant values of ζ.

Fig. 3.2 shows the behavior of the magnetic moments for the edge case, $\zeta = 1$, in which the grad-B drift and the curvature drift are on equal footing. Note that both $\mu_{\nabla B}$ and μ_{R_c} retain the linear ϵ_B scaling but experience a small reduction (less than an order of magnitude) of the prefactor. However, $\mu_{B(x)}$ scales as ϵ_B^2, representative of a more robust conservation.

Since ζ is an explicit measure of the relative importance of the curvature drift to the grad-B drift, we expect $\mu_{R_c} \xrightarrow[\zeta\to 0]{} \mu_1$ and $\mu_{\nabla B} \xrightarrow[\zeta\to 0]{} \mu_{B(x)}$. Since the former primarily constitutes a change in the prefactor, we only illustrate the latter's behavior in Fig. 3.3. The quantity $\mu_{\nabla B}$ behaves in a piecewise manner about a critical value of ϵ_B. For ϵ_B less than this critical value, the scaling

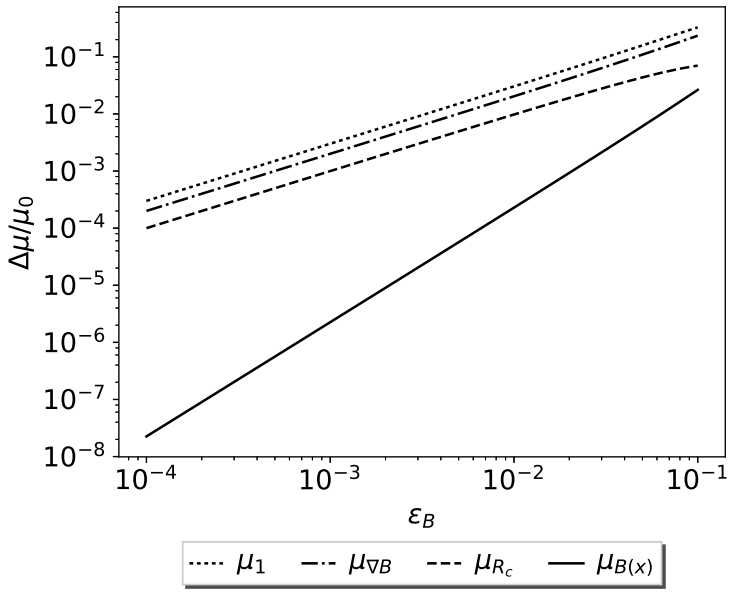

Figure 3.2: Plot of the dependencies of the maximum perturbation on ϵ_B for each of the magnetic moment definitions. The extreme case of $\zeta = 1$ is shown to highlight the differences in behaviors.

remains linear. For ϵ_B greater than the critical value, the scaling becomes quadratic. Essentially, the gradient drift is the dominant drift for large ϵ_B. We find that the critical value scales as ζ^2.

In the case of a curved spatially-dependent magnetic field, the basic definition of the magnetic moment fails as an invariant when the length scale of the gyromotion is comparable to the magnetic field's inherent length scale, $\epsilon_B \sim 1$. Non-conservation can be abated by correcting for the drift-motion of the particle, namely the grad-B and curvature drifts. The relative importance of these two effects can be measured by the parameter ζ, and in certain regions of ζ-space one can obtain sufficient conservation by correcting only for the gradient drift.

3.3.3 Summary

For both the straight and curved non-uniform magnetic fields analyzed, μ_1 is conserved to $O(\epsilon_B)$; therefore, requiring $\epsilon_B \ll 1$ guarantees adequate magnetic moment conservation. In addition, correcting for both grad-B and curvature drifts conserves the magnetic moment up to

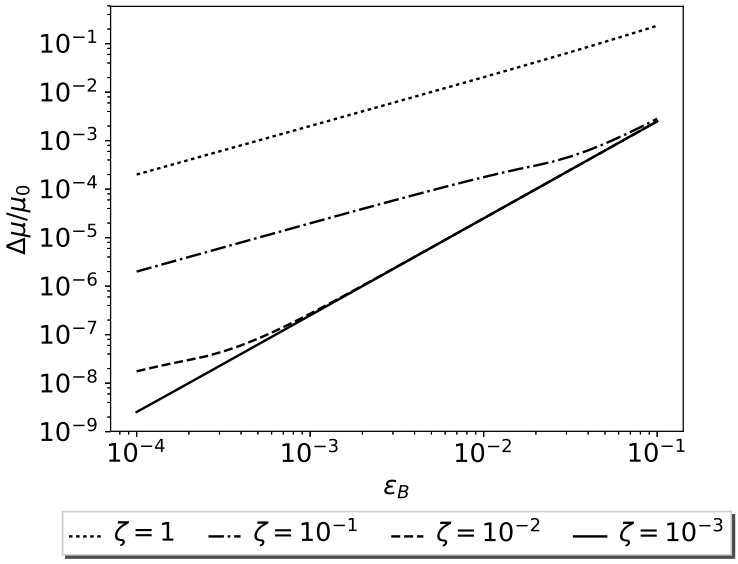

Figure 3.3: Plot of the dependencies of the maximum perturbation of $\mu_{\nabla B}$ on ϵ_B for varying values of ζ. There is a ζ dependent critical value of ϵ_B for which the scaling changes. For ϵ_B less than this value, the scaling is linear. And for ϵ_B greater than this value, the scaling is quadratic.

$O\left(\epsilon_B^2\right)$. Including these magnetic drifts improves magnetic moment conservation for the magnetic fields considered, and we expect similar results for general non-uniform magnetic fields. We next examine how a time dependent electric field breaks μ_1 conservation.

3.4 Time dependent electric field

We consider the motion of a charged particle in a static and uniform magnetic field with a perpendicular oscillating electric field:

$$\mathbf{B} = B_0\hat{\mathbf{z}}, \qquad B_0 > 0, \tag{3.84}$$

$$\mathbf{E} = E_0 \cos(\omega t)\hat{\mathbf{x}}. \tag{3.85}$$

The frequency of this oscillation ω is taken to be small compared to the cyclotron frequency $\Omega = \Omega_0$. We ignore any induced magnetic fields and take them to be small compared to B_0. We also set

$\text{sgn}(\omega) = \text{sgn}(\Omega)$ without loss of generality.

3.4.1 Equations of motion

From Newton's laws we write down the ODEs for this system, we obtain

$$m\ddot{x} = q\left(\frac{\dot{y}}{c}B_0 + E_0\cos(\omega t)\right), \tag{3.86}$$

$$m\ddot{y} = -q\frac{\dot{x}}{c}B_0. \tag{3.87}$$

We define the parameter $\alpha = cE_0/B_0$ and obtain

$$\ddot{x} = \Omega\dot{y} + \alpha\Omega\cos(\omega t), \tag{3.88}$$

$$\ddot{y} = -\Omega\dot{x}. \tag{3.89}$$

We use the initial conditions

$$\begin{aligned} x(0) &= x_0, \\ \dot{x}(0) &= v_{x0}, \\ y(0) &= y_0, \\ \dot{y}(0) &= v_{y0}, \end{aligned} \tag{3.90}$$

and solve for the equations of motion:

$$x(t) = \frac{v_{x0}}{\Omega}\sin(\Omega t) - \frac{v_{y0}}{\Omega}\cos(\Omega t) - \frac{\alpha}{\Omega}\frac{1}{1-\epsilon_\omega^2}\left(\cos(\Omega t) - \cos(\omega t)\right) + x_0 + \frac{v_{y0}}{\Omega}, \tag{3.91}$$

$$y(t) = \frac{v_{y0}}{\Omega}\sin(\Omega t) + \frac{v_{x0}}{\Omega}\cos(\Omega t) - \frac{\alpha}{\Omega}\frac{1}{1-\epsilon_\omega^2}\left(-\sin(\Omega t) + \frac{\sin(\omega t)}{\epsilon_\omega}\right) + y_0 - \frac{v_{x0}}{\Omega}. \tag{3.92}$$

We note that if we take the limit that $\omega \to 0$, the equations of motion reproduce the same result as if the electric field were $\mathbf{E} = E_0\hat{\mathbf{x}}$.

Next, we subject the particle to the initial conditions in Eq. (3.51). The equations of motion then simplify to the following:

$$x(t) = \frac{1}{\Omega}\left(u - \frac{\alpha}{1-\epsilon_\omega^2}\right)\cos(\Omega t) + \frac{\alpha}{\Omega}\frac{1}{1-\epsilon_\omega^2}\cos(\omega t), \tag{3.93}$$

$$y(t) = -\frac{1}{\Omega}\left(u - \frac{\alpha}{1-\epsilon_\omega^2}\right)\sin(\Omega t) - \frac{\alpha}{\Omega\epsilon_\omega}\frac{1}{1-\epsilon_\omega^2}\sin(\omega t). \tag{3.94}$$

Thus, the velocity of the particle is

$$v_x(t) = -\left(u - \frac{\alpha}{1-\epsilon_\omega^2}\right)\sin(\Omega t) - \frac{\alpha}{1-\epsilon_\omega^2}\epsilon_\omega \sin(\omega t), \tag{3.95}$$

$$v_y(t) = -\left(u - \frac{\alpha}{1-\epsilon_\omega^2}\right)\cos(\Omega t) - \frac{\alpha}{1-\epsilon_\omega^2}\cos(\omega t). \tag{3.96}$$

3.4.2 Magnetic moment conservation

Now, we Taylor expand the factor of $1/\left(1-\epsilon_\omega^2\right)$ corresponding to $\sin(\omega t)$ and $\cos(\omega t)$, and to zeroth-order obtain that

$$\mu_1(t) = \mu_0\left[\left(\frac{\alpha}{u(1-\epsilon_\omega^2)} - 1\right)^2 - \frac{2\alpha}{u}\left(\frac{\alpha}{u(1-\epsilon_\omega^2)} - 1\right)\cos(\omega t)\cos(\Omega t) + \left(\frac{\alpha}{u}\right)^2\cos^2(\omega t)\right] + O\left(\epsilon_\omega\right). \tag{3.97}$$

We next calculate an upper bound for the maximum deviation of the magnetic moment from the center of its oscillation:

$$\frac{\Delta\mu_1}{\mu_0} = 2\epsilon_\delta\eta + \epsilon_\delta^2 + O\left(\epsilon_\omega\right), \tag{3.98}$$

where

$$\eta = \left|1 - \frac{\alpha}{u(1-\epsilon_\omega^2)}\right|. \tag{3.99}$$

Thus, in the limit that $|\epsilon_\omega|, \epsilon_\delta \ll 1$, we obtain $\eta \approx 1$ and $\Delta\mu_1/\mu_0 \approx 2\epsilon_\delta$.

Now, suppose we wish to take into account the guiding center motion when calculating the magnetic moment. To do this, we first take into account the $\mathbf{E}\times\mathbf{B}$ drift,

$$\mathbf{v}_E(t) = -\alpha\cos(\omega t)\hat{\mathbf{y}}, \tag{3.100}$$

by subtracting it from the velocity of the particle before calculating the magnetic moment:

$$\mathbf{v}_1 = \mathbf{v} - \mathbf{v}_E. \tag{3.101}$$

Then, the corrected magnetic moment is

$$\mu_E(t) = \mu_0\left[\left(\frac{\alpha}{u(1-\epsilon_\omega^2)} - 1\right)^2 - \frac{2\alpha}{u}\epsilon_\omega\left(\frac{\alpha}{u(1-\epsilon_\omega^2)} - 1\right)\cos(\omega t)\cos(\Omega t)\right] + O\left(\epsilon_\omega^2\right). \tag{3.102}$$

We note that in this case $\mu_E = \mu_\rho$. By correcting for the $\mathbf{E} \times \mathbf{B}$ drift, the time dependence of the corrected magnetic moment is $O(\epsilon_\omega)$, and the upper bound for the deviation is

$$\frac{\Delta\mu_E}{\mu_0} = 2\epsilon_\omega\epsilon_\delta\eta + O\left(\epsilon_\omega^2\right). \tag{3.103}$$

We can further correct for drift motion by also taking into account the polarization drift,

$$\mathbf{v}_p(t) = \frac{c\dot{\mathbf{E}}_\perp}{\Omega B} = -\alpha\epsilon_\omega \sin(\omega t)\hat{\mathbf{x}}. \tag{3.104}$$

Then, the corrected magnetic moment is

$$\mu_p(t) = \mu_0\left[\left(\frac{\alpha}{u(1-\epsilon_\omega^2)} - 1\right)^2 - \frac{2\alpha}{u}\epsilon_\omega^2\left(\frac{\alpha}{u(1-\epsilon_\omega^2)} - 1\right)\cos(\omega t)\cos(\Omega t)\right] + O\left(\epsilon_\omega^3\right). \tag{3.105}$$

Now, the deviation is $O\left(\epsilon_\omega^2\right)$, and the upper bound of the deviation can be written as

$$\frac{\Delta\mu_p}{\mu_0} = 2\epsilon_\omega^2\epsilon_\delta\eta + O\left(\epsilon_\omega^3\right). \tag{3.106}$$

This is consistent with Littlejohn's result in Ref. (27), which predicts that a polarization drift correction leads to higher order magnetic moment conservation.

If we correct for even higher order drifts, then the magnetic moment will be conserved to higher order. We label the nth drift as $\mathbf{v}_{D,n}$, where n is a natural number, and the nth corrected magnetic moment as $\mu_{D,n}$. The guiding center experiences an acceleration $\mathbf{a}_{D,n} = \dot{\mathbf{v}}_{D,n}$. In the non-inertial frame of the guiding center, a fictitious force $\mathbf{F}_n = -m\mathbf{a}_n$ is felt. This produces a general force drift,

$$\mathbf{v}_{D,n+1} = \frac{c}{q}\frac{\mathbf{F}_n \times \mathbf{B}}{B^2}. \tag{3.107}$$

For an example of this method, if $\mathbf{v}_{D,1} = \mathbf{v}_E$, then

$$\mathbf{F}_1 = -m\dot{\mathbf{v}}_E = \frac{-m\dot{\mathbf{E}} \times c\mathbf{B}}{B^2}, \tag{3.108}$$

$$\mathbf{v}_{D,2} = \frac{1}{q}\frac{\mathbf{F}_1 \times c\mathbf{B}}{B^2} = \frac{-mc^2}{qB^4}((\dot{\mathbf{E}} \times \mathbf{B}) \times \mathbf{B}), \tag{3.109}$$

$$\implies \mathbf{v}_{D,2} = \frac{c\dot{\mathbf{E}}_\perp}{\Omega B} = \mathbf{v}_p. \tag{3.110}$$

This process can be repeated indefinitely, and for this system we obtain that

$$\mathbf{v}_{D,n} = \begin{cases} -\dfrac{\omega^{n-1}}{\Omega^{n-1}}\alpha\cos(\omega t)\hat{\mathbf{y}} & \text{if } n \text{ is odd,} \\ -\dfrac{\omega^{n-1}}{\Omega^{n-1}}\alpha\sin(\omega t)\hat{\mathbf{x}} & \text{if } n \text{ is even.} \end{cases} \tag{3.111}$$

We then define the nth corrected velocity vector to be:

$$\mathbf{v}_n = \mathbf{v} - \sum_{j=1}^{n} \mathbf{v}_{D,j}. \tag{3.112}$$

This allows us to calculate the corrected velocity:

$$v_{n,x}(t) = \begin{cases} -\left(u - \dfrac{\alpha}{1-\epsilon_\omega^2}\right)\sin(\Omega t) - \dfrac{\alpha}{1-\epsilon_\omega^2}\epsilon_\omega^n \sin(\omega t) & \text{if } n \text{ is odd,} \\ -\left(u - \dfrac{\alpha}{1-\epsilon_\omega^2}\right)\sin(\Omega t) - \dfrac{\alpha}{1-\epsilon_\omega^2}\epsilon_\omega^{n+1} \sin(\omega t) & \text{if } n \text{ is even,} \end{cases} \tag{3.113}$$

$$v_{n,y}(t) = \begin{cases} -\left(u - \dfrac{\alpha}{1-\epsilon_\omega^2}\right)\cos(\Omega t) - \dfrac{\alpha}{1-\epsilon_\omega^2}\epsilon_\omega^{n+1} \cos(\omega t) & \text{if } n \text{ is odd,} \\ -\left(u - \dfrac{\alpha}{1-\epsilon_\omega^2}\right)\cos(\Omega t) - \dfrac{\alpha}{1-\epsilon_\omega^2}\epsilon_\omega^{n} \cos(\omega t) & \text{if } n \text{ is even.} \end{cases} \tag{3.114}$$

Then, the corrected magnetic moment is

$$\mu_{D,n}(t) = \mu_0 \left[\left(\frac{\alpha}{u(1-\epsilon_\omega^2)} - 1 \right)^2 - \frac{2\alpha}{u}\epsilon_\omega^n \left(\frac{\alpha}{u(1-\epsilon_\omega^2)} - 1 \right) \cos(\omega t)\cos(\Omega t) \right] + O\left(\epsilon_\omega^{n+1}\right). \tag{3.115}$$

Therefore, by subtracting n drifts, the magnetic moment becomes conserved up through order $O\left(\epsilon_\omega^{n+1}\right)$. The maximum deviation is,

$$\frac{\Delta\mu_{D,n}}{\mu_0} = 2\epsilon_\omega^n \epsilon_\delta \eta + O\left(\epsilon_\omega^{n+1}\right). \tag{3.116}$$

Thus, for every higher order drift that we correct for, our corrected magnetic moment is conserved up through another order of ϵ_ω. Meanwhile, for $\epsilon_\delta \ll 1$, all of our perturbations are to lowest-order linear in ϵ_δ.

For the given system, we can actually calculate the sum of all the drifts:

$$\mathbf{v}_{D,\infty} = \sum_{n=1}^{\infty} \mathbf{v}_{D,n}. \tag{3.117}$$

To do so,we note that since $|\epsilon_\omega| < 1$,

$$\frac{1}{1-\epsilon_\omega^2} = \sum_{n=0}^{\infty} \epsilon_\omega^{2n}. \tag{3.118}$$

Therefore,

$$\mathbf{v}_{D,\infty} = -\frac{\alpha}{1-\epsilon_\omega^2}(\epsilon_\omega \sin(\omega t)\hat{\mathbf{x}} + \cos(\omega t)\hat{\mathbf{y}}). \tag{3.119}$$

If we correct for $\mathbf{v}_{D,\infty}$, then

$$\mathbf{v}_\infty = \mathbf{v} - \mathbf{v}_D, \tag{3.120}$$

$$v_{\infty,x}(t) = \left(\frac{\alpha}{1-\epsilon_\omega^2} - u\right)\sin(\Omega t), \tag{3.121}$$

$$u_{\infty,y}(t) = \left(\frac{\alpha}{1-\epsilon_\omega^2} - u\right)\cos(\Omega t). \tag{3.122}$$

Thus, after for correcting for every drift, the corrected magnetic moment is perfectly conserved and stays at the value $\mu_0\eta^2$, and the corrected velocity traces out a perfect circle.

3.4.3 Adiabatic invariant

Finally, we calculate the adiabatic invariant associated with this system. We choose the following potentials:

$$\mathbf{A} = B_0 x\hat{\mathbf{y}}, \tag{3.123}$$

$$\varphi = -E(t)x. \tag{3.124}$$

The adiabatic invariant is

$$I = \oint p_x\, dx = 2\int_{x_{\min}}^{x_{\max}} \sqrt{2mH_\perp - \left(p_y - \frac{q}{c}B_0 x\right)^2 + 2qmE(t)x}\, dx, \tag{3.125}$$

where we integrate over the domain in which the integrand is real. Here, the two-dimensional Hamiltonian is

$$H_\perp = mv_\perp^2/2 - qE(t)x \tag{3.126}$$

while $p_x = m\dot{x}$ and $p_y = m\dot{y} + qB_0x/c$ are the canonical momenta. We assume $E(t)$ is slowly varying compared to the cyclotron frequency, so that $H_\perp$, along with p_y, can be considered constants of motion while carrying out the integral:

$$\frac{m}{qc}\frac{I}{2\pi} = \frac{1}{B_0}\left(H_\perp + \frac{1}{2}mv_E^2 - mv_Ev_y - v_E\frac{q}{c}Bx\right). \tag{3.127}$$

Here $v_E = -cE(t)/B_0$. Plugging in the expression for the Hamiltonian, we finally obtain that

$$\mu_I = \frac{q}{mc}\frac{I}{2\pi} = \frac{1}{2}\frac{(\mathbf{v}_\perp - \mathbf{v}_E)^2}{B_0} = \mu_E. \tag{3.128}$$

Thus, the adiabatic invariant is precisely the magnetic moment calculated in the frame of the $\mathbf{E}\times\mathbf{B}$ velocity.

3.4.4 Summary

In short, we have demonstrated how to generate higher order drifts that further conserve the magnetic moment when $\epsilon_\omega < 1$. For each drift, the perturbation picks up an additional power of ϵ_ω. Meanwhile, the deviations are always linear in ϵ_δ. Therefore, $\epsilon_\delta \ll 1$ guarantees good magnetic moment conservation. Additionally, the adiabatic invariant corresponds exactly to μ_E. Now, we turn to the case of a spatially dependent electric field.

3.5 Spatially dependent electric field

Finally, we consider a single charged particle subject to a spatially dependent electric field perpendicular to a constant and uniform magnetic field. The electric field is sinusoidal with an arbitrary phase ϕ and wavenumber $k = k_\perp$:

$$\mathbf{B} = B_0\hat{\mathbf{z}}, \qquad B_0 > 0, \tag{3.129}$$

$$\mathbf{E} = E_0\sin(kx + \phi)\hat{\mathbf{x}}. \tag{3.130}$$

We assume $k > 0$ for simplicity, and subject our particle to the initial conditions in Eq. (3.51):

$$\begin{aligned} \ddot{x} &= \Omega\dot{y} + \alpha\Omega\sin(kx+\phi), \\ \ddot{y} &= -\Omega\dot{x}. \end{aligned} \tag{3.131}$$

We next integrate the y-component of the acceleration:

$$\dot{y} = -\Omega x + v_{y0} + \Omega x_0 = -\Omega x. \tag{3.132}$$

We then plug this into the x-component of the acceleration:

$$\ddot{x} = -\Omega^2 x + \alpha\Omega\sin(kx+\phi). \tag{3.133}$$

The following analysis is split up into three sections. In the first section, we linearize the electric field for small values of $|kx|$ to find approximate equations of motion. Then, we consider the full nonlinear problem analytically and then computationally.

3.5.1 Long-wavelength approximation

If $|kx| \ll 1$ for all time, then using the small angle approximation, then we approximate the electric field as

$$\tilde{\mathbf{E}} = E_0(\sin(\phi) + kx\cos(\phi))\hat{\mathbf{x}}. \tag{3.134}$$

3.5.1.1 Equations of motion

Using the above linearization instead of the exact electric field, we obtain

$$\ddot{x} = -\Omega^2 x + \alpha\Omega(\sin\phi + kx\cos\phi). \tag{3.135}$$

This is simply the differential equation for simple harmonic motion. Given our initial conditions, the solution is

$$x(t) = \left(\rho_0 - \frac{\alpha\Omega\sin\phi}{\omega_{\text{eff}}^2}\right)\cos\omega_{\text{eff}}t + \frac{\alpha\Omega\sin\phi}{\omega_{\text{eff}}^2}, \tag{3.136}$$

where the frequency of the oscillation is

$$\omega_{\text{eff}} = \sqrt{\Omega^2 - \alpha k \Omega \cos\phi} = |\Omega|\eta. \tag{3.137}$$

Here, we have defined for convenience that

$$\eta = \sqrt{1 - \frac{\alpha}{u}\epsilon_\perp \cos\phi}. \tag{3.138}$$

We note that for our assumption of small oscillations to be valid, the effective frequency of the oscillation must be real (and thus, η^2 must be positive). This implies that

$$\frac{\alpha}{u}\epsilon_\perp \cos(\phi) < 1 \tag{3.139}$$

must be true for the our linearization to be valid. Physically, this means that $\epsilon_\delta \epsilon_\perp < 1$ for the linearization to hold for all values of the phase ϕ. In the limit that $\epsilon_\delta \epsilon_\perp \ll 1$, $\eta \approx 1$ and $|\omega_{\text{eff}}/\Omega| \approx 1$.

We can simplify $x(t)$ and integrate the ODE for $y(t)$ to obtain:

$$x(t) = \frac{1}{\Omega}\left(u - \frac{\alpha \sin\phi}{u\eta^2}\right)\cos\omega_{\text{eff}} t + \frac{\alpha \sin\phi}{\Omega\eta^2}, \tag{3.140}$$

$$y(t) = -\frac{1}{\omega_{\text{eff}}}\left(u - \frac{\alpha \sin\phi}{u\eta^2}\right)\sin\omega_{\text{eff}} t - \frac{\alpha \sin\phi}{\eta^2} t. \tag{3.141}$$

We note that the particle undergoes an overall drift in the y-direction. The drift velocity is

$$\mathbf{v}_D = -\frac{\alpha \sin\phi}{\eta^2}\hat{\mathbf{y}} = v_D \hat{\mathbf{y}}. \tag{3.142}$$

This is the gyro-averaged $\mathbf{E} \times \mathbf{B}$ drift velocity. This can be seen by explicitly averaging the electric field,

$$\left\langle \tilde{\mathbf{E}} \right\rangle = \frac{1}{T}\int_0^T E_0(\sin(\phi) + kx\cos(\phi))\hat{\mathbf{x}}\, dt = E_0(\sin(\phi) + k\,\langle x\rangle \cos(\phi))\hat{\mathbf{x}}. \tag{3.143}$$

We calculate $\langle x\rangle = (\alpha \sin\phi)\,/\left(\Omega\eta^2\right)$ explicitly using the equations of motion, and plugging the result into $\langle \mathbf{v}_E \rangle$ gives us

$$\mathbf{v}_D = \langle \mathbf{v}_E \rangle = \frac{\left\langle \tilde{\mathbf{E}} \right\rangle \times c\mathbf{B}}{B^2}. \tag{3.144}$$

In this case, gyroaveraging the electric field is equivalent to evaluating the electric field at the gyrocenter. In addition, we note that for our linearization to be valid, not only do we require that $\epsilon_\perp \ll 1$, but we also require that $\epsilon_\delta \epsilon_\perp |\sin(\phi)| \ll 1$.

3.5.2 Magnetic moment conservation

We define the constant dimensionless constant λ to be

$$\lambda = 1 - \frac{\alpha \sin\phi}{\rho_0 \Omega \eta^2} = 1 + \frac{v_D}{u}. \tag{3.145}$$

Note that in the limit that $|v_D/u| \ll 1$, then $\lambda \approx 1$. Now, we can write our equations of motion as:

$$x(t) = \rho_0 \lambda \cos(\omega_{\text{eff}} t) - \frac{v_D}{\Omega}, \tag{3.146}$$

$$y(t) = -\frac{\rho_0 \Omega}{\omega_{\text{eff}}} \lambda \sin(\omega_{\text{eff}} t) + v_D t. \tag{3.147}$$

We next correct for the drift velocity when calculating the magnetic moment and obtain

$$\begin{aligned} \mu_D(t) &= \frac{m}{2B_0}\left(\dot{x}^2 + (\dot{y} - v_D)^2\right) \\ &= \mu_0 \lambda^2 \left(1 - \frac{\alpha k}{\Omega}\cos(\phi)\sin^2(\omega_{\text{eff}} t)\right) \\ &= \mu_0 \lambda^2 \left(1 - \frac{\alpha k}{2\Omega}\cos(\phi)\left(1 - \cos(2\omega_{\text{eff}} t)\right)\right). \end{aligned} \tag{3.148}$$

We next extract the amplitude of μ_D's oscillation:

$$\frac{\Delta \mu_D}{\mu_0} = \frac{\lambda^2}{2}\epsilon_\delta \epsilon_\perp \ll 1. \tag{3.149}$$

We note that when $\phi = 0$ or $\phi = \pi$, the drift velocity, which goes as $\sin(\phi)$, vanishes. In these cases, correcting the magnetic moment is not necessary to obtain the above result, and $\mu_1 = \mu_D$. Otherwise, the perturbation of μ_1 will be linear in ϵ_δ, but it will also go as $\epsilon_\perp^0$. Thus, in the linearized case μ_E is conserved to higher order.

3.5.2.1 Adiabatic invariant

We next calculate the adiabatic invariant for our linearized system. Our potentials are:

$$\mathbf{A} = B_0 x \hat{\mathbf{y}}, \tag{3.150}$$

$$\varphi(x) = -E_0 \sin(\phi) x - \frac{1}{2} E_0 k \cos(\phi) x^2. \tag{3.151}$$

The adiabatic invariant is

$$I = \oint p_x \, dx = 2 \int_{x_{\min}}^{x_{\max}} \sqrt{2mH_\perp - \left(\frac{p_y}{m} - \Omega x\right)^2 - 2qm\varphi(x)} \, dx, \tag{3.152}$$

where we integrate over the domain in which the integrand is real. If we do so and express $H_\perp$ and p_y in terms of our initial conditions, then our final expression is

$$\mu_I = \frac{q}{mc} \frac{I}{2\pi} = \eta \frac{1}{2} \frac{m \left(\mathbf{v}_0 - \mathbf{v}_D\right)^2}{B_0} = \mu_0 \eta \lambda^2, \tag{3.153}$$

where $\mathbf{v}_0 = -u\hat{\mathbf{y}}$ is the initial velocity of our particle. Note that

$$\mu_I - \mu_D = \mu_0 \lambda^2 \left(\eta - 1 + \frac{\alpha k}{\Omega} (1 - \cos(2\omega_{\text{eff}} t)) \right). \tag{3.154}$$

Thus, in the limit that $|v_D/u| \ll 1$, then we have $\mu_I \approx \mu_D$. We now consider the fully nonlinear problem using the same initial conditions.

3.5.3 Fully nonlinear analysis

3.5.3.1 Effective potential and magnetic moment conservation

We can repeat the first few steps of the above derivation again with the same initial conditions to obtain

$$\ddot{x} = -\Omega^2 x + \alpha \Omega \sin(kx + \phi), \tag{3.155}$$

$$\dot{y} = -\Omega x. \tag{3.156}$$

The ODE for $x(t)$ can be rewritten using an effective potential. We write that

$$m\ddot{x} = -\frac{dV_{\text{eff}}}{dx}, \tag{3.157}$$

where

$$V_{\text{eff}}(x) = \frac{1}{2}m\Omega^2 x^2 + m\alpha\frac{\Omega}{k}\cos(kx + \phi). \tag{3.158}$$

The effective potential is that of a harmonic oscillator perturbed by the spatially dependent electric potential.

It may be the case that $V_{\text{eff}}(x)$ has multiple local minima, and thus multiple wells that the particle could be trapped in. In that case, the oscillatory behavior would be sensitive to initial conditions, as changing $x(0)$ could result in the particle becoming trapped in a different potential well. To simplify the analysis, we restrict ourselves to the case where there is only one potential well near the center of the parabola such that there exists only one point where the derivative of the effective potential is zero. The condition is

$$\epsilon_\delta \epsilon_\perp < 1. \tag{3.159}$$

Before considering arbitrary phase ϕ, we study the case of $\phi = 0$ (the case of $\phi = \pi$ is essentially equivalent). Here, the effective potential is an even function of x, and thus the two turning points are ρ_0 and $-\rho_0$. Knowing the turning points and that the particle passes through $x = 0$ (since the turning points are of opposite sign), we can use conservation of energy to determine how $\mu_1(t)$ oscillates:

$$\frac{1}{2}mv_\perp^2 + q\varphi = H_\perp = \frac{1}{2}m\rho_0^2\Omega^2 + \frac{qE_0}{k}\cos(k\rho_0), \tag{3.160}$$

where

$$\varphi(x) = \frac{E_0}{k}\cos(kx). \tag{3.161}$$

Then, writing the magnetic moment as a function of x,

$$\mu_1(x) = \frac{H_\perp}{B_0} - \frac{q\alpha}{ck}\cos(kx). \tag{3.162}$$

In the case that $\epsilon_\perp \leq \pi$, the magnetic moment oscillates between $\mu(x = 0)$ and $\mu(x = \rho_0)$. Thus, the amplitude of oscillation is

$$\Delta\mu_1 = \left|\frac{q\alpha}{2ck}(\cos(k\rho_0) - 1)\right| = \left|\mu_0 \frac{\alpha}{u}\frac{1}{\rho_0 k}(\cos(k\rho_0) - 1)\right|, \tag{3.163}$$

$$\frac{\Delta\mu_1}{\mu_0} = \frac{\epsilon_\delta}{\epsilon_\perp}\left|\cos(\epsilon_\perp) - 1\right|. \tag{3.164}$$

Here, we calculate the amplitude by taking the difference between the maximum and minimum values of the magnetic moment and dividing by 2. For $\epsilon_\perp \ll 1$, we can Taylor expand to obtain

$$\frac{\Delta\mu_1}{\mu_0} \approx \epsilon_\delta\epsilon_\perp. \tag{3.165}$$

This is exactly the same perturbation we obtained using the small angle approximation before with $\phi = 0$.

However, if $\epsilon_\perp > \pi$, then the amplitude of oscillation is instead

$$\frac{\Delta\mu_1}{\mu_0} = \frac{\epsilon_\delta 1}{2\epsilon_\perp}. \tag{3.166}$$

From this, we can say that for small $\epsilon_\perp$, the perturbation the magnetic moment is approximately linear in $\epsilon_\delta\epsilon_\perp$. As $\epsilon_\delta \sim 1$ increases, the amplitude becomes nonlinear in k and is still linear in ϵ_δ. Then, when the bound saturates the amplitude of the perturbation is proportional to $\epsilon_\delta/\epsilon_\perp$.

The same analysis approximately generalizes for arbitrary phase. For small $\epsilon_\perp$, the amplitude of oscillation of the magnetic moment is linear in ϵ_δ and as we saw earlier is also linear in $\epsilon_\perp$ if we properly correct for the drift velocity of the particle, and otherwise is of order $\epsilon_\perp^0$. As $\epsilon_\perp$ increases, the amplitude of oscillation is still linear in ϵ_δ but nonlinear in $\epsilon_\perp$ until finally the bound saturates. When the bound saturates, the perturbation is proportional to $\epsilon_\delta/\epsilon_\perp$. Thus, we conclude that if $\epsilon_\perp \ll 1$ and if $\epsilon_\delta\epsilon_\perp \ll 1$, and if we correct for the gyro-averaged $\mathbf{E}\times\mathbf{B}$ drift, then $\Delta\mu_1/\mu_0 \ll 1$. Meanwhile, if $\epsilon_\perp \gg 1$ and if $\epsilon_\delta/\epsilon_\perp \ll 1$, then $\Delta\mu/\mu_0 \ll 1$, where in this case we do not correct for any drifts.

3.5.3.2 Equations of motion

Ideally, one would hope to exactly solve for the equations of motion and then calculate the exact magnetic moment. Unfortunately, one obtains an integral that is analytically intractable. We consider again the equation

$$m\ddot{x} = -\frac{dV_{\text{eff}}}{dx}. \tag{3.167}$$

We can multiply by $\dot{x}$ and write the equation as a total derivative:

$$m\dot{x}\ddot{x} = m\frac{d}{dt}\left(\frac{\dot{x}^2}{2}\right) = -\frac{dV_{\text{eff}}}{dt} = -\dot{x}\frac{dV_{\text{eff}}}{dx}. \tag{3.168}$$

Therefore, since $\dot{x}(0) = 0$ and $x(0) = \rho_0$, we can integrate and obtain

$$\frac{m}{2}\dot{x}^2 = V_{\text{eff}}(\rho_0) - V_{\text{eff}}(x). \tag{3.169}$$

This can also be integrated. If ρ_0 is the rightmost turning point, then

$$t = \int_{\rho_0}^{x} \frac{-dx'}{\sqrt{\frac{2}{m}\left(V_{\text{eff}}(\rho_0) - V_{\text{eff}}(x')\right)}} \text{ for } 0 < t < \frac{T}{2}. \tag{3.170}$$

If ρ_0 is the leftmost turning point, then the sign in the integral is flipped.

To find the period, one must solve for the other turning point, $x*$. If $\phi = 0$ or $\phi = \pi$, then the other turning point is simply $x^* = -\rho_0$, but for arbitrary phase one must numerically solve a transcendental equation. Once the other turning point is obtained, the period can be numerically calculated:

$$T = 2\left|\int_{x^*}^{\rho_0} \frac{dx}{\sqrt{\frac{2}{m}\left(V_{\text{eff}}(\rho_0) - V_{\text{eff}}(x)\right)}}\right|. \tag{3.171}$$

Note that since $x(t)$ is bounded and periodic, it can be expanded as a Fourier series. Because $x(t)$ is even, we can write

$$x(t) = a_0 + \sum_{n=1}^{\infty} a_n \cos\frac{2\pi n t}{T}. \tag{3.172}$$

If we plug this into $\dot{y} = -\Omega x$, not only do we notice that $\dot{y}$ is periodic (and thus the magnetic moment is periodic as well), but we also find that $-\Omega a_0$ is an overall drift! If we were to integrate

$\dot{y}$ to get $y(t)$, then one of the terms would be $-\Omega a_0 t$. To obtain it, we note that if we integrate $x(t)$ over the entire period,

$$\int_0^T \cos\frac{2\pi n t}{T}\,dt = 0 \text{ for integer } n. \tag{3.173}$$

Therefore, we can integrate $x(t)$ to find the drift velocity, and abuse a change in variables:

$$\begin{aligned} v_D = -\Omega a_0 &= \frac{-\Omega}{T}\int_{t=0}^{t=T} x(t)\,dt = \frac{-\Omega}{T}\int_{t=0}^{t=T} x\frac{dt}{dx}\,dx \\ &= \frac{-\Omega}{T}\int_{t=0}^{t=T}\frac{x}{\dot{x}}\,dx = \frac{2}{T}\int_{x=\rho_0}^{x=x^*}\frac{\Omega x\,dx}{\sqrt{\frac{2}{m}\left(V_{\text{eff}}(\rho_0)-V_{\text{eff}}(x)\right)}}. \end{aligned} \tag{3.174}$$

Here, it is assumed that $x = \rho_0$ is again the rightmost turning point and $x = x^*$ is the leftmost turning point. Otherwise, the sign in the integral flips. While this integral cannot be done analytically, it be calculated numerically.

Interestingly, when $\phi = 0$ or $\phi = \pi$, the calculation is integrating an overall odd function from ρ_0 to $-\rho_0$ since V_{eff} becomes an even function of x and $x^* = -\rho_0$, . Thus, when $\phi = 0$ or $\phi = \pi$ then $v_D = 0$ and there is no overall drift velocity.

Meanwhile, the gyro-averaged $\mathbf{E}\times\mathbf{B}$ velocity can be calculated by gyro-averaging the electric field:

$$\langle\mathbf{E}\rangle = \frac{1}{2\pi}\int_{-\pi}^{\pi}\mathbf{E}(\mathbf{X}+\boldsymbol{\rho})\,d\theta = J_0(k\rho)\mathbf{E}(\mathbf{X}). \tag{3.175}$$

Here, J_0 is a Bessel function of the first kind, $\mathbf{X}$ is the gyrocenter, and $\boldsymbol{\rho}$ is the gyroradius. In our case, the gyro-averaged electric field is

$$\langle\mathbf{E}\rangle = E_0\sin(kX+\phi)J_0(k\rho)\hat{\mathbf{x}}. \tag{3.176}$$

This can then be substituted into the equation for the $\mathbf{E}\times\mathbf{B}$ velocity.

3.5.3.3 Adiabatic invariant

We next calculate the adiabatic invariant. Taylor analyzes the same electromagnetic field configuration, so we utilize his method in Ref. 58. The invariant is

$$I = \oint p_x\,dx = 2\int_{x_{\min}}^{x_{\max}}\sqrt{2mH_\perp - \left(p_y - \frac{q}{c}B_0 x\right)^2 - 2qm\varphi(x)}\,dx. \tag{3.177}$$

For small values of the electric potential, which occurs for large k, we can Taylor expand the integrand,

$$\frac{I}{2} \approx \int_{x_{\min}}^{x_{\max}} \sqrt{2mH_\perp - (m\Omega x - p_y)^2}\, dx - \frac{qmE_0}{k} \int_{x_{\min}}^{x_{\max}} \frac{\cos(kx+\phi)}{\sqrt{2mH_\perp - (m\Omega x - p_y)^2}}\, dx. \tag{3.178}$$

The first integral is elementary, while the second integral can be written in terms of a Bessel function of the first kind:

$$\mu_I = \frac{q}{mc}\frac{I}{2\pi} = \frac{H_\perp}{B_0} - \frac{q\alpha}{ck} J_0(ka)\cos\big(kx + kv_y/\Omega + \phi\big). \tag{3.179}$$

Here, $a = \sqrt{2mH_\perp}/(m\Omega) \approx \rho_0$. Therefore, the difference between this magnetic moment and the standard magnetic moment is

$$\mu_I - \mu_1 = \frac{q\alpha}{ck}(\cos(kx+\phi) - J_0(k\rho_0)\cos(\phi)). \tag{3.180}$$

Here, we have substituted in $x + v_y/\Omega = p_y/m = 0$ from our initial conditions. We then calculate an approximate drift that would give us this adiabatic invariant:

$$\mu_I = \frac{1}{2}\frac{m\,(\mathbf{v}-\mathbf{v}_I)^2}{B_0} \approx \mu_1 - 2\mu_0\frac{\dot{y}v_I}{u^2}. \tag{3.181}$$

Thus, we can write the drift as

$$v_I \approx -\frac{\alpha\Omega}{k\dot{y}}\left((\cos(kx+\phi) - J_0(k\rho_0)\cos(\phi)\right). \tag{3.182}$$

Noting that many of the above integrals cannot be done analytically, we turn to computational methods for more detailed analysis.

3.5.4 Simulation results

We conclude by simulating the orbit of a charged particle in the electromagnetic fields given by Eq. (3.130). We use the initial conditions found in Eq. (3.51), and use the fourth-order Runge-Kutta method to integrate our system of equations. Natural expressions for the fields and the system's parameters arise. We consider the case in which the effect of the electric field is thought of as a perturbation: $\epsilon_\delta\epsilon_\perp \ll 1$.

3.5.4.1 Magnetic moment definitions

In addition to the magnetic moments defined in the introduction, we are theoretically motivated to consider the behavior of a magnetic moment that has been corrected for a modified $\mathbf{E} \times \mathbf{B}$ drift. We can explicitly calculate the drift motion of the guiding center using Eqs. (3.171) and (3.174). Fortunately, we can avoid this integral form of the drift by taking advantage of our region of parameter space where $\epsilon_\delta \epsilon_\perp < 1$.

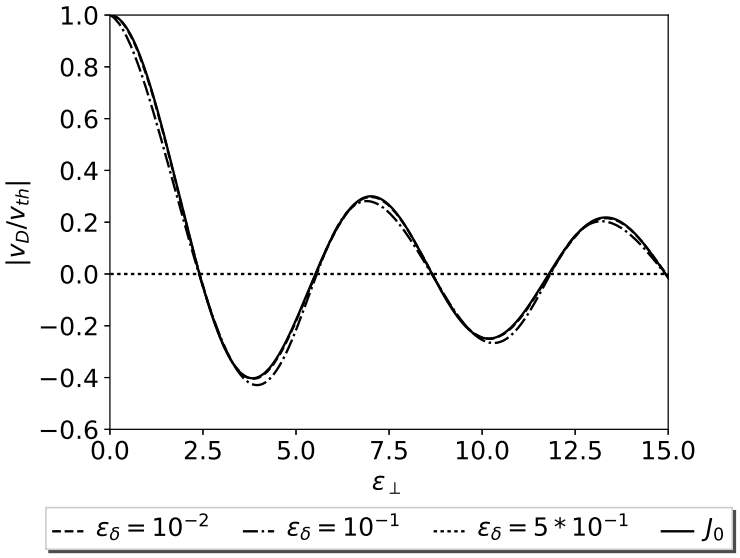

Figure 3.4: Plot of Eq. (3.174) for various values of $\epsilon_\perp$ compared to $J_0(\epsilon_\perp)$, rescaled to remove sensitivity in magnitude to ϵ_δ.

We can see in Fig. 3.4 that v_D only appreciably deviates in form from $J_0(\epsilon_\perp)$ for $\epsilon_\delta \epsilon_\perp > 1$. Since these values are explicitly omitted from our considerations, we substitute $v_D \sim v_J = -\alpha \sin(\phi) J_0(\epsilon_\perp)$ into our regime without consequence. This gives us a highly motivated definition for the magnetic moment:

$$\mu_J = \frac{1}{2} \frac{m \left(\mathbf{v}_\perp - \mathbf{v}_J\right)^2}{B}, \tag{3.183}$$

$$\mathbf{v}_J = -\alpha \sin(\phi) J_0(\epsilon_\perp) \hat{\mathbf{y}}. \tag{3.184}$$

According to the definition of μ_J, $\mu_J(\phi = 0) = \mu_E(\phi = 0) = \mu_1$. We also note the result is

indistinguishable from the $\phi = 0$ calculation at the zeros of the Bessel function.

3.5.4.2 Magnetic moment conservation

Our analytical calculations have established that the non-conservation of μ scales linearly with the strength of the electric field, ϵ_δ. Here, we scan over the parameter $\epsilon_\perp$ and observe the maximum relative change of the magnetic moment to probe the impact of the relative length scales on μ conservation. As theoretically predicted, the behavior changes when $|\nabla E/E|$ becomes comparable to $1/\rho_0$. As Fig. 3.5 shows, each definition exhibits two scalings: one for $\epsilon_\perp < 2\pi$ and another for $\epsilon_\perp > 2\pi$.

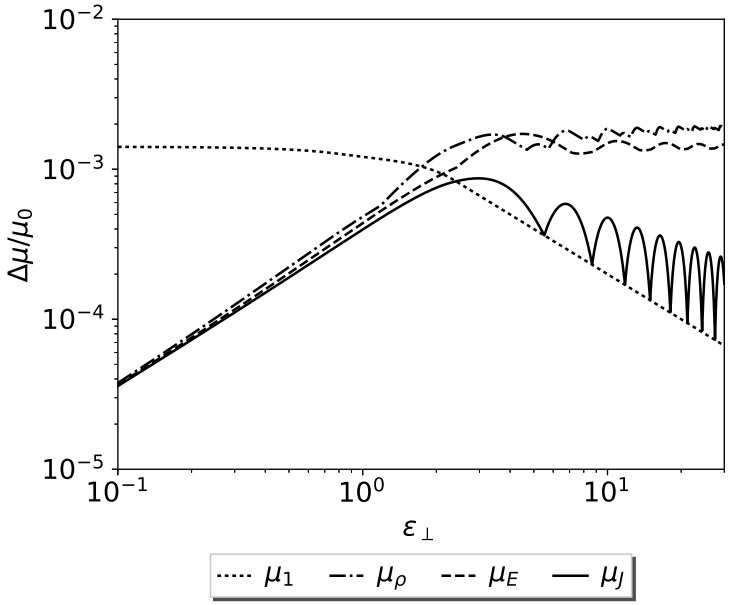

Figure 3.5: Plot of the dependencies of the maximum perturbation on $\epsilon_\perp$ for each of the four magnetic moment definitions.

We first inspect the sensitivities of the first three definitions to $\epsilon_\perp$. For nontrivial phase ϕ, each of these moments fail to conserve well for either large or small values of $\epsilon_\perp$. The fact that these definitions fail for entire regions of parameter space provides further motivation to use the fourth definition. Fig. 3.4 indicates that this definition is conserved well for both $\epsilon_\perp \ll 2\pi$ and $\epsilon_\perp \gg 2\pi$.

$\phi = \pi/4$	$\epsilon_\perp \ll 2\pi$	$\epsilon_\perp \gg 2\pi$
$\Delta\mu_{1_{\max}}$	$\sim \epsilon_\perp^0$	$\sim \epsilon_\perp^{-1}$
$\Delta\mu_{\rho_{\max}}$	$\sim \epsilon_\perp$	$\sim \epsilon_\perp^0$
$\Delta\mu_{E_{\max}}$	$\sim \epsilon_\perp$	$\sim \epsilon_\perp^0$

Table 3.1: Summary of scalings for different definitions of μ.

By inspecting Fig. 3.6, we can see that the scalings for $0 < \phi < \pi/2$ are bounded between $\epsilon_\perp$ and $\epsilon_\perp^2$ for $\epsilon_\perp \ll 2\pi$ and between $\epsilon_\perp^{-1}$ and $\epsilon_\perp^{-1/2}$ for $\epsilon_\perp \gg 2\pi$. In other words as $\epsilon_\perp$ departs from unity, we find increasingly well-conserved μ_J. These scalings are sensitive to ϕ in a non-trivial fashion; only the behaviors for extreme ϕ are easily readable. For $\epsilon_\perp > 2\pi$, the magnetic moment will scale with, at worst, the $\epsilon_\perp$-scaling of the envelope that is insensitive to the J_0's zeroes. For $\epsilon_\perp$ such that $J_0(\epsilon_\perp) \sim 0$, the scaling improves. Fig. 3.7 shows the envelope-scalings for arbitrary values of ϕ.

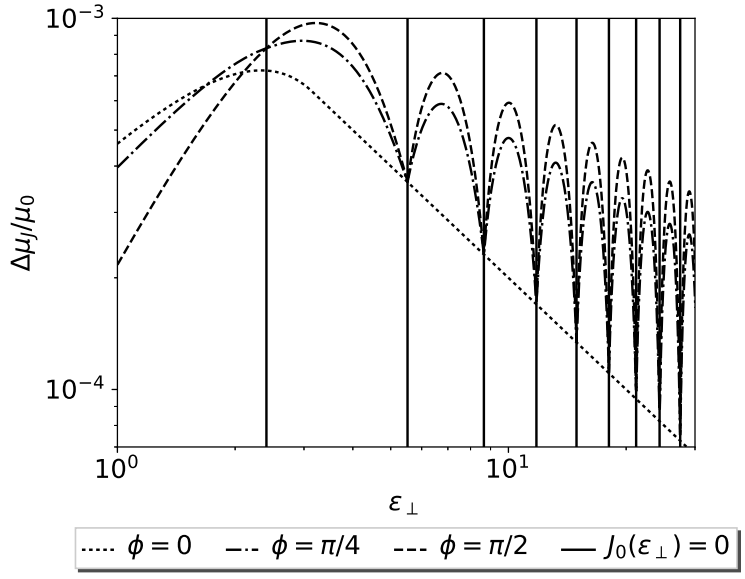

Figure 3.6: A closer look at the behavior of μ_J for differing values of ϕ. The solutions converge where $J_0(\epsilon_\perp) = 0$.

$\Delta\mu_{J_{\max}}$	$\epsilon_\perp \ll 2\pi$	$\epsilon_\perp \gg 2\pi$
$\phi = 0$	$\sim \epsilon_\perp$	$\sim \epsilon_\perp^{-1}$
$\phi = \pi/2$	$\sim \epsilon_\perp^2$	$\sim \epsilon_\perp^{-1/2}$

Table 3.2: Summary of scalings for μ_J.

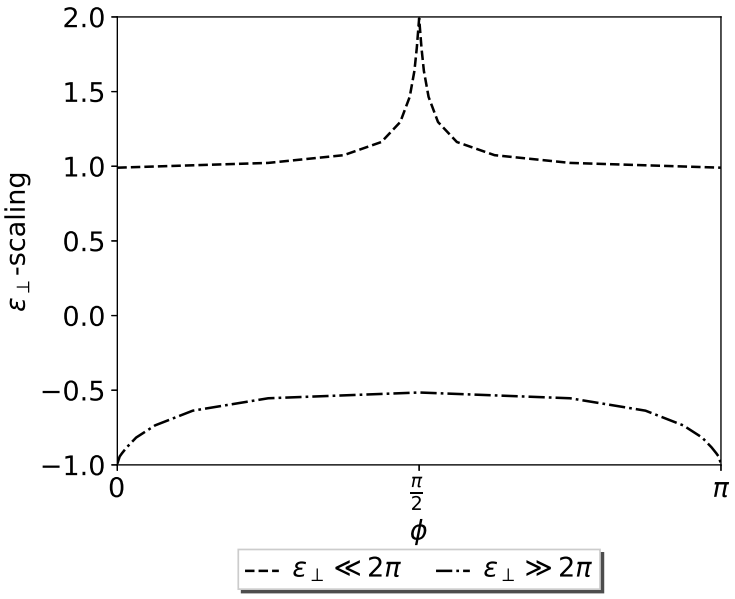

Figure 3.7: Plot of the peak-envelope scalings for μ_J for differing phase.

As we correct for the drift-motion of the guiding center, we obtain approximate invariants that are conserved in differing regions of parameter space. The closer the correction matches the true motion of the guiding center, the larger the region of parameter space in which the approximate invariant is conserved well. As was found in the case of the stochastic heating of ions, the magnetic moment is maximally perturbed when the field's wavelength is on the same scale as the gyroradius.[64]

3.5.5 Summary

If the long-wavelength approximation is assumed, then $\Delta\mu_1/\mu_0$ is at worst linear in ϵ_δ but does not scale with $\epsilon_\perp$. Meanwhile, correcting for the gyro-averaged $\mathbf{E}\times\mathbf{B}$ velocity results in the perturbation being linear in $\epsilon_\delta\epsilon_\perp$, and thus we obtain better magnetic moment conservation for long-wavelengths. For $\epsilon_\perp \gg 1$, the perturbation of μ_1 scales as $\epsilon_\delta/\epsilon_\perp$ and is therefore well conserved. Correcting for the gyro-averaged $\mathbf{E}\times\mathbf{B}$ velocity sometimes results in worse μ conservation in the short-wavelength regime. For $\epsilon_\perp \sim 1$, correcting for any drifts does not significantly change the maximum perturbation, and we require that $\epsilon_\delta \ll 1$ for adequate μ conservation.

3.6 Chapter summary

In this work, our goal was to shed light on the limitations of gyrokinetic theory by investigating the non-conservation of the magnetic moment in elementary electromagnetic fields. By calculating the perturbation of the magnetic moment under various conditions, we have determined quantitatively which parameters control the degree to which the magnetic moment is conserved.

In standard gyrokinetic theory, μ_1 is considered the lowest-order approximation of the true adiabatic invariant, the gyrocenter magnetic moment $\bar{\mu}$. In Ref. 65, Krommes shows that one obtains higher-order approximations of $\bar{\mu}$ if one evaluates the magnetic moment in a frame of reference moving with the local $\mathbf{E}\times\mathbf{B}$ velocity, in line with standard gyrokinetics, by performing calculations in the long-wavelength limit. Our calculations confirm this finding. In almost all of our elementary field configurations, μ_E is conserved to higher order than μ_1. Precise scalings for a robust conservation of μ_E in terms of the small parameters ϵ_δ, ϵ_ω, and ϵ_B (introduced in Sec. 3.1) are given in Table 3.3. Our calculations are also consistent with Littlejohn's guiding center theory; for the fields examined in this work, Littlejohn's corrections to the magnetic moment correspond exactly to guiding center drifts.

We note that depending on the field configuration, different small parameters impact the non-

$B(t)$	$B(\mathbf{x})$
$\epsilon_\omega^2 \ll 1$	$\epsilon_B \ll 1$

$E(t)$	$E(\mathbf{x}), \epsilon_\perp \ll 1$	$E(\mathbf{x}), \epsilon_\perp \approx 1$	$E(\mathbf{x}), \epsilon_\perp \gg 1$
$\epsilon_\delta \epsilon_\omega \ll 1$	$\epsilon_\delta \epsilon_\perp \ll 1$	$\epsilon_\delta \ll 1$	$\epsilon_\delta / \sqrt{\epsilon_\perp} \ll 1$

Table 3.3: Conditions necessary for $\Delta\mu_E/\mu_0 \ll 1$ for each system. The first table outlines the results of Secs. 3.2 and 3.3, while the second table does so for Secs. 3.4 and 3.5.

conservation of the magnetic moment in different ways. Consequently, assuming, e.g., $\epsilon_B \ll \epsilon_\delta$ instead of $\epsilon_B \sim \epsilon_\delta$ will result in distinct sets of reduced Vlasov-Maxwell equations.[66] Derivations with general orderings can be found in Refs. 67 and 68.

Clearly, in the presence of fast spatial changes (compared to the gyroradius) of the background magnetic field and/or high-amplitude electric field perturbations, magnetic moment conservation can break to a significant degree. In the present work, we have provided quantitative expressions for these violations, which should help to assess the validity of gyrokinetics in specific physical situations. In general, one can always achieve higher-order μ conservation by taking into account additional drifts (beyond the $\mathbf{E} \times \mathbf{B}$ velocity). The integration of these effects into an existing theoretical framework would be able to extend the applicability of gyrokinetic theory.

Appendix 3.A Calculations using Littlejohn's guiding center theory

We now apply Littlejohn's guiding center theory as outlined in Refs. 27 and 28 to the electromagnetic field configurations examined in this work, and demonstrate a direct correspondence between guiding center theory and our proposed magnetic moment corrections.

In Ref. 28, Littlejohn applies the method of Lie transforms to obtain expressions for guiding center variables in terms of particle variables. We only analyze the first-order results, which

Littlejohn helpfully provides. While Littlejohn includes an asymptotic parameter ϵ to keep track of orderings, we set the term equal to 1 to obtain physical results. He writes that the guiding center magnetic moment is

$$\begin{aligned}\bar{\mu} =& \frac{1}{2}\frac{mv_\perp^2}{B} + \frac{mv_\perp c}{B^2}\Bigg[- \mathbf{E}\cdot\hat{\mathbf{a}} \\ &+ \frac{mv_\perp v_\parallel}{4q}\left(3\left(\hat{\mathbf{a}}\cdot\nabla\hat{\mathbf{b}}\right)\cdot\hat{\mathbf{c}} - \left(\hat{\mathbf{c}}\cdot\nabla\hat{\mathbf{b}}\right)\cdot\hat{\mathbf{a}}\right) \\ &+ \frac{mv_\parallel^2}{q}\left(\left(\hat{\mathbf{b}}\cdot\nabla\hat{\mathbf{b}}\right)\cdot\hat{\mathbf{a}}\right) + \frac{mv_\perp^2}{2qB}\left(\hat{\mathbf{a}}\cdot\nabla B\right)\Bigg] + H.O.T.,\end{aligned} \tag{3.185}$$

where we define

$$\mathbf{B} = B\hat{\mathbf{b}}, \tag{3.186}$$

$$\mathbf{v}\cdot\hat{\mathbf{b}} = v_\parallel, \tag{3.187}$$

$$\mathbf{v}_\perp = \mathbf{v} - v_\parallel\hat{\mathbf{b}} = v_\perp\hat{\mathbf{c}}, \tag{3.188}$$

$$\hat{\mathbf{a}} = \hat{\mathbf{b}}\times\hat{\mathbf{c}}, \tag{3.189}$$

and where $H.O.T.$ denotes neglected higher order terms. Thus, $\hat{\mathbf{a}}, \hat{\mathbf{b}}, \hat{\mathbf{c}}$ form an orthonormal triad of unit vectors. We now examine Eq. (3.185) in different field configurations. We note that in the absence of an electric field, the above expression corresponds exactly to Brizard and Hahm's calculations in Ref. 39.

3.A.1 Uniform magnetic field

We first demonstrate that the $\mathbf{E}\times\mathbf{B}$ velocity is manifestly present in Eq. (3.185) by simplifying the equation. We use the field configuration

$$\mathbf{B} = B(t)\hat{\mathbf{z}}, \tag{3.190}$$

$$\mathbf{E} \neq \mathbf{0}. \tag{3.191}$$

In a uniform magnetic field, $\hat{\mathbf{b}}$ and $\mathbf{B}$ have no spatial dependence. Therefore, Eq. (3.185) becomes

$$\bar{\mu} = \frac{1}{2}\frac{mv_\perp^2}{B} - \frac{mv_\perp c}{B^2}\left(\mathbf{E}\cdot\hat{\mathbf{a}}\right) + H.O.T. \tag{3.192}$$

We rewrite the dot product in the second term,

$$\mathbf{E}\cdot\hat{\mathbf{a}} = \mathbf{E}\cdot\left(\hat{\mathbf{b}}\times\hat{\mathbf{c}}\right) = \hat{\mathbf{c}}\cdot\left(\mathbf{E}\times\hat{\mathbf{b}}\right). \tag{3.193}$$

Substituting in our expression for $\mathbf{v}_\perp$ and $\mathbf{B}$, we now have

$$\bar{\mu} = \frac{1}{2}\frac{mv_\perp^2}{B} - \frac{m\mathbf{v}_\perp\cdot\mathbf{v}_E}{B} + H.O.T. \tag{3.194}$$

We note that by assuming $\epsilon_\delta \ll 1$, we may add the term $(mv_E^2)/(2B)$ as a higher order term without affecting the expression. Therefore,

$$\bar{\mu} = \frac{1}{2}\frac{m\left(\mathbf{v}_\perp - \mathbf{v}_E\right)^2}{B} + H.O.T. = \mu_E + H.O.T. \tag{3.195}$$

We conclude that in the absence of magnetic field inhomogeneities, to first order the guiding center magnetic moment is simply μ_1. In the case that the electric field is spatially dependent, we gyroaverage $\mathbf{v}_E$ as done in Sec. 3.5 to obtain better conservation. Now that it is clear that the guiding center magnetic moment contains an $\mathbf{E}\times\mathbf{B}$ correction, we proceed to examining the case of inhomogeneous magnetic fields without curvature.

3.A.2 Straight, spatially dependent magnetic field

We examine the field configuration

$$\mathbf{B} = B(x,y)\hat{\mathbf{z}}, \tag{3.196}$$

$$\mathbf{E} = \mathbf{0}. \tag{3.197}$$

Because our magnetic field is straight, $\hat{\mathbf{b}}$ is not spatially dependent. Thus, Eq. (3.185) simplifies to

$$\bar{\mu} = \frac{1}{2}\frac{mv_\perp^2}{B} + \frac{m^2v_\perp^3 c}{2qB^3}\left(\hat{\mathbf{a}}\cdot\nabla B\right). \tag{3.198}$$

The dot product can be rewritten as

$$\hat{\mathbf{a}}\cdot\nabla B = (\nabla B)\cdot\left(\hat{\mathbf{b}}\times\hat{\mathbf{c}}\right) = -\hat{\mathbf{c}}\cdot\left(\hat{\mathbf{b}}\times\nabla B\right). \tag{3.199}$$

We plug this in and simplify to obtain

$$\bar{\mu} = \frac{1}{2}\frac{mv_\perp^2}{B} - \frac{m^2 v_\perp^2}{2qB^4}\mathbf{v}_\perp \cdot (c\mathbf{B} \times \nabla B) + H.O.T. \tag{3.200}$$

$$= \frac{1}{2}\frac{mv_\perp^2}{B} - \frac{m\mathbf{v}_\perp \cdot \mathbf{v}_{\nabla B}}{B} + H.O.T. \tag{3.201}$$

The grad-B drift is now manifest in Littlejohn's equation for $\bar{\mu}$. If we assume $\epsilon_B \ll 1$, then $\left(mv_{\nabla B}^2\right)/(2B)$ would be considered a higher order term. Therefore, we may rewrite $\bar{\mu}$ as

$$\bar{\mu} = \frac{1}{2}\frac{m\left(\mathbf{v}_\perp - \mathbf{v}_{\nabla B}\right)^2}{B} + H.O.T. = \mu_{\nabla B} + H.O.T. \tag{3.202}$$

It is now clear that, to first-order, the guiding center magnetic moment in the absence of curvature or electric fields is $\mu_{\nabla B}$. We now turn analyze the magnetic field of a wire to determine the basic effects curvature has on the guiding center magnetic moment.

3.A.3 Magnetic field of a wire

The electromagnetic fields are

$$\mathbf{B} = \frac{A_0}{s}\hat{\boldsymbol{\phi}}, \tag{3.203}$$

$$\mathbf{E} = \mathbf{0}. \tag{3.204}$$

Here, A_0 is a constant such that the expression has the correct units. We note that for any vector $\mathbf{C}$ we find

$$\mathbf{C} \cdot \nabla\hat{\boldsymbol{\phi}} = -\frac{\mathbf{C} \cdot \hat{\boldsymbol{\phi}}}{s}\hat{\mathbf{s}}. \tag{3.205}$$

Using this identity, as well as the fact that $\hat{\mathbf{b}} = \hat{\boldsymbol{\phi}}$, Eq. (3.185) simplifies to

$$\bar{\mu} = \frac{1}{2}\frac{mv_\perp^2}{B} - \frac{m\mathbf{v}_\perp \cdot \mathbf{v}_{\nabla B}}{B} - \frac{m^2 v_\parallel^2 v_\perp c}{qB^2 s^2}\left(\hat{\mathbf{a}} \cdot \mathbf{s}\right) + H.O.T. \tag{3.206}$$

We manipulate the rightmost dot product to show that

$$\hat{\mathbf{a}} \cdot \mathbf{s} = \mathbf{s} \cdot \left(\hat{\mathbf{b}} \times \hat{\mathbf{c}}\right) = \hat{\mathbf{c}} \cdot \left(\mathbf{s} \times \hat{\mathbf{b}}\right). \tag{3.207}$$

We note that due to the magnetic field geometry that $\mathbf{s} = \mathbf{R}_c$, the radius of curvature vector for the magnetic field. Substituting this, as well as the above vector manipulation, we obtain

$$\begin{aligned}\bar{\mu} =& \frac{1}{2}\frac{mv_\perp^2}{B} - \frac{m\mathbf{v}_\perp \cdot \mathbf{v}_{\nabla B}}{B} - \frac{m^2 v_\parallel^2}{qB^3 R_c^2}\left(\mathbf{v}_\perp \cdot (\mathbf{R}_c \times c\mathbf{B})\right) + H.O.T. \\ =& \frac{1}{2}\frac{mv_\perp^2}{B} - \frac{m\mathbf{v}_\perp \cdot \mathbf{v}_{\nabla B}}{B} - \frac{m\mathbf{v}_\perp \cdot \mathbf{v}_{R_c}}{B} + H.O.T.\end{aligned} \tag{3.208}$$

Now, both the grad-B and the curvature drifts are present in the guiding center magnetic moment. If $\epsilon_B \ll 1$, then any terms involving squared drift velocities would be considered higher order terms. Then, $\bar{\mu}$ can be rewritten as

$$\bar{\mu} = \frac{1}{2}\frac{m\left(\mathbf{v}_\perp - \mathbf{v}_{\nabla B} - \mathbf{v}_{R_c}\right)^2}{B} + H.O.T. = \mu_{B(x)} + H.O.T. \tag{3.209}$$

The first-order correction for the guiding center magnetic moment corrects for the grad-B drift and the curvature drift for the magnetic field of a wire. We now apply Littlejohn's theory as outlined in Ref. 27 to the case of a time dependent electric field.

3.A.4 Time dependent electric field

We consider the following field configuration:

$$\mathbf{B} = B_0\hat{\mathbf{z}}, \tag{3.210}$$

$$\mathbf{E} = E(t)\hat{\mathbf{x}}. \tag{3.211}$$

To derive a higher order correction, we use the guiding center theory found in Ref. 27. For the sake of brevity we simply substitute our fields into Littlejohn's calculations and find that

$$\bar{\mu} = \frac{1}{2}\frac{mw^2}{B} + \frac{mcw}{qB^2}\hat{\mathbf{w}} \cdot \left(\frac{\partial \mathbf{v}_E}{\partial t} \times \hat{\mathbf{z}}\right) + H.O.T. \tag{3.212}$$

where we have for convenience defined

$$\mathbf{w} = \mathbf{v}_\perp - \mathbf{v}_E. \tag{3.213}$$

From the definition of the polarization drift, we then note that this expression can be rewritten as

$$\bar{\mu} = \frac{1}{2}\frac{mw^2}{B} - \frac{m\mathbf{w}\cdot\mathbf{v}_p}{B} + H.O.T. \tag{3.214}$$

If $\epsilon_\delta \ll 1$ and $\epsilon_\omega \ll 1$, then terms quadratic in the polarization drift are higher order terms, and $\bar{\mu}$ simplifies as follows:

$$\begin{aligned}\bar{\mu} =& \frac{1}{2}\frac{mw^2}{B} - \frac{m\mathbf{w}\cdot\mathbf{v}_p}{B} + \frac{mv_p^2}{2B} + H.O.T. \\ =& \frac{1}{2}\frac{m\left(\mathbf{w}-\mathbf{v}_p\right)^2}{B} + H.O.T. \\ =& \mu_p + H.O.T.\end{aligned} \tag{3.215}$$

As expected, $\bar{\mu}$ is simply the magnetic moment in the reference frame of the $\mathbf{E}\times\mathbf{B}$ drift and the polarization drift.

To summarize, all of the basic corrected magnetic moments proposed in this work can be derived directly from Littlejohn's guiding center theory. As long as the dimensionless parameters discussed in this work are sufficiently small, we can more accurately approximate $\bar{\mu}$ with these corrections and obtain better magnetic moment conservation.

CHAPTER 4

Analytic guiding center formulas for bounce-transit motion in a concentric circular, finite inverse aspect ratio tokamak geometry

4.1 Introduction

Inhomogeneity in a magnetic field gives rise to charged particle orbits such that the particle either is trapped in the magnetic well or passes through the magnetic field.[17, 21, 69] The properties of these orbits have long been studied in tokamak plasmas and are instrumental in describing a wide range of kinetic and neoclassical phenomena.[70–76] For example, analysis of trapped electron modes requires knowledge of the lowest-order bounce-transit motion, and the toroidal drift frequency characterizes the stability of these modes.[77–79] In kinetic magnetohydrodynamics, the bounce-transit and drift frequencies underly the resonances with energetic particles that drive instabilities.[80–82] Moreover, neoclassical calculations of the zonal flow residual involve a series of bounce-transit time averaging, a process that is intimately related to the calculation of the toroidal drift frequency.[83–85] Thus, analytic formulas are indispensable in understanding these problems through analytical and computational means; this need has led to a great amount of work done solely on the bounce-transit motion itself in order obtain such formulas.[69, 86] Unfortunately, the complex magnetic geometry in a tokamak presents a difficult obstacle in deriving analytic formulas. The main goal of this work is to remove one of these obstacles to allow for more accurate calculations.

Previous analyses of guiding center bounce-transit motion have utilized concentric circular magnetic geometry to simplify the problem. In addition, the inverse aspect ratio is typically assumed to be small, resulting in an even more approximate magnetic geometry.[78, 86, 87] This

work takes direct inspiration from Ref. 86, which performed analogous calculations in the limit of small inverse aspect ratio. While this small inverse aspect ratio approximation does make the formulas easier to obtain and more compact, they are not necessary to carry out an analytic derivation. Instead, a finite, non-zero inverse aspect ratio can be retained throughout the entirety of the derivation. The calculations presented in this work are possible because the fundamental integrals used in this work are of the form

$$\int R(u, \sqrt{P(u)})du, \tag{4.1}$$

where P is a polynomial of degree 3 or 4 with no repeated roots, R is a rational function of u and $\sqrt{P(u)}$, and R contains at least one odd power of $\sqrt{P}$.

It is well known that such an integral can always be represented by the three Legendre forms of elliptic integrals.[60–62, 88] While previously derived formulas only used elliptic integrals of the first and second kind, these new formulas require the elliptic integral of the third kind. Closed form solutions for the field line-following equations of motion are found using modified functions similar to the classical Jacobi elliptic functions that are used, for instance, to describe particle trapping in waves.[89] We also show that the small inverse aspect ratio approximation can be directly applied to the finite inverse aspect ratio analysis. The resulting comparison demonstrates that the approximation is valid for moderately small inverse aspect ratio. In the cases where the approximation is not good enough, these analytic formulas can be used for increased accuracy. Spherical tokamaks such as the National Spherical Torus (NSTX) and the Mega Ampere Spherical Tokamak (MAST) are characterized by low aspect ratios; the inverse aspect ratios for these two tokamaks were both ~ 0.77.[90, 91] Thus, finite inverse aspect ratio effects can be important, even if the analysis is restricted to a concentric, circular geometry.

This work is organized as follows. Sec. 4.2 clarifies the analytic concentric circular magnetic geometry and the preliminaries for bounce-transit motion along the field line. Secs. 4.3 and 4.4 derive formulas for the bounce-transit frequency, the longitudinal adiabatic invariant, and the closed form solution to the bounce-transit motion. We next take into account deviations from the field line motion due to magnetic drifts and conservation of canonical toroidal momentum while still

retaining a finite inverse aspect ratio. Sec. 4.5 analyzes the radial excursion from the magnetic field line that results in banana orbits. Sec. 4.6 then calculates the slow toroidal drift frequency by analyzing the equation of motion in the toroidal direction. Finally, we summarize our work in Sec. 4.7. We also include a brief overview of our definitions and notation for elliptic integrals in Appendix 4.A, while a tabulation of specific elliptic integrals used to calculate the toroidal drift frequency can be found in Appendix 4.B.

4.2 Circular magnetic geometry

For a concentric circular tokamak geometry,[92] the magnetic field is defined to be

$$\mathbf{B} = \frac{B_0}{1 + \epsilon \cos(\theta)} \left(\hat{\boldsymbol{\phi}} + \frac{\epsilon}{\bar{q}(r)} \hat{\boldsymbol{\theta}} \right). \tag{4.2}$$

The triad (r, θ, ϕ) (minor radial distance, poloidal angle, azimuthal angle) defines a right-handed coordinate system with $\hat{\mathbf{r}} \times \hat{\boldsymbol{\theta}} = \hat{\boldsymbol{\phi}}$. The inverse aspect ratio $\epsilon = r/R_0$ and approximate safety factor $\bar{q}$ are functions of r only, where R_0 is the major radius. We do not take into account the Shafranov shift; thus, the flux surfaces considered are concentric circles.[93] We note that the magnetic field strength is typically approximated as

$$B = |\mathbf{B}| \approx B_0 \left(1 - \epsilon \cos\left(\theta\right)\right). \tag{4.3}$$

To retain a finite inverse aspect ratio, we do not use this approximation in this work.

The true safety factor $q(r)$ is given by

$$q(r) = \frac{1}{2\pi} \int_0^{2\pi} d\theta \, \frac{\mathbf{B} \cdot \nabla \phi}{\mathbf{B} \cdot \nabla \theta} = \frac{\bar{q}(r)}{\sqrt{1 - \epsilon^2}}. \tag{4.4}$$

We note that the magnetic field can be written in the Clebsch form[29]

$$\mathbf{B} = \nabla \alpha \times \nabla \psi, \tag{4.5}$$

where

$$\alpha = \phi - q(r)\chi(r,\theta), \tag{4.6}$$

$$\frac{d\psi}{dr} = \frac{rB_0}{\bar{q}(r)}. \tag{4.7}$$

We identify ψ with minus the poloidal flux normalized to 2π and note that ψ labels the flux surface while α labels the field line. The straight field line poloidal coordinate χ is defined as

$$\chi = 2\arctan\left[\sqrt{\frac{1-\epsilon}{1+\epsilon}}\tan\left(\frac{\theta}{2}\right)\right] \tag{4.8}$$

and is constructed to satisfy the property

$$\frac{\mathbf{B}\cdot\nabla\phi}{\mathbf{B}\cdot\nabla\chi} = q(r). \tag{4.9}$$

The unit vector $\hat{\mathbf{b}}$ denoting the direction of the magnetic field is

$$\hat{\mathbf{b}} = \frac{\mathbf{B}}{B} = \frac{1}{\sqrt{1+\epsilon^2/\bar{q}^2}}\left(\hat{\boldsymbol{\phi}} + \frac{\epsilon}{\bar{q}}\hat{\boldsymbol{\theta}}\right). \tag{4.10}$$

The guiding center approximation used in this work is justified by the adiabatic conservation of the magnetic moment, which requires that the gyroradius be small compared to other relevant length scales in the system.[39, 94–97] We impose two conditions on the guiding center particle orbit to determine the bounce-transit motion to lowest-order in the gyroradius:

$$\dot{\psi} = 0, \tag{4.11}$$

$$\dot{\alpha} = 0. \tag{4.12}$$

This restricts the particle to the magnetic field line. These conditions can be written in terms of our previous coordinates,

$$\dot{r} = 0, \tag{4.13}$$

$$\dot{\phi} = \frac{\bar{q}\dot{\theta}}{1+\epsilon\cos(\theta)}. \tag{4.14}$$

We then compute the parallel velocity with this restriction in mind,

$$v_{\|} = \mathbf{v} \cdot \hat{\mathbf{b}} = \sqrt{1 + \frac{\epsilon^2}{\bar{q}^2}}\, \bar{q} R_0 \dot{\theta}. \tag{4.15}$$

Accordingly, we can define the length along the field line to be

$$l = \sqrt{1 + \frac{\epsilon^2}{\bar{q}^2}}\, \bar{q} R_0 \theta. \tag{4.16}$$

From conservation of energy, the magnitude of the parallel velocity is

$$\left|v_{\|}\right| = \sqrt{\frac{2}{m}\left(E - \mu B\right)} = \sqrt{\frac{2E}{m}} \sqrt{1 - \frac{\mu B^0 / E}{1 + \epsilon \cos(\theta)}}, \tag{4.17}$$

where E is the kinetic energy (since we ignore the electrostatic potential), μ is the magnetic moment, and

$$B^0(r) = B_0 \sqrt{1 + \epsilon^2 / \bar{q}^2}. \tag{4.18}$$

We next parameterize the orbit via the trapping parameter κ,

$$\frac{\mu B^0}{E} = 1 + \epsilon - 2\epsilon\kappa^2. \tag{4.19}$$

Trapped particles reflect at a poloidal angle θ_b where their parallel velocity vanishes. We find that for trapped particles,

$$0 \leq \kappa < 1, \tag{4.20}$$

$$\theta_b = 2 \arcsin(\kappa), \tag{4.21}$$

Passing particle orbits, however, are not reflected. Instead, they continue along the magnetic field line and make a complete transit through the entire torus. Thus, the trapping parameter for passing particles is bounded by

$$1 < \kappa \leq \sqrt{\frac{1 + \epsilon}{2\epsilon}}. \tag{4.22}$$

The upper bound for κ corresponds to the situation where the perpendicular velocity is 0. A particle at the trapped-passing boundary ($\kappa = 1$) is analogous to a stationary pendulum at the top of its arc,

so we expect the period to approach infinity as $\kappa \to 1$ from both sides. We note that in the small inverse aspect ratio limit, the upper bound for κ approaches infinity.

The differential equation governing the motion of the particle is then

$$\sqrt{1+\frac{\epsilon^2}{\bar{q}^2}}\,\bar{q}R_0\left|\dot{\theta}\right| = \sqrt{\frac{2E}{m}}\sqrt{2\epsilon}\sqrt{\frac{\kappa^2-\sin^2(\theta/2)}{1+\epsilon\cos(\theta)}}. \tag{4.23}$$

The characteristic frequency for the periodic motion is

$$\omega_0 = \frac{\sqrt{E/m}\sqrt{\epsilon}}{\bar{q}R_0\sqrt{1+\epsilon^2/\bar{q}^2}}, \tag{4.24}$$

while the characteristic length is

$$l_0 = \sqrt{1+\frac{\epsilon^2}{\bar{q}^2}}\,\bar{q}R_0. \tag{4.25}$$

This gives us

$$\left|\dot{\theta}\right| = 2\omega_0\sqrt{\frac{\kappa^2-\sin^2(\theta/2)}{1+\epsilon\cos(\theta)}}. \tag{4.26}$$

We confirm that in the small ϵ limit

$$\omega_0 \approx \frac{\sqrt{E/m}\sqrt{\epsilon}}{\bar{q}R_0}, \tag{4.27}$$

$$l_0 \approx \bar{q}R_0. \tag{4.28}$$

Having defined the exact concentric circular geometry and identified the lowest-order equation of motion, we proceed to deriving analytic formulas for the bounce-transit frequency and the longitudinal adiabatic invariant.

4.3 Bounce-transit frequency

Although the guiding center deviates from the magnetic field line, we can calculate the longitudinal invariant J (also known as the bounce-transit action); J is an adiabatic invariant, meaning that if the time scale of the deviation is longer than the bounce-transit period then it can be treated

as a constant.[36] J is defined to be

$$J = \frac{1}{2\pi} \oint m v_{\parallel} dl. \tag{4.29}$$

Meanwhile, the bounce-transit frequency is defined as

$$\omega = \left(\frac{\partial J}{\partial E} \right)^{-1}, \tag{4.30}$$

or equivalently

$$\omega = \frac{2\pi}{T} = 2\pi \left(\oint \frac{dl}{v_{\parallel}} \right)^{-1}. \tag{4.31}$$

Because the bounce and transit motions are qualitatively different, we separate the calculation for trapped and passing particles. This distinction will apply to all other calculations in this work.

The elliptic integrals calculated here and elsewhere in this work are functions of parameters called the modulus and the characteristic. These parameters are functions of κ and ϵ and take on different forms for trapped and passing particles. For trapped particles, the modulus and characteristic are

$$k_b = \kappa \sqrt{\frac{1-\epsilon}{1+\epsilon-2\epsilon\kappa^2}}, \tag{4.32}$$

$$n_b = \frac{-2\epsilon\kappa^2}{1+\epsilon-2\epsilon\kappa^2}. \tag{4.33}$$

For passing particles, the modulus and characteristic are

$$k_t = \frac{1}{\kappa} \sqrt{\frac{1+\epsilon-2\epsilon\kappa^2}{1-\epsilon}}, \tag{4.34}$$

$$n_t = \frac{-2\epsilon}{1-\epsilon}. \tag{4.35}$$

Throughout this work, we simplify many elliptic integrals into an analytically tractable form; Ref. 60 contains tables of elliptic integrals, whereas Refs. 61 and 62 outline the method to reduce and simplify these integrals.

4.3.1 Trapped particles

The longitudinal invariant for trapped particles is

$$J_b = \frac{8m\omega_0 l_0^2}{2\pi}\int_0^{\theta_b} d\theta \sqrt{\frac{\kappa^2 - \sin^2(\theta/2)}{1+\epsilon\cos(\theta)}}. \tag{4.36}$$

We perform the substitution

$$\theta = 2\arcsin\left(\sqrt{u}\kappa\right) \tag{4.37}$$

and find that

$$J_b = \frac{8m\omega_0 l_0^2}{2\pi\sqrt{2\epsilon}}\int_0^1 du \frac{\sqrt{1-u}}{\sqrt{u}\sqrt{\frac{1}{\kappa^2}-u}\sqrt{\frac{1+\epsilon}{2\epsilon\kappa^2}-u}}. \tag{4.38}$$

Consulting Refs. 60–62, we find that this integral can be expressed analytically:

$$J_b = \frac{4m\omega_0 l_0^2}{\pi\epsilon}\sqrt{1+\epsilon-2\epsilon\kappa^2}\left(\frac{(1+\epsilon)\,\Pi(n_b,k_b)}{1+\epsilon-2\epsilon\kappa^2} - K(k_b)\right). \tag{4.39}$$

In the small ϵ limit, we find that

$$J_b \approx \frac{8m\omega_0 l_0^2}{\pi}\left(E(\kappa) - (1-\kappa^2)K(\kappa)\right). \tag{4.40}$$

Meanwhile, for small κ we can approximate the bounce action as

$$J_b \approx \frac{2m\omega_0 l_0^2}{\sqrt{1+\epsilon}}\kappa^2. \tag{4.41}$$

For both small κ and small ϵ, it is then clear that

$$J_b \approx 2m\omega_0 l_0^2\kappa^2. \tag{4.42}$$

Next, we compute the period

$$T_b = \frac{4}{2\omega_0}\int_0^{\theta_b} d\theta \sqrt{\frac{1+\epsilon\cos(\theta)}{\kappa^2-\sin^2(\theta/2)}}. \tag{4.43}$$

We again perform the substitution $\theta = 2\arcsin\left(\sqrt{u}\kappa\right)$ and obtain

$$T_b = \frac{2\sqrt{2\epsilon}}{\omega_0}\int_0^1 du \frac{\sqrt{\frac{1+\epsilon}{2\epsilon\kappa^2}-u}}{\sqrt{u}\sqrt{1-u}\sqrt{\frac{1}{\kappa^2}-u}}, \tag{4.44}$$

and using Refs. 60–62 once again,

$$T_b = \frac{4}{\omega_0} \frac{(1+\epsilon)\,\Pi\,(n_b, k_b)}{\sqrt{1+\epsilon-2\epsilon\kappa^2}}. \tag{4.45}$$

Therefore, the bounce frequency is

$$\omega_b = \frac{2\pi}{T_b} = \frac{\pi\omega_0}{2} \frac{\sqrt{1+\epsilon-2\epsilon\kappa^2}}{(1+\epsilon)\,\Pi\,(n_b, k_b)}. \tag{4.46}$$

Taylor expanding the bounce period for small ϵ, we find that

$$T_b \approx \frac{4K\,(\kappa)}{\omega_0}, \tag{4.47}$$

so the bounce frequency can be approximated by

$$\omega_b \approx \frac{\pi\omega_0}{2K\,(\kappa)}. \tag{4.48}$$

In the limit of small κ, we instead have

$$T_b \approx \frac{2\pi}{\omega_0\sqrt{1+\epsilon}}, \tag{4.49}$$

$$\omega_b \approx \omega_0\sqrt{1+\epsilon}. \tag{4.50}$$

In the limit such that both ϵ and κ are small,

$$T_b \approx \frac{2\pi}{\omega_0}, \tag{4.51}$$

$$\omega_b \approx \omega_0. \tag{4.52}$$

4.3.2 Passing particles

The longitudinal invariant for trapped particles is

$$J_t = \frac{4m\omega_0 l_0^2}{2\pi} \int_0^\pi d\theta \sqrt{\frac{\kappa^2 - \sin^2(\theta/2)}{1+\epsilon\cos(\theta)}}. \tag{4.53}$$

We perform the substitution

$$\theta = 2\arcsin\left(\sqrt{u}\right), \tag{4.54}$$

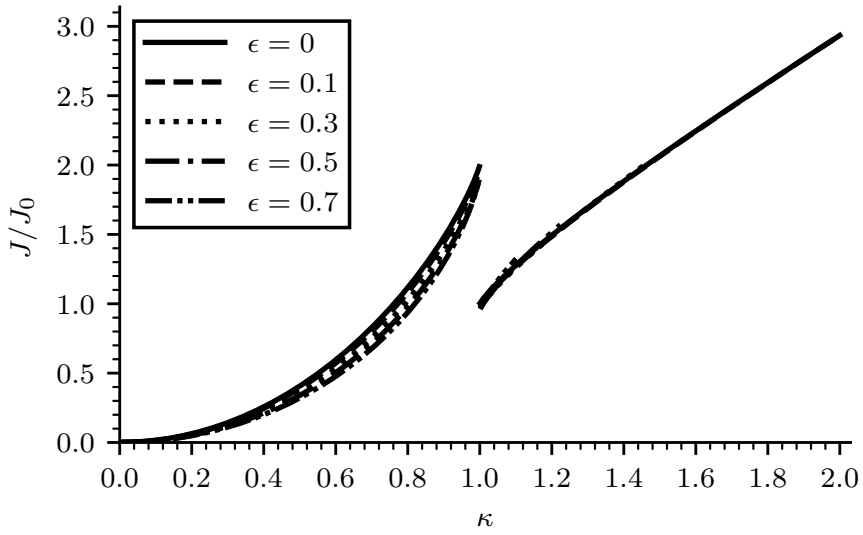

Figure 4.1: Normalized longitudinal invariant J/J_0 versus the trapping parameter κ, where $J_0 = 8m\omega_0 l_0^2/\pi$. The bounce invariant corresponds to $\kappa < 1$ and the transit invariant corresponds to $\kappa > 1$. The upper bound for κ is ϵ dependent, so each case is plotted up until its respective upper bound.

which is similar to the substitution performed for passing particles. Upon doing so, we find that

$$J_t = \frac{4m\omega_0 l_0^2}{2\pi\sqrt{2\epsilon}} \int_0^1 du \frac{\sqrt{\kappa^2 - u}}{\sqrt{u}\sqrt{1-u}\sqrt{\frac{1+\epsilon}{2\epsilon} - u}}. \tag{4.55}$$

Consulting Refs. 60–62, we find that this integral can be written analytically as

$$J_t = \frac{2m\omega_0 l_0^2}{\pi\epsilon} \left(\frac{1 + \epsilon - 2\epsilon\kappa^2}{\kappa\sqrt{1-\epsilon}} \right) \left(\frac{(1+\epsilon)\,\Pi\,(n_t, k_t)}{1 + \epsilon - 2\epsilon\kappa^2} - K\,(k_t) \right). \tag{4.56}$$

Taking a Taylor expansion of J_t about $\epsilon = 0$, we obtain

$$J_t \approx \frac{4m\omega_0 l_0^2}{\pi} \kappa E\left(\kappa^{-1}\right). \tag{4.57}$$

Meanwhile, for large κ transit action is approximately

$$J_t \approx \frac{m\omega_0 l_0^2 \sqrt{2\epsilon}}{\epsilon\,(1+\epsilon)}. \tag{4.58}$$

For both small ϵ and large κ, the expression simplifies to

$$J_t \approx \sqrt{2mE}\,\bar{q} R_0 \approx m\left|v_\parallel\right| \bar{q} R_0. \tag{4.59}$$

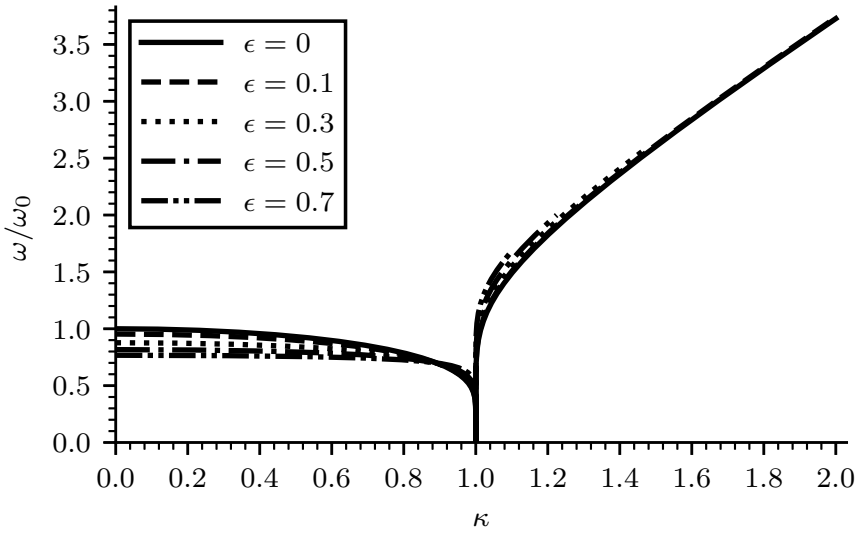

Figure 4.2: Normalized bounce-transit frequency ω/ω_0 versus the trapping parameter κ. The bounce frequency corresponds to $\kappa < 1$ and the transit frequency corresponds to $\kappa > 1$. The upper bound for κ is ϵ dependent, so each case is plotted up until its respective upper bound.

The transit period is

$$T_t = \frac{2}{2\omega_0}\int_0^{\pi} d\theta \sqrt{\frac{1+\epsilon\cos(\theta)}{\kappa^2 - \sin^2(\theta/2)}}. \tag{4.60}$$

Again performing the substitution $\theta = 2\arcsin\left(\sqrt{u}\right)$, we obtain

$$T_t = \frac{\sqrt{2\epsilon}}{\omega_0}\int_0^{1} du \frac{\sqrt{\frac{1+\epsilon}{2\epsilon} - u}}{\sqrt{u}\sqrt{1-u}\sqrt{\kappa^2 - u}}. \tag{4.61}$$

Using Refs. 60–62 again, we find that

$$T_t = \frac{2}{\omega_0}\frac{(1+\epsilon)\,\Pi(n_t, k_t)}{\kappa\sqrt{1-\epsilon}}. \tag{4.62}$$

Therefore, the transit frequency is

$$\omega_t = \frac{2\pi}{T_b} = \pi\omega_0 \frac{\kappa\sqrt{1-\epsilon}}{(1+\epsilon)\,\Pi(n_t, k_t)}. \tag{4.63}$$

Taylor expanding the transit period for small ϵ, we find that

$$T_t \approx \frac{2K\left(\kappa^{-1}\right)}{\omega_0\kappa}. \tag{4.64}$$

Therefore, the transit frequency can be approximated by

$$\omega_t \approx \frac{\pi\omega_0\kappa}{K\left(\kappa^{-1}\right)}. \tag{4.65}$$

In the limit of large κ, we instead have

$$T_t \approx \frac{\pi\sqrt{2\epsilon}}{\omega_0} = \frac{2\pi l_0}{\sqrt{2E/m}}, \tag{4.66}$$

$$\omega_t \approx \sqrt{\frac{2}{\epsilon}}\omega_0 = \frac{\sqrt{2E/m}}{l_0}. \tag{4.67}$$

Finally, for small ϵ and large κ we obtain

$$T_t \approx \frac{2\pi l_0}{\sqrt{2E/m}} \approx \frac{2\pi\bar{q}R_0}{\left|v_\parallel\right|}, \tag{4.68}$$

$$\omega_t \approx \frac{\sqrt{2E/m}}{l_0} \approx \frac{\left|v_\parallel\right|}{\bar{q}R_0}. \tag{4.69}$$

4.3.3 Comparison to the small ϵ limit

Having derived analytic expressions for both the longitudinal invariant and the bounce-transit frequency, we can easily compare the exact expressions to the small ϵ approximation. Fig. 4.1 plots the longitudinal invariant while Fig. 4.2 plots the bounce-transit frequency for various values of ϵ, where $\epsilon = 0$ refers to the small ϵ limit. The $\epsilon = 0.3$ case corresponds to the edge region in many tokamaks; $\epsilon = 0.5, 0.7$ are also plotted to account for low aspect ratio tokamaks. We can see that the small ϵ approximation is suitable even for the extreme case of $\epsilon = 0.7$.

We note that the discontinuity in Fig. 4.1 at $\kappa = 1$ arises from the discrepancy in defining J for the bounce and transit cases. J is calculated with a closed line integral; a trapped particle undergoes a back and forth motion, whereas a passing particle's velocity never changes direction. Thus, there is a factor of 2 difference for the closed line integral depending on whether we consider the particle trapped or passing at $\kappa = 1$. No discontinuity arises in Fig. 4.2 since the frequency at the trapped-passing boundary is 0.

Having characterized the periodicity of the motion, we next develop closed form solutions to the equation of motion and find explicit expressions for $\theta(t)$.

4.4 Closed form solution to the bounce-transit motion

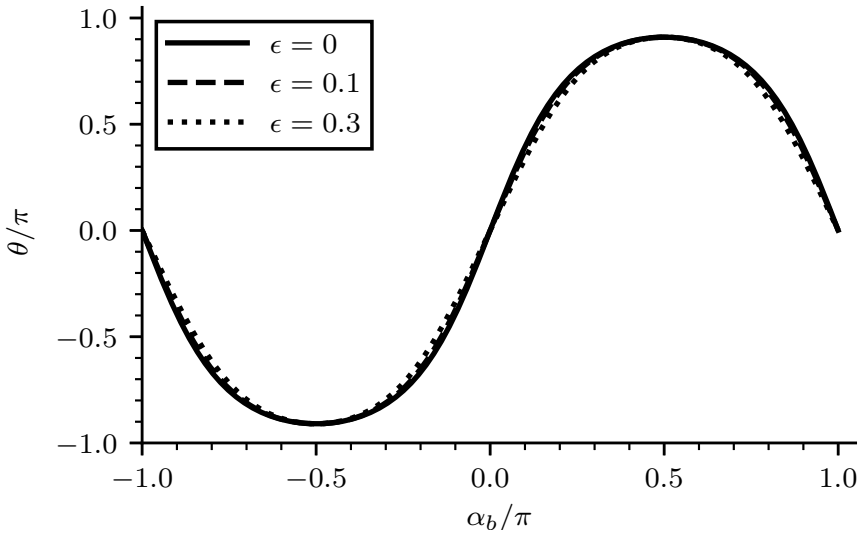

Figure 4.3: Normalized poloidal angle θ/π versus normalized action angle α_b/π for $\kappa = 0.99$. The particle undergoes a nearly sinusoidal motion with little discrepancy between different values of ϵ.

To calculate the closed form solution for the bounce-transit motion we reformulate problem as follows: find $\theta(\alpha)$ where $\alpha(t)$ satisfies

$$\frac{d\alpha}{dt} = \omega. \tag{4.70}$$

The function α is called the action angle, and is linked to the adiabatic invariant associated with the periodic motion. The strategy is to first find $\alpha(\theta)$ and then invert the function to obtain the closed form solution. Using the chain rule, we can write

$$\frac{d\alpha}{dt} = \frac{d\alpha}{d\theta}\dot{\theta} = \omega, \tag{4.71}$$

$$\alpha = \omega \int^{\theta} \frac{d\theta'}{\dot{\theta}'}. \tag{4.72}$$

The specific form of this integral is elliptic and depends on whether we consider trapped or passing particles. In the following calculations, we constrain α such that $-\pi \leq \alpha \leq \pi$ for one whole periodic motion and use the initial condition $\alpha(\theta = 0) = 0$. To invert the elliptic integral, we define

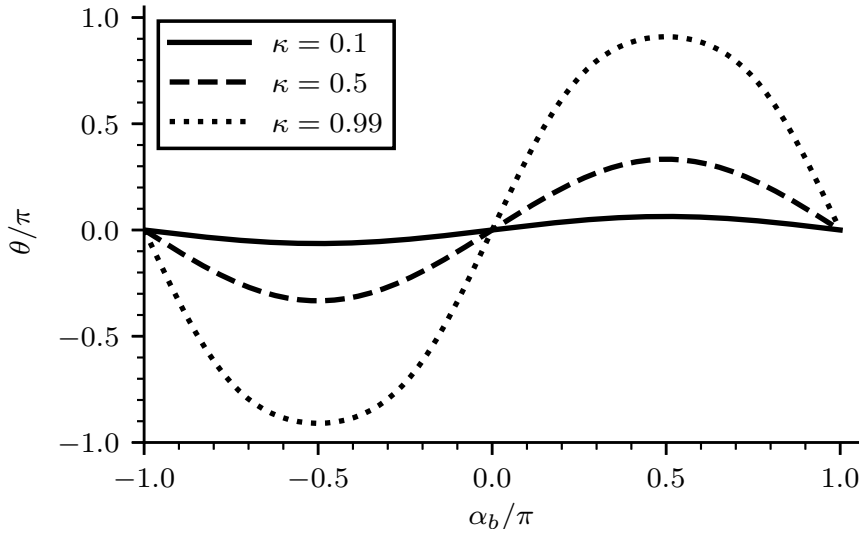

Figure 4.4: Normalized poloidal angle θ/π versus normalized action angle α_b/π for $\epsilon = 0.3$. The amplitude of the motion increases with κ as expected.

a function am_π such that

$$\mathrm{am}_\pi\left(\Pi\left(\varphi, n, k\right), n, k\right) = \varphi. \tag{4.73}$$

This is analogous to the Jacobi amplitude function that is used for elliptic integrals of the first kind. For ease of notation, we drop n and k. We also define analogous trigonometric functions,

$$\mathrm{sn}_\pi\left(u\right) = \sin\left(\mathrm{am}_\pi\left(u\right)\right), \tag{4.74}$$

$$\mathrm{cn}_\pi\left(u\right) = \cos\left(\mathrm{am}_\pi\left(u\right)\right), \tag{4.75}$$

$$\mathrm{dn}_\pi\left(u\right) = \sqrt{1 - k^2\,\mathrm{sn}_\pi\left(u\right)}\left(1 - \alpha^2\,\mathrm{sn}_\pi\left(u\right)\right). \tag{4.76}$$

These functions satisfy the relations

$$\mathrm{sn}_\pi^2(u) + \mathrm{cn}_\pi^2(u) = 1, \tag{4.77}$$

$$\frac{d}{du}\,\mathrm{sn}_\pi(u) = \mathrm{cn}_\pi(u)\,\mathrm{dn}_\pi(u), \tag{4.78}$$

$$\frac{d}{du}\,\mathrm{cn}_\pi(u) = -\,\mathrm{sn}_\pi(u)\,\mathrm{dn}_\pi(u). \tag{4.79}$$

We clarify that these functions do not have the same properties as the typical Jacobi elliptic functions, so care must be taken in using them.

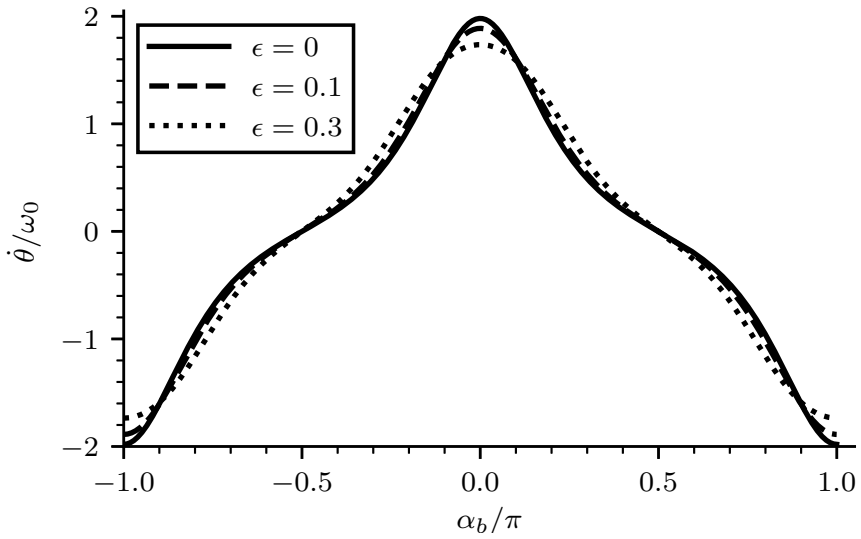

Figure 4.5: Normalized poloidal velocity $\dot{\theta}/\omega_0$ versus normalized action angle α_b/π for $\kappa = 0.99$. It is more clear that the particle's motion deviates from sinusoidal motion.

4.4.1 Trapped particles

For trapped particles, the integral we wish to compute can be simplified to

$$\alpha_b = \frac{\pi}{2} \frac{\int_0^{\theta} d\theta' \sqrt{\frac{1+\epsilon\cos(\theta')}{\kappa^2 - \sin^2(\theta'/2)}}}{\int_0^{\theta_b} d\theta' \sqrt{\frac{1+\epsilon\cos(\theta')}{\kappa^2 - \sin^2(\theta'/2)}}} \tag{4.80}$$

where for convenience we temporarily restrict our domain to $0 \leq \alpha_b \leq \pi/2$ and $0 \leq \theta \leq \theta_b$. We define a new angle φ_b

$$\sin^2(\varphi_b) = \frac{\sin^2(\theta/2)}{\kappa^2} \frac{1 + \epsilon - 2\epsilon\kappa^2}{1 + \epsilon - 2\epsilon\kappa^2 \sin^2(\theta/2)} \tag{4.81}$$

and obtain

$$\alpha_b = \frac{\pi}{2} \frac{\Pi\left(\varphi_b, n_b, k_b\right)}{\Pi\left(n_b, k_b\right)}. \tag{4.82}$$

As a sanity check, we note that $\varphi_b = \pi/2$ corresponds to $\theta = \theta_b$, in which case the numerator (having become a complete integral) cancels with the denominator. Using our previously defined inverse functions, we find that

$$\sin^2(\varphi_b) = \mathrm{sn}_\pi^2 \left(\frac{2\alpha_b}{\pi} \Pi\left(n_b, k_b\right), n_b, k_b \right). \tag{4.83}$$

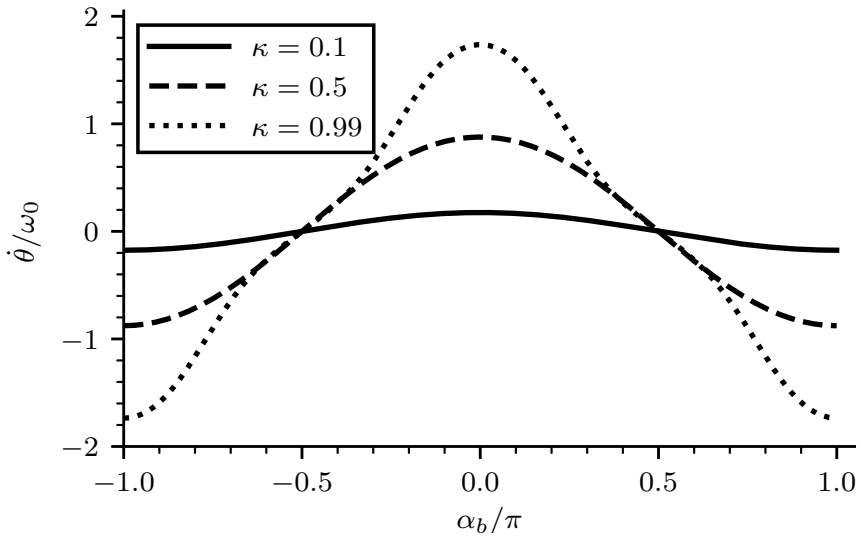

Figure 4.6: Normalized poloidal velocity $\dot{\theta}/\omega_0$ versus normalized action angle α_b/π for $\epsilon = 0.3$. The amplitude of the motion increases with κ as expected.

We abbreviate the right-hand side as $\mathrm{sn}_\pi^2\left(\frac{2\alpha_b}{\pi}\Pi\right)$. We can then solve for θ,

$$\sin(\theta/2) = \kappa\ \mathrm{sn}_\pi\left(\frac{2\alpha_b}{\pi}\Pi\right)\sqrt{\frac{1+\epsilon}{1+\epsilon-2\epsilon\kappa^2\ \mathrm{cn}_\pi^2\left(\frac{2\alpha_b}{\pi}\Pi\right)}}, \tag{4.84}$$

$$\cos(\theta/2) = \sqrt{\frac{1+\epsilon-2\epsilon\kappa^2-\kappa^2\,(1-\epsilon)\ \mathrm{sn}_\pi^2\left(\frac{2\alpha_b}{\pi}\Pi\right)}{1+\epsilon-2\epsilon\kappa^2\ \mathrm{cn}_\pi^2\left(\frac{2\alpha_b}{\pi}\Pi\right)}}. \tag{4.85}$$

These equations are now valid for all α_b and by extension valid for all time. Taking the time derivative, we find that

$$\dot{\theta} = \frac{2\kappa\omega_0\ \mathrm{cn}_\pi\left(\frac{2\alpha_b}{\pi}\Pi\right)}{\sqrt{1+\epsilon}}. \tag{4.86}$$

Thus, we have closed form expressions for θ and $\dot{\theta}$ as functions of $\alpha_b(t)$.

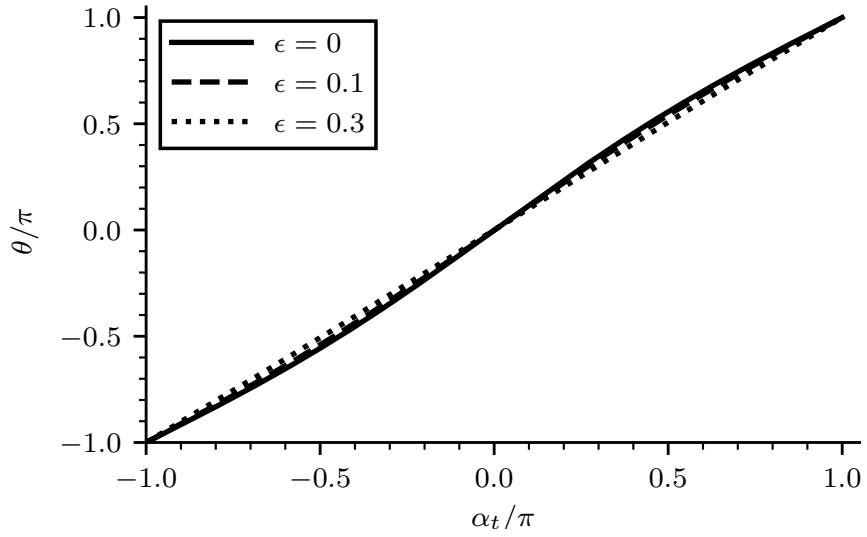

Figure 4.7: Normalized poloidal angle θ/π versus normalized action angle α_t/π for $\kappa = 1.4$. In the extreme passing limit the particle has a nearly constant poloidal velocity, with very little deviation between different values of ϵ.

In the small ϵ limit, we can approximate these expressions as

$$\sin(\theta/2) \approx \kappa \,\mathrm{sn}\left(\frac{2\alpha_b}{\pi}K(\kappa), \kappa\right), \tag{4.87}$$

$$\cos(\theta/2) \approx \kappa \,\mathrm{cn}\left(\frac{2\alpha_b}{\pi}K(\kappa), \kappa\right), \tag{4.88}$$

$$\dot{\theta} \approx 2\kappa\omega_0 \,\mathrm{cn}\left(\frac{2\alpha_b}{\pi}K(\kappa), \kappa\right), \tag{4.89}$$

where sn and cn are the usual Jacobi elliptic functions. We plot θ and $\dot{\theta}$ for trapped particles in Figs. 4.3–4.6.

4.4.2 Passing particles

For passing particles, we instead calculate

$$\alpha_t = \pi \frac{\int_0^\theta d\theta' \sqrt{\frac{1+\epsilon\cos(\theta')}{\kappa^2 - \sin^2(\theta'/2)}}}{\int_0^\pi d\theta' \sqrt{\frac{1+\epsilon\cos(\theta')}{\kappa^2 - \sin^2(\theta'/2)}}}. \tag{4.90}$$

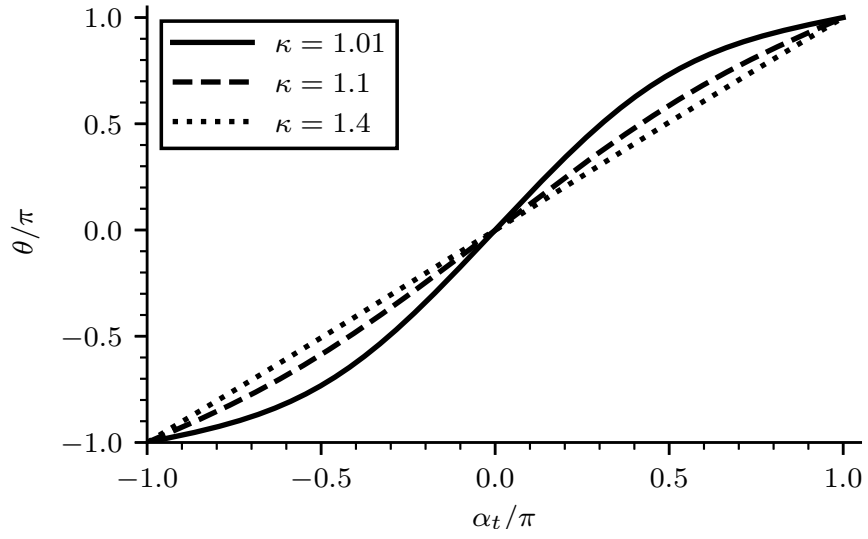

Figure 4.8: Normalized poloidal angle θ/π versus normalized action angle α_t/π for $\epsilon = 0.3$. As κ increases the motion becomes straighter and less sinusoidal.

Similar to φ_b, we define a new variable φ_t

$$\sin^2(\varphi_t) = \sin^2(\theta/2)\frac{1-\epsilon}{1+\epsilon-2\epsilon\sin^2(\theta/2)} \tag{4.91}$$

and obtain

$$\alpha_t = \pi\frac{\Pi\left(\varphi_t, n_t, k_t\right)}{\Pi\left(n_t, k_t\right)}. \tag{4.92}$$

Note that $\varphi_t = \pi/2$ corresponds to $\theta = \pi$. Performing the inversion, we find that

$$\sin^2(\varphi_t) = \mathrm{sn}_\pi^2\left(\frac{\alpha_t}{\pi}\Pi\left(n_t, k_t\right), n_t, k_t\right). \tag{4.93}$$

Abbreviating the right-hand side as $\mathrm{sn}_\pi^2\left(\frac{\alpha_t}{\pi}\Pi\right)$, we can then solve for θ,

$$\sin(\theta/2) = \mathrm{sn}_\pi\left(\frac{\alpha_t}{\pi}\Pi\right)\sqrt{\frac{1+\epsilon}{1+\epsilon-2\epsilon\,\mathrm{cn}_\pi^2\left(\frac{\alpha_t}{\pi}\Pi\right)}}, \tag{4.94}$$

$$\cos(\theta/2) = \mathrm{cn}_\pi\left(\frac{\alpha_t}{\pi}\Pi\right)\sqrt{\frac{1-\epsilon}{1+\epsilon-2\epsilon\,\mathrm{cn}_\pi^2\left(\frac{\alpha_t}{\pi}\Pi\right)}}. \tag{4.95}$$

These equations are valid for all α_t and thus all time.

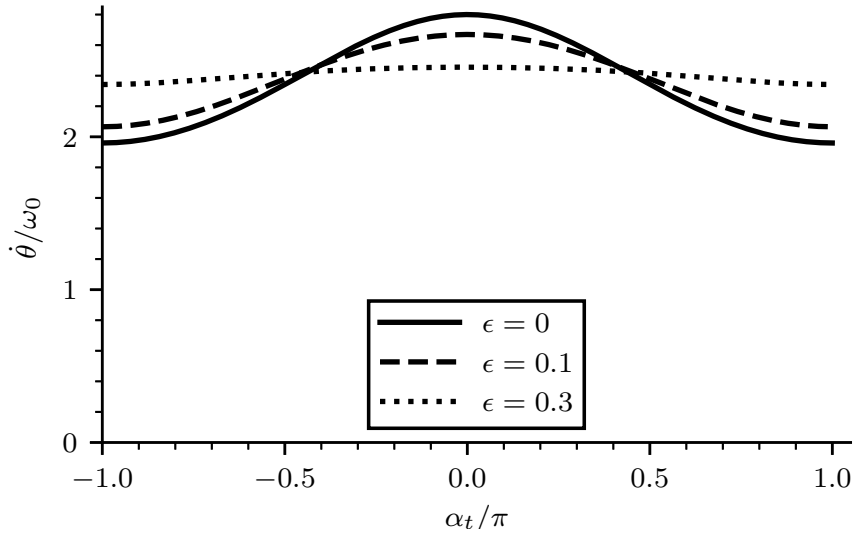

Figure 4.9: Normalized poloidal velocity $\dot{\theta}/\omega_0$ versus normalized action angle α_t/π for $\kappa = 1.4$. The case where $\kappa = 1.4$ is very close to the maximum allowed trapping parameter for $\epsilon = 0.3$, hence why its plot is the straightest.

We can also calculate $\dot{\theta}$ for passing particles. However, we need to take into account the fact that the parallel velocity can either be positive or negative and never changes sign. To accommodate for the potential sign difference we define $\epsilon_\parallel$ to be the sign of $v_\parallel$:

$$v_\parallel = \epsilon_\parallel \left| v_\parallel \right|. \tag{4.96}$$

Then, since we previously defined ω_t to be strictly positive, we need to write

$$\frac{d\alpha_t}{dt} = \epsilon_\parallel \omega_t. \tag{4.97}$$

We can then proceed to safely calculating $\dot{\theta}$ by taking a time derivative and simplifying,

$$\dot{\theta} = \frac{2\kappa\omega_0\epsilon_\parallel \sqrt{1 - \frac{1+\epsilon-2\epsilon\kappa^2}{\kappa^2(1-\epsilon)}\, \mathrm{sn}_\pi^2\left(\frac{\alpha_t}{\pi}\Pi\right)}}{\sqrt{1+\epsilon}}. \tag{4.98}$$

We have now obtained closed form solutions for θ and $\dot{\theta}$ that are valid for all time.

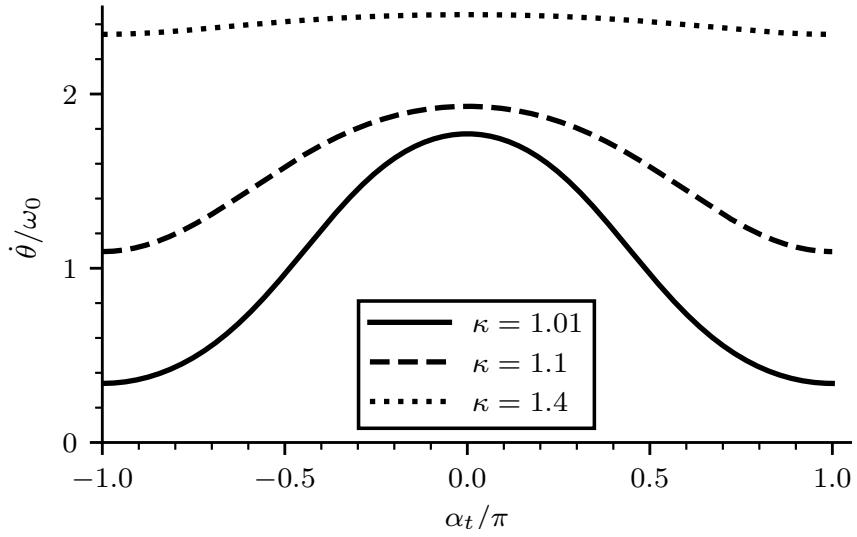

Figure 4.10: Normalized poloidal velocity $\dot{\theta}/\omega_0$ versus normalized action angle α_t/π for $\epsilon = 0.3$. The maximum velocity increases for larger κ and in turn the variation of the velocity decreases.

In the small ϵ limit, these expressions are approximately

$$\sin(\theta/2) \approx \operatorname{sn}\left(\frac{\alpha_t}{\pi}K\left(\kappa^{-1}\right), \kappa^{-1}\right), \tag{4.99}$$

$$\cos(\theta/2) \approx \operatorname{cn}\left(\frac{\alpha_t}{\pi}K\left(\kappa^{-1}\right), \kappa^{-1}\right), \tag{4.100}$$

$$\dot{\theta} \approx 2\kappa\omega_0\epsilon_{\parallel} \operatorname{dn}\left(\frac{\alpha_t}{\pi}K\left(\kappa^{-1}\right), \kappa^{-1}\right). \tag{4.101}$$

We then plot θ and $\dot{\theta}$ for passing particles in Figs. 4.7–4.10.

4.4.3 Phase space portrait

Having calculated the closed form solutions for the bounce-transit motion, we can easily plot the phase-space portrait as shown in Fig. 4.11 for $\epsilon = 0.3$ and Fig. 4.12 for $\epsilon = 0$. The bounce orbits reside in the interior of the separatrix where the particle follows a closed loop. On the exterior of the separatrix, the particle instead continues its motion such that $\dot{\theta}$ never changes sign. The phase-space portrait for the case of $\epsilon = 0$ is mathematically identical to that of a simple pendulum. While the portrait for $\epsilon = 0.3$ looks qualitatively similar to a simple pendulum's, there is an important difference. In the case of a simple pendulum, the phase portrait is unbounded in the

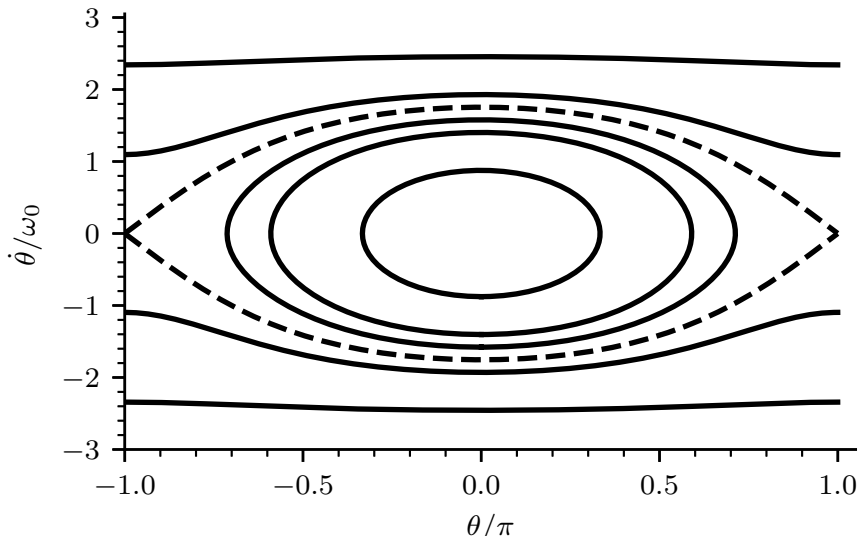

Figure 4.11: Phase space plot of $\dot{\theta}/\omega_0$ versus θ/π for $\epsilon = 0.3$. The separatrix represented by the dotted curve corresponds to the trapped-passing boundary at $\kappa = 1$.

$\dot{\theta}$ direction; one can find an orbit corresponding to any value of $\dot{\theta}_{\max}/\omega_{0,\text{pend.}}$. For transit orbits in a concentric circular geometry, the phase-space orbit curves are bounded by the curve corresponding to $\kappa = \sqrt{(1+\epsilon)/(2\epsilon)}$. We can see in Fig. 4.11 that the outermost curves corresponding to $\kappa = 1.4$ are very straight and already nearly bound any interior curves. In contrast, for the small ϵ limit κ is unbounded from above, so a phase-space orbit curve can found for any value of $\dot{\theta}_{\max}/\omega_0$. This can be seen in Fig. 4.12 where the outermost curves are not straight; indeed, they never become perfectly straight, regardless of what value κ takes.

This completes our discussion of the lowest-order guiding center orbit. Without assuming anything about ϵ in a concentric circular geometry, we have derived analytical expressions for the bounce-transit frequencies and closed form solutions to the bounce-transit equation of motion. We then proceed to the next order in the gyroradius by considering deviations from the field line.

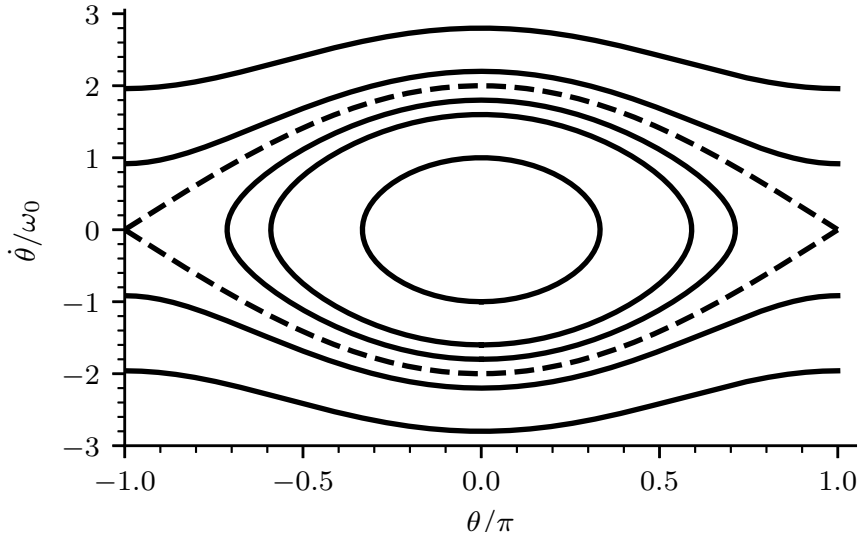

Figure 4.12: Phase space plot of $\dot{\theta}/\omega_0$ versus θ/π for $\epsilon = 0$. The separatrix represented by the dotted curve corresponds to the trapped-passing boundary at $\kappa = 1$.

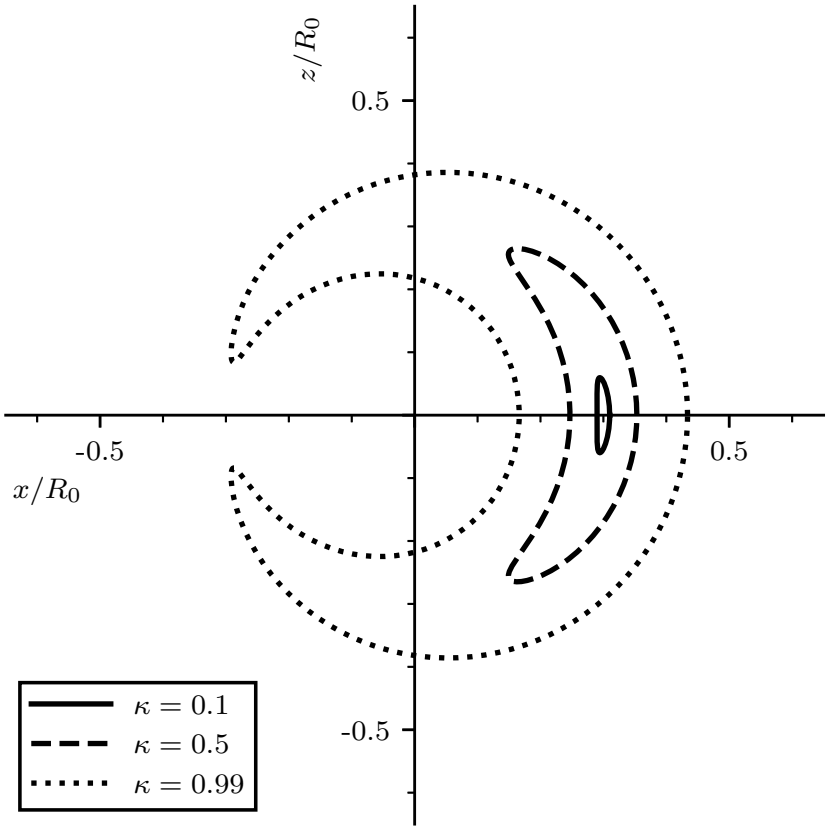

Figure 4.13: Banana orbits in the normalized poloidal $(x/R_0, z/R_0)$ plane for $\epsilon = 0.3, \delta_b/R_0 = 0.05$, using ψ_0 as the reference magnetic flux surface. The origin corresponds to the magnetic axis.

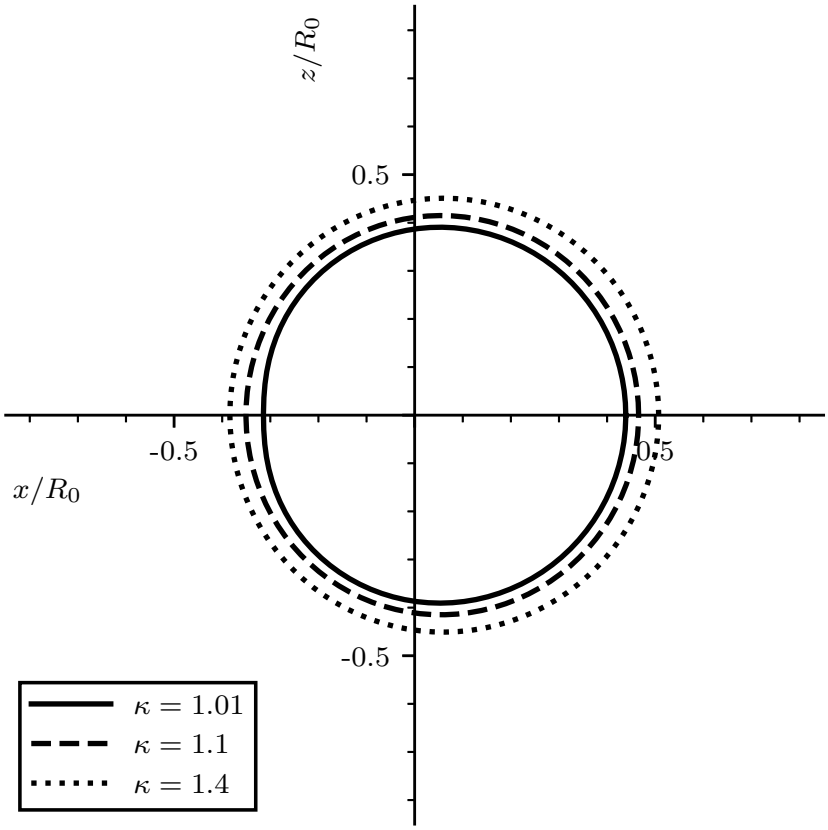

Figure 4.14: Transit orbits in the normalized poloidal $(x/R_0, z/R_0)$ plane for $\epsilon = 0.3, \delta_b/R_0 = 0.05$, using ψ_0 as the reference magnetic flux surface. The origin corresponds to the magnetic axis.

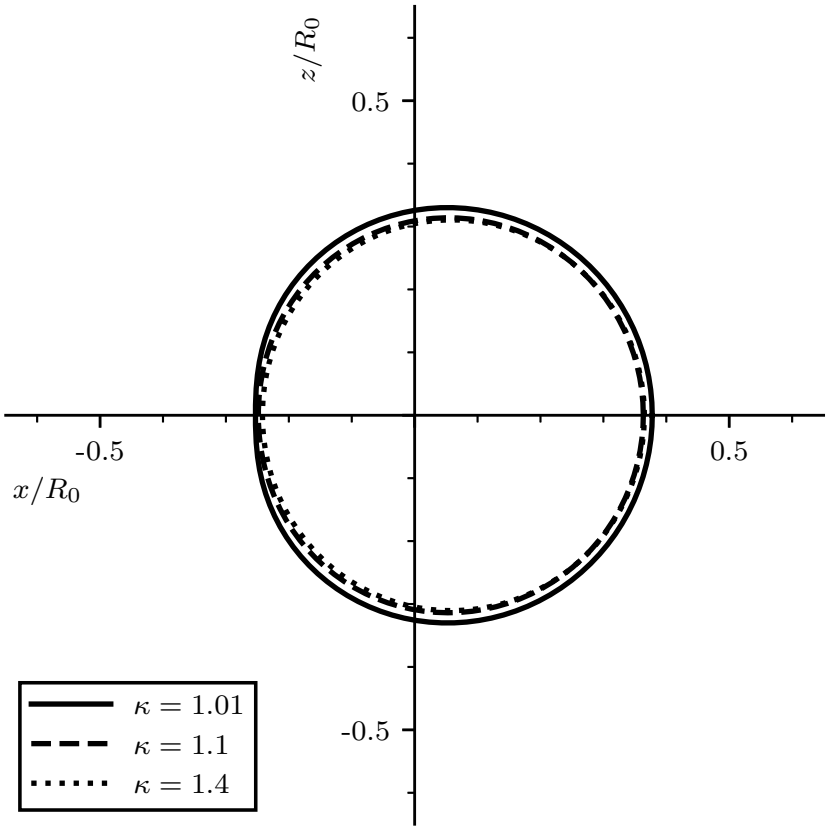

Figure 4.15: Transit orbits in the normalized poloidal $(x/R_0, z/R_0)$ plane for $\epsilon = 0.3, \delta_b/R_0 = 0.05$, using $\langle\psi\rangle$ as the reference magnetic flux surface. The origin corresponds to the magnetic axis. As expected, expanding about the time averaged flux surface results in a smaller deviation.

4.5 Banana orbits

First, we consider the radial deviation from the lowest-order guiding center orbit. To calculate the radial deviation, we expand about a reference magnetic surface $\psi = \psi_0$, noting that $\psi = \psi(r)$. We define a reference radial position r_0 such that

$$\psi_0 = \psi(r_0), \tag{4.102}$$

$$P_\phi = -e\psi + \frac{mB_0R_0v_\parallel}{B} = -e\psi_0, \tag{4.103}$$

where P_ϕ is the canonical toroidal momentum. Performing an expansion about r_0, we find that

$$r \approx r_0 + \left.\frac{dr}{d\psi}\right|_{\psi_0}(\psi - \psi_0) = r_0 + \frac{\bar{q}R_0}{r_0}\frac{mv_\parallel}{eB}. \tag{4.104}$$

We can simplify by writing $v_\parallel$ and B in terms of θ and $\dot{\theta}$, which in turn are functions of the action angle α. For trapped particles, we obtain

$$r \approx r_0 + 2\frac{\bar{q}^2R_0^2}{r_0}\frac{m\omega_0}{eB_0}\frac{\kappa\sqrt{1+\epsilon}\left(1+\epsilon-2\epsilon\kappa^2\right)\ \mathrm{cn}_\pi\left(\frac{2\alpha_b}{\pi}\Pi\right)}{1+\epsilon-2\epsilon\kappa^2\ \mathrm{cn}_\pi^2\left(\frac{2\alpha_b}{\pi}\Pi\right)}. \tag{4.105}$$

We isolate one of the factors and find that

$$\frac{\bar{q}^2R_0^2}{r_0}\frac{m\omega_0}{eB_0} = \frac{\bar{q}}{\Omega_c\sqrt{\epsilon}}\sqrt{\frac{E}{m}}, \tag{4.106}$$

where $\Omega_c = eB^0/m$ is the characteristic cyclotron frequency. We then write

$$\frac{\bar{q}}{\Omega_c\sqrt{\epsilon}}\sqrt{\frac{E}{m}} = \frac{\bar{q}\rho_c}{\sqrt{2\epsilon}}\sqrt{\frac{E}{\mu B^0}} = \frac{\delta_b}{\sqrt{1+\epsilon-2\epsilon\kappa^2}}, \tag{4.107}$$

where we have used the cyclotron radius ρ_c and the banana width

$$\delta_b = \frac{\bar{q}\rho_c}{\sqrt{2\epsilon}}. \tag{4.108}$$

Therefore, for trapped particles the expression simplifies to

$$r \approx r_0 + 2\delta_b\kappa\frac{\sqrt{1+\epsilon}\sqrt{1+\epsilon-2\epsilon\kappa^2}\ \mathrm{cn}_\pi\left(\frac{2\alpha_b}{\pi}\Pi\right)}{1+\epsilon-2\epsilon\kappa^2\ \mathrm{cn}_\pi^2\left(\frac{2\alpha_b}{\pi}\Pi\right)}. \tag{4.109}$$

The banana orbits are plotted in the poloidal plane in Fig. 4.13, where the characteristic banana shape is readily apparent.

For passing particles, we instead obtain the expression

$$r \approx r_0 + 2\epsilon_\parallel \delta_b \kappa \sqrt{\frac{1-\epsilon^2}{1+\epsilon-2\epsilon\kappa^2}} \frac{\sqrt{1-\epsilon-\left(1+\epsilon-2\epsilon\kappa^2\right)\ \mathrm{sn}_\pi^2\left(\frac{\alpha_t}{\pi}\Pi\right)}}{1+\epsilon-2\epsilon\ \mathrm{cn}_\pi^2\left(\frac{\alpha_t}{\pi}\Pi\right)}. \tag{4.110}$$

However, the radial deviation from ψ_0 can be rather large for passing particles given a high enough velocity. If we instead expand about the time average of ψ, we would obtain an expression with a lower deviation. It is easily shown that in our case

$$\langle\psi\rangle = \psi_0 + \frac{mR_0^2\bar{q}\epsilon_\parallel\omega_t}{e}. \tag{4.111}$$

Defining $\langle r\rangle$ such that $\psi(\langle r\rangle) = \langle\psi\rangle$, we find that the equation for the radial deviation is modified in the following way:

$$\begin{aligned} r \approx \langle r\rangle + 2\epsilon_\parallel \delta_b \kappa \sqrt{\frac{1-\epsilon^2}{1+\epsilon-2\epsilon\kappa^2}} \frac{\sqrt{1-\epsilon-\left(1+\epsilon-2\epsilon\kappa^2\right)\ \mathrm{sn}_\pi^2\left(\frac{\alpha_t}{\pi}\Pi\right)}}{1+\epsilon-2\epsilon\ \mathrm{cn}_\pi^2\left(\frac{\alpha_t}{\pi}\Pi\right)} \\ - \frac{\pi\delta_b\epsilon_\parallel\kappa\sqrt{1-\epsilon}}{(1+\epsilon)\,\Pi\left(n_t,k_t\right)\sqrt{1+\epsilon-2\epsilon\kappa^2}}. \end{aligned} \tag{4.112}$$

We can compare the two methods by plotting the transit orbits in the poloidal plane as shown in Figs. 4.14 and 4.15. As predicted, expanding from the time averaged flux surface corresponds to less deviation from the flux surface.

Having studied the radial excursion from the magnetic field line, we now calculate the change in the toroidal motion after accounting for magnetic drifts and the conservation of canonical toroidal momentum.

4.6 Toroidal drift frequency

Magnetic drifts and the conservation of canonical toroidal momentum alter the toroidal motion so that it no longer follows the magnetic field line. Rather, the guiding center drifts toroidally

through the magnetic field lines lying on a flux surface. The toroidal drift frequency characterizes this motion and can be calculated by time averaging the equation of motion corresponding to the toroidal direction.

As in the case of banana orbits, we define a reference magnetic surface $\psi = \psi_0$ and Taylor expand around it; because the radial excursion is proportional to the gyroradius, this is equivalent to a gyroradius expansion. We note that the exactly conserved canonical toroidal momentum is again

$$P_\phi = -e\psi + \frac{mB_0R_0v_\parallel}{B} = -e\psi_0. \tag{4.113}$$

We then find that

$$\psi = \psi_0 + \frac{mB_0R_0v_\parallel}{eB} = \psi_0 + \psi_1. \tag{4.114}$$

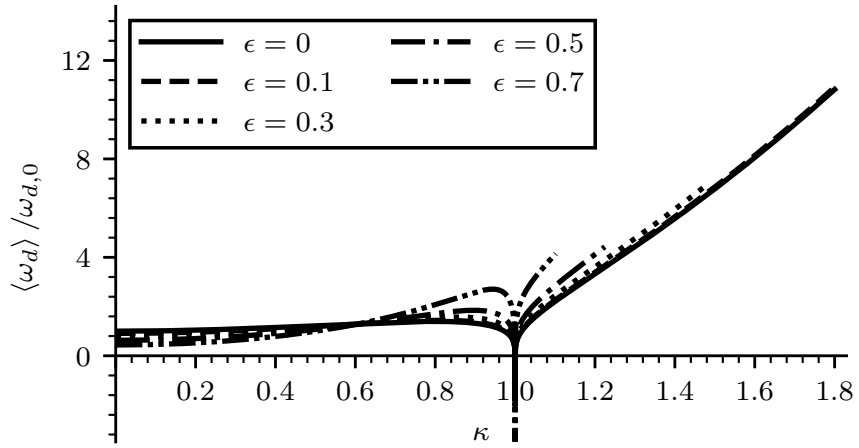

Figure 4.16: Normalized toroidal drift frequency $\langle\omega_d\rangle / \omega_{d,0}$ versus the trapping parameter κ for $\hat{s} = 1$, $\bar{q} = 2$. The trapped-passing boundary can easily be seen at $\kappa = 1$, around which the toroidal drift frequency changes sign. Discrepancies from the small ϵ limit are large only for $\epsilon = 0.7$

The guiding center equations of motion without an electric field in a static magnetic field are

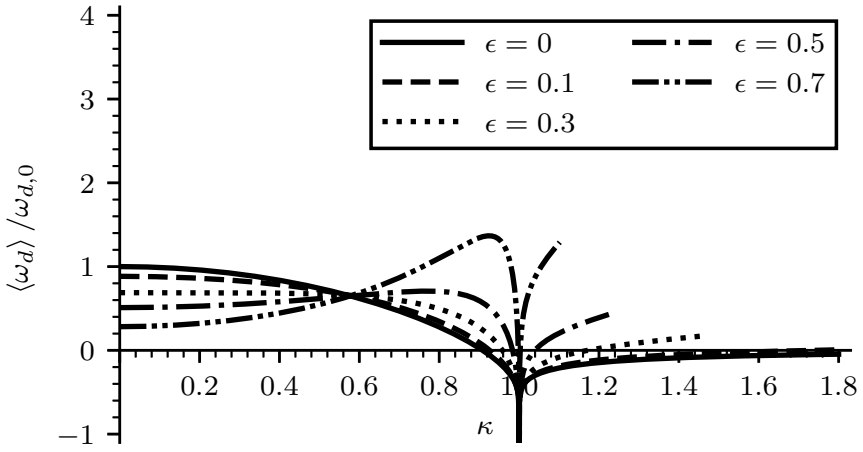

Figure 4.17: Normalized toroidal drift frequency $\langle \omega_d \rangle / \omega_{d,0}$ versus the trapping parameter κ for $\hat{s} = 0$, $\bar{q} = 2$. The trapped-passing boundary can easily be seen at $\kappa = 1$, around which the toroidal drift frequency changes sign. Discrepancies from the small ϵ limit become large for $\epsilon = 0.5, 0.7$.

given by

$$\frac{dx}{dt} = \left(v_{\parallel} \hat{\mathbf{b}} + \mathbf{v}_D \right) \cdot \nabla x, \tag{4.115}$$

$$\frac{dv_{\parallel}}{dt} = -\frac{\mu}{m} \nabla B, \tag{4.116}$$

where $\mathbf{v}_D$ is the magnetic drift. We apply these equations of motion to the coordinates ψ, χ, ϕ and expand:

$$\frac{d\psi}{dt} \approx \mathbf{v}_D \cdot \nabla \psi |_{\psi_0}, \tag{4.117}$$

$$\frac{d\chi}{dt} \approx \Omega_\chi \big|_{\psi_0} + \left. \frac{d\Omega_\chi}{d\psi} \right|_{\psi_0} \psi_1 + \mathbf{v}_D \cdot \nabla \chi |_{\psi_0}, \tag{4.118}$$

$$\frac{d\phi}{dt} \approx q\Omega_\chi \big|_{\psi_0} + \left. \frac{d}{d\psi} \left(q\Omega_\chi \right) \right|_{\psi_0} \psi_1 + \mathbf{v}_D \cdot \nabla \phi |_{\psi_0}, \tag{4.119}$$

where the lowest-order magnetic drift is the sum of the classical curvature and grad-B drifts,

$$\mathbf{v}_D = \frac{\hat{\mathbf{b}}}{eB} \times \left(m v_{\parallel}^2 \mathbf{k} + \mu \nabla B \right). \tag{4.120}$$

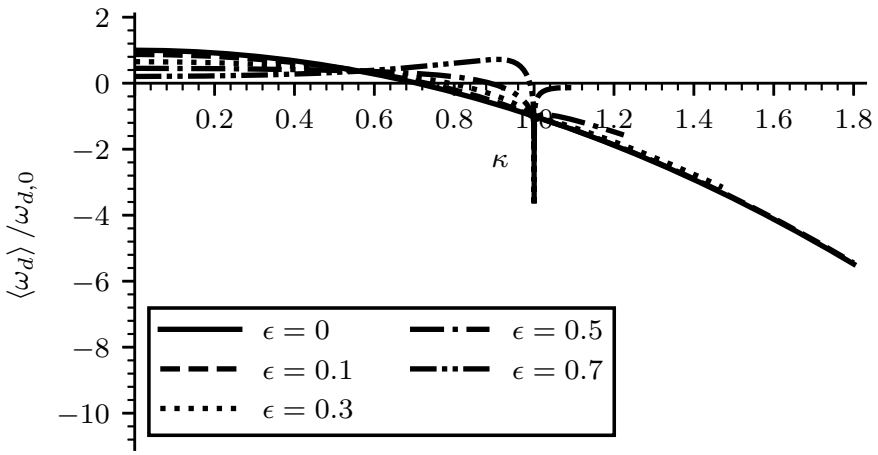

Figure 4.18: Normalized toroidal drift frequency $\langle\omega_d\rangle/\omega_{d,0}$ versus the trapping parameter κ for $\hat{s} = -0.5$, $\bar{q} = 2$. For small ϵ, the toroidal drift frequency undergoes sign reversal relatively far from the trapped-passing boundary. The behavior near the trapped-passing boundary at $\kappa = 1$ noticeably differs from the small ϵ limit for $\epsilon = 0.7$.

Here, e is the charge of the particle and $\mathbf{k}$ is the curvature vector defined such that

$$\hat{\mathbf{b}} \times \mathbf{k} = \nabla \times \hat{\mathbf{b}} - \left(\hat{\mathbf{b}} \cdot \nabla \times \hat{\mathbf{b}}\right) \hat{\mathbf{b}}. \tag{4.121}$$

We have also introduced Ω_χ,

$$\Omega_\chi = v_\parallel \hat{\mathbf{b}} \cdot \nabla\chi = \frac{v_\parallel c}{qR_0\left(1 + \epsilon\cos(\theta)\right)}, \tag{4.122}$$

where for convenience we have defined the function

$$c(r) = \frac{1}{\sqrt{1 + \epsilon^2/\bar{q}^2}}. \tag{4.123}$$

Using these equations of motion, we find that

$$\begin{aligned}\dot{\phi} &= \frac{dq}{d\psi}\Omega_\chi\bigg|_{\psi_0} \psi_1 + \mathbf{v}_D \cdot \nabla\phi|_{\psi_0} - q\mathbf{v}_D \cdot \nabla\chi|_{\psi_0} + q\frac{d\chi}{dt} \\ &= \omega_d + q\frac{d\chi}{dt},\end{aligned} \tag{4.124}$$

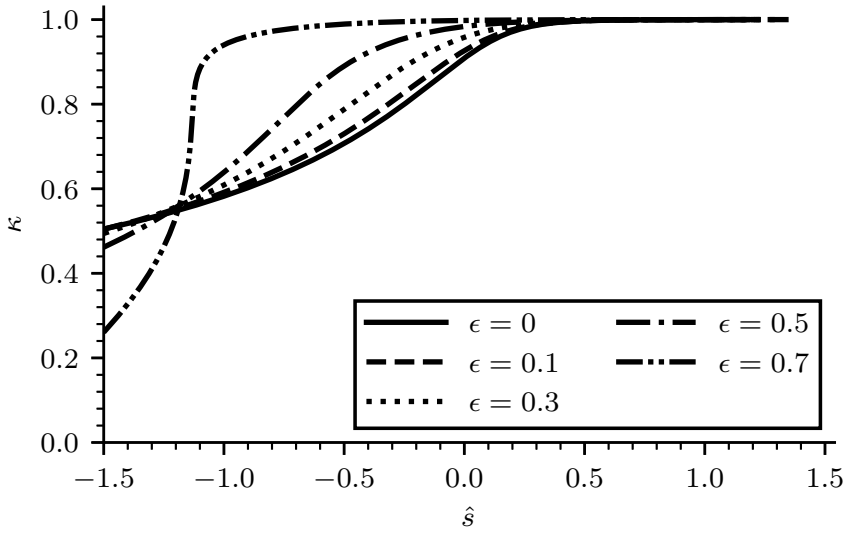

Figure 4.19: The trapping parameter κ at which the toroidal drift frequency changes sign versus the magnetic shear $\hat{s}$ for $\bar{q} = 2$. A decrease in magnetic shear corresponds to drift reversal occurring at a lower value of κ. Discrepancies from the small ϵ limit are large for $\epsilon = 0.5, 0.7$.

where ω_d is the term that corresponds to the deviation from the magnetic field line.

To proceed with the calculation, we define a time average using the field-line-following orbit as reference. For trapped particles, the time average of a function $F(\epsilon_\parallel, \chi)$, also called the bounce average, is

$$\langle F \rangle = \frac{\omega_b}{2\pi} \int_{-\chi_b}^{\chi_b} \frac{d\chi}{\left|\Omega_\chi\right|} \left(F(\epsilon_\parallel, \chi) + F(-\epsilon_\parallel, \chi) \right). \tag{4.125}$$

For passing particles, we instead have the transit average

$$\langle F \rangle = \frac{\omega_t}{2\pi} \int_{-\pi}^{\pi} \frac{d\chi}{\left|\Omega_\chi\right|} F(\epsilon_\parallel, \chi). \tag{4.126}$$

To simplify our calculations we perform a change of variables from χ to θ,

$$\int_{-\chi_b}^{\chi_b} \frac{d\chi}{\left|\Omega_\chi\right|} = \int_{-\theta_b}^{\theta_b} d\theta \frac{\bar{q} R_0}{c \left|v_\parallel\right|}. \tag{4.127}$$

We then find that for trapped particles

$$\left\langle \dot{\phi} \right\rangle = \langle \omega_d \rangle \tag{4.128}$$

and for passing particles

$$\left\langle \dot{\phi} \right\rangle = \langle \omega_d \rangle + q\epsilon_{\|}\omega_t, \tag{4.129}$$

where ω_t is the transit frequency. The additional term for passing particles accounts for the change in the toroidal coordinate after a 2π change in the poloidal angle. Thus, it is associated with the lowest-order transit motion examined in Secs. 4.3 and 4.4.

The explicit expression for ω_d is

$$\omega_d = \frac{m\bar{q}v_{\|}^2}{eB_0r^2}\left(c^2\hat{s} + \frac{1}{2}I_1\right) + \frac{E\bar{q}}{eB_0r^2}I_2. \tag{4.130}$$

We have defined the magnetic shears,

$$s = \frac{r}{\bar{q}}\frac{d\bar{q}}{dr}, \tag{4.131}$$

$$\hat{s} = \frac{r}{q}\frac{dq}{dr} = \left(s + \frac{\epsilon^2}{1-\epsilon^2}\right), \tag{4.132}$$

and the functions $I_1(\theta)$, $I_2(\theta)$

$$I_1 = 1 - (s-1)(1-c^2) + \frac{1-2c^2}{1+\epsilon\cos(\theta)} + \frac{c^2\epsilon^2\sin^2(\theta)}{\left(1-\epsilon^2\right)\left(1+\epsilon\cos(\theta)^2\right)}, \tag{4.133}$$

$$I_2 = (s-1)\left(1-c^2\right) + 1 - \frac{1}{1+\epsilon\cos(\theta)} + \frac{c^2\epsilon^2\sin^2(\theta)}{\left(1-\epsilon^2\right)\left(1+\epsilon\cos(\theta)^2\right)}. \tag{4.134}$$

We can then perform a time average, noting that

$$v_{\|}^2 = \frac{4E\epsilon}{m}\frac{\kappa^2 - \sin^2(\theta/2)}{1+\epsilon\cos(\theta)}. \tag{4.135}$$

Using the elliptic integrals tabulated in the appendix, we obtain for trapped particles

$$\begin{aligned}\langle \omega_d \rangle = \frac{E\bar{q}}{eB_0r^2F_1}\Bigg[&\left((s-1)\left(1-c^2\right)+1\right)F_1 - F_2 + \frac{c^2\epsilon^2}{1-\epsilon^2}F_3 \\ &+2\epsilon\left(2\hat{s}+1-(s-1)\left(1-c^2\right)\right)F_4 \\ &+2\epsilon\left(1-2c^2\right)F_5 + \frac{2c^2\epsilon^3}{1-\epsilon^2}F_6\Bigg].\end{aligned} \tag{4.136}$$

For passing particles, we instead have

$$\langle \omega_d \rangle = \frac{E\bar{q}}{eB_0 r^2 G_1}\left[\left((s-1)\left(1-c^2\right)+1\right)G_1 - G_2 + \frac{c^2\epsilon^2}{1-\epsilon^2}G_3 \right. \\ +2\epsilon\left(2\hat{s}+1-(s-1)\left(1-c^2\right)\right)G_4 \\ \left. +2\epsilon\left(1-2c^2\right)G_5 + \frac{2c^2\epsilon^3}{1-\epsilon^2}G_6\right]. \tag{4.137}$$

We now take the limit that ϵ is small. In this limit,

$$s \approx \hat{s}, \tag{4.138}$$

$$c \approx 1, \tag{4.139}$$

and the elliptic integrals simplify as outlined in the appendix. We also see that the characteristic drift frequency is

$$\omega_{d,0} = \frac{E\bar{q}}{eB_0 r R_0} \approx \frac{\omega_0^2 \bar{q}^3}{\Omega_c \epsilon}. \tag{4.140}$$

For trapped particles, we then obtain

$$\langle \omega_d \rangle \approx \frac{\omega_{d,0}\left(\left(2+4\hat{s}\right)E(\kappa) - \left(1+4\hat{s}\left(1-\kappa^2\right)\right)K(\kappa)\right)}{K(\kappa)}, \tag{4.141}$$

which is the standard result. For passing particles, the drift frequency is approximately

$$\langle \omega_d \rangle \approx \frac{\omega_{d,0}\left(2\kappa^2\left(1+2\hat{s}\right)E\left(\kappa^{-1}\right) - \left(2\kappa^2-1\right)K\left(\kappa^{-1}\right)\right)}{K\left(\kappa^{-1}\right)}. \tag{4.142}$$

Figs. 4.16-4.18 compare the toroidal drift frequency for various values of ϵ and $\hat{s}$. We note that we only plot up to each individual case's respective upper bound for κ shown in Eq. (4.22). We see that the exact formula is well approximated by the small ϵ limit for $\epsilon \lesssim 0.3$. However, finite inverse aspect ratio effects become important for larger values of ϵ. Departure from the small ϵ limit is more noticeable for low magnetic shear in Fig. 4.17 and negative magnetic shear in Fig. 4.18. One can show that the magnetic drift at the trapped-passing boundary is

$$\langle \omega_d \rangle (\kappa = 1) = \omega_{d,0}\left(\frac{(s-1)\left(1-c^2\right)}{\epsilon} - \frac{1}{1-\epsilon}\right). \tag{4.143}$$

The ϵ dependence results in a large discrepancy for large values of ϵ. For the negative magnetic shear case, there is thus a large spike near the trapped-passing boundary for large values of ϵ that is absent for small values of ϵ.

Figs. 4.16-4.18 demonstrate not only that a sign reversal for the toroidal drift frequency takes place, but also that the value of κ corresponding to the drift reversal is dependent on both ϵ and $\hat{s}$. Fig. 4.19 plots the value of κ at which the reversal takes place as a function of $\hat{s}$. The $\epsilon = 0.5$ case diverges from the small ϵ limit, and the extreme $\epsilon = 0.7$ case shows markedly different behavior. The difference is not noticeable for large, positive $\hat{s}$.

4.7 Chapter summary

The calculations in this work demonstrate that analytical formulas for the bounce-transit motion in a concentric circular geometry can be obtained without a small ϵ approximation. In addition, the standard small ϵ formulas can be easily obtained from the exact formulas; this method guarantees that a consistent ordering is applied in deriving the approximate expressions. A comparison using the analytical expressions reveals that the approximation is well suited for $\epsilon \lesssim 0.3$. The approximate expressions for the longitudinal invariant and bounce-transit frequency are also robust for larger values of ϵ. However, the toroidal drift frequency is not well approximated for large ϵ, even absent the inclusion of shaping effects. Of course, one must keep in mind that the concentric circular geometry is itself an approximation which can significantly break down in the edge region. However, additional shaping effects such as the Shafranov shift could also be perturbatively included while retaining a finite ϵ.

Our analysis demonstrates that in cases where a concentric circular geometry is justified, applying a small ϵ approximation to the geometry itself and subsequent calculations is also often justified. The formulas derived in this work can be utilized while restricting oneself to a concentric circular geometry if additional accuracy is required, which may prove useful for spherical tokamaks.

Appendix 4.A Elliptic integral notation

We clarify the notation used for elliptic integrals, as different sources will often have conflicting notation. The complete elliptic integral of the first kind is defined as

$$K(k) = \int_0^{\pi/2} \frac{d\varphi}{\sqrt{1 - k^2 \sin^2(\varphi)}}, \tag{4.144}$$

where k is the modulus. The complete elliptic integral of the second kind is

$$E(k) = \int_0^{\pi/2} d\varphi \sqrt{1 - k^2 \sin^2(\varphi)}. \tag{4.145}$$

The incomplete integral of the third kind is

$$\Pi(\varphi, n, k) = \int_0^{\varphi} \frac{d\varphi'}{\sqrt{1 - k^2 \sin^2(\varphi')}\left(1 - n \sin^2(\varphi')\right)}, \tag{4.146}$$

where n is the characteristic. The integral is called complete when $\varphi = \pi/2$,

$$\Pi(n, k) = \int_0^{\pi/2} \frac{d\varphi}{\sqrt{1 - k^2 \sin^2(\varphi)}\left(1 - n \sin^2(\varphi)\right)}. \tag{4.147}$$

We note that n is allowed to be positive or negative.

For trapped particles, the modulus k and characteristic n are

$$k_b = \kappa \sqrt{\frac{1 - \epsilon}{1 + \epsilon - 2\epsilon\kappa^2}}, \tag{4.148}$$

$$n_b = \frac{-2\epsilon\kappa^2}{1 + \epsilon - 2\epsilon\kappa^2}. \tag{4.149}$$

For passing particles, the modulus and characteristic are

$$k_t = \frac{1}{\kappa} \sqrt{\frac{1 + \epsilon - 2\epsilon\kappa^2}{1 - \epsilon}}, \tag{4.150}$$

$$n_t = \frac{-2\epsilon}{1 - \epsilon}. \tag{4.151}$$

Appendix 4.B Specific elliptic integrals

The calculation of several elliptic integrals is necessary to carry out the analysis in Sec. 4.6. These integrals are tabulated below with the help of Refs. 60–62. We first list those corresponding to trapped particles:

$$\begin{aligned} F_1(\epsilon,\kappa) &= \int_0^{\theta_b} d\theta \sqrt{\frac{1+\epsilon\cos(\theta)}{\kappa^2-\sin^2(\theta/2)}} \\ &= \frac{2\,(1+\epsilon)\,\Pi\,(n_b,k_b)}{\sqrt{1+\epsilon-2\epsilon\kappa^2}}, \end{aligned} \tag{4.152}$$

$$\begin{aligned} F_2(\epsilon,\kappa) &= \int_0^{\theta_b} d\theta \sqrt{\frac{1+\epsilon\cos(\theta)}{\kappa^2-\sin^2(\theta/2)}}\frac{1}{1+\epsilon\cos(\theta)} \\ &= \frac{2K\,(k_b)}{\sqrt{1+\epsilon-2\epsilon\kappa^2}}, \end{aligned} \tag{4.153}$$

$$\begin{aligned} F_3(\epsilon,\kappa) &= \int_0^{\theta_b} d\theta \sqrt{\frac{1+\epsilon\cos(\theta)}{\kappa^2-\sin^2(\theta/2)}}\frac{\sin^2(\theta)}{(1+\epsilon\cos(\theta))^2} \\ &= \frac{2\left((1-\epsilon)\,K\,(k_b)+2\epsilon E\,(k_b)-(1+\epsilon)\Pi\,(n_b,k_b)\right)}{\epsilon^2\sqrt{1+\epsilon-2\epsilon\kappa^2}}, \end{aligned} \tag{4.154}$$

$$\begin{aligned} F_4(\epsilon,\kappa) &= \int_0^{\theta_b} d\theta \sqrt{\frac{\kappa^2-\sin^2(\theta/2)}{1+\epsilon\cos(\theta)}} \\ &= \frac{\sqrt{1+\epsilon-2\epsilon\kappa^2}}{\epsilon}\left(\frac{(1+\epsilon)\Pi\,(n_b,k_b)}{1+\epsilon-2\epsilon\kappa^2}-K\,(k_b)\right), \end{aligned} \tag{4.155}$$

$$\begin{aligned} F_5(\epsilon,\kappa) &= \int_0^{\theta_b} d\theta \sqrt{\frac{\kappa^2-\sin^2(\theta/2)}{1+\epsilon\cos(\theta)}}\frac{1}{1+\epsilon\cos(\theta)} \\ &= \frac{2\sqrt{1+\epsilon-2\epsilon\kappa^2}}{1-\epsilon^2}\left(E\,(k_b)-\left(1-k_b^2\right)K\,(k_b)\right), \end{aligned} \tag{4.156}$$

$$\begin{aligned} F_6(\epsilon,\kappa) &= \int_0^{\theta_b} d\theta \sqrt{\frac{\kappa^2-\sin^2(\theta/2)}{1+\epsilon\cos(\theta)}}\frac{\sin^2(\theta)}{(1+\epsilon\cos(\theta))^2} \\ &= \frac{(1+\epsilon)\,(a_bK\,(k_b)+b_b\Pi\,(n_b,k_b))+c_bE\,(k_b)}{3\epsilon^3\left(1-\epsilon^2\right)\sqrt{1+\epsilon-2\epsilon\kappa^2}}. \end{aligned} \tag{4.157}$$

We have defined additional coefficients for F_6,

$$a_b = 3 - 6\epsilon + \left(4\kappa^2 - 1\right)\epsilon^2, \tag{4.158}$$

$$b_b = -3\left(1 - \epsilon^2\right), \tag{4.159}$$

$$c_b = 2\epsilon\left(3 - \left(4\kappa^2 - 2\right) - \epsilon^2\right). \tag{4.160}$$

For passing particles, we have instead

$$\begin{aligned} G_1(\epsilon,\kappa) &= \int_0^\pi d\theta \sqrt{\frac{1+\epsilon\cos(\theta)}{\kappa^2 - \sin^2(\theta/2)}} \\ &= \frac{2(1+\epsilon)\Pi\left(n_t, k_t\right)}{\kappa\sqrt{1-\epsilon}}, \end{aligned} \tag{4.161}$$

$$\begin{aligned} G_2(\epsilon,\kappa) &= \int_0^\pi d\theta \sqrt{\frac{1+\epsilon\cos(\theta)}{\kappa^2 - \sin^2(\theta/2)}} \frac{1}{1+\epsilon\cos(\theta)} \\ &= \frac{2K\left(k_t\right)}{\kappa\sqrt{1-\epsilon}}, \end{aligned} \tag{4.162}$$

$$\begin{aligned} G_3(\epsilon,\kappa) &= \int_0^\pi d\theta \sqrt{\frac{1+\epsilon\cos(\theta)}{\kappa^2 - \sin^2(\theta/2)}} \frac{\sin^2(\theta)}{\left(1+\epsilon\cos(\theta)\right)^2} \\ &= \left(k_t^2\left(K\left(k_t\right) - \Pi\left(n_t, k_t\right)\right) + \frac{n_t\left(K\left(k_t\right) - E\left(k_t\right)\right)}{1-n_t}\right) \frac{2\kappa\left(1-\epsilon\right)^{3/2}\left(1-n_t\right)}{\epsilon^2\left(1+\epsilon-2\epsilon\kappa^2\right)}, \end{aligned} \tag{4.163}$$

$$\begin{aligned} G_4(\epsilon,\kappa) &= \int_0^\pi d\theta \sqrt{\frac{\kappa^2 - \sin^2(\theta/2)}{1+\epsilon\cos(\theta)}} \\ &= \frac{(1+\epsilon)\Pi\left(n_t, k_t\right) - \left(1+\epsilon-2\epsilon\kappa^2\right)K\left(k_t\right)}{\epsilon\kappa\sqrt{1-\epsilon}}, \end{aligned} \tag{4.164}$$

$$\begin{aligned} G_5(\epsilon,\kappa) &= \int_0^\pi d\theta \sqrt{\frac{\kappa^2 - \sin^2(\theta/2)}{1+\epsilon\cos(\theta)}} \frac{1}{1+\epsilon\cos(\theta)} \\ &= \frac{2\kappa E\left(k_t\right)}{\sqrt{1-\epsilon}(\epsilon+1)}, \end{aligned} \tag{4.165}$$

$$\begin{aligned} G_6(\epsilon,\kappa) &= \int_0^\pi d\theta \sqrt{\frac{\kappa^2 - \sin^2(\theta/2)}{1+\epsilon\cos(\theta)}} \frac{\sin^2(\theta)}{\left(1+\epsilon\cos(\theta)\right)^2} \\ &= \frac{(1+\epsilon)\left(a_t K\left(k_t\right) + b_t\Pi\left(n_t, k_t\right)\right) + c_t E\left(k_t\right)}{3\epsilon^3\kappa\sqrt{1-\epsilon}(1+\epsilon)\left(1+\epsilon-2\epsilon\kappa^2\right)}. \end{aligned} \tag{4.166}$$

The coefficients for G_6 are

$$a_t = 3 - \left(12\kappa^2 - 6\right)\epsilon + \left(8\kappa^4 - 8\kappa^2 + 3\right)\epsilon^2, \tag{4.167}$$

$$b_t = -3\left(1 - 2\left(\kappa^2 - 1\right)\epsilon - \left(2\kappa^2 - 1\right)\epsilon^2\right), \tag{4.168}$$

$$c_t = 2\epsilon\kappa^2\left(3 - \left(4\kappa^2 - 2\right)\epsilon - \epsilon^2\right). \tag{4.169}$$

We also tabulate the small ϵ expansions used in Sec. 4.6,

$$F_1 \approx 2K(\kappa) + \epsilon\left(2E(\kappa) - K(\kappa)\right), \tag{4.170}$$

$$F_2 \approx 2K(\kappa) - \epsilon\left(2E(\kappa) - K(\kappa)\right), \tag{4.171}$$

$$F_3 \approx \frac{8}{3}\left((2\kappa^2 - 1)E(\kappa) - (1 - \kappa^2)K(\kappa)\right), \tag{4.172}$$

$$F_4 \approx 2\left(E(\kappa) - \left(1 - \kappa^2\right)K(\kappa)\right), \tag{4.173}$$

$$F_5 \approx 2\left(E(\kappa) - \left(1 - \kappa^2\right)K(\kappa)\right), \tag{4.174}$$

$$F_6 \approx -\frac{8}{15}\left(\left(2 - 3\kappa^2 + \kappa^4\right)K(\kappa) - 2\left(1 - \kappa^2 + \kappa^4\right)E(\kappa)\right), \tag{4.175}$$

$$G_1 \approx \frac{2}{\kappa}K\left(\kappa^{-1}\right) + \frac{\epsilon}{\kappa}\left(2E\left(\kappa^{-1}\right) - \left(2\kappa^2 - 1\right)K\left(\kappa^{-1}\right)\right), \tag{4.176}$$

$$G_2 \approx \frac{2}{\kappa}K\left(\kappa^{-1}\right) - \frac{\epsilon}{\kappa}\left(2E\left(\kappa^{-1}\right) - \left(2\kappa^2 - 1\right)K\left(\kappa^{-1}\right)\right), \tag{4.177}$$

$$G_3 \approx \frac{8}{3}\kappa\left(\left(2\kappa^2 - 1\right)E\left(\kappa^{-1}\right) - 2\left(\kappa^2 - 1\right)K\left(\kappa^{-1}\right)\right), \tag{4.178}$$

$$G_4 \approx 2\kappa E\left(\kappa^{-1}\right), \tag{4.179}$$

$$G_5 \approx 2\kappa E\left(\kappa^{-1}\right), \tag{4.180}$$

$$G_6 \approx \frac{8}{15}\kappa\left(2\left(\kappa^4 - \kappa^2 + 1\right)E\left(\kappa^{-1}\right) - \left(\kappa^2 - 1\right)\left(2\kappa^2 - 1\right)K\left(\kappa^{-1}\right)\right). \tag{4.181}$$

CHAPTER 5

Quasilinear gyrokinetic theory: A derivation of QuaLiKiz

5.1 Introduction

The development of tractable transport models is crucial to further the study and operation of tokamaks. Accurately characterizing the particle, angular momentum, and heat transport in the tokamak core requires the understanding of turbulence driven by microinstabilities, as these instabilities drive much of the particle, momentum, and heat transport in the core. Integrated modeling codes seek to predict and simulate tokamak discharges via the inclusion of various different physics and sources, including from microinstabilities. Nonlinear simulations of the kinetic equations are the most accurate way to compute the transport from microinstabilities. For reference, the cost of such a nonlinear simulation is on the order of 10^4 CPUh to 10^5 CPUh at a single radial point, while integrated modeling frameworks require thousands of flux calculations for every second of a plasma discharge in a large tokamak device.[24] Multi-scale simulations that take into account the interplay of instabilities across wide ranges of time scales are even more expensive.[98] Even linear kinetic simulations can prove to be intractable for integrated modeling if not reduced enough. Thus, it is imperative to develop and refine kinetic models that are both accurate enough to account for transport from microinstabilities and fast enough to be coupled to an integrated modeling framework.

QuaLiKiz is a quasilinear gyrokinetic transport model originally based on the linear eigenvalue code Kinezero. Pieces of the derivation have been published throughout the years including in Refs. 99–101. The underlying principles of the code regarding the variational and action-angle

approaches can be traced to Ref. 102, and upgrades to the physics including angular momentum transport[103] and numerical improvements[24] have been made since its original development. The goal of QuaLiKiz is to calculate the quasilinear transport that arise from microinstabilities. The core principle is to develop linearize the kinetic equations and solve the dispersion relation to find the complex frequencies for microinstabilities, namely the ion temperature gradient (ITG), electron temperature gradient (ETG), and trapped electron mode (TEM) instabilities. Upon solving the linear problem, we then incorporate nonlinear physics to compute particle, angular momentum, and heat fluxes. We do so via a quasilinear approach by coupling the linear characteristics of the problem together and using previously performed nonlinear kinetic simulations to saturate the perturbed state. Thus, while the amplitudes of the modes are set by nonlinear physics, the key transport features can be constructed from the linear regime. Quasilinear methods have been shown to be valid in the tokamak core. Moreover, the quasilinear codes are much faster than fully nonlinear kinetic codes. QuaLiKiz in particular can perform a full computation in $\sim$ 1 CPUs per wavenumber.[24]

As a gyrokinetic code, QuaLiKiz is well suited to model the core of tokamak devices which are strongly magnetized. Gyrokinetics is a popular approach to investigate turbulent phenomena in magnetized plasmas such as those of fusion devices.[39, 96] Gyrokinetics is well suited in scenarios where the microscopic dynamics are subject to the gyrokinetic ordering. Essentially, we apply gyrokinetics to situations where we can decouple the fast gyromotion of the charged particle from the slow drift motion; this can be done when the time scale of the gyromotion is significantly faster than all other time scales in the system and when the gyroradius is smaller than almost all other length scales in the system. In such a scenario, the magnetic moment is conserved, leading to a significant reduction in the complexity of the dynamics.[97] Moreover, gyrokinetics incorporates an ordering where the modes are anisotropic and flute-like, meaning that the characteristic parallel wavelength of the mode is large but perpendicular wavelengths can be comparable to the gyroradius. Thus, gyrokinetics is well suited for theoretical and quantitative investigations of magnetized plasma microturbulence. As a result, gyrokinetics has been used and applied in a wide variety of

systems.[43–52] Even beyond tokamaks, progress is being made in simulating stellarator plasmas in gyrokinetic codes.[104–108] QuaLiKiz in particular, however, assumes an axisymmetric geometry to simplify the dynamics, meaning QuaLiKiz is only suitable for tokamaks and not stellarators.

Aside from the well established gyrokinetic approach, the key assumption behind QuaLiKiz is the quasilinear approximation. In nonlinear simulations, turbulent fluctuations eventually saturate due to coupling mechanisms between different modes. However, it has been found that the nonlinear mode structure can resemble the underlying linear mode structure; in particular, the cross phases between fluctuating quantities in nonlinear simulations are identical to that of linear simulations.[109, 110] In such situations, one also finds that ratios of the particle and heat fluxes calculated in the linear regime match those calculated in the nonlinear regime and that the real part of the nonlinear mode frequency resembles that of the linear mode.[111, 112] Moreover, it has been found that when different instabilities are found in the linear regime, their interplay can manifest in the nonlinear regime.[113] This motivates a quasilinear approach where the equilibrium distribution function slowly evolves in comparison to the time scale of the instability, essentially taking a mean field theory approach. Then, the linear response is acquired and used to inform the the first order nonlinear behavior of the system. Quasilinear flux ratios are then calculated and each flux is appropriately saturated to the correct magnitude using a nonlinear saturation rule informed by nonlinear physics. The approach allows us to exploit the fact that the nonlinear state resembles the linear state to perform flux calculations without needing to carry out a full nonlinear simulation.[114]

However, constructing a quasilinear code instead of a nonlinear code is alone not enough to increase the speed of calculations. Rather, a litany of approximations and reductions are necessary. Aside from other typical approximations for gyrokinetic tokamak codes (e.g. nonrelativistic particles, quasineutrality), QuaLiKiz makes use of the following assumptions:

- Adiabatic invariance. By exploiting the adiabatic invariants of the system, we can formulate the Vlasov equation with action-angle variables. This requires that the single-particle Hamiltonian be slowly varying in time in comparison to the characteristic frequencies of motion. These frequencies correspond to the cyclotron motion, the bounce-transit motion, and the

toroidal drift and precession.

- Shifted Maxwellian with low Mach number and the δf approximation. QuaLiKiz linearizes the Vlasov equation by assuming a small perturbation from the shifted Maxwellian. Although we include the effect of bulk plasma rotation, we operate in the limit that the Mach number associated with the rotation is small.

- Electrostatic fluctuations. The code allows for electrostatic perturbations and an equilibrium electric field. The absence of magnetic perturbations allows for the exclusive use of Poisson's equation while neglecting Ampere's law, thus simplifying the linear problem. To simplify the guiding center motion, we require that the equilibrium electrostatic potential is small compared to the characteristic thermal energy.

- Trapped electron collisions. As an approximation, we utilize a Krook collision operator for trapped electrons and neglect collisions entirely for passing electrons and all ions.

- Shifted circle geometry with small inverse aspect ratio. This simplified geometry is used to calculate the magnetic drifts and perform integrals over the pitch angle with ease. The $s - \alpha$ model gives rise to a radial shift in the concentric flux surfaces called the Shafranov shift. The effect of this shift is included when calculating the magnetic drifts, but ignored when considering the bounce-transit motion. Thus, the treatment of guiding center motion with respect to the geometry is inherently inconsistent. Moreover, the $s - \alpha$ model is ad-hoc and does not solve the Grad-Shafranov equation.

- Gaussian eigenfunctions. Instead of using a self-consistent eigenfunction for the electrostatic modes, QuaLiKiz assumes the modes take the form of a Gaussian. The shift and width of the Gaussian are calculated in the high mode frequency limit as functions of the mode frequency, and substituted back into the dispersion relation.

- Strong ballooning. The electrostatic modes are assumed to be heavily localized around their rational flux surface. This allows for a Fourier link between the minor radius r and the

poloidal angle θ, thus simplifying the calculation. The localization also creates a separation of scales, thus allowing the integrals to be more easily approximated.

- Strongly passing and strongly trapped particles. Trapped and passing particles are considered to be respectively strongly trapped and strongly passing. For trapped particles, this greatly simplifies the relation between the physical toroidal and poloidal angles and the action angles and leads to a kinetic bounce average that is similar to the gyro-average. For passing particles, the strongly passing assumption simplifies the integrals over the pitch angle due to the dominating parallel velocity.

The goal of this work is to derive the analytic equations for QuaLiKiz step by step. Although various overviews of the QuaLiKiz and Kinezero framework have already been published,[24, 115, 116] no combination of currently published works derive the entirety of the model from first principles. We seek to fill this gap by offering a comprehensive and complete formulation of QuaLiKiz. This work will then as a result serve as a guide for improving upon QuaLiKiz and attaining physical and mathematical intuition as to its key principles, approximations, and computational methods. In addition, we also outline the new computational method used to numerically calculate 1-dimensional and 2-dimensional integrals. Moreover, this sort of work serves as a tutorial for those seeking to understand the fundamental considerations in the formulation of any quasilinear tokamak code. While many codes offer comprehensive manuals and describe the key principles at play, the process of creating such a code from scratch can often appear opaque and unintuitive. Thus, this derivation also serves as a tutorial for those who seek to understand the physical, mathematical, and computational aspects of quasilinear modeling in all their gory details.

The paper is organized as follows: Sec. 5.2 reviews the action-angle formalism and derives explicit expressions for the action-angle variables from physical variables. In Sec. 5.3, we linearize the Vlasov equation and expand the perturbed distribution function and electrostatic potential using a Fourier series to derive the dispersion relation. To solve the dispersion relation, we must integrate over all of phase space, resulting in a functional that depends on the complex frequency of the

mode. Sec. 5.4 examines the ballooning transform and its role in simplifying the dispersion relation as well as the characteristics of the electrostatic perturbation. Secs. 5.5–5.7 calculate the adiabatic, trapped, and passing parts of the functional, respectively, resulting in a reduced expression for the dispersion relation. Sec. 5.8 applies these results to the quasilinear problem to derive expressions for the particle, toroidal angular momentum, and heat fluxes. Sec. 5.9 connects the quasilinear results with nonlinear physics with the use of a saturation rule. Sec. 5.10 explains the method of contour integration used in QuaLiKiz to find the eigenmodes and the newly implemented numerical integration method based on the Genz and Malik algorithm.[117] Finally, we summarize our work Sec. 5.11. We include Appendix 5.A to serve as a brief explanation of Fried and Conte integrals. In addition, we derive the magnetic drift velocity in an $s - \alpha$ equilibrium in Appendix 5.B and briefly discuss the inclusion trapped electron collisions in Appendix 5.C. The derivation is performed in SI units, and we set the Boltzmann constant $k_B = 1$ such that our temperatures are in units of energy.

5.2 Action-angle variables

We first restrict ourselves to the collisionless Vlasov equation. Since the inclusion of collisions do not affect the fundamental approach, we examine them later in Appendix 5.C. The Vlasov equation is

$$\frac{\partial f}{\partial t} + \{f, H\} = 0, \tag{5.1}$$

where f is the distribution function, H is the single particle Hamiltonian, and $\{\cdot, \cdot\}$ denotes the Poisson bracket. Using phase space coordinates, this can be written as

$$\frac{\partial f}{\partial t} + \dot{\mathbf{q}} \cdot \frac{\partial f}{\partial \mathbf{q}} + \dot{\mathbf{p}} \cdot \frac{\partial f}{\partial \mathbf{p}} = 0, \tag{5.2}$$

where, for a single particle $\mathbf{q}$ is the position, $\mathbf{p}$ is the canonical momentum, and the time derivatives are given by Hamilton's equations of motion. For electromagnetic fields relevant to a tokamak, the Hamiltonian of a single charged particle is non-trivial. Although this form of the Vlasov equation and others like it offer an intuitive physical picture, these coordinates can make solving the system quite cumbersome. QuaLiKiz instead employs an action-angle formalism to simplify the

perturbative analysis. Such a formalism in the context of tokamak physics was first elaborated in Ref. 118 and expanded upon in Ref. 40. The core principle is to define a canonical transformation,

$$(\mathbf{q}, \mathbf{p}) \rightarrow (\boldsymbol{\alpha}, \mathbf{J}), \tag{5.3}$$

for which Hamilton's equations of motion simplify in the new phase space $(\boldsymbol{\alpha}, \mathbf{J})$. By restricting ourselves to a canonical transformation, we preserve the form of Vlasov's equation. The coordinates $\boldsymbol{\alpha}$ and $\mathbf{J}$ respectively correspond to the action angles and adiabatic invariants of our system. It is well known[32] that Hamilton's equations of motion then reduce to

$$\frac{\partial H}{\partial \boldsymbol{\alpha}} = -\dot{\mathbf{J}} = \mathbf{0}, \tag{5.4}$$

$$\frac{\partial H}{\partial \mathbf{J}} = \dot{\boldsymbol{\alpha}} = \boldsymbol{\Omega}, \tag{5.5}$$

where $\boldsymbol{\Omega}$ are the constant angular frequencies associated with each adiabatic invariant. At first glance, it may seem that we have simply shifted the difficulty of the problem to calculating this new canonical transformation itself. The power of this method comes from analyzing the unperturbed system and then including electromagnetic fluctuations in the Hamiltonian.

We define the Hamiltonian to be

$$H = H_0 + \delta h, \tag{5.6}$$

where the unperturbed Hamiltonian is simply

$$H_0 = \frac{1}{2m}\left(\mathbf{p}^2 - e\mathbf{A}_0^2\right) + e\Phi. \tag{5.7}$$

Here, m and e are respectively the mass and charge of the particle, $\mathbf{A}_0$ is the equilibrium vector potential, and Φ is the equilibrium electrostatic potential. Since QuaLiKiz operates in the electrostatic limit, we therefore apply a perturbation δh such that

$$\delta h = e\phi, \tag{5.8}$$

where ϕ is the electrostatic perturbation. We then define the action-angle coordinates in reference

to the unperturbed Hamiltonian,

$$\frac{\partial H_0}{\partial \boldsymbol{\alpha}} = \mathbf{0}, \tag{5.9}$$

$$\frac{\partial H_0}{\partial \mathbf{J}} = \boldsymbol{\Omega}. \tag{5.10}$$

Hamilton's equations of motion then become

$$\frac{\partial H}{\partial \boldsymbol{\alpha}} = -\dot{\mathbf{J}} = e\frac{\partial \phi}{\partial \boldsymbol{\alpha}}, \tag{5.11}$$

$$\frac{\partial H}{\partial \mathbf{J}} = \dot{\boldsymbol{\alpha}} = \boldsymbol{\Omega} + e\frac{\partial \phi}{\partial \mathbf{J}}. \tag{5.12}$$

We note that because the unperturbed Hamiltonian is a function of $\mathbf{J}$ and not $\boldsymbol{\alpha}$, all equilibrium quantities are also only functions of $\mathbf{J}$. Furthermore, any function of $\boldsymbol{\alpha}$ is periodic with respect to $\boldsymbol{\alpha}$; thus, the perturbed quantities in our system admit a Fourier series expansion. Moreover, it can be shown that $\boldsymbol{\alpha}, \mathbf{J}$ are canonical coordinates even after introducing a perturbation.[40] These features will simplify the derivation greatly.

The next task is to define the canonical transformation by specifying the action-angle variables in terms of the position $\mathbf{r}$ and the velocity $\mathbf{v}$ of the particle. The three adiabatic invariants in a tokamak correspond to the magnetic moment, the longitudinal invariant (also known as the bounce-transit action), and the poloidal flux. They are defined as follows:

$$J_1 = \frac{m}{e}\mu, \tag{5.13}$$

$$J_2 = \frac{1}{2\pi}\oint m p_\parallel dl = \frac{1}{2\pi}\oint \left(m v_\parallel + e A_\parallel\right) dl, \tag{5.14}$$

$$J_3 = P_\varphi = \frac{m v_\parallel R_0 B_\varphi^0}{B} - e\psi. \tag{5.15}$$

Here, $\mu = W_\perp / B$ is the magnetic moment, where $W_\perp = \frac{1}{2} m v_\perp^2$ is the kinetic energy associated with the velocity perpendicular to the magnetic field $\mathbf{B}$. Meanwhile, $v_\parallel$ and $A_\parallel$ are the components of the velocity and vector potential parallel to the magnetic field, respectively, with dl being the signed differential length along the particle orbit. We also define ψ to be minus the poloidal magnetic flux normalized to 2π, which is calculated by integrating the flux of the magnetic field through a disk

tangent to the flux surface everywhere:

$$\psi = -\frac{1}{2\pi}\int_S \mathbf{B}\cdot d\mathbf{S}. \tag{5.16}$$

The following subsections discuss each of the three adiabatic invariants and define their associated action angles and angular frequencies. For the remainder of the derivation, we also use the spatial coordinates $\mathbf{r} = (r, \theta, \varphi)$, where r is the minor radial position, θ is the geometric poloidal angle, and φ is the geometric toroidal angle. We use a right-handed coordinate system such that $\hat{\mathbf{r}}\times\hat{\boldsymbol{\theta}} = \hat{\boldsymbol{\varphi}}$. For further references characterizing the action angles $\boldsymbol{\alpha}$, we refer the reader to Garbet's work in Refs. 119 and 102.

5.2.1 Magnetic moment

In the presence of a magnetic field, charged particles gyrate about the field line at the cyclotron frequency $\Omega_1 = eB/m$. With a strong enough magnetic field, the cylcotron frequency is much larger than any other characteristic frequency in the plasma. Under such conditions, the magnetic moment μ is adiabatically conserved,[39, 94–97] and the gyromotion can be decoupled from the guiding center motion:

$$r = r_G + \rho\cos(\alpha_1), \tag{5.17}$$

$$\theta = \theta_G + \frac{\rho}{r}\sin(\alpha_1), \tag{5.18}$$

$$\varphi = \varphi_G, \tag{5.19}$$

where α_1 is equivalent to the gyrophase, ρ is the gyroradius, and the subscript "G" refers to the location of the particle's guiding center. These guiding center variables obey the guiding center equations of motion. Ordinarily, the exact invariant associated with the gyromotion depends on the electrostatic potential. For QuaLiKiz, we assume that the electrostatic field is small compared to the kinetic energy. Thus, we simply take J_1 to be the ordinary magnetic moment $\mu = W_\perp/B$.

Later in the derivation, we will need to take average various functions over the gyrophase α_1 by

integrating over α_1. We therefore consider the general integral

$$g_{n_1} = \int_{-\pi}^{\pi} \frac{d\alpha_1}{2\pi} g(\mathbf{r}) e^{-in_1\alpha_1}, \tag{5.20}$$

where n_1 is an integer. It will be shown that later that factors of $e^{-in_1\alpha_1}$ arise from taking Fourier expansions in terms of α_1. We define the Fourier transform of g to be

$$\tilde{g}(\mathbf{k}) = \int d^3r g(\mathbf{r}) e^{i\mathbf{k}\cdot\mathbf{r}}, \tag{5.21}$$

with the corresponding inverse Fourier transform

$$g(\mathbf{r}) = \int \frac{d^3k}{(2\pi)^3} \tilde{g}(\mathbf{k}) e^{-i\mathbf{k}\cdot\mathbf{r}}. \tag{5.22}$$

We use the Fourier transform to obtain

$$g_{n_1} = \int_{-\pi}^{\pi} \frac{d\alpha_1}{2\pi} \int \frac{d^3k}{(2\pi)^3} \tilde{g}(\mathbf{k}) e^{-i\mathbf{k}\cdot\mathbf{r} - in_1\alpha_1} = \int_{-\pi}^{\pi} \frac{d\alpha_1}{2\pi} \int \frac{d^3k}{(2\pi)^3} \tilde{g}(\mathbf{k}) e^{-i\mathbf{k}\cdot\boldsymbol{\rho} - in_1\alpha_1} e^{-i\mathbf{k}\cdot\mathbf{R}_G}. \tag{5.23}$$

Here, we have decoupled the gyromotion from the guiding center motion via $\mathbf{r} = \mathbf{R}_G + \boldsymbol{\rho}$. We then write

$$\mathbf{k}\cdot\boldsymbol{\rho} = k_\perp \rho \cos(\alpha_1), \tag{5.24}$$

where

$$k_\perp = \left|\mathbf{k} - \mathbf{k}\cdot\hat{\mathbf{b}}\right| \approx \sqrt{k_r^2 + k_\theta^2}. \tag{5.25}$$

Note that according to our definition of the Fourier transform, k_r and k_θ are operators in real space such that

$$k_r \to i\frac{\partial}{\partial r}, \tag{5.26}$$

$$k_\theta \to \frac{i}{r}\frac{\partial}{\partial\theta}. \tag{5.27}$$

We may then integrate over α_1 independently, leading to

$$\int_{-\pi}^{\pi} \frac{d\alpha_1}{2\pi} e^{-ik_\perp\rho\cos(\alpha_1) - in_1\alpha_1} = (-i)^{n_1} J_{n_1}(k_\perp\rho), \tag{5.28}$$

where J_n is the nth Bessel function of the first kind. Therefore, we finally have that

$$g_{n_1} = \int \frac{d^3k}{(2\pi)^3}(-i)^{n_1} J_{n_1}(k_\perp \rho)\tilde{g}(\mathbf{k})e^{-i\mathbf{k}\cdot\mathbf{R}_G} = (-i)^{n_1}\left(J_{n_1}(k_\perp\rho)\cdot g\right)(\mathbf{R}_G). \tag{5.29}$$

As a shorthand, we treat the Bessel function in real space as a differential operator that acts on g, after which we evaluate the resulting function at the guiding center. The Bessel function is simply a scalar function in Fourier space instead of a differential operator. The case of $n_1 = 0$ corresponds to the well known gyro-average. After completing the gyro-average, all functions are evaluated at the guiding center. Thus, we drop the subscript "G" for convenience and treat all spatial variables as those corresponding to the guiding center. The adiabatic invariants J_2 and J_3 are explicitly calculated within the guiding center framework where we hold μ constant and ignore the cyclotron motion.

5.2.2 Longitudinal invariant

To calculate J_2, we consider the guiding center particle motion along a magnetic field line; such a particle completes bounce-transit orbits with frequency Ω_2. This is the bounce frequency for trapped particles and the transit frequency for passing particles. Here, we neglect excursions from the field line due to various guiding center drifts by holding r constant. For an extended treatment of bounce-transit motion, see Refs. 86 and 120.

Assuming that the equilibrium electrostatic potential is small, the guiding center velocity parallel to the magnetic field is

$$\left|v_\parallel\right| = \sqrt{\frac{2}{m}(E-\mu B)}, \tag{5.30}$$

where E is the total kinetic energy of the particle. As an approximation, we take the typical equilibrium magnetic field to be of the form

$$\mathbf{B} = B_\varphi(r,\theta)\hat{\boldsymbol{\varphi}} + B_\theta(r,\theta)\hat{\boldsymbol{\theta}} = \frac{1}{1+r/R_0\cos(\theta)}\left(B^0_\varphi(r)\hat{\boldsymbol{\varphi}} + B^0_\theta(r)\hat{\boldsymbol{\theta}}\right), \tag{5.31}$$

where R_0 is the major radius. This corresponds to the magnetic field in a circular-cross section tokamak without any Shafranov shift. Defining the inverse aspect ratio $\epsilon = r/R_0$, we recognize

that this circular equilibrium is the small ϵ limit of a more general axisymmetric equilibrium. QuaLiKiz is thus well suited to machines where the aspect ratio of the device is ~ 3 or larger. Devices which smaller aspect ratios such as spherical tokamaks, however, cannot be reliably simulated in QuaLiKiz.

A particle is considered trapped if it reflects at a bounce angle θ_b, which requires

$$\frac{\mu B^0(r)}{E} \geq 1 - \epsilon. \tag{5.32}$$

Otherwise, the particle is considered passing since it will simply continue traveling along the magnetic field line without reflecting. We rewrite $v_\parallel$ to be

$$v_\parallel = \sqrt{\frac{2T}{m}} \epsilon_\parallel \sqrt{\xi} \sqrt{1 - \lambda b(r, \theta)}. \tag{5.33}$$

Here, $\xi = E/T$ where T is the temperature and $\epsilon_\parallel = \pm 1$ determines the sign of the parallel velocity. We also define

$$\lambda = \frac{\mu B\,(r, \theta = 0)}{E} = \frac{v_\perp^2}{v^2 b(r, \theta)}, \tag{5.34}$$

$$b(r, \theta) = \frac{B(r, \theta)}{B(r, \theta = 0)}. \tag{5.35}$$

It is clear then that λ is a pitch angle parameter and determines whether the particle is trapped or passing.

The bounce-transit frequency is defined as

$$|\Omega_2| = \frac{2\pi}{T_2}, \tag{5.36}$$

where

$$T_2 = \oint \frac{d\theta}{\left|\frac{d\theta}{dt}\right|}. \tag{5.37}$$

We note that one full poloidal orbit for trapped particles includes both the forward motion, where θ goes from $-\theta_b$ to θ_b, and the backward motion, where θ goes from θ_b to $-\theta_b$. For passing particles, the poloidal orbit only includes one full pass where θ goes from $-\pi$ to π. The sign of the transit frequency for passing particles is aligned with that of the parallel velocity and is thus

determined by $\epsilon_\parallel$, while the bounce frequency is always positive for trapped particles. Assuming that $B_\varphi \gg B_\theta$, then $\hat{\mathbf{b}}$, the direction of the magnetic field, is approximately $\hat{\boldsymbol{\varphi}}$. We again emphasize that this approximation breaks down for devices such as spherical tokamaks. Therefore, we write

$$v_\parallel = \mathbf{v} \cdot \hat{\mathbf{b}} \approx \dot{\varphi} \left(R_0 + r\cos(\theta)\right) \approx qR_0\dot{\theta}. \tag{5.38}$$

Here, we have defined the safety factor

$$q(r) = \frac{d\varphi}{d\theta} \approx \frac{rB_\varphi}{R_0 B_\theta}. \tag{5.39}$$

The safety factor describes how many times a magnetic field line wraps around toroidally per poloidal turn. The magnitude of the bounce-transit frequency is then

$$|\Omega_2| = \sqrt{\frac{2T}{m}} \frac{\sqrt{\xi}}{qR_0} \overline{\Omega}_2(r, \lambda), \tag{5.40}$$

where we define

$$\overline{\Omega}_2(r, \lambda) = \frac{2\pi}{\oint d\theta \frac{1}{\sqrt{1-\lambda b(r,\theta)}}}. \tag{5.41}$$

Note that for passing particles, we take the sign of the transit frequency to be the sign of the parallel velocity and multiply by $\epsilon_\parallel$ accordingly. We then calculate $\overline{\Omega}_2$ in the small ϵ limit to

$$\overline{\Omega}_2 \approx \begin{cases} \dfrac{\pi\sqrt{\epsilon}}{2\sqrt{2}K(\kappa)} & \text{if } 0 \le \kappa < 1 \text{ (trapped)}, \\ \dfrac{\pi\kappa\sqrt{\epsilon}}{\sqrt{2}K\left(\kappa^{-1}\right)} & \text{if } 1 < \kappa < \infty \text{ (passing)}. \end{cases} \tag{5.42}$$

Here, K is the complete elliptic integral of the first kind and κ is a trapped parameter defined such that

$$\lambda = 1 - 2\epsilon\kappa^2. \tag{5.43}$$

In the small ϵ limit, $0 \le \kappa < 1$ for trapped particles and $1 < \kappa < \infty$ for passing particles. We also calculate the bounce-transit action to be

$$J_2 \approx \begin{cases} \dfrac{8mqR_0\sqrt{E/m}\sqrt{\epsilon}}{\pi}\left(E\left(\kappa\right) - \left(1-\kappa^2\right)K\left(\kappa\right)\right) & \text{if } 0 \le \kappa < 1 \text{ (trapped)}, \\ \dfrac{4mqR_0\sqrt{E/m}\sqrt{\epsilon}}{\pi}\kappa E\left(\kappa^{-1}\right) + e\Phi_t & \text{if } 1 < \kappa < \infty \text{ (passing)}, \end{cases} \tag{5.44}$$

where E is the complete elliptic integral of the second kind and Φ_t is the toroidal flux normalized by 2π. The flux term is absent for trapped particles since the closed line integral of $A_\parallel$ is zero for trapped orbits.

Calculating the angular variable α_2 requires the explicit equation of motion

$$\frac{d\alpha_2}{dt} = \Omega_2. \tag{5.45}$$

This is of course the definition of α_2 such that it is conjugate to the action variable J_2. To find an explicit expression for α_2 in terms of the poloidal angle θ, we make use of the chain rule,

$$\frac{d\alpha_2}{dt} = \frac{d\alpha_2}{d\theta}\dot{\theta} = \frac{d\alpha_2}{d\theta}\frac{v_\parallel}{qR_0} = \Omega_2. \tag{5.46}$$

We emphasize that Ω_2 is not dependent on α_2 or θ. Thus, this differential equation can be integrated using elliptic functions, leading to an expression of α_2 in terms of θ. We use the convention that $\alpha_2(\theta = 0) = 0$, leading to

$$\alpha_2 = \int_0^\theta d\theta' \frac{qR_0\Omega_2}{v_\parallel} = \int^\theta d\theta' \frac{qR_0\Omega_2}{\sqrt{2T/m}\epsilon_\parallel\sqrt{\xi}\sqrt{1-\lambda b}}. \tag{5.47}$$

For trapped particles, we must keep in mind that $\epsilon_\parallel$ switches sign after the particle bounces. The integral can then be simplified in the small ϵ limit, leading to

$$\alpha_2 \approx \begin{cases} \dfrac{\pi}{2}\dfrac{F\left(\sin^{-1}\left[\kappa\sin\left(\frac{\theta}{2}\right)\right],\kappa\right)}{K(\kappa)} & \text{if } 0 \le \kappa < 1 \text{ (trapped)}, \\ \pi\dfrac{F\left(\frac{\theta}{2},\kappa^{-1}\right)}{K\left(\kappa^{-1}\right)} & \text{if } 1 < \kappa < \infty \text{ (passing)}, \end{cases} \tag{5.48}$$

where F is the incomplete integral of the first kind. Essentially, the integral takes the same form as when calculating Ω_2, the primary difference being that we integrate up to arbitrary θ rather than up to the bounce angle θ_b for trapped particles or up to π for passing particles.

Finally, let $G\left(\epsilon_\parallel,\theta\right)$ be a quantity that varies over the bounce-transit orbit along the field line. It is often of interest to time average G over the orbit; we define the bounce-transit average $\left\langle G\left(\epsilon_\parallel,\theta\right)\right\rangle$ to be

$$\left\langle G\left(\epsilon_\parallel,\theta\right)\right\rangle = \frac{1}{T_2}\oint \frac{d\theta}{\left|\frac{d\theta}{dt}\right|} G\left(\epsilon_\parallel,\theta\right) = \frac{\oint d\theta \frac{G\left(\epsilon_\parallel,\theta\right)}{\sqrt{1-\lambda b}}}{\oint d\theta \frac{1}{\sqrt{1-\lambda b}}}. \tag{5.49}$$

For passing particles, the average is explicitly

$$\oint d\theta \frac{G\left(\epsilon_{\|}, \theta\right)}{\sqrt{1-\lambda b}} = \int_{-\pi}^{\pi} d\theta \frac{G\left(\epsilon_{\|}, \theta\right)}{\sqrt{1-\lambda b}}, \tag{5.50}$$

while for trapped particles the average is instead

$$\oint d\theta \frac{G\left(\epsilon_{\|}, \theta\right)}{\sqrt{1-\lambda b}} = \int_{-\theta_b}^{\theta_b} d\theta \frac{G\left(\epsilon_{\|}, \theta\right) + G\left(-\epsilon_{\|}, \theta\right)}{\sqrt{1-\lambda b}}. \tag{5.51}$$

Note that because the line integral must be closed, a sum over $\epsilon_{\|}$ must be performed for trapped particles so that quantities such as $v_{\|}$ average to 0.

In this discussion so far, we have neglected any magnetic drifts and excursions from the field line. We include such effects in the next section, as they characterize the third adiabatic invariant — the poloidal flux.

5.2.3 Poloidal flux

In an axisymmetric equilibrium, the canonical toroidal momentum, P_φ, is conserved since no external quantities depend explicitly on the toroidal angle φ. From guiding center theory, we can write the canonical toroidal momentum as

$$P_\varphi = \frac{m v_{\|} R_0 B_\varphi^0}{B} - e\psi. \tag{5.52}$$

This is an exact invariant of the system. We construct J_3 such that it approximates P_φ provided that the poloidal flux term dominates. For typical parameters in a tokamak plasma this is indeed the case, since $\left(P_\varphi + e\psi\right)/(e\psi) \sim \sqrt{mT}/(eBR_0)$. Inputting JET-like parameters, $T = 5$ keV, $m = m_D$, $B = 3$ T, $R_0 = 3$ m, then $\sqrt{mT}/(eBR_0) \sim 10^{-3}$, making this a very reasonable approximation. We therefore write

$$J_3 = -e\psi. \tag{5.53}$$

To calculate the poloidal flux, we utilize Stoke's theorem; the surface integral of $\mathbf{B}$ simply becomes a closed line integral of $\mathbf{A}$ to find

$$A_\varphi(r, \theta) = \frac{1}{1+\epsilon\cos(\theta)} \int^r B_\theta(r', \theta)(1 + r'/R_0\cos(\theta))dr' = \frac{\int^r B_\theta^0(r')dr'}{1+\epsilon\cos\left(\theta\right)}. \tag{5.54}$$

Thus, we obtain

$$J_3 = -e\psi = -\frac{1}{2\pi}\int_0^{2\pi} e(1+\epsilon\cos(\theta))A_\varphi d\varphi = e\int^r R_0 B_\theta^0(r')dr'. \tag{5.55}$$

We see then that J_3 is purely a function of r such that

$$\frac{dJ_3}{dr} \approx -\frac{erB}{q}. \tag{5.56}$$

We next calculate Ω_3, which is the toroidal precession frequency for trapped particles and the toroidal rotation frequency for passing particles. Along the bounce-transit orbit, guiding center drifts cause radial excursions from the magnetic field line. In addition, passing particles wind around the magnetic field line toroidally due to the lack of any bounce point. To calculate this frequency, we need to first calculate deviations from the field line orbit, noting that radial excursions from the field line are of the order of the gyroradius. To aid in the calculation, we exploit the exact conservation of the canonical toroidal momentum:

$$\psi = \bar{\psi} + \frac{mB_\varphi^0 R_0 v_\parallel}{eB} = \bar{\psi} + \psi_1. \tag{5.57}$$

Here, $\bar{\psi}$ corresponds to the reference magnetic flux surface defined to be

$$\bar{\psi} = -\frac{P_\varphi}{e} \tag{5.58}$$

and ψ_1 is the deviation from that flux surface. Recall that the field line orbit assumed that

$$\frac{d\theta}{dt} \approx \frac{v_\parallel}{qR_0}, \tag{5.59}$$

where we hold r and thus ψ fixed. Since the exact field line-following orbit breaks P_φ conservation, we need to include deviations from the field line caused by conservation of P_φ along with guiding center drifts in order to consistently expand the guiding center equation of motion with respect to the gyroradius.

The guiding center equation of motion is

$$\frac{dx}{dt} = \left(v_\parallel \hat{\mathbf{b}} + \mathbf{v}_D\right)\cdot\nabla x, \tag{5.60}$$

where x is any spatial coordinate and $\mathbf{v}_D$ are the guiding center drifts. We then expand the guiding center equation of motion for variables ψ, θ, and φ and find that

$$\frac{d\psi}{dt} \approx (\mathbf{v}_D \cdot \nabla\psi)|_{\bar{\psi}}\,, \tag{5.61}$$

$$\frac{d\theta}{dt} \approx \left(\frac{v_\parallel}{qR_0}\right)\bigg|_{\bar{\psi}} + \frac{d}{d\psi}\left(\frac{v_\parallel}{qR_0}\right)\bigg|_{\bar{\psi}} \psi_1 + (\mathbf{v}_D \cdot \nabla\theta)|_{\bar{\psi}}\,, \tag{5.62}$$

$$\frac{d\varphi}{dt} \approx \left(\frac{v_\parallel}{qR_0}\frac{d\varphi}{d\theta}\right) + \frac{d}{d\psi}\left(\frac{v_\parallel}{qR_0}\frac{d\varphi}{d\theta}\right)\bigg|_{\bar{\psi}} \psi_1 + (\mathbf{v}_D \cdot \nabla\varphi)|_{\bar{\psi}}\,. \tag{5.63}$$

We take the $\mathbf{v}_D$ to be the the sum of the classical curvature, grad-B, and E-cross-B drifts:

$$\mathbf{v}_D = \frac{\hat{\mathbf{b}}}{eB}\left(mv_\parallel^2\mathbf{k} + \mu\nabla B + e\nabla\Phi\right), \tag{5.64}$$

where $\hat{\mathbf{k}}$ is the curvature vector defined such that

$$\hat{\mathbf{b}} \times \mathbf{k} = \nabla \times \hat{\mathbf{b}} - \left(\hat{\mathbf{b}} \cdot \nabla \times \hat{\mathbf{b}}\right)\hat{\mathbf{b}}. \tag{5.65}$$

We can simplify the equation of motion in the toroidal direction by noting that

$$\begin{aligned}\frac{d}{d\psi}\left(\frac{v_\parallel}{qR_0}\frac{d\varphi}{d\theta}\right)\psi_1 &= \frac{d}{d\psi}\left(\frac{v_\parallel}{qR_0}\right)\frac{d\varphi}{d\theta}\psi_1 + \frac{d}{d\psi}\left(\frac{d\varphi}{d\theta}\right)\frac{v_\parallel}{qR_0}\psi_1 \\ &= \frac{d\varphi}{d\theta}\frac{d\theta}{dt} + \frac{d}{d\psi}\left(\frac{d\varphi}{d\theta}\right)\frac{v_\parallel}{qR_0}\psi_1 - \frac{d\varphi}{d\theta}\frac{v_\parallel}{qR_0} - \frac{d\varphi}{d\theta}\left(\mathbf{v}_D \cdot \nabla\theta\right),\end{aligned} \tag{5.66}$$

where we used the equation of motion in the poloidal direction. Substituting this in and evaluating $\frac{d\varphi}{d\theta}$, we obtain

$$\dot{\varphi} = \frac{d}{d\psi}\left(\frac{q}{1+\epsilon\cos(\theta)}\right)\psi_1\frac{v_\parallel}{qR_0} + \mathbf{v}_D \cdot \nabla\varphi - \frac{q}{1+\epsilon\cos(\theta)}\mathbf{v}_D \cdot \nabla\theta + \frac{q}{1+\epsilon\cos(\theta)}\frac{d\theta}{dt}, \tag{5.67}$$

where we evaluate all radial coordinates at $\bar{r}$ such that

$$\psi(\bar{r}) = \bar{\psi}. \tag{5.68}$$

Finally, we take the bounce-transit average of $\dot{\varphi}$ and find that

$$\Omega_3 = \langle\dot{\varphi}\rangle = \langle\omega_d\rangle + \bar{\epsilon}q(\bar{r})\Omega_2 = \Omega_d + \bar{\epsilon}q(\bar{r})\Omega_2. \tag{5.69}$$

Here, $\bar{\epsilon}$ is 0 for trapped particles and 1 for passing particles, Ω_d is the frequency purely due to the guiding center drifts, and ω_d is associated with the instantaneous deviation from the magnetic field line. The extra term for passing particles is due to the toroidal rotation from following the field line in a complete poloidal turn. This parallel velocity dependent term is absent for trapped particles since their average toroidal position does not change as a result of a complete field line-following bounce. We approximate ω_d as

$$\omega_d \approx \frac{dq}{d\psi}\frac{\psi_1 v_\parallel}{q} + \mathbf{v}_D \cdot \nabla\varphi - q\mathbf{v}_D \cdot \nabla\theta. \tag{5.70}$$

The poloidal component of the magnetic drift dominates, thus we ignore the toroidal component. Using the $s-\alpha$ equilibrium, we calculate the guiding center drift in Appendix 5.B. Thus, Ω_3 is computed with a finite Shafranov shift. The poloidal component of the guiding center drift is

$$\mathbf{v}_D \cdot \nabla\theta \approx -\frac{m}{eBrR_0}\left(v_\parallel^2 + \frac{v_\perp^2}{2}\right)\left(\cos(\theta) - \alpha\sin^2(\theta)\right) - \frac{E_r}{rB}, \tag{5.71}$$

where E_r is the radial electric field. We also define α such that

$$\alpha = -q^2\beta\frac{R_0}{P}\frac{dP}{dr}. \tag{5.72}$$

Here, $\beta = 2\mu_0 P/B^2$ with μ_0 being the vacuum permeability. The E-cross-B drift can be separated from the magnetic drifts, so that we obtain

$$\mathbf{v}_{D,B} \cdot \nabla\theta \approx -\frac{v_{D,B}}{r}\left(\cos(\theta) - \alpha\sin^2(\theta)\right), \tag{5.73}$$

where $v_{D,B}$ characterizes the magnetic drifts and can be written as

$$v_{D,B} = \frac{m}{eBR_0}\left(v_\parallel^2 + \frac{v_\perp^2}{2}\right) = \frac{\xi T}{eBR_0}\left(2 - \lambda b\right), \tag{5.74}$$

where the magnetic shear is

$$s = \frac{r}{q}\frac{dq}{dr}. \tag{5.75}$$

We can therefore rewrite Ω_d as

$$\Omega_d = \frac{q}{r}\frac{T\xi}{eBR_0}\left\langle (2-\lambda b)\left(\cos(\theta) - \alpha\sin^2(\theta)\right) + \frac{2s}{\epsilon}(1-\lambda b)\right\rangle + \left\langle\frac{qE_r}{rB}\right\rangle = \omega_{d0}\xi F_d(\kappa) + \omega_E, \tag{5.76}$$

where $F = F_d(\kappa)$ is the bounce-transit averaged term, ω_{d0} is characteristic of the magnetic precession frequency and defined to be

$$\omega_{d0} = \frac{qT}{reBR_0}, \tag{5.77}$$

and ω_E corresponds to the E-cross-B velocity. We explicitly carry out the bounce-transit average by rewriting the λb terms in terms of κ and θ and find that

$$F_d(\kappa) \approx \begin{cases} -1 + \dfrac{2E(\kappa)}{K(\kappa)} + 4s\left(\kappa^2 - 1 + \dfrac{E(\kappa)}{K(\kappa)}\right) \\ \qquad - \dfrac{4\alpha}{3}\left(1 - \kappa^2 - \left(1 - 2\kappa^2\right)\dfrac{E(\kappa)}{K(\kappa)}\right) & \text{if } 0 \le \kappa < 1 \text{ (trapped)}, \\ -\left(2\kappa^2 - 1\right) + 2\kappa^2\dfrac{E\left(\kappa^{-1}\right)}{K\left(\kappa^{-1}\right)} + 4s\kappa^2\dfrac{E\left(\kappa^{-1}\right)}{K\left(\kappa^{-1}\right)} \\ \qquad - \dfrac{4\alpha}{3}\kappa^2\left(\left(2\kappa^2 - 1\right)\dfrac{E\left(\kappa^{-1}\right)}{K\left(\kappa^{-1}\right)} - 2\kappa^2 + 2\right) & \text{if } 1 < \kappa < \infty \text{ (passing)}. \end{cases} \tag{5.78}$$

Rather than calculating α_3 explicitly, it suffices to write its generic integral form. We also include the various oscillating quantities associated with the precession motion. In general, we have

$$\psi = \bar{\psi} + \tilde{\psi}, \tag{5.79}$$

$$\varphi = \alpha_3 + q(\bar{r})\tilde{\theta} + \tilde{\varphi}, \tag{5.80}$$

$$\theta = \bar{\epsilon}\alpha_2 + \tilde{\theta}. \tag{5.81}$$

Here, $\tilde{\psi}$ represents the excursion from the reference flux surface $\bar{\psi}$ during the poloidal orbit. Meanwhile, $\tilde{\varphi}$ is the difference in toroidal precession between a circular geometry and a more general equilibrium magnetic field. Later, we will use $\tilde{r}$ instead of $\tilde{\psi}$ with the understanding that $\psi(\tilde{r}) = \tilde{\psi}$. Meanwhile, $\tilde{\theta}$ is associated with the oscillatory poloidal motion. We define these

quantities as

$$\tilde{\psi} = \int^{\alpha_2} \frac{d\alpha_2'}{\Omega_2} \mathbf{v}_D \cdot \nabla\psi = \psi_1 \tag{5.82}$$

$$\tilde{\theta} = \int^{\alpha_2} d\alpha_2' \left(\frac{1}{\Omega_2} \frac{d\theta}{dt} - \bar{\epsilon} \right), \tag{5.83}$$

$$\tilde{\varphi} = \frac{dq}{d\psi}\tilde{\theta}\tilde{\psi} + \int^{\alpha_2} \frac{d\alpha_2'}{\Omega_2} \left(\bar{\epsilon}\frac{dq}{d\psi}\tilde{\psi}\Omega_2 + \mathbf{v}_D \cdot \nabla\varphi - \frac{dq}{d\psi}\tilde{\theta}\mathbf{v}_D \cdot \nabla\psi - q\mathbf{v}_D \cdot \nabla\theta - \Omega_d \right). \tag{5.84}$$

$$\tag{5.85}$$

This guarantees that

$$\frac{d\alpha_3}{dt} = \Omega_d + \bar{\epsilon} q \Omega_2. \tag{5.86}$$

Note that in the above, q and $dq/d\psi$ are evaluated at $\bar{r}$ and thus are time independent. Having characterized action-angle coordinates, we can proceed to solving the Vlasov equation using these coordinates.

5.3 Vlasov equation

To begin, we write the Vlasov equation in action-angle variables:

$$\frac{df}{dt} = \frac{\partial f}{\partial t} + \dot{\boldsymbol{\alpha}} \cdot \frac{\partial f}{\partial \boldsymbol{\alpha}} + \dot{\mathbf{J}} \cdot \frac{\partial f}{\partial \mathbf{J}} = 0. \tag{5.87}$$

We remind ourselves that Hamilton's equations of motion in these coordinates are

$$\dot{\mathbf{J}} = -\frac{\partial H}{\partial \boldsymbol{\alpha}} = -e\frac{\partial \phi}{\partial \boldsymbol{\alpha}}, \tag{5.88}$$

$$\dot{\boldsymbol{\alpha}} = \frac{\partial H}{\partial \mathbf{J}} = e\frac{\partial \phi}{\partial \mathbf{J}} + \boldsymbol{\Omega}, \tag{5.89}$$

We later generalize the above equation with a Krook-style operator to add collisions for trapped electrons in Appendix 5.C, but for now we work in the collisionless limit. The next step is to linearize the system by assuming the distribution function is composed of an equilibrium part $f_0 = f_0(\mathbf{J})$ and a perturbed part $\delta f = \delta f(\boldsymbol{\alpha}, \mathbf{J}, t)$. Dropping any quadratic perturbative terms, we obtain

$$\frac{\partial \delta f}{\partial t} + \boldsymbol{\Omega} \cdot \frac{\partial \delta f}{\partial \boldsymbol{\alpha}} - e\frac{\partial \phi}{\partial \boldsymbol{\alpha}} \cdot \frac{\partial f_0}{\partial \mathbf{J}} = 0. \tag{5.90}$$

As stated earlier, any perturbative functions we consider must be periodic in the angular variables $\boldsymbol{\alpha}$. Therefore, we utilize a discrete Fourier transform in δf and ϕ:

$$\delta f = \sum_{\mathbf{n}} f_{\mathbf{n}}(\mathbf{J}) e^{i(\mathbf{n}\cdot\boldsymbol{\alpha}-\omega t)}, \tag{5.91}$$

$$\phi = \sum_{\mathbf{n}} \phi_{\mathbf{n}}(\mathbf{J}) e^{i(\mathbf{n}\cdot\boldsymbol{\alpha}-\omega t)}. \tag{5.92}$$

To extract the physical quantity, we take the real part of the Fourier series. Here, $\mathbf{n}$ corresponds to the mode number of the Fourier term and ω is the complex frequency of oscillation. We decompose the complex frequency as $\omega = \omega_r + i\gamma$, where ω_r is the real frequency and γ is the growth rate. Note that in QuaLiKiz, we only consider unstable modes with $\gamma > 0$ and ignore stable modes; although this does not change the fundamental approach, it does afford us some slight computational simplicity since we do not have to search for solutions in the entire complex plane. As an ansatz, we treat $\omega = \omega_{n_3}$ to be dependent on n_3 only, not n_1 and n_2. To consistently solve the dispersion relation, we will eventually need to sum over n_1 and n_2. The individual Fourier components can be calculated from the physical quantity via

$$f_{\mathbf{n}} = \int \frac{d^3\alpha}{(2\pi)^3} \delta f(t=0) e^{-i\mathbf{n}\cdot\boldsymbol{\alpha}}, \tag{5.93}$$

$$\phi_{\mathbf{n}} = \int \frac{d^3\alpha}{(2\pi)^3} \phi(t=0) e^{-i\mathbf{n}\cdot\boldsymbol{\alpha}}, \tag{5.94}$$

where we integrate each angular variable from 0 to 2π.

To proceed, we assume the equilibrium distribution is a shifted Maxwellian:

$$f_0(\mathbf{J}) = n_0 \left(\frac{m}{2\pi T}\right)^{3/2} \exp\left(-\frac{m\left(\mathbf{v}-\mathbf{U}\right)^2}{2T}\right) = n_0 \left(\frac{m}{2\pi T}\right)^{3/2} \exp\left(\frac{-H_0 + e\Phi + m\mathbf{v}\cdot\mathbf{U} - \frac{mU^2}{2}}{T}\right). \tag{5.95}$$

Here, n_0 is the equilibrium number density, T is the temperature, and $\mathbf{U}$ is the equilibrium plasma rotation velocity. In general, n_0, T and $\mathbf{U}$ will vary with position and therefore depend on $\mathbf{J}$. By only considering toroidal rotation, we make the approximation

$$U_\varphi \hat{\boldsymbol{\varphi}} \approx U_\parallel \hat{\mathbf{b}}, \tag{5.96}$$

which allows us to write

$$U^2 \approx U_\parallel^2, \tag{5.97}$$

$$\mathbf{v} \cdot \mathbf{U} \approx v_\parallel U_\parallel. \tag{5.98}$$

We also take into account gradients of the parallel rotation velocity. Due to the presence of rotation, we also include the radial electric field as well as its gradient. We use the natural natural frequency parameter for the electric field shear γ_E defined as

$$\gamma_E = -\frac{1}{B}\frac{dE_r}{dr}. \tag{5.99}$$

This will allow us to Taylor expand the characteristic E-cross-B frequency such that

$$\omega_E \approx \omega_{E0} + \omega_E' x, \tag{5.100}$$

where we expand about the radial distance $x = 0$ and $\partial_r \omega_E = \omega_E'$ is related to the radial electric shear.

Additionally, in QuaLiKiz we ignore terms that go as the square of fluctuating quantities. Since we assume a small Mach number as well as a small derivative in the parallel velocity, we thus assume that

$$mU_\parallel \left| \frac{\partial v_\parallel}{\partial \mathbf{J}} \right| \ll \boldsymbol{\omega}_*. \tag{5.101}$$

This term is responsible for turbulent acceleration and arises from the presence of rotation in the equilibrium distribution function. We expect this term to be negligible for non-impurities in the low Mach number limit and will thus neglect it as an approximation.[121]

Substituting the above expressions as well as the Fourier series into the linearized Vlasov equation, we isolate each term mode by mode due to completeness and orthogonality of the Fourier series to find $f_\mathbf{n}$ in terms of $\phi_\mathbf{n}$. The result is

$$f_\mathbf{n} = \frac{e\phi_\mathbf{n}\mathbf{n} \cdot \frac{\partial f_0}{\partial \mathbf{J}}}{\mathbf{n} \cdot \boldsymbol{\Omega} - \omega} = \frac{f_0}{T}\frac{e\phi_\mathbf{n}\mathbf{n} \cdot (\boldsymbol{\omega}_* + \boldsymbol{\omega}_E - \boldsymbol{\Omega})}{\mathbf{n} \cdot \boldsymbol{\Omega} - \omega}, \tag{5.102}$$

where the diamagnetic frequency ω_* is

$$\omega_* = T\left(\frac{1}{n_0}\frac{\partial n_0}{\partial \mathbf{J}} + \left(\xi - \frac{3}{2} - \frac{U_\parallel}{v_T^2}\left(2v_\parallel - U_\parallel\right)\right)\frac{1}{T}\frac{\partial T}{\partial \mathbf{J}}\right) + \frac{2\left(v_\parallel - U_\parallel\right)}{v_T^2}\frac{\partial U_\parallel}{\partial \mathbf{J}}, \tag{5.103}$$

where the thermal velocity is $v_T = \sqrt{2T/m}$ and the frequency associated with the E-cross-B drift is

$$\omega_E = \frac{e}{T}\frac{d\Phi}{d\mathbf{J}}. \tag{5.104}$$

We then rewrite the equation to be

$$f_{\mathbf{n}} = -\frac{e\phi_{\mathbf{n}}}{T} f_0 \left(1 - \frac{\omega - \mathbf{n}\cdot\boldsymbol{\omega}_* - \mathbf{n}\cdot\boldsymbol{\omega}_E}{\omega - \mathbf{n}\cdot\boldsymbol{\Omega}}\right), \tag{5.105}$$

where it is now clear that there is an adiabatic part and a frequency dependent part of the equation.

The next step to solving the dispersion relation is to use Poisson's equation,

$$\nabla^2\phi = \sum_s -\frac{e_s n_s}{\epsilon_0}, \tag{5.106}$$

where the s subscript labels the particle species and ϵ_0 is the vacuum permittivity. In the earlier parts of the derivation, we had suppressed the subscript for various quantities (e.g. $m, T, n_0, f_0, \delta f, \ldots$); we include the subscript for the time being. The total number density n_s is

$$n_s = \int d^3v\, f_s. \tag{5.107}$$

The perturbed electrostatic potential is calculated using the perturbed charge density

$$\delta n_s = \int d^3v\, \delta f_s. \tag{5.108}$$

To enforce quasineutrality, we take the sum of the total charge density to be 0 and require that

$$\lambda_D \ll \left|\frac{\phi}{\nabla\phi}\right|, \tag{5.109}$$

where λ_D is the Debye length. Because we are interested in length scales much longer than the Debye length, the Laplacian term in Poisson's equation is negligible. We thus obtain

$$\sum_s \int d^3v\, e_s \delta f_s = 0. \tag{5.110}$$

Since $\phi = \phi(\mathbf{r})$ is independent of velocity, if we multiply both sides of the above equation by ϕ^*, the complex conjugate of ϕ, we can simply move it inside the integral. We then integrate over space, resulting in

$$\sum_s \int d^3r d^3v e_s \phi^* \delta f_s = 0. \tag{5.111}$$

By multiplying by the electrostatic potential and integrating, we have recast the differential equation via a weak formulation using the variational method.[102, 119, 122, 123] Instead of solving for the exact function ϕ or δf that satisfies Poisson's equation, we can simply approximate ϕ and δf with a suitable function and focus on the dispersion relation itself. Typically, when the Laplacian is kept, the differential equation is put into the weak formulation by integrating the Laplacian term by parts; this technique is well established in other fields such as finite element analysis.[124]

We next substitute in the Fourier expansions and the expression relating $\phi_{\mathbf{n}}$ and $f_{\mathbf{n}}$. The result is

$$\sum_s \sum_{\mathbf{n},\mathbf{n}'} \int d^3r d^3v \frac{e_s^2 \phi_{\mathbf{n}} \phi^*_{\mathbf{n}'}}{T_s} f_{0,s} \left(1 - \frac{\omega - \mathbf{n}\cdot\boldsymbol{\omega}_* - \mathbf{n}\cdot\boldsymbol{\omega}_E}{\omega - \mathbf{n}\cdot\boldsymbol{\Omega}}\right) e^{i(\mathbf{n}-\mathbf{n}')\cdot\boldsymbol{\alpha}} e^{-i(\omega-(\omega')^*)t} = 0. \tag{5.112}$$

To simplify this integral, we first perform the change of variables $(\mathbf{r}, \mathbf{v}) \to (\mathbf{r}, \mathbf{p})$; the Jacobian of this transformation is simply m_s^{-1}. We then perform the change of variables $(\mathbf{r}, \mathbf{p}) \to (\boldsymbol{\alpha}, \mathbf{J})$; the Jacobian of this particular transformation is 1 because this is guaranteed to be a canonical transformation. We therefore obtain

$$\sum_s \sum_{\mathbf{n},\mathbf{n}'} \int d^3\alpha d^3J \frac{e_s^2 \phi_{\mathbf{n}} \phi^*_{\mathbf{n}'}}{m_s T_s} f_{0,s} \left(1 - \frac{\omega - \mathbf{n}\cdot\boldsymbol{\omega}_* - \mathbf{n}\cdot\boldsymbol{\omega}_E}{\omega - \mathbf{n}\cdot\boldsymbol{\Omega}}\right) e^{i(\mathbf{n}-\mathbf{n}')\cdot\boldsymbol{\alpha}} e^{-i(\omega-(\omega')^*)t} = 0. \tag{5.113}$$

We note that the exponential terms are $\boldsymbol{\alpha}$ dependent. We then use orthogonality of the Fourier series to find that

$$\sum_s \sum_{n_1,n_2} \int d^3J \frac{e_s^2 |\phi_{\mathbf{n}}|^2}{m_s T_s} f_{0,s} \left(1 - \frac{\omega - \mathbf{n}\cdot\boldsymbol{\omega}_* - \mathbf{n}\cdot\boldsymbol{\omega}_E}{\omega - \mathbf{n}\cdot\boldsymbol{\Omega}}\right) = 0. \tag{5.114}$$

Because we developed the Fourier series such that ω only depends on the mode number n_3, we can solve for each value of n_3 individually while summing over n_1 and n_2. While the summation arising from this convention seems to make the problem more difficult at first glance, we shall see later it

allows for a variety of simplifications. Moreover, the integrand is now completely independent of $\boldsymbol{\alpha}$. As such, we integrate over the action angles again and transform back to conventional variables, leading to

$$\sum_s \sum_{n_1,n_2} \int d^3r d^3v \frac{e_s^2 \left|\phi_{\mathbf{n}}\right|^2}{T_s} f_{0,s} \left(1 - \frac{\omega - \mathbf{n}\cdot\boldsymbol{\omega}_* - \mathbf{n}\cdot\boldsymbol{\omega}_E}{\omega - \mathbf{n}\cdot\boldsymbol{\Omega}}\right) = 0. \tag{5.115}$$

Even though the integrand is a function of only $\mathbf{J}$, the parameters in the integrand are more naturally expressed in terms of other coordinates such as the minor radius and the pitch angle parameter. Thus, further coordinate transformations to simplify this expression are inevitable. As such, they are most easily carried out when starting from the typical configuration space variables $(\mathbf{r}, \mathbf{v})$.

For ease of notation, we split up the dispersion relation as follows:

$$\sum_s \mathcal{L}_{0,s} - \mathcal{L}_{\text{passing},s} - \mathcal{L}_{\text{trapped},s} = 0. \tag{5.116}$$

Here, $\mathcal{L}_0$ is the portion of the integral that is simply multiplied by 1, which we call the adiabatic part. $\mathcal{L}_{\text{passing}}$ is the portion of the integral that is frequency dependent and integrated over the part of velocity space that encompasses passing particles, while $\mathcal{L}_{\text{trapped}}$ consists of the trapped particles instead.

To proceed with solving the dispersion relation, we must first calculate $|\phi_{\mathbf{n}}|^2$. This requires a 3-dimensional integral over $d^3\alpha$. Once that is done, we then proceed to calculate the integral in the dispersion relation itself for the adiabatic part, trapped part, and passing part separately. Although our expression appears to be a 6-dimensional integral, we can utilize a number of symmetries, transformations, and approximations to simplify the form down to at most 2-dimensional integrals. Although integrals of higher dimension can be in principle calculated numerically, the curse of dimensionality renders such integrals computationally expensive. Thus, a reduction to two dimensions affords us a great deal of speed at the cost of some amount of accuracy.

5.4 Ballooning representation

Before integrating $|\phi_{\mathbf{n}}|^2$ with respect to the action angles, we review key results regarding the ballooning representation. Because $\phi(r, \theta, \varphi)$ must be periodic in θ and φ, we may expand ϕ as a Fourier series,

$$\phi(r, \theta, \varphi) = \sum_{m,n} \phi_{m,n}(r - r_0) e^{i(m\theta + n\varphi)}. \tag{5.117}$$

Here, r_0 is the location of the resonant flux surface for each given m and n; in other words, $q(r_0) = -m/n$. We take these modes to be localized around the resonant flux surface. These modes are often radially localized such that the distance between any two adjacent resonant rational flux surfaces is much longer than the characteristic length scale of the plasma equilibrium. If that condition holds, then all modes $\phi_{n,m}$ all have nearly identical radial envelopes where each radial profile is centered on their corresponding reference flux surface.[125] These flux surfaces are all rational flux surfaces since m and n are integers. Meanwhile, the general ballooning representation of ϕ is

$$\phi(r, \theta, \varphi) = \sum_{p} \sum_{n} \hat{\phi}_n(\theta + 2p\pi, \theta_0) e^{in(\varphi - q(r)(\theta - \theta_0 + 2p\pi))}, \tag{5.118}$$

where θ_0 is the ballooning angle and p denotes the various harmonics. Here, we have approximated the potential by separating it into a quickly varying eikonal and a slowly varying envelope. This representation ultimately comes from the fact that the instabilities in question are strongly anisotropic and flute-like where $k_{\parallel} \gg k_{\perp}$. In absence of toroidal rotation, the ballooning angle is typically taken to be zero since the most unstable modes are localized around $\theta_b = 0$. In the presence of finite toroidal rotation and an equilibrium electrostatic potential, the ballooning angle is shifted away from zero. However, this shift is typically on the order of 10^{-1} in relevant cases.[126] Thus, for the rest of the derivation we take the ballooning angle to be zero as an approximation. This is equivalent to assuming that the envelope is radially independent. Moreover, if the profile is heavily localized around $\theta = 0$, we can use the strong ballooning approximation and ignore all

harmonics except for $p = 0$, leading to

$$\phi(r, \theta, \varphi) = \sum_n \hat{\phi}_n(\theta) e^{in(\varphi - q(r)\theta)}. \tag{5.119}$$

It is important to note that the decomposition in terms of $\phi_{m,n}$ describes how the same radial profile is localized about adjacent flux surfaces. Meanwhile, the decomposition in terms of $\hat{\phi}_n$ describes how the linear eigenmode balloons along the field line. This can be seen more explicitly if one considers that

$$\mathbf{B} \cdot \nabla \psi = 0, \tag{5.120}$$

$$\mathbf{B} \cdot \nabla (\varphi - q\theta) = 0, \tag{5.121}$$

$$\mathbf{B} \cdot \nabla \theta \neq 0, \tag{5.122}$$

indicating that with the above set of variables that θ indicates the location on any given field line. Because the magnetic curvature is unfavorable on the low field side of the tokamak when one considers the interplay between the curvature vector and the pressure gradient for normal tokamak profiles, we expect fluctuations to peak about $\theta = 0$. We can demonstrate a direct link between $\phi_{m,n}$ and $\hat{\phi}_n$ by calculating the Fourier components of ϕ, leading to

$$\int_{-\pi}^{\pi} \frac{d\varphi}{2\pi} \int_{-\pi}^{\pi} \frac{d\theta}{2\pi} \phi(r, \theta, \varphi) e^{-in\varphi - im\theta} = \phi_{m,n}(r - r_0) = \int_{-\pi}^{\pi} \frac{d\theta}{2\pi} \hat{\phi}_n(\theta) e^{-i\theta(nq(r)+m)}. \tag{5.123}$$

We then make two approximations. First, we Taylor expand the term in the eikonal around the reference flux surface,

$$nq(r) + m = nq_0 + \frac{r - r_0}{d} + m = \frac{r - r_0}{d} = \frac{x}{d} + \frac{\tilde{r}}{d}, \tag{5.124}$$

where $q_0 = q(r_0)$, the radial difference between different rational flux surfaces is defined as,

$$\frac{1}{nd} = \left.\frac{dq}{dr}\right|_{r=r_0}, \tag{5.125}$$

and x is defined as

$$x = \bar{r} - r_0, \tag{5.126}$$

where we ignore second derivatives of the safety factor. After doing so, we find that

$$\phi_{m,n}(r - r_0) \approx \int_{-\pi}^{\pi} \frac{d\theta}{2\pi} \hat{\phi}_n(\theta) e^{-i\frac{\theta(r-r_0)}{d}}. \tag{5.127}$$

Second, we invoke the strong ballooning approximation by treating $\hat{\phi}_n$ as heavily localized around $\theta = 0$; this allows us to integrate from $-\infty$ to ∞ instead of from $-\pi$ to π. The result is

$$\phi_{m,n}(r - r_0) \approx \int_{-\infty}^{\infty} \frac{d\theta}{2\pi} \hat{\phi}_n(\theta) e^{-i\frac{\theta(r-r_0)}{d}}. \tag{5.128}$$

Comparing it with our previous definition of the Fourier transform, we find that $\hat{\phi}_n(\theta)$ is simply the Fourier transform of $\phi_{m,n}(r)$, with $k_r = \theta/d$. The transformation is given by

$$\hat{\phi}_n(\theta) = \int_{-\infty}^{\infty} \frac{dr}{|d|} \phi_{m,n}(r - r_0) e^{i\frac{\theta(r-r_0)}{d}}. \tag{5.129}$$

We are now in a position to integrate over the action angles to fully calculate $\phi_{\mathbf{n}}$. The procedure to integrate over α_1 has already been discussed in Sec. 5.2, where we find that

$$\int_{-\pi}^{\pi} \frac{d\alpha_1}{2\pi} g(\mathbf{r}) e^{-in_1\alpha_1} = (-i)^{n_1} \left(J_{n_1}\left(k_\perp \rho\right) \cdot g \right) (\mathbf{R}_G). \tag{5.130}$$

We therefore only need to discuss in detail the integrations over α_2 and α_3 while treating all variables within the guiding center framework. Trapped particle motion and passing particle motion differ such that the two cases must be handled separately.

5.4.1 Trapped

For deeply trapped particles, the equations for the action variables simplify to

$$r = \bar{r} + \delta_b \cos(\alpha_2), \tag{5.131}$$

$$\theta = \theta_b \sin(\alpha_2), \tag{5.132}$$

$$\varphi = \alpha_3 + q(\bar{r})\theta_b \sin(\alpha_2) + \tilde{\varphi}. \tag{5.133}$$

Here, we define the banana width δ_b as

$$\delta_b = \frac{q\rho}{\sqrt{\epsilon}}. \tag{5.134}$$

While more exact expressions for the bounce motion can be given using Jacobi elliptic functions, we use the above equations for all trapped particles as an approximation. We first integrate over α_2, once again utilizing the Fourier transform,

$$\int_{-\pi}^{\pi} \frac{d\alpha_2}{2\pi} \phi(\mathbf{r}) e^{-in_2\alpha_2} = \int_{-\pi}^{\pi} \frac{d\alpha_2}{2\pi} \int \frac{d^3k}{(2\pi)^3} \tilde{\phi}(\mathbf{k}) e^{-i\mathbf{k}\cdot\mathbf{r} - in_2\alpha_2}. \tag{5.135}$$

We then proceed in fashion similar to the gyro-average derivation in Sec. 5.2 by noting that $\mathbf{k}\cdot\mathbf{r} = \mathbf{k}\cdot\bar{\mathbf{r}} + k_r\delta_b\cos(\alpha_2)$. The result is

$$\int_{-\pi}^{\pi} \frac{d\alpha_2}{2\pi} \phi(\mathbf{r}) e^{-in_2\alpha_2} = \int \frac{d^3k}{(2\pi)^3} (-i)^{n_2} J_{n_2}(k_r\delta_b) \tilde{\phi}(\mathbf{k}) e^{-i\mathbf{k}\cdot\bar{\mathbf{r}}}. \tag{5.136}$$

In essence, we obtain a bounce average over the banana width.[73] We note that this in particular is a rather crude approximation. The particularities of the bounce motion such as the bounce angle and the radial excursion technically depend on the pitch angle of the particle; we are in essence smearing this out by taking a representative trapped particle such that the banana width is constant. The averaging procedure is also approximate as we only take into account the radial deviation. As seen in Ref. 127, we would normally obtain a θ dependence in the argument of the Bessel function; the k_r term manifests as the Fourier link established earlier. As a result, trapped particles have two Bessel operators acting on the potential corresponding to the gyromotion and the banana orbit respectively.

We now proceed to integrating over α_3, for now leaving the Bessel functions aside and evaluating the position at $\mathbf{r} = \bar{\mathbf{r}}$. In doing so, we must be aware that for trapped particles $\bar{\theta} = 0$; that is, the variation of θ only comes from the bounce orbit which we averaged over. We also ignore $\tilde{\varphi}$ for the same reason. Moreover, because we assume the modes to have an identical radial structure, we are free to keep only one of the poloidal harmonics. Making the strong assumption that the actual radial envelope can be approximated in this way, we pick $m_0 = -n_3 q_0$, as this forces any θ dependence we approximately neglected in the eikonal to vanish. Thus, we obtain

$$\int_{-\pi}^{\pi} \frac{d\alpha_3}{2\pi} \phi(\bar{\mathbf{r}}) e^{-in_3\alpha_3} = \sum_n \int_{-\pi}^{\pi} \frac{d\alpha_3}{2\pi} \phi_{m_0,n}(\bar{r} - r_0) e^{i(n\alpha_3 - n_3\alpha_3)} = \phi_{m_0,n_3}(\bar{r} - r_0). \tag{5.137}$$

To compensate for choosing only one poloidal harmonic, we must extend the radial limits of integration to $-\infty < r < \infty$. Aside from the Bessel functions, nothing in the trapped part of the dispersion relation is dependent on $\theta = k_r d$. Therefore, we are free to take the amplitude squared of the averaged potential to obtain

$$|\phi_{\mathbf{n}}|^2 = \left|J_{n_1}(k_\perp \rho) J_{n_2}(\delta_b k_r) \cdot \phi_{m_0,n_3}\right|^2 (\bar{r} - r_0) = \left|J_{n_1}(k_\perp \rho) J_{n_2}(\delta_b k_r) \cdot \phi_{m_0,n_3}\right|^2 (x), \tag{5.138}$$

where we evaluate the function at $x = \bar{r} - r_0$.

5.4.2 Passing

We now calculate $\phi_{\mathbf{n}}$ for passing particles. Instead of utilizing the poloidal harmonics, it is more useful to use the ballooning representation directly. Substituting in the expression for α_3 and then integrating over α_3 leads to

$$\int_{-\pi}^{\pi} \frac{d\alpha_3}{2\pi} \phi(\mathbf{r}) e^{-in_3\alpha_3} = \sum_n \int_{-\pi}^{\pi} \frac{d\alpha_3}{2\pi} \hat{\phi}_n(\theta(\alpha_2)) e^{in(\alpha_3 + \tilde{\varphi} - q(r)\alpha_2 + (q(\bar{r}) - q(r))\tilde{\theta}) - in_3\alpha_3}. \tag{5.139}$$

Here, θ is taken to be a function of α_2. It is crucial that we recognize not all the safety factors in the eikonal are evaluated at the same point. We have both $q(r) = q(\bar{r} + \tilde{r})$ and $q(\bar{r})$. The term $q(r) - q(\bar{r})$ can be Taylor expanded about r_0:

$$q(r) - q(\bar{r}) \approx q_0 + \frac{r - r_0}{nd} - q_0 - \frac{\bar{r} - r_0}{nd} = \frac{r - \bar{r}}{nd} = \frac{\tilde{r}}{nd}. \tag{5.140}$$

Carrying out the integral then gives us

$$\int_{-\pi}^{\pi} \frac{d\alpha_3}{2\pi} \phi(\mathbf{r}) e^{-in_3\alpha_3} = \hat{\phi}_{n_3}(\theta(\alpha_2)) e^{in_3(\tilde{\varphi} - q(r)\alpha_2 - \frac{\tilde{r}}{n_3 d}\tilde{\theta})}. \tag{5.141}$$

We now multiply by $e^{-in_2\alpha_2}$ and integrate with respect to α_2. The eikonal can be simplified if we only keep $n_2 = m_0 = -nq_0$,

$$i\left(n_3\tilde{\varphi} - n_3 q(r)\alpha_2 - \frac{\tilde{r}}{d}\tilde{\theta} - m_0\alpha_2\right) = i\left(n_3\tilde{\varphi} - \frac{x}{d}\alpha_2 - \frac{\tilde{r}}{d}\left(\alpha_2 + \tilde{\theta}\right)\right) = i\left(n_3\tilde{\varphi} - \frac{x}{d}\alpha_2 - \frac{\tilde{r}}{d}\theta(\alpha_2)\right), \tag{5.142}$$

where we have used

$$-n_3 q(r)\alpha_2 - m_0\alpha_2 \approx -n_3 q_0\alpha_2 - \frac{r-r_0}{d}\alpha_2 - m_0\alpha_2 = -\frac{r-r_0}{d}\alpha_2 = -\frac{x}{d}\alpha_2 - \frac{\tilde{r}}{d}\alpha_2 \tag{5.143}$$

and the expression $\alpha_2 = \theta - \tilde{\theta}$. We then obtain

$$\int_{-\pi}^{\pi} \frac{d\alpha_2}{2\pi}\hat{\phi}_{n_3}(\theta(\alpha_2))e^{i\left(n_3\tilde{\varphi} - \frac{x}{d}\alpha_2 - \frac{\tilde{r}}{d}\theta(\alpha_2)\right)} \approx \int_{-\infty}^{\infty} \frac{d\alpha_2}{2\pi}\hat{\phi}_{n_3}(\theta(\alpha_2))e^{i\left(n_3\tilde{\varphi} - \frac{\tilde{r}}{d}\theta(\alpha_2)\right)}e^{-i\frac{x}{d}\alpha_2}, \tag{5.144}$$

where we have invoked the strong ballooning approximation. We can see that this is simply an inverse Fourier transform going from α_2 to x. Thus, we write that

$$\phi_{\mathbf{n}} = \phi_{n_1,m_0,n_3} = \left(J_{n_1}(k_\perp\rho)\cdot\mathcal{F}^{-1}\left(\hat{\phi}_{n_3}(\theta(\alpha_2))e^{i\left(n_3\tilde{\varphi} - \frac{\tilde{r}}{d}\theta(\alpha_2)\right)}\right)\right)(x), \tag{5.145}$$

where $\mathcal{F}^{-1}$ inverts the Fourier transform as described above with respect to α_2. While the $\tilde{\varphi}$ dependence can be approximately ignored in a circular geometry, the $\tilde{r}\theta(\alpha_2)$ dependence in the eikonal must be kept.

We shall see that the mode numbers n_1 and n_2 do not appear explicitly in the final expression. For convenience, we thus write $n_3 = n$ and identify it as the toroidal mode number.

5.4.3 Gaussian eigenfunction

We now introduce the functional form of the potential. We use the ansatz that the poloidal harmonic structure is a shifted Gaussian:

$$\phi_{m_0,n}(x) \sim \phi_0 e^{-\frac{(x-x_0)^2}{2w^2}}. \tag{5.146}$$

This Gaussian corresponds to the lowest-order eigenfunction from the corresponding ballooning equation; the higher-order terms utilize the Hermite polynomials and are neglected here. This Gaussian has a complex width w and shift x_0. In the limit of no rotation, $x_0 = 0$ and the Gaussian is centered about $x = 0$. Although the amplitude ϕ_0 cannot be obtained from quasilinear theory, it factors out of the dispersion relation and does not affect the linear mode frequency calculation. Setting the amplitude will be necessary to calculate the quasilinear fluxes and requires the use of a saturation rule, which is detailed in Sec. 5.9.

To obtain expressions for w and x_0, we move into the high-frequency fluid limit. The original derivation can be found in Ref. 103 and an extensive, revised derivation can be found in Ref. 24; here, we shall only discuss the basic principle. We consider the dispersion relation

$$D\left(\omega\right) = \sum_s \int d^3v \frac{f_0 e_s^2}{T_s} \left(1 - J_{0,s}^2 \frac{\omega - n\omega_E - n\omega_{*,s}}{\omega - n\omega_E - k_\parallel v_\parallel - n\omega_{d,s}}\right) \phi_{m_0,n}(x). \tag{5.147}$$

This is the local dispersion relation obtained if we consider the strong form of Poisson's equation rather than the weak form; we do not multiply by ϕ^* and integrate over space. The Bessel function is such that $J_{0,s} = J_0\left(k_\perp \rho_s\right) J_0\left(k_r \delta_{b,s}\right)$ for trapped particles and $J_{0,s} = J_0\left(k_\perp \rho_s\right)$ for passing particles. Meanwhile, we define the parallel wave number as $k_\parallel = \left(k_\theta s x\right)/\left(q R_0\right)$. The local drift frequency $\omega_{d,s}$ is

$$\omega_{d,s} = \begin{cases} \omega_{d0,s}\xi\left(-1 + \dfrac{2E\left(\kappa\right)}{K\left(\kappa\right)} + 4s\left(\kappa^2 - 1 + \dfrac{E\left(\kappa\right)}{K\left(\kappa\right)}\right)\right. \\ \qquad\qquad \left. - \dfrac{4\alpha}{3}\left(1 - \kappa^2 - \left(1 - 2\kappa^2\right)\dfrac{E\left(\kappa\right)}{K\left(\kappa\right)}\right)\right) & \text{if trapped,} \\ \omega_{d0,s}\xi\left(2 - \lambda b\right)\left(\cos\left(\theta\right) + \left(s\theta - \alpha\sin\left(\theta\right)\right)\sin\left(\theta\right)\right) & \text{if passing.} \end{cases} \tag{5.148}$$

The passing form of the drift frequency is due to the radial structure of the eigenfunction as covered in Sec. 5.7. We also note the Fourier link in the passing drift frequency that $\theta^2 \rightarrow k_r^2 d^2$. To proceed, we take $\overline{\omega} = \omega - n\omega_E$ to be larger than $k_\parallel v_\parallel$ and $\omega_{d0,s}$, and for trapped particles we approximate $k_\parallel v_\parallel \approx 0$. We also take $\delta_{b,e} \ll \delta_{b,i}$ and $\rho_e \ll \rho_i$, where the "e" subscript is for electrons and the "i" subscript is for ions, to obtain

$$\begin{aligned} D\left(\omega\right) = \left[\frac{n_e}{T_e}\left(1 - \left\langle\left(1 - \frac{n\omega_{*,e}}{\overline{\omega}}\right)\left(1 + \frac{n\omega_{d,e}}{\overline{\omega}} + \frac{n^2\omega_{d,e}^2}{\overline{\omega}^2}\right)\right\rangle_t\right)\right. \\ + \sum_i \frac{n_i Z_i}{T_i}\left(1 - \left\langle\left(1 - \frac{n\omega_{*,i}}{\overline{\omega}}\right)\left(1 + \frac{n\omega_{d,i}}{\overline{\omega}} + \frac{n^2\omega_{d,i}^2}{\overline{\omega}^2}\right)\left(1 - \frac{k_r^2\delta_{b,i}^2}{2}\right)\left(1 - \frac{k_\theta^2\rho_i^2}{2}\right)\right\rangle_t\right. \\ - \left\langle\left(1 - \frac{n\omega_{*,i}}{\overline{\omega}}\right)\left(1 + \frac{n\omega_{d,i}}{\overline{\omega}} + \frac{k_\parallel v_\parallel}{\overline{\omega}} + \left(\frac{n\omega_{d,i}}{\overline{\omega}} + \frac{k_\parallel v_\parallel}{\overline{\omega}}\right)^2\right)\right. \\ \left.\left.\left.\times\left(1 - \frac{k_\theta^2\rho_i^2}{2} - \frac{k_r^2\rho_i^2}{2}\right)\right\rangle_p\right)\right]\phi_{m_0,n}(x), \end{aligned} \tag{5.149}$$

where Z_i is the proton number of the ion species. We define the averages over velocity space as

$$\langle g\left(\mathbf{v}\right)\rangle_t = \int_{\text{trapped}} d^3v f_0 g\left(\mathbf{v}\right), \tag{5.150}$$

$$\langle g\left(\mathbf{v}\right)\rangle_p = \int_{\text{passing}} d^3v f_0 g\left(\mathbf{v}\right). \tag{5.151}$$

Do to the θ dependent terms, this is a differential equation. We approximate the differential operators on ϕ in the limit of small mode shift x_0, leading to

$$\frac{\partial^2\phi}{\partial x^2} = \left(\frac{x^2}{w^4} - \frac{2x_0 x}{w^4} - \frac{1}{w^2}\right)\phi. \tag{5.152}$$

Next, we carry out the integrals both analytically and numerically as appropriate and multiply the dispersion relation by ω^3 to obtain a modified dispersion relation,

$$\omega^3 D\left(\omega\right) = D_0\left(\omega\right) + D_1\left(\omega\right)x + D_2\left(\omega\right)x^2 = 0. \tag{5.153}$$

Here, we separate terms proportional to x^0, x^1, and x^2. With three equations we can solve for the three unknowns (ω_0, w, x_0). We then find the solution ω_0 such that

$$D_0\left(\omega_0\right) = 0. \tag{5.154}$$

Having found this zeroth-order solution, we then find x and w such that

$$D_1\left(\omega_0\right) = 0, \tag{5.155}$$

$$D_2\left(\omega_0\right) = 0. \tag{5.156}$$

We do not cite the full solution here and direct the reader to Ref. 24 for a complete derivation. Now that we have characterized $\phi_{\mathbf{n}}$ by calculating x_0 and w, we move to the dispersion relation itself, beginning with the adiabatic term.

5.5 Adiabatic functional

We first examine the adiabatic part of the functional, as it is the simplest to treat. It takes the form

$$\mathcal{L}_0 = \sum_{n_1,n_2}\int d^3r d^3v \frac{e^2\left|\phi_{\mathbf{n}}\right|^2}{T} f_0. \tag{5.157}$$

Here, we have suppressed the subscript s as we will be working with each species independently. We first define a new function $\phi_n = \phi_n(\alpha_1, \alpha_2, \mathbf{J})$ such that

$$\phi_n = \int_{-\pi}^{\pi} \frac{d\alpha_3}{2\pi} \phi(\mathbf{r}) e^{-in\alpha_3} = \sum_{n_1,n_2} \phi_{\mathbf{n}} e^{i(n_1\alpha_1 + n_2\alpha_2)}. \tag{5.158}$$

We then note due to the orthogonality of the Fourier series that

$$\int_{-\pi}^{\pi} \frac{d\alpha_1}{2\pi} \int_{-\pi}^{\pi} \frac{d\alpha_2}{2\pi} |\phi_n|^2 = \sum_{n_1,n_2} |\phi_{\mathbf{n}}|^2 . \tag{5.159}$$

Thus, it is more convenient to switch back to action-angle coordinates for an intermediate calculation:

$$\mathcal{L}_0 = \sum_{n_1,n_2} \int d^3\alpha d^3J \frac{e^2 |\phi_{\mathbf{n}}|^2}{mT} f_0 = \sum_{n_1,n_2} \int 4\pi^2 d\alpha_3 d^3J \frac{e^2 |\phi_{\mathbf{n}}|^2}{mT} f_0 = \int 4\pi^2 d\alpha_3 d^3J \frac{e^2 |\phi_n|^2}{mT} f_0. \tag{5.160}$$

This then simplifies to

$$\mathcal{L}_0 = \int 4\pi^2 d\alpha_3 d^3J \frac{e^2}{mT} f_0 \int_{-\pi}^{\pi} \frac{d\alpha_1}{2\pi} \int_{-\pi}^{\pi} \frac{d\alpha_2}{2\pi} |\phi_n|^2 = \int d^3r d^3v \frac{e^2 |\phi_n|^2}{T} f_0. \tag{5.161}$$

The velocity space integration is straightforward,

$$\mathcal{L}_0 = \int d^3r d^3v \frac{e^2 |\phi_n|^2}{T} f_0 = \int d^3r \frac{e^2 n_0 |\phi_n|^2}{T}, \tag{5.162}$$

so all that is left is the spatial integration. Because we use toroidal coordinates, the differential volume element is

$$d^3r = rR_0 \left(1 + \epsilon \cos(\theta)\right) dr d\theta d\varphi. \tag{5.163}$$

We proceed to calculating ϕ_n using the poloidal harmonic expansion as detailed in Sec. 5.4,

$$\phi(r, \theta, \varphi) = \sum_{m,n} \phi_{m,n}(r - r_0) e^{i(m\theta + n\varphi)}. \tag{5.164}$$

When we examined the trapped Fourier modes, we already calculated ϕ_n. We simply need to generalize it for passing particles as well, resulting in

$$\phi_n = \sum_{m} \phi_{m,n}(r - r_0) e^{i(m\theta + nq(\bar{r})\tilde{\theta} + n\tilde{\varphi})}. \tag{5.165}$$

As before, we only keep the poloidal harmonic corresponding to $m_0 = -nq_0$ and expand the limits of integration for r to compensate. The result is

$$|\phi_n|^2 = \left|\phi_{m_0,n}(r - r_0)\right|^2 . \tag{5.166}$$

Because the integrand in the adiabatic functional now only depends on r, the integral simplifies to

$$\mathcal{L}_0 = \int_{-\infty}^{\infty} (2\pi R_0)\, 2\pi r dr \frac{e^2 n_0}{T} \left|\phi_{m_0,n}(r - r_0)\right|^2 \approx \int dx R_0 r_0\, (2\pi)^2\, \frac{e^2 n_0}{T} \left|\phi_{m_0,n}(x)\right|^2 . \tag{5.167}$$

Here, we make use of the localization approximation which transforms the factor of r in the integrand into r_0. Due to the Gaussian structure of $\phi_{m_0,n}$, this integral is easily performed and we find that

$$\mathcal{L}_0 = 4\pi^2 R_0 r_0 \left|\phi_0\right|^2 |w|^2 \exp\left(\frac{\mathrm{Im}\,(x_0)^2}{\mathrm{Re}\,(w^2)}\right) \sqrt{\frac{\pi}{\mathrm{Re}\,(w^2)}}. \tag{5.168}$$

Now that we have calculated the adiabatic functional, we next calculate the trapped functional.

5.6 Trapped functional

The trapped part of the dispersion relation reads

$$\mathcal{L}_{\text{trapped}} = \sum_{n_1,n_2} \int d^3 r d^3 v \frac{e^2}{T} f_0 \left(\frac{\mathbf{n}\cdot\boldsymbol{\omega}_* + \mathbf{n}\cdot\boldsymbol{\omega}_E - \omega}{\mathbf{n}\cdot\boldsymbol{\Omega} - \omega}\right) |\phi_{\mathbf{n}}|^2. \tag{5.169}$$

We emphasize that although this aspect of the derivation is collisionless, QuaLiKiz includes collisions for trapped electrons. Strictly speaking, this section concerns trapped ions. The majority of the derivation remains the same for trapped electrons, the key difference being that the eventual integral over the particle energy cannot be analytically simplified.

The first step is to determine the appropriate variables to integrate over. For the spatial variables, we use once again use toroidal coordinates,

$$d^3 r = R_0 \bar{r}\, (1 + \epsilon \cos(\theta))\, d\bar{r} d\theta d\varphi. \tag{5.170}$$

For velocity space, we use the variables $\left(v, \lambda, v_\phi\right)$ which correspond to the speed v, pitch angle

parameter λ, and cylindrical velocity phase v_ϕ. The result is

$$d^3v = \sum_{\epsilon_\parallel} v^2 \frac{b}{2\sqrt{1-\lambda b}} dv d\lambda dv_\phi, \tag{5.171}$$

where the sum over $\epsilon_\parallel$ accounts for both possible signs of the parallel velocity. Because the integrand is independent of φ or v_ϕ, we obtain

$$d^3r d^3v = \sum_{\epsilon_\parallel} 2\pi^2 R_0 \bar{r} \left(1 + \epsilon \cos(\theta)\right) d\bar{r} d\theta v^2 \frac{b}{\sqrt{1-\lambda b}} dv d\lambda. \tag{5.172}$$

It is important to note that the limits of integration depend on the order of integration. For a given θ, the pitch angle parameter λ for a trapped particle is bounded by

$$\frac{1-\epsilon}{1+\epsilon} \leq \lambda \leq \frac{1+\epsilon\cos(\theta)}{1+\epsilon}. \tag{5.173}$$

The lower bound corresponds to the trapped-passing boundary, while the upper bound corresponds to a particle that has $v_\parallel = 0$ at a given angle θ. We can, however, exchange the order of integration as follows:

$$\int_0^{2\pi} d\theta \int_{\frac{1-\epsilon}{1+\epsilon}}^{\frac{1+\epsilon\cos(\theta)}{1+\epsilon}} d\lambda f(\theta,\lambda) = \int_{\frac{1-\epsilon}{1+\epsilon}}^{1} d\lambda \int_{-\theta_b}^{\theta_b} d\theta f(\theta,\lambda). \tag{5.174}$$

We recall that the definition of a bounce average is

$$\left\langle G(\epsilon_\parallel,\theta)\right\rangle = \frac{\int_{-\theta_b}^{\theta_b} d\theta \frac{G(\epsilon_\parallel,\theta)+G(-\epsilon_\parallel,\theta)}{\sqrt{1-\lambda b}}}{\int_{-\theta_b}^{\theta_b} \frac{2d\theta}{\sqrt{1-\lambda b}}} = \sum_{\epsilon_\parallel} \frac{\overline{\Omega}_2}{2\pi} \int_{-\theta_b}^{\theta_b} d\theta \frac{G(\epsilon_\parallel,\theta)}{\sqrt{1-\lambda b}}. \tag{5.175}$$

By exchanging our limits of integration and integrating over θ first, part of the trapped functional simplifies to become a bounce average.

Next, we approximate the equilibrium distribution function assuming the Mach number $U_\parallel \,/\, c_s$ is small, where $c_s = \sqrt{T/m}$ is the sound speed. Since the electron and ion rotation velocity is quite small compared to the sound speed in tokamak plasmas, expanding to second-order in the Mach number will be sufficient. The distribution function then simplifies to

$$f_0 \approx n_0 \left(\frac{m}{2\pi T}\right)^{3/2} e^{-\xi} \left(1 + \frac{2v_\parallel U_\parallel}{v_T^2} + \frac{U_\parallel^2}{v_T^2}\left(\frac{2v_\parallel^2}{v_T^2} - 1\right)\right). \tag{5.176}$$

Moreover, because $|\Omega_1|, |\Omega_2| \gg |\omega|$, we can approximate this integral by truncating the sum at $n_1 = n_2 = 0$. We also perform a change of variables from v to ξ to obtain

$$\mathcal{L}_{\text{trapped}} = \int d\bar{r} d\lambda d\xi \, (2\pi)^2 \frac{n_0 e^2}{T} \frac{R_0 \bar{r}}{\sqrt{\pi}} \frac{\sqrt{\xi} e^{-\xi}}{\bar{\Omega}_2} \times \frac{\left\langle (\mathbf{n} \cdot \boldsymbol{\omega}_* + \mathbf{n} \cdot \boldsymbol{\omega}_E - \omega) \left(1 + \frac{2v_\parallel U_\parallel}{v_T^2} + \frac{U_\parallel^2}{v_T^2} \left(\frac{2v_\parallel^2}{v_T^2} - 1\right)\right)\right\rangle}{n\Omega_3 - \omega} \left|\phi_{0,0,n}\right|^2 . \tag{5.177}$$

The Bessel functions from the gyromotion and the banana motion are implicit in $\phi_{0,0,n}$. We next simplify the partial derivatives with respect to $\mathbf{J}$. Because $n_1 = n_2 = 0$, we only keep the partial derivative with respect to J_3. Knowing that $J_3 = J_3(\bar{r})$, we perform a change in variables from J_3 to $\bar{r}$ and find that

$$\frac{\partial g}{\partial J_3} = \frac{\partial g}{\partial \bar{r}} \frac{d\bar{r}}{dJ_3} \approx \frac{-R_0 \omega_{d0}}{T} \frac{\partial g}{\partial \bar{r}}, \tag{5.178}$$

where g is a generic scalar function. We then define the following normalized gradients:

$$A_n = -\frac{R_0}{n} \frac{dn}{d\bar{r}}, \tag{5.179}$$

$$A_T = -\frac{R_0}{T} \frac{dT}{d\bar{r}}, \tag{5.180}$$

$$A_U = -\frac{R_0}{v_T} \frac{dU_\parallel}{d\bar{r}}. \tag{5.181}$$

To perform the bounce average, we note that only $v_\parallel$ is dependent on θ. We perform the calculation explicitly to find that

$$\left\langle v_\parallel \right\rangle = \left\langle v_\parallel^3 \right\rangle = 0, \tag{5.182}$$

$$\left\langle v_\parallel^2 \right\rangle = \frac{4E\epsilon}{m} \frac{\left(E(\kappa) - \left(1 - \kappa^2\right) K(\kappa)\right)}{K(\kappa)} = v_T^2 \xi H(\kappa), \tag{5.183}$$

where we define

$$H(\kappa) = \frac{2\epsilon \left(E(\kappa) - \left(1 - \kappa^2\right) K(\kappa)\right)}{K(\kappa)}. \tag{5.184}$$

To simplify our expressions, we also fold $\mathbf{n} \cdot \boldsymbol{\omega}_E$ into the mode frequency such that

$$\bar{\omega} = \omega - \mathbf{n} \cdot \boldsymbol{\omega}_E \approx \omega - n\omega_E \approx \omega - n\omega_{E0} - n\omega_E' x, \tag{5.185}$$

where, as discussed earlier, we Taylor expand ω_E about $x = 0$ and $\partial_r \omega_E = \omega'_E$ is related to the radial electric shear. Rather than including x fully, we instead approximate the term by averaging it over the Gaussian eigenfunctions:

$$\langle x \rangle_r = \frac{\int_{-\infty}^{\infty} dx \left|\phi_{m_0,n}(x)\right|^2 x}{\int_{-\infty}^{\infty} dx \left|\phi_{m_0,n}(x)\right|^2} = \mathrm{Re}(x_0) + \frac{\mathrm{Im}(x_0)\,\mathrm{Im}\left(w^2\right)}{\mathrm{Re}\left(w^2\right)}. \tag{5.186}$$

We then obtain

$$\overline{\omega} \approx \omega - n\omega_{E0} - n\omega'_E \langle x \rangle_r . \tag{5.187}$$

Ignoring all terms that are order cubic or higher with the Mach number, we then find that

$$\left\langle (\mathbf{n}\cdot\boldsymbol{\omega}_* + \mathbf{n}\cdot\boldsymbol{\omega}_E - \omega)\left(1 + \frac{2v_\parallel U_\parallel}{v_T^2} + \frac{U_\parallel^2}{v_T^2}\left(\frac{2v_\parallel^2}{v_T^2} - 1\right)\right)\right\rangle = n\omega_{d0}\left(\mathcal{A}_t + \mathcal{B}_t\xi + C_t\xi^2\right), \tag{5.188}$$

where

$$\mathcal{A}_t = \left(1 - \frac{U_\parallel^2}{v_T^2}\right)\left(A_n - \frac{3}{2}A_T - z^2 F_d(\kappa)\right) - \frac{U_\parallel}{v_T}\left(2A_U - \frac{U_\parallel}{v_T}A_T\right), \tag{5.189}$$

$$\begin{aligned}\mathcal{B}_t &= \left(1 - \frac{U_\parallel^2}{v_T^2}\right)A_T + 4A_U\frac{U_\parallel}{v_T}H(\kappa) + \frac{U_\parallel^2}{v_T^2}H(\kappa)\left(2A_n - 7A_T - 2z^2F_d(\kappa)\right)\\ &\approx \left(1 - \frac{U_\parallel^2}{v_T^2}\right)A_T + 4A_U\frac{U_\parallel}{v_T}H(\kappa),\end{aligned} \tag{5.190}$$

$$C_t = 2A_T\frac{U_\parallel^2}{v_T^2}H(\kappa) \approx 0. \tag{5.191}$$

Here, we have defined

$$z^2 = \frac{\overline{\omega}}{n\omega_{d0}F_d(\kappa)}. \tag{5.192}$$

Moreover, we take note that $H(\kappa) \sim \mathcal{O}(\epsilon)$; since the inverse aspect ratio ϵ is small, we can safely ignore all terms proportional to $U_\parallel^2 H(\kappa)/v_T^2$.

Substituting the above into the integrand, we obtain

$$\mathcal{L}_{\mathrm{trapped}} = \int d\bar{r}\,d\lambda\,d\xi\,(2\pi)^2\frac{n_0e^2}{T}\frac{R_0\bar{r}}{\sqrt{\pi}}\frac{\sqrt{\xi}e^{-\xi}}{\overline{\Omega}_2}\left|\phi_{0,0,n}\right|^2\frac{\mathcal{A}_t + \mathcal{B}_t\xi}{F_d(\kappa)\left(\xi - z^2\right)}. \tag{5.193}$$

Due to the localization of the mode, we evaluate any functions of $\bar{r}$ at r_0 in the above expression aside from the electrostatic potential. We then rewrite the trapped functional as

$$\mathcal{L}_{\text{trapped}} = \int d\bar{r} d\lambda d\xi \, (2\pi)^2 \frac{n_0 e^2}{T} \frac{R_0 r_0}{\sqrt{\pi}} \frac{\sqrt{\xi} e^{-\xi}}{\overline{\Omega}_2} \left| J_0 \left(k_\perp \rho \right) J_0 \left(k_r \delta_b \right) \cdot \phi_{m_0,n} \right|^2 \frac{\mathcal{A}_t + \mathcal{B}_t \xi}{F_d \left(\kappa \right) \left(\xi - z^2 \right)}. \tag{5.194}$$

The gyromotion and bounce motion appear in two separate Bessel functions. Since the only explicit radial dependence is contained in the electrostatic potential, we can change variables using Parseval's theorem to integrate over k_r,

$$\int_{-\infty}^{\infty} dx f(x) g(x)^* = \int_{-\infty}^{\infty} \frac{dk_r}{2\pi} \hat{f}(k_r) \hat{g}(k_r)^*. \tag{5.195}$$

After transforming to Fourier space, we treat the Bessel functions as normal scalar functions instead of differential operators. We next note that the Bessel functions are dependent on velocity through the gyroradius and banana width,

$$\rho = \frac{v_\perp}{\Omega_1}, \tag{5.196}$$

$$\delta_b \approx \frac{q}{\sqrt{\epsilon}} \rho. \tag{5.197}$$

We approximate this energy dependence by averaging each Bessel function separately over velocity space using a Maxwellian distribution. Doing so allows us to retain finite Larmor radius and finite banana width effects while also making the energy and pitch angle integration tractable. We find that

$$\frac{\int d^3 v J_0 \left(k_\perp \rho \right)^2 f_0}{\int d^3 v f_0} = e^{-\frac{k_\perp^2 \rho_{\text{th}}^2}{2}} I_0 \left(\frac{k_\perp^2 \rho_{\text{th}}^2}{2} \right) = \Gamma_0 \left(k_\perp \rho_{\text{th}} \right), \tag{5.198}$$

where I_0 is a modified Bessel function of the first kind and the characteristic thermal gyroradius ρ_{th} is defined as

$$\rho_{\text{th}} = \frac{\sqrt{2T/m}}{\Omega_1}. \tag{5.199}$$

Similarly, for the average over the banana orbit we obtain

$$\frac{\int d^3 v J_0 \left(k_\perp \rho \right)^2 f_0}{\int d^3 v f_0} = e^{-\frac{k_\perp^2 \delta_{b,\text{th}}^2}{2}} I_0 \left(\frac{k_\perp^2 \delta_{b,\text{th}}^2}{2} \right) = \Gamma_0 \left(k_\perp \delta_{b,\text{th}} \right), \tag{5.200}$$

where the thermal banana width is

$$\delta_{b,\mathrm{th}} = \frac{q}{\sqrt{\epsilon}}\rho_{\mathrm{th}}. \tag{5.201}$$

Note that $k_\perp^2$ is written as

$$k_\perp^2 = k_r^2 + k_\theta^2 = k_r^2 + \frac{n^2 q_0^2}{r_0^2}, \tag{5.202}$$

where we have evaluate k_θ at r_0. That $k_\theta^2 = n^2 q^2/r^2$ comes from differentiating with respect to θ in the ballooning expansion due to the eikonal term. Because the k_r dependence is now completely separable from the κ and ξ dependence, we write the trapped functional as

$$\begin{aligned}\mathcal{L}_{\mathrm{trapped}} = \int d\lambda d\xi\, (2\pi)^2 \frac{n_0 e^2}{T}\frac{R_0 r_0}{\sqrt{\pi}}\frac{\sqrt{\xi}e^{-\xi}}{\overline{\Omega}_2}\frac{\mathcal{A}_t + \mathcal{B}_t\xi}{F_d(\kappa)\left(\xi - z^2\right)} \\ \times \int_{-\infty}^{\infty}\frac{dk_r}{2\pi}\Gamma_0\left(k_\perp\rho_{\mathrm{th}}\right)\Gamma_0\left(k_r\delta_{b,\mathrm{th}}\right)\left|d\hat{\phi}_n\left(k_r d\right)\right|^2,\end{aligned} \tag{5.203}$$

where $\hat{\phi}_n$ is computed using a Fourier transform:

$$\hat{\phi}_n\left(k_r d\right) = \sqrt{2\pi} w \phi_0 e^{-\frac{k_r^2 w^2}{2}} e^{ik_r x_0}. \tag{5.204}$$

We next simplify the integral over ξ, which is of the form

$$\int_0^\infty d\xi \frac{\sqrt{\xi}}{\sqrt{\pi}}\frac{\mathcal{A}_t + \mathcal{B}\xi}{\xi - z^2}e^{-\xi} = \int_{-\infty}^{\infty} du \frac{u^2}{\sqrt{\pi}}\frac{\mathcal{A}_t + \mathcal{B}_t u^2}{(u+z)(u-z)}e^{-u^2}, \tag{5.205}$$

where we performed the change of variables $\xi = u^2$. Using the plasma dispersion function detailed in Appendix 5.A, this simplifies to

$$\int_{-\infty}^{\infty} du \frac{u^2}{\sqrt{\pi}}\frac{\mathcal{A}_t + \mathcal{B}_t u^2}{(u+z)(u-z)}e^{-u^2} = \mathcal{A}_t G_2(z,-z) + \mathcal{B}_t G_4(z,-z) = \frac{\mathcal{A}_t Z_2(z) + \mathcal{B}_t Z_4(z)}{z}, \tag{5.206}$$

where the final simplification is made using the fact that Z_{2n} is an even function for $n \geq 0$. Meanwhile, we rewrite the integration over λ with a change in variables,

$$\frac{d\lambda}{\overline{\Omega}_2} = 4 f_t K(\kappa)\kappa d\kappa, \tag{5.207}$$

where we utilize the transformation

$$\lambda \approx 1 - 2\epsilon\kappa^2 \tag{5.208}$$

and define the flux surface averaged trapped particle fraction

$$f_t = \frac{2\sqrt{2\epsilon}}{\pi}. \tag{5.209}$$

Thus, the trapped functional simplifies to

$$\mathcal{L}_{\text{trapped}} = (2\pi)^3 \frac{e^2 n_0}{T} r_0 R_0 f_t \left\langle \mathcal{I}_t \right\rangle_{\xi,\kappa} \left\langle \Gamma_0 \left(k_\perp \rho_{\text{th}}\right) \Gamma_0 \left(k_r \delta_{b,\text{th}}\right) \left| d\hat{\phi}\left(k_r d\right)\right|^2 \right\rangle_{k_r}, \tag{5.210}$$

where

$$\left\langle \mathcal{I}_t \right\rangle_{\xi,\kappa} = \frac{2}{\pi} \int_0^1 d\kappa \frac{K\left(\kappa\right)\kappa}{z F_d\left(\kappa\right)} \left(\mathcal{A}_t Z_2\left(z\right) + \mathcal{B}_t Z_4\left(z\right)\right) \tag{5.211}$$

and

$$\left\langle \Gamma_0 \left(k_\perp \rho_{\text{th}}\right) \Gamma_0 \left(k_r \delta_{b,\text{th}}\right) \left| d\hat{\phi}\left(k_r d\right)\right|^2 \right\rangle_{k_r} = \int_{-\infty}^{\infty} \frac{dk_r}{2\pi} \Gamma_0 \left(k_\perp \rho_{\text{th}}\right) \Gamma_0 \left(k_r \delta_{b,\text{th}}\right) \left| d\hat{\phi}\left(k_r d\right)\right|^2. \tag{5.212}$$

The remaining integrals are to be calculated numerically, where we note that z is a function of both $\overline{\omega}$ and κ. Thus, the trapped functional is the product of two separate 1-dimensional integrals, one of which is ω independent; we therefore characterize the trapped functional as a 1-dimensional integral that must be calculated numerically. Now that we have simplified the expression for the trapped functional, we turn to calculating the passing functional.

5.7 Passing functional

The passing part of the dispersion relation reads

$$\mathcal{L}_{\text{passing}} = \sum_{n_1,n_2} \int d^3 r d^3 v \frac{e^2}{T} f_0 \left(\frac{\mathbf{n}\cdot\boldsymbol{\omega}_* + \mathbf{n}\cdot\boldsymbol{\omega}_E - \omega}{\mathbf{n}\cdot\boldsymbol{\Omega} - \omega}\right) |\phi_{\mathbf{n}}|^2. \tag{5.213}$$

We reuse many of the same arguments in Sec. 5.6 regarding changes in variables and approximating the equilibrium distribution function. One key difference is that instead of the bounce average, we use the transit average

$$\left\langle G\left(\epsilon_\parallel, \theta\right)\right\rangle = \frac{\int_{-\pi}^{\pi} d\theta \frac{G\left(\epsilon_\parallel,\theta\right)}{\sqrt{1-\lambda b}}}{\int_{-\pi}^{\pi} \frac{d\theta}{\sqrt{1-\lambda b}}} = \frac{\overline{\Omega}_2}{2\pi} \int_{-\pi}^{\pi} d\theta \frac{G\left(\epsilon_\parallel,\theta\right)}{\sqrt{1-\lambda b}}. \tag{5.214}$$

We note here that the bounce angle θ_b is set to π and that we do not perform a sum over $\epsilon_\parallel$ to compute the transit average. Moreover, the integration bounds for λ are such that

$$0 \leq \lambda \leq \frac{1-\epsilon}{1+\epsilon}. \tag{5.215}$$

These bounds hold regardless of whether we integrate over θ before or after integrating over λ. Since they are independent of θ, the order of integration of the two variables can be freely interchanged. As in the trapped case, we only keep $n_1 = 0$ since $|\Omega_1| \gg |\omega|$. As discussed in Sec. 5.4, n_2 refers to the poloidal harmonic. We keep only $n_2 = m_0$ and use the approximation that

$$m_0 + nq\left(\bar{r}\right) \approx \frac{x}{d}. \tag{5.216}$$

In the resonant denominator we then obtain

$$n\Omega_3 + m_0\Omega_2 - \omega \approx n\omega_{d0}\xi F + \frac{x}{d}\Omega_2 + n\omega_{E0} + n\omega_E' x - \omega, \tag{5.217}$$

where we also expand ω_E about $x = 0$. The passing functional is then

$$\begin{aligned}\mathcal{L}_{\text{passing}} = \sum_{\epsilon_\parallel} \int d\bar{r} d\lambda d\xi \left(2\pi\right)^2 \frac{n_0 e^2}{T} \frac{R_0 \bar{r}}{\sqrt{\pi}} \frac{\sqrt{\xi} e^{-\xi}}{\bar{\Omega}_2} \\ \times \frac{\left\langle \left(\mathbf{n}\cdot\boldsymbol{\omega}_* + n\omega_{E0} + n\omega_E' x - \omega\right)\left(1 + \frac{2v_\parallel U_\parallel}{v_T^2} + \frac{U_\parallel^2}{v_T^2}\left(\frac{2v_\parallel^2}{v_T^2} - 1\right)\right)\right\rangle}{n\omega_{d0}\xi F + \frac{x}{d}\Omega_2 + n\omega_{E0} + n\omega_E' x - \omega} \left|\phi_{0,m_0,n}\right|^2.\end{aligned} \tag{5.218}$$

Here, we have evaluated all functions at $r = r_0$ except for the terms proportional to x in the resonant denominator and numerator. These terms must be kept if we wish to take into account the effects of the poloidal motion as well as the radial electric field shear. We now evaluate the integration over $\bar{r}$ while leaving aside the term proportional to x in the numerator.

To proceed, we use Parseval's theorem to integrate over α_2 instead of $\bar{r}$,

$$\int_{-\infty}^{\infty} d\bar{r} f(\bar{r}) g(\bar{r})^* = \int_{-\infty}^{\infty} \frac{d\alpha_2}{2\pi} |d| \hat{f}(\alpha_2)\hat{g}(\alpha_2)^*. \tag{5.219}$$

For convenience, we compute the radial integral in isolation and relabel variables,

$$\int_{-\infty}^{\infty} d\bar{r} \frac{1}{a\frac{x}{d} - b} \left|\phi_{0,m_0,n}\right|^2 = \int_{-\infty}^{\infty} \frac{d\alpha_2}{2\pi} |d| \mathcal{F}\left(\frac{\phi_{0,m_0,n}}{a\frac{x}{d} - b}\right) \mathcal{F}\left(\phi_{0,m_0,n}\right)^*. \tag{5.220}$$

We calculated in Sec. 5.4 that

$$\mathcal{F}\left(\phi_{0,m_0,n}\right) = J_0(k_\perp(\alpha_2)\rho)\hat{\phi}_n(\theta(\alpha_2))e^{in\tilde{\varphi}(\alpha_2)-i\frac{\tilde{r}(\alpha_2)}{d}\theta(\alpha_2)}. \tag{5.221}$$

We note that $k_\perp$ is defined such that

$$k_\perp\left(\alpha_2\right)^2 = \frac{\theta\left(\alpha_2\right)^2}{d^2} + \frac{n^2 q_0^2}{r_0^2}. \tag{5.222}$$

We next use the convolution theorem to calculate the other Fourier transform,

$$\mathcal{F}\left(\frac{\phi_{0,m_0,n}}{a\frac{x}{d}-b}\right) = \frac{1}{2\pi}\mathcal{F}\left(\phi_{0,m_0,n}\right) * \mathcal{F}\left(\frac{1}{a\frac{x}{d}-b}\right). \tag{5.223}$$

Computing the Fourier transform of both functions and performing the convolution, we find that

$$\begin{aligned}\mathcal{F}\left(\phi_{0,m_0,n}\frac{1}{1+a\frac{x}{d}-b}\right) = \int_{-\infty}^{\infty} d\alpha_2' \frac{i}{|a|}\Theta\left(\frac{\alpha_2-\alpha_2'}{a}\right) J_0(k_\perp(\alpha_2')\rho)\hat{\phi}_n(\theta(\alpha_2')) \\ \times e^{\frac{-ib}{a}\left(\alpha_2'-\alpha_2\right)} e^{in\tilde{\varphi}(\alpha_2')-i\frac{\tilde{r}(\alpha_2)}{d}\theta(\alpha_2')},\end{aligned} \tag{5.224}$$

where Θ is the Heaviside step function. Here, we have assumed that $\mathrm{Im}\left(b\right) > 0$. This is justified since $b \sim \omega$ and we are only interested in positive growth rates. Combining the results, we obtain for the passing integral $I_{p,r}$ that

$$\begin{aligned}I_{p,r} = \int d\bar{r}\frac{1}{a\frac{x}{d}-b}\left|\phi_{0,m_0,n}\right|^2 = \int \frac{d\alpha_2 d\alpha_2'}{2\pi}\frac{i|d|}{|a|}\Theta\left(\frac{\alpha_2-\alpha_2'}{a}\right) J_0^*(k_\perp(\alpha_2)\rho)J_0(k_\perp(\alpha_2')\rho) \\ \times \hat{\phi}_n(\theta(\alpha_2))^*\hat{\phi}_n(\theta(\alpha_2'))e^{\Lambda(\alpha_2)-\Lambda(\alpha_2')},\end{aligned} \tag{5.225}$$

where

$$\Lambda(\alpha_2) = i\left(\frac{b}{a}\alpha_2 - n\tilde{\varphi}\left(\alpha_2\right) + \frac{\tilde{r}\left(\alpha_2\right)}{d}\theta\left(\alpha_2\right)\right). \tag{5.226}$$

We then substitute in

$$a = \Omega_2 + nd\omega_E', \tag{5.227}$$

$$b = \omega - n\omega_{d0}\xi F - n\omega_{E0} \tag{5.228}$$

and rewrite the eikonal term to obtain

$$\Lambda(\alpha_2) = i\left(\frac{\omega - n\omega_{d0}\xi F - n\omega_{E0}}{\Omega_2 + nd\omega_E'}\alpha_2 - n\tilde{\varphi}\left(\alpha_2\right) + \frac{\tilde{r}\left(\alpha_2\right)}{d}\theta\left(\alpha_2\right)\right). \tag{5.229}$$

It is important to recognize the physical importance of Λ. In the ballooning representation, we encoded a certain particle trajectory in the eikonal that differs from the magnetic drift trajectory. The function Λ encapsulates the phase difference between these two trajectories.

Before proceeding, we must recognize that integrating over α_2 and α_2' is inconvenient. The function $\hat{\phi}_n$ has Gaussian structure in θ, but not in α_2. Thus, the next goal is to write the integrand in terms of θ and θ'. First, we introduce new variables,

$$\theta_+ = \frac{\theta + \theta'}{2}, \tag{5.230}$$

$$\theta_- = \theta - \theta'. \tag{5.231}$$

We next Taylor expand the terms in the exponential around θ_+ to find that

$$\Lambda(\alpha_2) - \Lambda(\alpha_2') \approx \theta_- \frac{d\alpha_2}{d\theta}\left(\theta = \theta_+\right)\Lambda'\left(\theta = \theta_+\right), \tag{5.232}$$

where Λ' denotes the derivative of Λ with respect to α_2. Due to the rapidly varying phase in the exponential, the factor of $i\omega \sim -\gamma$ in the exponential, and the Gaussian integrand, we ignore higher order terms to obtain the dominant contribution. From the equations listed in Sec. 5.2, we find

$$\frac{d}{d\alpha_2}\left(n\tilde{\varphi} - \frac{\tilde{r}}{d}\theta\right) = \frac{n}{\Omega_2}\left(\mathbf{v}_D \cdot \nabla\varphi - q\mathbf{v}_D \cdot \nabla\theta - \theta\frac{dq}{d\psi}\mathbf{v}_D \cdot \nabla\psi - \Omega_d\right). \tag{5.233}$$

The leading terms can be computed explicitly in much the same manner as when calculating the magnetic precession frequency,

$$\begin{aligned}\overline{\Omega}_d &= \mathbf{v}_D \cdot \nabla\varphi - q\mathbf{v}_D \cdot \nabla\theta - \theta\frac{dq}{d\psi}\mathbf{v}_D \cdot \nabla\psi \\ &= \omega_{d0}\xi\left(2 - \lambda b\right)\left(\cos\left(\theta\right) + \left(s\theta - \alpha\sin\left(\theta\right)\sin^2\left(\theta\right)\right)\right) + \frac{qE_r}{rB}.\end{aligned} \tag{5.234}$$

Although somewhat similar to the magnetic drift frequency proper, there are two key differences. Firstly, the magnetic shear term is different and proportional to $\theta\sin\left(\theta\right)$. Secondly, this frequency is explicitly θ dependent and no bounce-transit average is performed. In carrying out the calculation the bounce-averaged magnetic drift terms partially cancel; for sufficiently small radial electric field shear we obtain

$$\Lambda\left(\alpha_2\right) - \Lambda\left(\alpha_2'\right) \approx -i\theta_-\left(\frac{n\overline{\Omega}_d\left(\theta_+\right) - \omega}{\Omega_2 + nd\omega_E'}\right), \tag{5.235}$$

where

$$n\overline{\Omega}_d \approx n\omega_{d0}\xi\left(2-\lambda b\right)\left(\cos\left(\theta\right)+\left(s\theta-\alpha\sin\left(\theta\right)\sin^2\left(\theta\right)\right)\right)+n\omega_{E0}. \tag{5.236}$$

We next change the variables of integration from α_2, α_2' to θ, θ' using

$$\frac{d\theta}{d\alpha_2}=\frac{\sqrt{1-\lambda b}}{\overline{\Omega}_2}. \tag{5.237}$$

The integral then becomes

$$\begin{aligned} I_{p,r}=\int\frac{d\theta d\theta'}{2\pi}\frac{i\left|d\right|}{\left|\Omega_2+nd\omega_E'\right|}\Theta\left(\frac{\theta_-}{\Omega_2+nd\omega_E'}\right)J_0\hat{\phi}_n(\theta)^*J_0'\hat{\phi}_n(\theta') \\ \times\frac{\overline{\Omega}_2}{\sqrt{1-\lambda b(\theta)}}\frac{\overline{\Omega}_2}{\sqrt{1-\lambda b(\theta')}}e^{-i\theta_-\frac{\overline{\Omega}_2}{\sqrt{1-\lambda b(\theta_+)}}\left(\frac{n\overline{\Omega}_d(\theta_+)-\omega}{\Omega_2+nd\omega_E'}\right)}, \end{aligned} \tag{5.238}$$

where the Bessel functions are evaluated in terms of θ and θ'. We now substitute in an expression for $\hat{\phi}_n$ in terms of a Fourier transform to obtain

$$\begin{aligned} I_{p,r}=\int\frac{d\theta d\theta' dxdx'}{2\pi}\frac{i\overline{\Omega}_2^2}{\left|\Omega_2+nd\omega_E'\right|\left|d\right|}\Theta\left(\frac{\theta_-}{\Omega_2+nd\omega_E'}\right)J_0\phi_{m_0,n}^*(x)J_0'\phi_{m_0,n}(x') \\ \times\frac{e^{-i\theta_-\frac{\overline{\Omega}_2}{\sqrt{1-\lambda b(\theta_+)}}\left(\frac{n\overline{\Omega}_d(\theta_+)-\omega}{\Omega_2+nd\omega_E'}\right)}e^{-i\frac{\theta x}{d}}e^{i\frac{\theta' x'}{d}}}{\sqrt{1-\lambda b\left(\theta\right)}\sqrt{1-\lambda b\left(\theta'\right)}}. \end{aligned} \tag{5.239}$$

We then make the following substitutions

$$x_+=\frac{x+x'}{2}, \tag{5.240}$$

$$x_-=x-x', \tag{5.241}$$

$$k_+=\frac{\theta_+}{\left|d\right|}, \tag{5.242}$$

$$k_-=\frac{\theta_-}{\left|d\right|}, \tag{5.243}$$

$$d\theta d\theta' dxdx'=dk_+dk_-dx_+dx_-\left|d\right|^2, \tag{5.244}$$

$$\frac{\theta' x'}{d}-\frac{\theta x}{d}=\left(-k_-x_+-k_+x_-\right)\frac{\left|d\right|}{d}, \tag{5.245}$$

to obtain

$$I_{p,r} = \int \frac{dk_+ dk_- dx_+ dx_-}{2\pi} \frac{i\,|d|\left(\overline{\Omega}_2\right)^2}{|\Omega_2 + nd\omega'_E|} \Theta\left(\frac{k_-}{\Omega_2 + nd\omega'_E}\right) J_0 \phi^*_{m_0,n}\left(x_+ + \frac{x_-}{2}\right) J'_0 \phi_{m_0,n}\left(x_+ - \frac{x_-}{2}\right) \times \frac{\exp\left(\frac{-ik_-|d|\overline{\Omega}_2}{\sqrt{1-\lambda b(k_+|d|)}}\left(\frac{n\overline{\Omega}_d(k_+|d|)-\omega}{\Omega_2+nd\omega'_E}\right)\right) e^{-i(k_- x_+ + k_+ x_-)\frac{|d|}{d}}}{\sqrt{1-\lambda b\left(k_+|d| + \frac{k_-|d|}{2}\right)}\sqrt{1-\lambda b\left(k_+|d| - \frac{k_-|d|}{2}\right)}}. \tag{5.246}$$

At first glance, it seems like we have only made the derivation more difficult. We are now performing a 4-dimensional integration over variables which do not have a convenient Gaussian structure. Fortunately, this simplifies. First, we notice that the integration over k_- via an integration by parts procedure. In general, for a complex parameter c we obtain

$$\begin{aligned}\int_a^b ds g(s) e^{ics} &= \int_a^b ds \frac{1}{ik}\left(\frac{d}{ds}\left(g(s)e^{ics}\right) - \frac{dg}{ds}e^{ics}\right) \\ &= \frac{g(s)e^{ics}}{ic}\Big|_a^b - \int_a^b ds \frac{1}{(ic)^2}\left(\frac{d}{ds}\left(\frac{dg}{ds}e^{ics}\right) - \frac{d^2g}{ds^2}e^{ics}\right). \\ &\approx \sum_{m=0}^{N} \frac{(-1)^m}{(ic)^{m+1}}\left[\frac{d^m g}{ds^m}(b) - \frac{d^m g}{ds^m}(a)\right].\end{aligned} \tag{5.247}$$

This is the asymptotic expansion for sufficiently large c. We apply a similar expansion to the integral over k_- and keep only the first term. Because $\mathrm{Im}(\omega) > 0$ and the integrand contains a Heaviside step function, the first term is guaranteed to converge. Note that we would normally need to apply the method of steepest descent to properly approximate the integral; however, this requires that the term in the exponential have a saddle point somewhere in the complex plane. Due to our previous approximation, the term in the exponential is monotonic in k_-, thus the method of steepest descent is not necessary for our purposes. We find then that

$$\begin{aligned}&\int_{-\infty}^{\infty} dk_- \frac{i\,|d|}{\left|\Omega_2 + nd\omega'_E\right|} g(k_-) e^{-ik_-\frac{|d|}{d}} \exp\left(\frac{-ik_-\,|d|\,\overline{\Omega}_2}{\sqrt{1-\lambda b(k_+\,|d|)}}\left(\frac{n\overline{\Omega}_d(k_+\,|d|)-\omega}{\Omega_2+nd\omega'_E}\right)\right) \\ &\qquad \approx \frac{g(0)}{\frac{\overline{\Omega}_2}{\sqrt{1-\lambda b(k_+|d|)}}\left(n\overline{\Omega}_d\left(k_+\,|d|\right) - \omega\right) + \Omega_2\frac{x_+}{d} + n\omega'_E x_+}.\end{aligned} \tag{5.248}$$

For convenience, we next replace all instances of $k_+ |d|$ with $k_+ d$; this is allowed since $\overline{\Omega}_d$ and b are even functions and the bounds of integration are symmetric. We obtain

$$I_{p,r} \approx \int \frac{dk_+ dx_+ dx_-}{2\pi} \frac{\overline{\Omega}_2 e^{-ik_+ x_-}}{\sqrt{1-\lambda b\left(k_+ d\right)}} \frac{J_0\left(\rho k_\perp\right)^2 \phi_{m0,n}\left(x_+ + \frac{x_-}{2}\right)^* \phi_{m0,n}\left(x_+ - \frac{x_-}{2}\right)}{n\overline{\Omega}_d\left(k_+ d\right) + \left(\frac{\Omega_2}{\overline{\Omega}_2}\frac{x_+}{d} + n\frac{\omega_E'}{\overline{\Omega}_2} x_+\right)\sqrt{1-\lambda b\left(k_+ d\right)} - \omega}, \quad (5.249)$$

where

$$k_\perp^2 = k_+^2 + \frac{n^2 q_0^2}{r_0^2}. \quad (5.250)$$

As with the trapped functional, we separately average over the Bessel functions,

$$\frac{\int d^3 v J_0\left(k_\perp \rho\right)^2 f_0}{\int d^3 v f_0} = \Gamma_0\left(k_\perp \rho_{\text{th}}\right). \quad (5.251)$$

We next carry out the integral over x_- by identifying it as the inverse Fourier transform of the product of two Gaussians, leading to

$$I_{p,r} = \int \frac{dx_+ dk_+}{\sqrt{\pi}} \frac{\overline{\Omega}_2}{\sqrt{1-\lambda b\left(k_+ d\right)}} \frac{\Gamma_0\left(k_\perp \rho_{\text{th}}\right)\sqrt{\frac{\text{Im}\left(w^2\right)^2}{\text{Re}\left(w^2\right)} + \text{Re}\left(w^2\right)} e^{-\rho_*^2} e^{-k_*^2} \exp\left(\frac{\text{Im}(x_0)^2}{\text{Re}\left(w^2\right)}\right)}{n\overline{\Omega}_d\left(k_+ d\right) + \left(\frac{\Omega_2}{\overline{\Omega}_2}\frac{x_+}{d} + n\frac{\omega_E'}{\overline{\Omega}_2} x_+\right)\sqrt{1-\lambda b\left(k_+ d\right)} - \omega}, \quad (5.252)$$

where

$$\rho_* = \frac{x_+ + k_+ \,\text{Im}\left(w^2\right) - \text{Re}\left(x_0\right)}{\sqrt{\text{Re}\left(w^2\right)}}, \quad (5.253)$$

$$k_* = \frac{k_+ \,\text{Re}\left(w^2\right) + \text{Im}\left(x_0\right)}{\sqrt{\text{Re}\left(w^2\right)}}. \quad (5.254)$$

It is more convenient to numerically integrate this over k_* and ρ_* to take advantage of the explicit Gaussian structure. Because the Jacobian of this variable transformation is 1, the change of variables is easily carried out. In addition, we approximate the λ dependent terms by averaging over the pitch angle parameter. We also use the extremely-passing particle limit, where $\theta \approx \alpha_2$. We then obtain

$$I_{p,r} \approx \int_{-\infty}^{\infty}\int_{-\infty}^{\infty} \frac{d\rho_* dk_*}{\sqrt{\pi}} \frac{\Gamma_0\left(k_\perp \rho_{\text{th}}\right)\sqrt{\frac{\text{Im}\left(w^2\right)^2}{\text{Re}\left(w^2\right)} + \text{Re}\left(w^2\right)} e^{-\rho_*^2} e^{-k_*^2} \exp\left(\frac{\text{Im}(x_0)^2}{\text{Re}\left(w^2\right)}\right)}{n\omega_{d0}\xi F_p\left(k_+ d\right) + \epsilon_\parallel \sqrt{\xi}\frac{x_+}{d}\frac{\sqrt{2T/m}}{qR_0} - \overline{\omega}}, \quad (5.255)$$

where

$$\overline{\omega} = \omega - n\omega_{E0} - n\omega'_E x_+, \tag{5.256}$$

and

$$F_p\left(k_+ d\right) = \frac{4}{3}\left(\cos\left(k_+ d\right) + \left(sk_+ d - \alpha \sin\left(k_+ d\right)\right)\sin\left(k_+ d\right)\right). \tag{5.257}$$

We note here that the factor of $4/3$ comes from taking the pitch angle average of $2 - \lambda b$ in the small ϵ limit. This approximation can be improved by considering higher-order ϵ terms, although this is not done in the current formulation of QuaLiKiz.

We now address terms in the numerator of the original integrand that are proportional to x; these terms arise from the radial electric field shear. In principle, their inclusion can be treated fully consistently by using the appropriate Fourier transforms as well as the convolution theorem in much the same way we did before. However, as a crude approximation, we simply map $x \rightarrow x_+$ in the numerator as is effectively done in the denominator.

Next, we address the integration over λ and ξ in the full passing functional. Once these integrals are calculated, we fold them into the integration over ρ_* and k_*. We wish to compute

$$I_{p,E} = \sum_{\epsilon_\parallel} \int d\lambda d\xi \left(2\pi\right)^2 \frac{n_0 e^2}{T} \frac{R_0 \bar{r}}{\sqrt{\pi}} \frac{\sqrt{\xi} e^{-\xi}}{\overline{\Omega}_2} \frac{\left\langle \left(\mathbf{n}\cdot\boldsymbol{\omega}_* - \overline{\omega}\right)\left(1 + \frac{2v_\parallel U_\parallel}{v_T^2} + \frac{U_\parallel^2}{v_T^2}\left(\frac{2v_\parallel^2}{v_T^2} - 1\right)\right)\right\rangle}{n\omega_{d0}\xi F_p\left(k_+ d\right) + \epsilon_\parallel \sqrt{\xi}\frac{x_+}{d}\frac{\sqrt{2T/m}}{qR_0} - \overline{\omega}}. \tag{5.258}$$

Because we averaged out the pitch angle dependence in the denominator of the integrand, the pitch angle integration in the numerator is completely separable and only dependent on the inverse aspect ratio ϵ. This is perhaps the largest single approximation used in the passing part of the dispersion; it is necessary to ensure that the numerical integral is 2-dimensional rather than 3-dimensional. It is of potential interest to study the impact this approximation has; one could calculate a more exact (albeit slower) integral to quantify the exact impact this has on the resulting solutions and flux calculations.

Since only $v_\parallel$ terms in the numerator are dependent on λ. We also use the fact that

$$\int_0^{\frac{1-\epsilon}{1+\epsilon}} \frac{d\lambda}{2\overline{\Omega}_2} = f_p, \tag{5.259}$$

where $f_p = 1 - f_t$ is the flux surface averaged passing particle fraction. We then compute

$$\int_0^{\frac{1-\epsilon}{1+\epsilon}} \frac{d\lambda}{\overline{\Omega}_2} \left\langle v_\parallel^m \right\rangle = 2 f_p v_T^m \epsilon_\parallel^m \xi^{m/2} \lambda_m, \tag{5.260}$$

where we define λ_m as

$$\lambda_m = \frac{\int_0^{\frac{1-\epsilon}{1+\epsilon}} d\lambda \int_{-\pi}^{\pi} \frac{d\theta \left(\sqrt{1-\lambda b}\right)^m}{\sqrt{1-\lambda b}}}{\int_0^{\frac{1-\epsilon}{1+\epsilon}} d\lambda \int_{-\pi}^{\pi} \frac{d\theta}{\sqrt{1-\lambda b}}}. \tag{5.261}$$

We numerically calculate λ_m separately from the rest of the dispersion relation since λ_m is only dependent on ϵ. Once again ignoring terms order cubic or higher with the Mach number, we find that

$$\begin{aligned} \int_0^{\frac{1-\epsilon}{1+\epsilon}} \frac{d\lambda}{\overline{\Omega}_2} \left\langle (\mathbf{n} \cdot \boldsymbol{\omega}_* - \overline{\omega}) \left(1 + \frac{2 v_\parallel U_\parallel}{v_T^2} + \frac{U_\parallel^2}{v_T^2} \left(\frac{2 v_\parallel^2}{v_T^2} - 1\right)\right)\right\rangle = \\ 2 f_p n \omega_{d0} \left(\mathcal{A}_p + \mathcal{B}_p \epsilon_\parallel \xi^{1/2} + C_p \xi + \mathcal{D}_p \epsilon_\parallel \xi^{3/2} + \mathcal{E}_p \xi^2\right), \end{aligned} \tag{5.262}$$

where we define the terms

$$\mathcal{A}_p = \left(1 - \frac{U_\parallel^2}{v_T^2}\right) \left(A_n - \frac{3}{2} A_T - z^2 F_p\right) - \frac{U_\parallel}{v_T} \left(2 A_U - \frac{U_\parallel}{v_T} A_T\right), \tag{5.263}$$

$$\mathcal{B}_p = \left(A_U \left(2 - 6 \frac{U_\parallel^2}{v_T^2}\right) + U_\parallel \left(2 A_n - 5 A_T - 2 z^2 F_p\right)\right) \lambda_1, \tag{5.264}$$

$$C_p = \left(1 - \frac{U_\parallel^2}{v_T^2}\right) A_T + 4 A_U \frac{U_\parallel}{v_T} \lambda_2 + \frac{U_\parallel^2}{v_T^2} \lambda_2 \left(2 A_n - 7 A_T - 2 z^2 F_p\right), \tag{5.265}$$

$$\mathcal{D}_p = 2 A_T \frac{U_\parallel}{v_T} \lambda_1 + 4 A_U \frac{U_\parallel^2}{v_T^2} \lambda_3, \tag{5.266}$$

$$\mathcal{E}_p = 2 A_T \frac{U_\parallel^2}{v_T^2} \lambda_2, \tag{5.267}$$

and where

$$z^2 = \frac{\overline{\omega}}{n \omega_{d0} F_p \left(k_+ d\right)}. \tag{5.268}$$

Thus, the integral simplifies to

$$I_{p,E} = \sum_{\epsilon_\parallel} 2 f_p \int_0^\infty d\xi \, (2\pi)^2 \frac{n_0 e^2}{T} \frac{R_0 r_0}{\sqrt{\pi}} \sqrt{\xi} \frac{\mathcal{A}_p + \mathcal{B}_p \epsilon_\parallel \xi^{1/2} + C_p \xi + \mathcal{D}_p \epsilon_\parallel \xi^{3/2} + \mathcal{E}_p \xi^2}{F_p \left(k_+ d\right) \left(\xi + \epsilon_\parallel \sqrt{\xi} \frac{x_+}{d} \frac{v_T}{q R_0 F_p (k_+ d)} - z^2\right)}. \tag{5.269}$$

We then perform a change in variables to $u = \sqrt{\xi}$ and note that

$$\sum_{\epsilon_\parallel} \int_0^\infty d\xi \sqrt{\xi} g\left(\epsilon_\parallel \sqrt{\xi}\right) = \sum_{\epsilon_\parallel} \int_0^\infty du 2u^2 g\left(\epsilon_\parallel u\right) = \int_{-\infty}^\infty du 2u^2 g\left(u\right). \tag{5.270}$$

The integral then becomes

$$I_{p,E} = 4 f_p \int_{-\infty}^\infty du \left(2\pi\right)^2 \frac{n_0 e^2}{T} \frac{R_0 r_0}{\sqrt{\pi}} u^2 \frac{\mathcal{A}_p + \mathcal{B}_p u + C_p u^2 + \mathcal{D}_p u^3 + \mathcal{E}_p u^4}{F_p\left(k_+ d\right)\left(u^2 + u \frac{x_+}{d} \frac{v_T}{q R_0 F_p\left(k_+ d\right)} - z^2\right)}. \tag{5.271}$$

To simplify this integral further, we rewrite the denominator as

$$u^2 + u \frac{x_+}{d} \frac{v_T}{q R_0 F_p\left(k_+ d\right)} - z^2 = \left(u - z_+\right)\left(u - z_-\right), \tag{5.272}$$

where

$$z_\pm = -\frac{1}{2} \frac{x_+}{d} \frac{v_T}{q R_0 F_p\left(k_+ d\right)} \pm \sqrt{\left(\frac{1}{2} \frac{x_+}{d} \frac{v_T}{q R_0 F_p\left(k_+ d\right)}\right)^2 + z^2}. \tag{5.273}$$

This allows us to simplify the integral using the plasma dispersion functions defined in Appendix 5.A, allowing us to obtain

$$I_{p,E} = 4 f_p \left(2\pi\right)^2 \frac{n_0 e^2}{T} \frac{R_0 r_0}{F_p\left(k_+ d\right)} \left(\mathcal{A}_p G_2 + \mathcal{B}_p G_3 + C_p G_4 + \mathcal{D}_p G_5 + \mathcal{E}_p G_6\right), \tag{5.274}$$

where the associated Fried and Conte integrals $G_n = G_n\left(z_+, z_-\right)$ are evaluated at z_+ and z_-. Thus, the passing functional simplifies to

$$\begin{aligned} \mathcal{L}_{\text{passing}} = \int_{-\infty}^\infty \int_{-\infty}^\infty \frac{d\rho_* dk_*}{\sqrt{\pi}} \left(2\pi\right)^3 \frac{e^2 n_0}{T} r_0 R_0 f_p \left\langle \mathcal{I}_p \right\rangle_{\xi,\lambda} \Gamma_0\left(k_\perp \rho_{\text{th}}\right) \\ \times \sqrt{\frac{\text{Im}\left(w^2\right)^2}{\text{Re}\left(w^2\right)} + \text{Re}\left(w^2\right)} e^{-\rho_*^2} e^{-k_*^2} \exp\left(\frac{\text{Im}\left(x_0\right)^2}{\text{Re}\left(w^2\right)}\right), \end{aligned} \tag{5.275}$$

where

$$\left\langle \mathcal{I}_p \right\rangle_{\xi,\lambda} = \frac{2}{\pi F_p\left(k_+\right)} \left(\mathcal{A}_p G_2 + \mathcal{B}_p G_3 + C_p G_4 + \mathcal{D}_p G_5 + \mathcal{E}_p G_6\right). \tag{5.276}$$

We have now reduced all parts of the dispersion relation to a numerically tractable form. The adiabatic piece can be calculated analytically, whereas the trapped and passing functionals require 1- and 2-dimensional integrals, respectively. With the dispersion relation in hand, we can proceed to applying quasilinear theory.

5.8 Quasilinear approximation

The core principle of quasilinear theory is to consider the slow time variation of the total distribution function f and the resultant fluxes that attempt to drive the distribution function back to equilibrium. The validity of the quasilinear approximation depends on the decorrelation time of the potential being shorter than the eddy turn-over time. The ratio of these two quantities is known as the Kubo number.[128, 129] The single particle analogue to this is that the individual particle must not be trapped in the field; this allows the dynamics to be characterized as a random walk process, leading to a justification for the quasilinear approach. These characteristic times have been calculated and compared for both ETG and ITG-TEM turbulence.[114, 130, 131] For these general cases, the Kubo number is less than unity and well developed turbulence for tokamak plasma parameters manifests random walk processes. Moreover, it has been found that quasilinear models are successful in reproducing experimental results such as temperature profiles within 15% rms error.[132]

To proceed, we first recall the Vlasov equation for a given species (again omitting the species label):

$$\frac{\partial f}{\partial t} + \dot{\boldsymbol{\alpha}} \cdot \frac{\partial f}{\partial \boldsymbol{\alpha}} + \dot{\mathbf{J}} \cdot \frac{\partial f}{\partial \mathbf{J}} = 0. \tag{5.277}$$

When we obtained the dispersion relation, we considered the linear response and neglected terms that are quadratic in the fluctuations. Moreover, we also assumed f_0 was time independent. To proceed with the quasilinear approximation, we now suppose that f_0 varies slowly in time on a time scale longer than that of the linear modes. We may then perform a time average over the Vlasov equation such that $\langle f \rangle_t = f_0$ and the linear response averages to zero. We define the time average as

$$\langle g\,(t) \rangle_t = \frac{1}{T} \int_{-T/2}^{T/2} g\,(t + t')\, dt', \tag{5.278}$$

where T is the time scale associated with the linear modes. The time averaged Vlasov equation then reads

$$\left\langle \frac{\partial f}{\partial t} + \dot{\boldsymbol{\alpha}} \cdot \frac{\partial f}{\partial \boldsymbol{\alpha}} + \dot{\mathbf{J}} \cdot \frac{\partial f}{\partial \mathbf{J}} \right\rangle_t \approx \frac{\partial f_0}{\partial t} + \langle \{ \mathrm{Re}(\delta f), \mathrm{Re}(e\phi) \} \rangle_t = 0. \tag{5.279}$$

Here, we take the real part of δf or ϕ to obtain the physical quantity in accordance with our convention. To proceed, we rewrite the Poisson bracket as

$$\{\mathrm{Re}(\delta f), \mathrm{Re}(e\phi)\} = \frac{\partial}{\partial \boldsymbol{\alpha}} \cdot \left(\mathrm{Re}(\delta f) \frac{\partial \,\mathrm{Re}(e\phi)}{\partial \mathbf{J}} \right) - \frac{\partial}{\partial \mathbf{J}} \cdot \left(\mathrm{Re}(\delta f) \frac{\partial \,\mathrm{Re}(e\phi)}{\partial \boldsymbol{\alpha}} \right). \tag{5.280}$$

The time average can be simplified by noting that for any two general vectors $\mathbf{A}$ and $\mathbf{B}$ we have

$$\left\langle \mathrm{Re}\left(\mathbf{A}e^{-i\omega t}\right) \cdot \mathrm{Re}\left(\mathbf{B}e^{-i\omega t}\right) \right\rangle_t = \frac{1}{2} \mathrm{Re}\left(\mathbf{A} \cdot \mathbf{B}^*\right). \tag{5.281}$$

Due to the Fourier structure of δf and ϕ, we also note that

$$\frac{\partial}{\partial \boldsymbol{\alpha}} \left\langle \mathrm{Re}\left(\delta f\right) \mathrm{Re}\left(e\phi\right) \right\rangle_t = \mathbf{0}. \tag{5.282}$$

Essentially, the $\boldsymbol{\alpha}$ dependence disappears after performing the time average. Moreover, taking the real part of δf and ϕ commutes with taking derivatives of real variables. We therefore obtain

$$\frac{\partial f_0}{\partial t} + \frac{\partial}{\partial \mathbf{J}} \cdot \boldsymbol{\Gamma}_Q = 0, \tag{5.283}$$

where we define the quasilinear flux $\boldsymbol{\Gamma}_Q$ as

$$\boldsymbol{\Gamma}_Q = \frac{1}{2} \mathrm{Re}\left(\sum_{\mathbf{n}} i\mathbf{n} f_{\mathbf{n}} e\phi_{\mathbf{n}}^* \right) = -\frac{1}{2} \mathrm{Im}\left(\sum_{\mathbf{n}} \mathbf{n} \frac{e^2 \left|\phi_{\mathbf{n}}\right|^2}{T} f_0 \left(1 - \frac{\omega - \mathbf{n}\cdot\boldsymbol{\omega}_* - \mathbf{n}\cdot\boldsymbol{\omega}_E}{\omega - \mathbf{n}\cdot\boldsymbol{\Omega}}\right) \right). \tag{5.284}$$

Here, $f_{\mathbf{n}}$ and $\phi_{\mathbf{n}}$ are related via the dispersion relation in the linearized problem. Thus, the quasilinear flux is computed by substituting in the solution of the dispersion relation including the found eigenvalues ω, again only considering unstable modes. Modes that lack unstable solutions do not contribute to the quasilinear flux.

We are now in a position to calculate the flux surface averaged particle, toroidal angular momentum, and energy fluxes by averaging the Vlasov equation over velocity and space. This is analogous to calculating the fluid equations by taking moments of the Vlasov equation. The radial fluxes can be calculated via a change in variables from J_3 to r. We find that

$$\frac{\partial \left\langle n \right\rangle}{\partial t} + \frac{d\Gamma}{dr} = 0, \tag{5.285}$$

$$\frac{\partial \left\langle mnRU_{\parallel} \right\rangle}{\partial t} + \frac{d\Pi}{dr} = 0, \tag{5.286}$$

$$\frac{3}{2} \frac{\partial \left\langle p \right\rangle}{\partial t} + \frac{dQ}{dr} = 0, \tag{5.287}$$

where Γ, Π, and Q_E are the particle, toroidal momentum, and energy fluxes defined as

$$\Gamma = \frac{1}{4\pi^2 d}\int d^3v d^3r \frac{1}{2}\,\mathrm{Im}\left(\sum_{\mathbf{n}} \frac{nq}{rB} f_{\mathbf{n}} \phi^*_{\mathbf{n}}\right), \tag{5.288}$$

$$\Pi = \frac{1}{4\pi^2 d}\int d^3v d^3r \frac{mRv_{\parallel}}{2}\,\mathrm{Im}\left(\sum_{\mathbf{n}} \frac{nq}{rB} f_{\mathbf{n}} \phi^*_{\mathbf{n}}\right), \tag{5.289}$$

$$Q_E = \frac{1}{4\pi^2 d}\int d^3v d^3r \frac{m\left(v^2 - U_{\parallel}^2\right)}{4}\,\mathrm{Im}\left(\sum_{\mathbf{n}} \frac{nq}{rB} f_{\mathbf{n}} \phi^*_{\mathbf{n}}\right). \tag{5.290}$$

Here, we can see that the integrations to calculate the particle, toroidal momentum, and energy fluxes are of the same form to solve the dispersion relation. The particle flux calculation is identical. Meanwhile, we must take into account an extra factor of $v_{\parallel}$ and v^2 for the angular momentum flux and energy flux integrations, respectively. These changes can be easily accommodated for without affecting the fundamental approach. For instance, the inclusion of v^2 simply changes the associated Fried and Conte integral. The physical significance of these fluxes can be further solidified by examining the perturbed E-cross-B velocity. We find that

$$\delta \mathbf{v}_{E\times B} \cdot \hat{\mathbf{r}} = \hat{\mathbf{r}} \cdot -\frac{\nabla \delta\phi \times \mathbf{B}}{B^2} \approx \sum_{\mathbf{n}} \frac{ik_\theta \phi_{\mathbf{n}}}{B} = \sum_{\mathbf{n}} \frac{inq}{rB}\phi_{\mathbf{n}}, \tag{5.291}$$

where we have again used the convention that $k_\theta \rightarrow (i/r)\,\partial_\theta$. We then find that

$$\langle \mathrm{Re}\,(\delta \mathbf{v}_{E\times B}\cdot\hat{\mathbf{r}})\,\mathrm{Re}\,(\delta f)\rangle_t = \frac{1}{2}\,\mathrm{Re}\left(\sum_{\mathbf{n}} f_{\mathbf{n}}\left(\frac{inq}{rB}\phi_{\mathbf{n}}\right)^*\right) = \frac{1}{2}\,\mathrm{Im}\left(\sum_{\mathbf{n}} f_{\mathbf{n}}\frac{nq}{rB}\phi^*_{\mathbf{n}}\right). \tag{5.292}$$

This lets us write the fluxes as

$$\Gamma = \langle \delta\,(n)\,\delta \mathbf{v}_{E\times B}\cdot\hat{\mathbf{r}}\rangle_{t,r}\,, \tag{5.293}$$

$$\Pi = \left\langle \delta\left(mnRU_{\parallel}\right)\delta \mathbf{v}_{E\times B}\cdot\hat{\mathbf{r}}\right\rangle_{t,r}, \tag{5.294}$$

$$Q_E = \langle \delta\,(P)\,\delta \mathbf{v}_{E\times B}\cdot\hat{\mathbf{r}}\rangle_{t,r}\,. \tag{5.295}$$

Therefore, the particle, angular momentum, and energy fluxes are simply related to moments of the perturbed distribution function integrated against the perturbed E-cross-B velocity, where $\langle \ldots \rangle_{t,r}$

denotes a time and spatial average. We also define

$$\delta n = \int d^3v \delta f, \tag{5.296}$$

$$\delta \left(nmRU_{\parallel} \right) = \int d^3v mv_{\parallel} \delta f, \tag{5.297}$$

$$\delta P = \int d^3v \frac{1}{2} m \left(v^2 - U_{\parallel}^2 \right) \delta f, \tag{5.298}$$

where we calculate the particle, angular momentum, and energy fluxes for every species. We note that the toroidal angular momentum flux is only non-zero in the presence of rotations. The energy flux calculation can be approximated by noting in the small Mach number limit that

$$\delta P = \delta \left(nT \right) = -\frac{1}{2} m U_{\parallel}^2 \delta n + \int d^3v \frac{1}{2} m v^2 \approx \int d^3v \frac{1}{2} m v^2. \tag{5.299}$$

We also note that often we are concerned with the heat flux Q relative to the convective energy flux[133] $\frac{3}{2} T\Gamma$. The heat flux is simply

$$Q = Q_E - \frac{3T}{2} \Gamma. \tag{5.300}$$

It is important to note that while we may obtain quasilinear flux ratios from the above procedure, we cannot with linear physics alone obtain the physical fluxes. Throughout the derivation, we have kept the amplitude of the fluctuating potential $\delta\phi$ arbitrary. The amplitude ϕ_0 can only be obtained through the use of nonlinear physics by saturating the amplitude. Thus, the complete calculation of these fluxes must be obtained via a saturation rule obtained from a nonlinear computational code, in this case from the Gyrokinetic Electromagnetic Numerical Experiment (GENE).[134] This saturation rule is the topic of the next section.

5.9 Saturation rule

To formulate a saturation rule, we introduce the well known mixing length estimate with an effective diffusivity D:

$$D = \left. \frac{\gamma_n}{\left\langle k_{\perp}^2 \right\rangle} \right|_{\max}, \tag{5.301}$$

where we compute the value of γ_n such that the quantity $\gamma_n/\langle k_\perp^2 \rangle$ is at its maximum over the linear spectrum for a given mode. Meanwhile, we average $k_\perp^2$ over the electrostatic mode. We enforce this mixing length estimate for our various flux calculations by approximating the underlying process as a random walk.[101] For instance, we mandate that the particle flux for a given species must be

$$\Gamma_s = \sum_n C_{\mathrm{NL}} \frac{S_n}{R_0 n_{0s}} \left. \frac{\gamma_n}{\langle k_\perp^2 \rangle} \right|_{\mathrm{max}} \frac{k_\theta}{k_{\theta,\mathrm{max}}} L_{s,n,0}, \tag{5.302}$$

where C_{NL} is a dimensionless constant from nonlinear physics, the form factor S_n is a mode-dependent form factor, $k_{\theta,\mathrm{max}}$ corresponds to the mode that maximizes $\gamma_n/k_\perp^2$, and $L_{s,n,0}$ is the dimensionless integral that actually computes the flux terms. The above expression is only valid when there is only one mode present in the linear spectrum. We can generalize the expression to account for the existence of multiple types of linear modes by introducing another form factor $S_{n'}$ into the expression and summing over both n and n', while we compute the maximum $\gamma_n/k_\perp^2$ for a given n'.

We model C_{NL} with the use of nonlinear gyrokinetic simulations. We distinguish between ITG scales, which we define as $k_\theta \rho_s < 2$, and ETG scales, which we define as $k_\theta \rho_s > 2$. Here, ρ_s is the gyroradius of the main ion species such that $\rho_s = \sqrt{T_s/m_s}/\Omega_{1,s}$ (note that lack of $\sqrt{2}$). The ITG scales are tuned to the GA-Standard nonlinear ion heat flux computed by GENE, whereas the ETG scales are tuned to a single-scale nonlinear GENE simulation based on JET parameters.[24] These parameters are current as of QuaLiKiz version 2.8.1 and are subject to future change depending on updates to the nonlinear physics. The result is

$$C_{\mathrm{NL}} = \begin{cases} 271/s_{\mathrm{fac}} & \text{if } k_\theta \rho_s < 2 \text{ (ITG)}, \\ 122 f_{\text{multi-scale}}/s_{\mathrm{fac}} & \text{if } k_\theta \rho_s > 2 \text{ (ETG)}. \end{cases} \tag{5.303}$$

Here, we have also introduced an ad hoc factor s_{fac} for the case of low magnetic shear,[114]

$$s_{\mathrm{fac}} = \begin{cases} 2.5\,(1 - |s|) & \text{if } |s| < 0.6, \\ 1 & \text{if } |s| > 0.6, \end{cases} \tag{5.304}$$

as well as a multi-scale rule determined from the maximum of the respective spectra,

$$f_{\text{multi-scale}} = \frac{1}{1 + \exp\left(-\frac{1}{5}\left(\frac{\gamma_{\text{ETG, max}}}{\gamma_{\text{ITG, max}}} - \sqrt{\frac{m_i}{m_e}}\right)\right)}, \tag{5.305}$$

where m_e and m_i are the masses of the electron and main ion respectively. Here, the sigmoid guarantees a smooth transition from a strongly driven ion-scale mode regime and a strongly driven electron-scale mode regime, since it has been observed that ETG turbulence is suppressed when the ion-scale instability dominates.

Lastly, we provide an explicit expression for $k_\perp^2$. In the ITG regime, we need to take into account contributions to k_r^2 that arise from the magnetic shear, the mode structure of the electrostatic perturbation, and nonlinear effects. Meanwhile, in the ETG regime we assume full isotropization of the mode such that $k_r^2 = k_\theta^2$. The result is

$$\left\langle k_\perp^2 \right\rangle = \begin{cases} k_\theta^2 + (k_{r-\text{NL}} + k_{r-\text{shear}})^2 & \text{if } k_\theta \rho_s < 2 \text{ (ITG)}, \\ 2k_\theta^2 & \text{if } k_\theta \rho_s > 2 \text{ (ETG)}. \end{cases} \tag{5.306}$$

The shear contribution can be calculated analytically as

$$k_{r-\text{shear}} = k_\theta \left|s\right| \sqrt{\left\langle \theta^2 \right\rangle} = \frac{k_\theta s d}{\sqrt{2}\,\text{Re}\left(w^2\right)} \sqrt{\text{Re}\left(w^2\right) + 2\,\text{Im}\left(x_0\right)^2}, \tag{5.307}$$

where we use

$$\left\langle \theta^2 \right\rangle = \frac{\int_{-\infty}^{\infty} \theta^2 \left|\hat{\phi}\left(\theta\right)\right|^2 d\theta}{\int_{-\infty}^{\infty} \left|\hat{\phi}\left(\theta\right)\right|^2 d\theta} = \frac{d^2}{2\,\text{Re}\left(w^2\right)} + \left(d \frac{\text{Im}\left(x_0\right)}{\text{Re}\left(w^2\right)}\right)^2. \tag{5.308}$$

Meanwhile, the nonlinear contribution has been tuned[114] such that

$$k_{r-\text{NL}} \rho_s = 0.4 e^{-2|s|} q^{-0.5} + 1.5 \max\left\{k_\theta \rho_s - 0.2, 0\right\}. \tag{5.309}$$

Having now fully derived analytic expressions for the dispersion relation and quasilinear fluxes, we now discuss the numerical implementation of QuaLiKiz.

5.10 Numerical implementation

Recall that the dispersion relation is written as

$$\sum_s \mathcal{L}_{0,s} - \mathcal{L}_{\text{passing},s} - \mathcal{L}_{\text{trapped},s} = 0. \tag{5.310}$$

The trapped and passing functionals discussed in Secs. 5.6 and 5.7 are both functions of the complex frequency ω. Solving the dispersion relation is therefore a matter of finding the zeros of the complex analytic function $D(\omega)$, where

$$D(\omega) = \sum_s \mathcal{L}_{0,s} - \mathcal{L}_{\text{passing},s} - \mathcal{L}_{\text{trapped},s}. \tag{5.311}$$

To solve this, we use the Davies method, a numerical technique developed in Ref. 135 to find the zeros of an analytic function within the complex plane. The strategy takes advantage of the argument principle in complex analysis, which states that given a meromorphic function $f(z)$ that

$$\frac{1}{2\pi i}\oint_C \frac{f'(z)}{f(z)}dz = N - P, \tag{5.312}$$

where N and P are respectively the number of zeros and poles of $f(z)$ contained within the simple counter-clockwise contour C. Here, zero multiplicity and pole order are taken into account. For our purposes, we assume that $f(z)$ has no poles, leading to

$$\frac{1}{2\pi i}\oint_C \frac{f'(z)}{f(z)}dz = N. \tag{5.313}$$

The key of the method is to recognize from Cauchy's residue theorem that, for integer n such that $1 \leq n \leq N$, we can calculate the integral S_n such that

$$S_n = \frac{1}{2\pi i}\oint_C z^n \frac{f'(z)}{f(z)}dz = \sum_{j=1}^{N} z_{0j}^n, \tag{5.314}$$

where z_{0j} is the jth root of $f(z)$ (counting repeated roots as separate). We then construct the polynomial

$$P_N(z) = \prod_{j=1}^{N}(z - z_{0j}) = \sum_{j=0}^{N} A_j z^{N-j}, \tag{5.315}$$

where the coefficients A_j can be computed from the relations

$$A_0 = 1, \tag{5.316}$$

$$S_1 + A_1 = 0, \tag{5.317}$$

$$S_2 + A_1 S_1 + 2A_2 = 0, \tag{5.318}$$

$$S_n + A_1 S_{n-1} + A_2 S_{n-2} + \cdots + nA_n = 0, \qquad n = 1, 2, \ldots, N, \tag{5.319}$$

Excluding the trivial A_0 term, this is a linear system of N equations. After solving this system, we can then construct the polynomial P_N which has zeros that are precisely the solutions of the dispersion relation. We then extract a zero from the polynomial P_N using a Newton solver and then define a new set of coefficients such that

$$S_n^{(1)} = S_n - z_{01}^n, \qquad n = 0, 1, \ldots, N-1 \tag{5.320}$$

where z_{01} is the first zero found. With this new set of coefficients, we may then construct a new polynomial $P_{N-1}(z)$ and extract another zero. This process is repeated until all zeros are found. If the contour of integration is a unit circle, then a clever integration by parts results in

$$S_n = -\frac{n}{2\pi i} \int_0^{2\pi} d\theta e^{in\theta} \ln\left(e^{-iN\theta} f\left(e^{i\theta}\right)\right), \qquad n > 0. \tag{5.321}$$

The inclusion of $e^{-iN\theta}$ inside the logarithm is to handle the branch cut of the logarithm, and can be obtained by using $z^{-N} f(z)$ instead of $f(z)$ in the preceding formulas; such a substitution does not affect the value of S_n for $n > 0$. For the $n = 0$ case, we simply compute the total change of the argument of $f\left(e^{i\theta}\right)$ for $0 \leq \theta \leq 2\pi$ while keeping track of any jumps in the argument that would indicate a full winding. Thus, S_n can be computed via standard quadrature methods for 1-dimensional integration.

To apply this to the dispersion relation, we make use of a bijective mapping $\omega = \omega(z)$ (to be determined momentarily). This will allow us to retain the simplifications that come from integrating around a unit circle. The first step is to define $f(z)$ such that

$$f(z) = D(\omega(z)). \tag{5.322}$$

Then, we compute S_n via numerical quadrature, leading to roots z_{0n} such that

$$f\left(z_{0n}\right) = D\left(\omega\left(z_{0n}\right)\right) = 0 \tag{5.323}$$

Because the mapping is bijective, we may then simply apply the mapping onto the roots z_{n0} to obtain

$$\omega_{0n} = \omega\left(z_{0n}\right), \tag{5.324}$$

where ω_{0n} are all the roots within the contour C in the complex ω-plane such that

$$D\left(\omega_{0n}\right) = 0. \tag{5.325}$$

The only task remaining is to define a suitable bijective mapping $\omega\left(z\right)$. Because QuaLiKiz only considers unstable modes, we demand that $\mathrm{Im}\left(\omega\right) > 0$ along the entirety of the contour in the z-plane. We first define the bijective mapping $(u, v) \rightarrow (x, y)$ as

$$x\left(u, v\right) = \frac{\mathrm{sgn}\left(uv\right)}{v\sqrt{2}}\sqrt{u^2 + v^2 - \sqrt{\left(u^2 + v^2\right)\left(u^2 + v^2 - 4u^2v^2\right)}}, \tag{5.326}$$

$$y\left(u, v\right) = \frac{\mathrm{sgn}\left(uv\right)}{u\sqrt{2}}\sqrt{u^2 + v^2 - \sqrt{\left(u^2 + v^2\right)\left(u^2 + v^2 - 4u^2v^2\right)}}. \tag{5.327}$$

The inverse mapping is given by

$$u\left(x, y\right) = \frac{x\sqrt{x^2 + y^2 - x^2y^2}}{\sqrt{x^2 + y^2}}, \tag{5.328}$$

$$v\left(x, y\right) = \frac{y\sqrt{x^2 + y^2 - x^2y^2}}{\sqrt{x^2 + y^2}}. \tag{5.329}$$

Since this mapping does not satisfy the Cauchy-Riemann equations, it is merely bijective, not conformal. This is known as a squircle mapping since it appears to be a square with rounded edges, and this specific kind was first formulated in Ref. 136. Denoting $\omega = x' + iy'$ and $z = u + iv$, we modify this mapping such that

$$x' = R_x + \frac{r_x}{a}x\left(au, av\right), \tag{5.330}$$

$$y' = R_y + \frac{1}{a}\left(R_y - \epsilon_y\right)y\left(au, av\right), \tag{5.331}$$

With C being the unit circle in the complex z-plane, let C' be the mapped curve in the complex ω-plane. Here, $\left(R_x, R_y\right)$ determines the approximate center C', r_x and a are scaling factors chosen to manipulate C' into a rectangular shape, and ϵ_y is chosen to guarantee that C' lies above the real axis. While the mapping is not conformal, it is sufficient for our method, since not only is it bijective but points interior to C are mapped to the interior of C'. Thus, if we make the interior area of C' sufficiently large and place it slightly above the real axis in the complex ω-plane, then we will determine all eigenmodes of interest to us. After the solution frequencies are found, they are then refined using a standard Newton root-finding method.

While the contour integral and the Newton root-finding are done when QuaLiKiz is used on its own, when coupled to an integrated modeling suite a slight modification is made to algorithm. We assume that the quasilinear transport changes slowly compared to the timescale of evolution of the plasma equilibrium. A typical transport solver iterates on a time step that is on the order of $\lesssim 10^{-2}\tau_E$, where τ_E is the energy confinement time. To speed up the code, QuaLiKiz will often only use the previous solution as an initial guess for the Newton solver rather than perform the full contour integral. Since codes like QuaLiKiz are often the bottleneck for the whole integrated modeling suite, such a speedup is necessary to make the simulation tractably feasible. In practice, QuaLiKiz will only perform the full contour integral once every ~ 10 iterations.

Lastly, we discuss the numerical integration scheme currently in use by QuaLiKiz to calculate the trapped and passing functionals, which require 2-dimensional integrations. Although QuaLiKiz used to rely on integration routines provided by the Numerical Algorithms Group (NAG), it now uses open source routines based the Genz and Malik algorithm, dubbed "hcubature". This algorithm was originally developed in Ref. 117; the current implementation is based on the C++ implementation in Ref. 137. The version of the algorithm in QuaLiKiz has been ported to Fortran and is slightly modified as a result.

The goal of hcubature is to estimate

$$\mathbf{I} = \int_{a_1}^{b_1} \int_{a_2}^{b_2} \cdots \int_{a_n}^{b_n} \mathbf{f}(\mathbf{x}) \mathrm{d}^n x. \tag{5.332}$$

Here, $\mathbf{I}$ is the estimate of the integral, while a_i and b_i are respectively the individual components of the lower and upper bounds of the integral $\mathbf{a}$ and $\mathbf{b}$, which are both constant vectors with dimension n. Meanwhile, $\mathbf{f}$ is a vector function of arbitrary dimension, and $\mathbf{x}$ is the argument of the function $\mathbf{f}$ and is of dimension n. The vectors $\mathbf{I}$ and $\mathbf{f}$ are of the same dimension. Thus, hcubature approximately integrates a vector integrand over a hyperrectangle (or equivalently a scaled hypercube, hence the name "cubature"). The routine terminates when the global estimate of the absolute or relative error of the integral reach the desired tolerance and also calculates an error vector $\boldsymbol{e}$ with the same dimensionality as the integrand. While calculating the error vector is straightforward, incorporating it into the convergence criterion is non-trivial. In general, to estimate the error, we make a higher order estimate $\mathbf{I}_0$ and a lower order, less accurate estimate $\mathbf{I}_1$ and set the ith component of $\boldsymbol{\epsilon}$ to be

$$\epsilon_i = |(I_0)_i - (I_1)_i| \,. \tag{5.333}$$

For simplicity, we first consider a scalar function that we integrate over a hypercube,

$$I = \int_{-1}^{1} \int_{-1}^{1} \cdots \int_{-1}^{1} f(x_1, x_2, \ldots, x_n) \mathrm{d}^n x. \tag{5.334}$$

We estimate the integral using the following rule,

$$\begin{aligned} I \approx I_0 = & w_1 f\,(0, 0, \ldots, 0) + w_2 \sum f\,(\lambda_2, 0, 0, \ldots, 0) + w_3 \sum f\,(\lambda_3, 0, 0, \ldots, 0) \\ & + w_4 \sum f\,(\lambda_4, \lambda_4, 0, 0, \ldots, 0) + w_5 \sum f\,(\lambda_5, \lambda_5, \ldots, \lambda_5)\,. \end{aligned} \tag{5.335}$$

Here, we sum over all possible permutations of coordinates while also allowing for sign changes. For example, if f takes three arguments, then

$$\begin{aligned} \sum f\,(\lambda_1, 0, 0) = & f\,(\lambda_1, 0, 0) + f\,(0, \lambda_1, 0) + f\,(0, 0, \lambda_1) \\ & + f\,(-\lambda_1, 0, 0) + f\,(0, -\lambda_1, 0) + f\,(0, 0, -\lambda_1)\,. \end{aligned} \tag{5.336}$$

Genz and Malik constrain the parameters w_i and λ_i by requiring that the integration be exact for

the functions

$$\begin{aligned} f_1(x_1, x_2, \ldots, x_n) &= 1, \\ f_2(x_1, x_2, \ldots, x_n) &= x_1^2, \\ f_3(x_1, x_2, \ldots, x_n) &= x_1^4, \\ f_4(x_1, x_2, \ldots, x_n) &= x_1^6, \\ f_5(x_1, x_2, \ldots, x_n) &= x_1^2 x_2^2, \\ f_6(x_1, x_2, \ldots, x_n) &= x_1^4 x_2^2, \\ f_7(x_1, x_2, \ldots, x_n) &= x_1^2 x_2^2 x_3^2. \end{aligned} \tag{5.337}$$

In addition, they also fix the parameters $\lambda_3 = \lambda_4$ to be a specific number, and solve the resulting nonlinear system of equations. The result can be found in Ref. 117. To estimate the error, we reuse λ_i but calculate different weights w_i' to make a lower-order estimate,

$$\begin{aligned} I \approx I_1 = w_1' f(0, 0, \ldots, 0) + w_2' \sum f(\lambda_2, 0, 0, \ldots, 0) \\ + w_3' \sum f(\lambda_3, 0, 0, \ldots, 0) + w_4' \sum f(\lambda_4, \lambda_4, 0, 0, \ldots, 0). \end{aligned} \tag{5.338}$$

We calculate the weights with the same method as previously discussed and require the integration be exact for the functions f_1, f_2, f_3, and f_5. By keeping λ_i the same, we can estimate the error without reusing function evaluations. The error is taken to be

$$\epsilon = |I_0 - I_1|. \tag{5.339}$$

The estimate procedure easily generalizes to that of a hyperrectangle by using linear transformations. The calculation of I_0, I_1, and ϵ can also be extended to the case of vector integrands by integrating every component simultaneously.

In the case that $n = 1$, the above rule no longer applies. Instead, hcubature uses a 15-point Kronrod extension of a 7-point Gaussian quadrature rule. For n-point Gaussian quadrature, we estimate the integral

$$I = \int_{-1}^{1} f(x) \mathrm{d}x \approx \sum_{i=1}^{n} w_i' f(x_i). \tag{5.340}$$

To calculate the weights w_i and the abscissa x_i, we require that the integration be exact for all polynomials up to degree $2n-1$. It can be shown using Lagrange interpolating polynomials and the theory of orthogonal polynomials that the abscissa x_i correspond to the roots of the Legendre polynomial P_n and that the weights are

$$w_i' = \frac{2}{\left(1-x_i^2\right)\frac{dP_n}{dx}\left(x_i\right)^2}, \tag{5.341}$$

where the Legendre polynomials are normalized such that $P_n(1) = 1$.

One downside to this method is that the abscissa will in general be completely different for different order rules. Thus, naively comparing an n-point rule with an $n+1$-point rule to estimate the error is inefficient. Kronrod discovered that one for an n-point Gaussian quadrature rule, one could add $n+1$ abscissa to exactly integrate polynomials up to order $3n+1$, reusing the previous abscissa and computing new weights w_i. These new nodes correspond to the zeros of Legendre-Stieltjes polynomials, and their derivation will not be covered here. Thus, the 15-point rule corresponds to

$$I \approx I_0 = \sum_{i=1}^{15} w_i f(x_i), \tag{5.342}$$

the 7-point rule to

$$I \approx I_1 = \sum_{i=1}^{7} w_i' f(x_i), \tag{5.343}$$

and the estimated error

$$\epsilon = \left|I_0 - I_1\right|. \tag{5.344}$$

Extending this to more general limits of integration simply requires a linear transformation.

Now that we have our integration schemes and error estimation rules for arbitrary n, we may proceed to describe the general algorithm. Here, **f** is the vector integrand, **a** and **b** are respectively the lower and upper bounds of the integrand, ϵ_a and ϵ_r are respectively the requested absolute and relative error tolerances, maxEval is the maximum number of function evaluations to be allowed by the routine, and norm determines the convergence criterion (in conjunction with the requested error tolerances). The integer eval keeps track of the total number of function evaluations, the

Input: **f**, **a**, **b**, ϵ_a, ϵ_r, maxEval, norm

Output: **I**, **e**, ifail

Initialize eval = 0

Create a hyperrectangle from **a**, **b**

Calculate $\mathbf{I}_0$, $\mathbf{I}_1$, $\boldsymbol{\epsilon}$ in the hyperrectangle

Calculate s, the suggested dimension along which to further discretize, in the hyperrectangle

Update eval to be the number of points evaluated so far

$\mathbf{I} = \mathbf{I}_0, \mathbf{e} = \boldsymbol{\epsilon}$

Push hyperrectangle into the binary heap with associated value $\max_i |\epsilon_i|$ and with stored values $\mathbf{I}_0$, $\boldsymbol{\epsilon}$, s

if *converged* **then** exit;

else

    repeat

        Pop a hyperrectangle from the binary heap

        Update $\mathbf{I} = \mathbf{I} - \mathbf{I}_0$, $\mathbf{e} = \mathbf{e} - \boldsymbol{\epsilon}$ from the popped hyperrectangle

        Split the hyperrectangle in half along the suggested dimension s

        Calculate $\mathbf{I}_0$, $\mathbf{I}_1$, $\boldsymbol{\epsilon}$, and s for each hyperrectangle

        Update eval to be the number of points evaluated so far

        Update $\mathbf{I} = \mathbf{I} + \sum \mathbf{I_0}$, $\mathbf{e} = \mathbf{e} + \sum \boldsymbol{\epsilon}$ from the two hyperrectangles

        Push each hyperrectangle into the binary heap with associated value $\max_i |\epsilon_i|$ and with stored values $\mathbf{I}_0$, $\boldsymbol{\epsilon}$, s

    until *converged or eval* $\geq$ *maxEval*;

Figure 5.1: Algorithm for hcubature

vectors $\mathbf{I}_0$ and $\mathbf{I}_1$ correspond to the integration estimates for a given hyperrectangle, $\boldsymbol{\epsilon}$ is the error estimate for the hyperrectangle, and s is the suggested dimension of splitting. As for the output, $\mathbf{I}$ is the total integration estimate, $\mathbf{e}$ is the total error, and ifail is an integer denoting whether any errors occurred while carrying out the procedure or whether the eval reached maxEval before convergence. Convergence is determined using the global error vector $\mathbf{e}$.

The algorithm splits the initial hyperrectangle into pieces and stores them in a binary heap. The heap is sorted according to the largest component of the local error vector, where the root of the heap corresponds to the region with the largest error. Until the integral converges, we pop a hyperrectangle from the root of the heap, split it into two regions, evaluate both regions accordingly, update the global integration and error estimates, and push both regions into the heap. This guarantees that the split region contributes the greatest to the global error. To determine which direction to split the hyperrectangle along, we calculate a fourth divided difference using the same evaluation points,

$$\begin{aligned} D_i = \sum_j \Big| & f_j(0,0,\ldots,0,-\lambda_2,0,0,\ldots,0) \\ & - 2f_j(0,0,\ldots,0) + f_j(0,0,\ldots,0,\lambda_2,0,0\ldots,0) \\ & - \frac{\lambda_1^2}{\lambda_2^2}\left[f_j(0,0,\ldots,0,-\lambda_1,0,0,\ldots,0) - 2f_j(0,0,\ldots,0)\right. \\ & \left. + f_j(0,0,\ldots,0,\lambda_1,0,0\ldots,0)\right]\Big|. \end{aligned} \tag{5.345}$$

Here, i corresponds to the dimension at which we evaluate the functions at. For example, if $i = 2$, then

$$\begin{aligned} D_2 = \sum_j \Big| & f_j(0,-\lambda_2,0,0,\ldots,0) - 2f_j(0,0,\ldots,0) + f_j(0,\lambda_2,0,0\ldots,0) \\ & - \frac{\lambda_1^2}{\lambda_2^2}\left[f_j(0,-\lambda_1,0,0,\ldots,0) - 2f_j(0,0,\ldots,0) + f_j(0,\lambda_1,0,0\ldots,0)\right]\Big|. \end{aligned} \tag{5.346}$$

Note that here we take the difference along each component of $\mathbf{f}$ and sum the absolute value of each difference. We determine s, the dimension along which we split the hyperrectangle, by calculating the maximum component of $\mathbf{D}$. The coordinate corresponding to the maximum of $\mathbf{D}$ is the one

in which we split the hyperrectangle in half. For the 1-dimensional case using the Gauss-Kronrod rule, no such calculation is required. We continually split the whole hyperrectangle into smaller and smaller pieces until convergence is achieved.

5.11 Chapter summary

In this work, we derived the linear dispersion relation of quasilinear gyrokinetic transport code QuaLiKiz from first principles. With the aid of nonlinear simulations, we also extended the linear physics to a quasilinear regime to calculate particle, toroidal angular momentum, and heat fluxes. The formulation of QuaLiKiz relies upon multiple theoretical principles in fusion plasma physics. First, we examined single particle motion in a circular magnetic geometry and identified the adiabatic invariants of motion within a guiding center framework. This allowed us to characterize electrostatic perturbations to the system with the aid of action-angle variables. We used this formulation to analyze the linearized Vlasov equation and Poisson's equation. We then simplified the resulting dispersion relation using the ballooning representation, an eigenfunction ansatz, and various approximations. The solution of this dispersion relation is computed using the Davies method and numerical cubature methods. Finally, upon finding the eigenmodes of the system, we use the solutions to compute the quasilinear fluxes with the aid of a saturation rule informed by nonlinear simulations.

This derivation serves not only to help explain the inner workings of the model, but also to guide potential improvement in QuaLiKiz. With the formulation finally laid out, it is now clear where each individual approximation enters the derivation. This will ease future QuaLiKiz development that aims to extend the underlying physics or relax the various approximations. Examples of such work includes introducing electromagnetic perturbations, incorporating a more general magnetic geometry, and a more accurate pitch angle integration for passing particles. Improvements made to QuaLiKiz will allow for more accurate integrated modeling as well as further optimization of the code.

An additional goal of this work is to provide an extensive, line-by-line derivation for the sake of demonstrating how such a model can be formulated in principle. Explicitly drawing upon multiple theoretical principles, such as the action-angle variable formalism, helps to illustrate the utility of these principles and their physical motivation. It is also useful to lay out the various mathematical and numerical techniques necessary in a model such as this, since many such tricks, methods, or approximations are often crucial in making a problem computationally tractable. We hope that this work will function not just as a tutorial for understanding and improving QuaLiKiz, but also further development in quasilinear fusion codes in general.

Appendix 5.A Fried and Conte integrals

The Fried and Conte integral, also known as the plasma dispersion function, is utilized frequently in kinetic plasma physics. It is defined as

$$Z(x) = \begin{cases} \frac{1}{\sqrt{\pi}} \int_{-\infty}^{\infty} dv \frac{e^{-v^2}}{v-x}, & \text{if } \mathrm{Im}(x) > 0, \\ \mathcal{P} \frac{1}{\sqrt{\pi}} \int_{-\infty}^{\infty} dv \frac{e^{-v^2}}{v-x} + \sqrt{\pi} i e^{-x^2}, & \text{if } \mathrm{Im}(x) = 0, \\ \frac{1}{\sqrt{\pi}} \int_{-\infty}^{\infty} dv \frac{e^{-v^2}}{v-x} + 2\sqrt{\pi} i e^{-x^2}, & \text{if } \mathrm{Im}(x) < 0, \end{cases} \tag{5.347}$$

where the case $\mathrm{Im}(x) \leq 0$ is calculated by analytically continuing the integral defined for $x > 0$. When solving the Vlasov equation as an initial value problem in time, a Laplace transform is implied when obtaining this integral. To apply the Laplace transform correctly for the case of stable modes, we must analytically continue the function. Luckily, since we only consider unstable modes, we are free to restrict ourselves instead to the related function

$$Z_0(x) = \frac{1}{\sqrt{\pi}} \int_{-\infty}^{\infty} dv \frac{e^{-v^2}}{v-x}. \tag{5.348}$$

If $\mathrm{Im}(x) = 0$, we take the Cauchy principle value of Z_0.

In carrying out the calculation, we define a generalization of the plasma dispersion function

defined as

$$Z_m(x) = \frac{1}{\sqrt{\pi}} \int_{-\infty}^{\infty} dv \frac{v^m e^{-v^2}}{x - v}, \tag{5.349}$$

where m is a nonnegative integer. It can be shown that these associated Fried and Conte integrals can be written in terms of $Z_0(x)$:

$$Z_m(x) = \begin{cases} x^m Z_0(x) + \frac{1}{\sqrt{\pi}} \sum_{k=0}^{\frac{m-1}{2}} x^{2k} \Gamma(\frac{m}{2} - k), & \text{if m odd,} \\ x^m Z_0(x) + \frac{1}{\sqrt{\pi}} \sum_{k=0}^{\frac{m}{2}-1} x^{2k+1} \Gamma(\frac{m-1}{2} - k), & \text{if m even,} \end{cases} \tag{5.350}$$

where $\Gamma(x)$ is the gamma function. For integer n we note that $Z_{2n+1}(x)$ is an even function and $Z_{2n}(x)$ is odd. The first few of these associated Fried and Conte integrals are

$$Z_1(x) = 1 + xZ_0(x), \tag{5.351}$$

$$Z_2(x) = x + x^2 Z_0(x), \tag{5.352}$$

$$Z_3(x) = \frac{1}{2} + x^2 + x^3 Z_0(x), \tag{5.353}$$

$$Z_4(x) = \frac{x}{2} + x^3 + x^4 Z_0(x). \tag{5.354}$$

We also define a further generalization of the Fried and Conte integral as described in Ref. 138:

$$G_m(x_1, x_2) = \frac{1}{\sqrt{\pi}} \int_{-\infty}^{\infty} dv \frac{v^m e^{-v^2}}{(v - x_1)(v - x_2)} \tag{5.355}$$

Through partial fraction decomposition, we can rewrite this as

$$G_m(x_1, x_2) = \frac{1}{\sqrt{\pi}} \int_{-\infty}^{\infty} dv \left(\frac{1}{v - x_1} + \frac{x_2}{(v - x_1)(v - x_2)} \right) v^{m-1} e^{-v^2} = Z_{m-1}(x_1) + x_2 G_{m-1}(x_1, x_2). \tag{5.356}$$

Because $G_m(x_1, x_2) = G_m(x_2, x_1)$, we obtain

$$G_m(x_1, x_2) = Z_{m-1}(x_1) + x_2 G_{m-1}(x_1, x_2) = G_m(x_2, x_1) = Z_{m-1}(x_2) + x_1 G_{m-1}(x_1, x_2), \tag{5.357}$$

which allows us to write

$$G_m(x_1, x_2) = \frac{Z_m(x_1) - Z_m(x_2)}{x_1 - x_2}. \tag{5.358}$$

Note that $G_m(x_1, x_2) = G_m(-x_1, -x_2)$.

Appendix 5.B Derivation of the magnetic drift velocity

The goal of this section is to calculate the magnetic drift velocity $\mathbf{v}_{D,B}$ in the $s-\alpha$ equilibrium by including a finite Shafranov shift. We define the right-handed coordinate system (r,θ,φ) using Cartesian coordinates and include the Shafranov shift explicitly:

$$x = (R_0 + r\cos(\theta) + \Delta(r))\cos(\varphi), \tag{5.359}$$

$$y = (R_0 + r\cos(\theta) + \Delta(r))\sin(\varphi), \tag{5.360}$$

$$z = r\sin(\theta). \tag{5.361}$$

Here, Δ is the outward radial shift of the circular flux surface's center. The coordinate system (r,θ,φ) is right-handed but not orthogonal, so we must specify the metric coefficients. They are

$$g_{rr} = 1 + (\Delta')^2 + 2\Delta'\cos(\theta), \tag{5.362}$$

$$g_{r\theta} = g_{\theta r} = -\Delta' r\sin(\theta), \tag{5.363}$$

$$g_{\theta\theta} = r^2, \tag{5.364}$$

$$g_{\varphi\varphi} = (R_0 + r\cos(\theta) + \Delta)^2, \tag{5.365}$$

$$g_{r\varphi} = g_{\varphi r} = g_{\theta\varphi} = g_{\varphi\theta} = 0, \tag{5.366}$$

where $\Delta' = \partial_r\Delta$. This leads to the Jacobian

$$J = \sqrt{g} = \frac{1}{\nabla r\cdot(\nabla\theta\times\nabla\varphi)} = r\,(R_0 + r\cos(\theta) + \Delta)\,(1 + \Delta'\cos(\theta)). \tag{5.367}$$

We next define a magnetic field for the $s-\alpha$ equilibrium. As an approximation, we ignore the poloidal magnetic field and only consider the toroidal magnetic. Thus, the magnetic field is

$$\mathbf{B} \approx B_0 R_0 \nabla\varphi. \tag{5.368}$$

This guarantees that the magnetic field strength is

$$B = \frac{B_0 R_0}{R_0 + r\cos(\theta) + \Delta} = \frac{B_0 R_0}{R}, \tag{5.369}$$

where $R = R(r, \theta)$. It is well known that one can obtain an approximate expression for Δ' from the Grad-Shafranov equation to lowest-order in the inverse aspect ratio.[78, 126, 139] The expression is

$$\Delta' \approx -\alpha = q^2 \beta \frac{R_0}{P} \frac{dP}{dr}. \tag{5.370}$$

The next step is to calculate the magnetic drift velocity,

$$\mathbf{v}_{D,B} = \frac{m}{eB}\left(v_\parallel^2 + \frac{v_\perp^2}{2}\right)\frac{\mathbf{B}\times\nabla B}{B^2} + \frac{m v_\parallel^2}{eB}\frac{\beta}{2p}\frac{\mathbf{B}\times\nabla p}{B}. \tag{5.371}$$

The first term is the sum of the grad-B drift as well as the dominant component of the curvature drift. The second term is the portion of the curvature drift that arises from considering the lowest-order MHD equilibrium. Since QuaLiKiz is applied in the regime where α is small, we ignore the second term entirely; this is equivalent to assuming that the magnetic field is approximately curl-free. Taking note that we are not using an orthogonal coordinate system, we find that the relevant cross product is

$$(\mathbf{B}\times\nabla B) = R_0 B_0 \left(\frac{\partial B}{\partial r}\nabla\varphi\times\nabla r + \frac{\partial B}{\partial \theta}\nabla\varphi\times\nabla\theta\right). \tag{5.372}$$

We can evaluate each component of the expression to obtain

$$(\mathbf{B}\times\nabla B)\cdot\nabla r = R_0 B_0 \frac{\partial B}{\partial \theta}\nabla r\cdot(\nabla\varphi\times\nabla\theta) = -\frac{R_0 B_0}{J}\frac{\partial B}{\partial\theta} = -\frac{B^2\sin(\theta)}{R(1+\Delta'\cos(\theta))}, \tag{5.373}$$

$$(\mathbf{B}\times\nabla B)\cdot\nabla\theta = R_0 B_0 \frac{\partial B}{\partial r}\nabla\theta\cdot(\nabla\varphi\times\nabla r) = \frac{R_0 B_0}{J}\frac{\partial B}{\partial r} = -\frac{B^2(\cos(\theta)+\Delta')}{Rr(1+\Delta'\cos(\theta))}, \tag{5.374}$$

$$(\mathbf{B}\times\nabla B)\cdot\nabla\varphi = 0. \tag{5.375}$$

We then use the approximation

$$\frac{1}{R_0(1+\Delta'\cos(\theta))} \approx \frac{1}{R_0}(1-\Delta'\cos(\theta)) \tag{5.376}$$

and substitute in $\Delta' = -\alpha$ to obtain to lowest-order

$$\mathbf{v}_D\cdot\nabla r \approx -v_{D,B}\sin(\theta), \tag{5.377}$$

$$\mathbf{v}_D\cdot\nabla\theta \approx -\frac{v_{D,B}}{r}\left(\cos(\theta) - \alpha\sin^2(\theta)\right), \tag{5.378}$$

$$\mathbf{v}_D\cdot\nabla\varphi \approx 0, \tag{5.379}$$

where we define the characteristic magnetic drift speed to be

$$v_{D,B} = \frac{m}{eBR_0}\left(v_{\parallel}^2 + \frac{v_{\perp}^2}{2}\right). \tag{5.380}$$

Appendix 5.C Collisions

The main sections of this work only consider the collisionless Vlasov equation. In actuality, QuaLiKiz implements a Krook-type collision operator for trapped electrons. To account for its inclusion, we modify the Vlasov equation to

$$\frac{\partial \delta f_s}{\partial t} + \mathbf{\Omega}\cdot\frac{\partial \delta f_s}{\partial \boldsymbol{\alpha}} - e_s\frac{\partial \phi}{\partial \boldsymbol{\alpha}}\cdot\frac{\partial f_{0s}}{\partial \mathbf{J}} = -\nu\left(\delta f_s + \frac{e\phi}{T_s}f_{0s}\right), \tag{5.381}$$

where ν is the collision frequency. Note that the $e_s\phi f_{0s}/T_s$ term accounts for the adiabatic response from the electrostatic perturbation. We only include this term for electron-ion collisions as ion-ion collisions and electron-electron collisions would produce only a small correction. Thus, we drop the "s" in favor of "e" and take $e_s \rightarrow -e$. Substituting in our Fourier expressions for δf and ϕ, we find that

$$f_{\mathbf{n}} = \frac{f_{0e}}{T_e}\frac{-e\phi_{\mathbf{n}}\left(\mathbf{n}\cdot\boldsymbol{\omega}_* - \mathbf{n}\cdot\mathbf{\Omega} - \nu\right)}{\mathbf{n}\cdot\mathbf{\Omega} - \overline{\omega} - i\nu} = \frac{e\phi_{\mathbf{n}}}{T_e}f_{0e}\left(1 - \frac{\overline{\omega} - \mathbf{n}\cdot\boldsymbol{\omega}_*}{\overline{\omega} + i\nu - \mathbf{n}\cdot\mathbf{\Omega}}\right). \tag{5.382}$$

Therefore, we can simply substitute $\omega \rightarrow \omega + i\nu$ in the denominator of the resonant term to capture the effect of this collision operator. The drawback is that we lose the ability to simplify the functional. In QuaLiKiz, we take the collisional frequency to be

$$\nu_e(\xi, \lambda, \epsilon) = \nu_{ei}\left(\xi\right)^{-3/2} Z_{\text{eff}}\frac{\epsilon}{(1 - 2\epsilon - \lambda)^2}\frac{0.111\delta + 1.31}{11.79\delta + 1}, \tag{5.383}$$

ν_{ei} is the electron-ion Coulomb collision frequency, Z_{eff} is the effective charge of the ion species interacting with the electrons, and the parameter δ is defined as

$$\delta = 12.0\left(\frac{|\overline{\omega}|\,\epsilon}{\nu_{ei}Z_{eff}}\right)^{3/2}. \tag{5.384}$$

The explicit definition of ν_{ei} is

$$\nu_{ei} = \frac{e^4\lambda_e}{4\pi\epsilon_0^2\left(2T_e\right)^{3/2}m_e^{1/2}}, \tag{5.385}$$

where λ_e is the Coulomb logarithm relevant for electron collisions. Details for this collision operator can be found in Ref. 140. The numerical values as well as the derivation of δ were originally calculated in Ref. 141 and then modified for QuaLiKiz's purposes. Because ν is a function non-trivial of ξ, we cannot simplify the functional using this collision operator using Fried and Conte integrals, and the integration over the energy must be done numerically. The inability to simplify the ξ integration results in 2-dimensional integral. That aside, all other aspects of the trapped functional derivation remain intact.

We note this specific form of the collision operator is modified in comparison to the one found in Ref. 140. It was found that the previous form of the collision operator led to incorrect predictions for density profiles when used in QuaLiKiz (coupled to integrated modeling suites) in highly collisional regimes. In response, numerical parameters in the Krook operator were tuned to linear simulations in GENE, as demonstrated in Chapter 5. In doing so, we keep unchanged the generic dependence and numerical parameters derived from fundamental principles.

CHAPTER 6

Quasilinear modeling of collisional trapped electron modes

6.1 Introduction

In tokamaks, electrostatic drift instabilities constitute an important component of turbulence. In particular, microinstabilities such as trapped electron modes (TEMs) and ion temperature gradient (ITG) driven modes are responsible for a large portion of anomalous radial transport and thus are key to modeling transport physics.[142, 143] Many effects such as $E \times B$ shearing, collisions, and high magnetic shears can stabilize the turbulent transport, a key goal in fusion research. Experimentally, it has been shown that turbulent convection is responsible for the peaking of the density profile in the tokamak core.[144] Meanwhile in the context of integrated modeling, it is known that an inaccurate treatment of collisionality can lead to severe discrepancies in density profiles in the core, thereby leading to an incorrect absence of core density peaking. While collisions can in principle be accounted for through the use of sufficiently complex collision operators when simulating microinstabilities, the use of such operators incur a large computational cost that restrict their usefulness when considering their inclusion in transport models. Reduced models of collisions are therefore necessary when computational speed is a priority.

Motivated by the aforementioned discrepancies in integrated modeling, our study of TEMs is the primary focus of this work. As suggested by the name, TEM instabilities are driven by the presence of a trapped electron population in the tokamak whereby the electrons perform a bounce motion along the magnetic field lines.[145] Collisions serve to detrap particles by scattering them into the passing part of velocity space; as a result, TEMs are typically divided into collisionless TEMs

(CTEMs) and dissipative TEMs (DTEMs).[146] High-collisionality regimes involve the particle undergoing many collisions before completing a full bounce motion, thus leading to detrapping of the particle and producing a stabilizing effect. However, it is also important to recognize that passing electrons can play a role in TEM instabilities, thus creating a complicating interaction between the trapped and passing electron populations that leads to collisions becoming a destabilizing effect in certain low-collisionality regimes.[79] Moreover, the trapped-passing boundary in velocity space constitutes a region where collisional effects are amplified.

One key component missing from analytical TEM research is that the collisional frequency and the bounce-transit frequency are both velocity dependent.[79, 140] Dimensionless quantities that attempt to characterize the collisional regime are typically constructed by calculating these frequencies for thermal particles. While these quantities are useful to describe the overall effect of collisions, it is important to realize that collisions do not impact trapped particles in a uniform manner. Thus, we expect reasonably realistic collision operators to incorporate both energy and pitch angle dependence in order to treat collisions properly for TEMs. An overview of collision operators used in this work is given in Sec. 6.2.

There are two primary goals for this work. First, we attempt to construct a model to characterize DTEM growth rates in the regime where collisions are stabilizing in Sec. 6.3. We do so with the aid of the Gyrokinetic Electromagnetic Numerical Experiment (GENE) code by simulating a number of linear TEMs.[134] The core idea is to construct an effective trapped electron fraction; this effective trapped fraction takes into account the fact that not all trapped electrons contribute to TEM destabilization at high collisionality.

The second goal is address the failure of the quasilinear gyrokinetic code QuaLiKiz to predict density peaking in the tokamak core in high collisionality regimes when coupled with integrated modeling suites. To do so, we seek to improve the Krook-like collision operator in QuaLiKiz to properly treat DTEMs. This improvement leads to proper predictions of density peaking in the core when using QuaLiKiz to predict Joint European Torus (JET) profiles; the quasilinear fluxes computed by QuaLiKiz are used in tandem with the core transport equation solver JETTO as part of

the JET Integrated Transport Code (JINTRAC) suite.[24, 147] To tune QuaLiKiz's collision operator, we use GENE simulations as a point of comparison. We mandate that DTEMs simulated by QuaLiKiz exhibit a collisionality dependence in the DTEM growth rates matching that of GENE. To verify the nature of the improvement, we use the newly improved version of QuaLiKiz to simulate heat and particle transport of JET H-mode and L-mode collisionality scans within JETTO, many of which were investigated in Ref. 148. The improvements made to QuaLiKiz are discussed in Sec. 6.4. We then present conclusions in Sec. 6.5. Due to the large number of simulations produced for this work, we present figures for isolated GENE simulatiosn in Appendix 6.A, figures involving QuaLiKiz standalone simulations in Appendix 6.B, and figures produced from JETTO simulations in Appendix 6.C.

6.2 Collision operators

In this work, we make use of two collision operators: the Landau-Boltzmann collision operator[149] in GENE and a Krook-like operator[141] in QuaLiKiz. In general, a collision operator enters the Boltzmann equation as

$$\frac{df_s}{dt} = \left(\frac{\partial f_s}{\partial t}\right)_{\text{coll}} = \sum_{s'} C_{ss'}, \tag{6.1}$$

where f_s is the distribution function of species s and the collision operator $C_{ss'}$ takes into account collisions between different species. The full Landau-Boltzmann operator is written as

$$C_{ss'} = C_{ss'}(f_s, f_s') = \frac{\gamma_{ss'}}{m_s}\frac{\partial}{\partial \mathbf{v}} \cdot \int \mathrm{d}^3 v' \left(\frac{u^2 \boldsymbol{I} - \mathbf{uu}}{u^3}\right) \cdot \left(\frac{f_{s'}'}{m_s}\frac{\partial f_s}{\partial \mathbf{v}} - \frac{f_s}{m_{s'}}\frac{\partial f_{s'}'}{\partial \mathbf{v}'}\right), \tag{6.2}$$

where we use notation such that $f = f(\mathbf{v})$ while $f' = f(\mathbf{v}')$.[149] We also use standard dyadic notation with $\boldsymbol{I}$ being the 3-dimensional identity matrix and define $\mathbf{u} = \mathbf{v} - \mathbf{v}'$. Meanwhile, the factor $\gamma_{ss'}$ is written as

$$\gamma_{ss'} = \frac{e_s^2 e_{s'}^2 \lambda_{ss'}}{8\pi\epsilon_0^2}, \tag{6.3}$$

where m and e are the mass of the indicated species respectively, ϵ_0 is the vacuum permittivity, and $\lambda = \ln(\Lambda)$ is the Coulomb logarithm. The Coulomb logarithm is obtained by considering

two-body Coulomb collisions; typically, we enforce radial cutoffs in the calculation to take into account Debye screening at long length scales and large-angle scattering at short length scales. In general, the Coulomb logarithm is dependent on the density n and the temperature T of the two species involved. The exact expression for the Coulomb logarithm depends on the temperature scale associated with the collision. Essentially, if the de Broglie wavelength of the scattering particle is comparable to the distance of closest approach for a Coulomb collision, quantum mechanical effects must be taken into consideration. Since the de Broglie wavelength is inversely proportional to the reduced mass of the two-particle system given a constant velocity, collisions involving electrons require the quantum mechanical correction for electron temperatures relevant to a tokamak while ion-ion collisions require no quantum mechanical correction. The exact formulas can be found in Ref. 150.

For a simulation where the gyrokinetic equation has been linearized, it is typical to also linearize the collision operator. This is carried out with the δf approximation; we write each distribution function as $f = f_0 + \delta f$, where f_0 is a local Maxwellian while δf is the perturbation. We then write

$$\begin{aligned} C_{ss'}\left(f_s, f_s'\right) &= C_{ss'}(f_{0s}, f_{0s'}) + C_{ss'}(f_{0s}, \delta f_{s'}) + C_{ss'}(\delta f_s, f_{0s'}) + C_{ss'}(\delta f_s, \delta f_{s'}) \\ &\approx C_{ss'}(f_{0s}, \delta f_{s'}) + C_{ss'}(\delta f_s, f_{0s'}). \end{aligned} \tag{6.4}$$

For self-collisions, $C_{ss}(f_{0s}, f_{0s}) = 0$, since a Maxwellian is an equilibrium distribution. Meanwhile, electron-ion and ion-electron collisions are neglected since the rate of thermalization between two species is proportional to the electron-ion mass ratio and thus is thousands of times slower than other relevant collision processes. The term $C_{ss'}(\delta f_s, \delta f_{s'})$ is also neglected since it is quadratic in the perturbed distribution function. The implementation of the Landau-Boltzmann collision operator in GENE also uses a model operator[151] in place of $C_{ss'}(f_{0s}, \delta f_{s'})$); the model operator is constructed such that the particle, momentum, and energy conservation laws hold:

$$\int \mathrm{d}^3 v \, C_{ss'} = 0, \tag{6.5}$$

$$\int \mathrm{d}^3 v \, m_s \mathbf{v} C_{ss'} = -\int \mathrm{d}^3 v \, m_{s'} \mathbf{v} C_{s's}, \tag{6.6}$$

$$\int \mathrm{d}^3 v \, \frac{1}{2} m_s v^2 C_{ss'} = -\int \mathrm{d}^3 v \, m_{s'} \frac{1}{2} m_{s'} v^2 C_{s's}. \tag{6.7}$$

In QuaLiKiz, a different approach is used. Any collision operator that uses derivatives would slow down QuaLiKiz considerably, as a fundamentally different approach would need to be taken to obtain a tractable dispersion relation. A much slower version of QuaLiKiz would render its primary niche of being coupled to integrated modeling suites impossible. An energy-dependent collision operator necessarily increases the computational complexity since the dispersion relation can no longer be treated analytically with respect to the energy variable with judicious use of Fried and Conte integrals as derived in Chapter 5. Thus, any additional complexity in the operator must be carefully considered to avoid a computationally intractable code. For instance, a pitch angle scattering operator involves derivatives in the pitch angle variable resulting in an ordinary differential equation in terms of the pitch angle variable.[152] Solving this is typically done by expanding the perturbed distribution function in terms of Legendre polynomials. Thus, including derivatives with respect to the pitch angle parameter would increase the computational cost of a collisional simulation by at least an additional order of magnitude beyond the computational cost incurred by including an energy-dependent operator. We therefore make use of a Krook-style operator[153, 154] constructed to mimic the qualities of a pitch angle operator.

To begin, we first consider the deflection frequency $\nu_D^{ss'}$ defined as

$$\nu_D^{ss'} = \frac{\nu_\perp^{ss'}}{2} = \nu_0^{ss'} \frac{1}{\hat{v}_s^3} H\left(\hat{v}_s \frac{v_{\text{th},s}}{v_{\text{th},s'}}\right), \tag{6.8}$$

where $\nu_\perp^{ss'}$ is the transfuse diffusion frequency and the characteristic collision frequency $\nu_0^{ss'}$ is defined as

$$\nu_0^{ss'} = \frac{n_s' e_s^2 e_{s'}^2 \lambda_{ss'}}{4\pi\epsilon_0^2 m_s^2 v_{\text{th},s}^3}, \tag{6.9}$$

where v is the speed and we use the thermal velocity $v_{\text{th},s} = \sqrt{2T_s/m_s}$ to define the normalized speed $\hat{v}_s = v/v_{\text{th}s}$. Meanwhile, the function H is defined as

$$H(x) = \frac{e^{-x^2}}{\sqrt{\pi}x} + \left(1 - \frac{1}{2x^2}\right) \text{erf}(x). \tag{6.10}$$

We make simplifying assumptions regarding the deflection frequency by considering the electron-

ion mass ratio. First, we note the property of H that

$$\lim_{x\to\infty} H(x) = 1. \tag{6.11}$$

For electron-ion collisions, the argument of H will be large for relevant velocity scales due the electron-ion mass ratio. We can then write

$$\sum_i \nu_D^{ei} \approx \sum_i \nu_0^{ei} \frac{1}{\hat{v}_e^3} H\left(\hat{v}_e \frac{v_{\mathrm{th},e}}{v_{\mathrm{th},i}}\right) \approx \sum_i \nu_0^{ei} \frac{1}{\hat{v}_e^3}, \tag{6.12}$$

where we sum over all ions i. Meanwhile, for temperatures relevant to the core of a tokamak, $\lambda_{ee} = \lambda_{ei}$ for all ions i. Motivated by the quasineutrality condition, we also define the the effective ion charge number $Z_{\mathrm{eff}} = \sum_i Z_i^2 n_i / n_e$ where Z_i is the ion charge number. This leads to

$$\sum_i \nu_0^{ei} = \frac{n_e e^4 Z_{\mathrm{eff}} \lambda_e}{4\pi\epsilon_0^2 m_e^2 v_{\mathrm{th},e}^3} = Z_{\mathrm{eff}} \nu_0^{ee}, \tag{6.13}$$

where λ_e is the Coulomb logarithm used for collisions involving electrons. We then obtain[150, 154]

$$\sum_{s'} \nu_D^{es'} = \frac{n_e e^4 \lambda_e}{4\pi\epsilon_0^2 m_e^2 v_{\mathrm{th},e}^3} \frac{Z_{\mathrm{eff}} + H(\hat{v}_e)}{\hat{v}_e^3} = \frac{\nu_{ei}}{\hat{v}_e^3}(Z_{\mathrm{eff}} + H(\hat{v}_e)), \tag{6.14}$$

where we define the characteristic electron-ion collision frequency as

$$\nu_{ei} = \frac{n_e e^4 \lambda_e}{4\pi\epsilon_0^2 m_e^2 v_{\mathrm{th},e}^3}. \tag{6.15}$$

When considering ion collisions, we neglect ion-electron collisions due to the electron-ion mass ratio since $H(0) = 0$ and the argument of H for ion-electron collisions will be small, leading to

$$\sum_{s'} \nu_D^{is'} = \sum_j \frac{\nu_{ij}}{\hat{v}_i^3} H_{ij}\left(\hat{v}_i \frac{v_{\mathrm{th},i}}{v_{\mathrm{th},j}}\right), \tag{6.16}$$

where we sum over all ions j and define the the characteristic ion-ion collision frequency as

$$\nu_{ij} = \frac{Z_i^2 Z_j^2 n_j e^4 \lambda_{ij}}{4\pi\epsilon_0^2 m_i^2 v_{\mathrm{th},i}^3}. \tag{6.17}$$

We next proceed with the construction of the Krook-style collision operator, following the analysis presented in DeLucia.[154, 155] For simplicity, we consider only one ion species; the final

result can be generalized for multiple ion species by replacing Z_i with Z_{eff} for electron collisions and sum over all ions for ion collisions. The key is to construct two separate preliminary collision operators for electrons and ions with collision frequencies

$$\nu_e = a_e \epsilon \frac{\nu_{ei}}{(\hat{v}_e)^3} \frac{Z_i + H\left(v/v_{T_e}\right)}{|1 - 2\epsilon - \lambda|^2}, \tag{6.18}$$

$$\nu_i = a_i \epsilon \frac{\nu_{ii}}{(\hat{v}_i)^3} \frac{H(\hat{v}_i)}{|1 - 2\epsilon - \lambda|^2}. \tag{6.19}$$

Here, $\epsilon = r/R_0$ is the inverse aspect ratio where r is the local minor radius and R_0 is the major radius, λ is the pitch angle parameter, and a_s is a constant. In QuaLiKiz, we use the following definition for the pitch angle parameter λ:

$$\lambda = \frac{\mu B_{\text{min}}}{E}, \tag{6.20}$$

where μ is the magnetic moment, B_{min} is the magnetic field strength evaluated at its minimum on a given flux surface, and E is the kinetic energy. Because QuaLiKiz assumes circular flux surfaces, for small ϵ, the magnetic field strength can be approximated as $B \approx B_0(1 - \epsilon \cos(\theta))$, where θ is the poloidal angle and B_0 is a constant characteristic field strength. Thus, $B_{\text{min}} = B_0(1 - \epsilon)$. The pitch angle parameter determines whether a given particle is either trapped ($\lambda > 1 - 2\epsilon$) or passing ($\lambda < 1 - 2\epsilon$). The trapped-passing boundary is given at $\lambda = 1 - 2\epsilon$. The pitch angle dependence in the collision operator mimics the effects of pitch angle scattering in a crude way without the use of differential equations. Meanwhile, the collision frequency is constructed to diverge at the trapped-passing boundary. This accounts for enhancement of collisions at this boundary in velocity space. It is important then that any implementation of this method correctly capture this divergence. We also note for deeply trapped, thermal particles that

$$\nu_e \sim \frac{Z\nu_{ei}}{\epsilon}, \tag{6.21}$$

$$\nu_i \sim \frac{\nu_{ii}}{\epsilon}. \tag{6.22}$$

The collision frequencies are constructed such that they mimic the effective collision frequency for a simple Krook operator ($\nu_{\text{eff}} = \nu/\epsilon$), which takes into account the fact that the typical scattering

process we are concerned with is not 90° scattering but rather diffusion from the trapped part of velocity space to the passing part of velocity space.

The coefficients a_e and a_i are determined by comparing the collisional models with a dispersion relation obtained using a Lorentz collision operation by means of the variational principle.[156] It is important to note that this is calculated in the regime where

$$\frac{\nu_{ii}}{\epsilon} \ll |\omega| \ll \frac{\nu_{ei}}{\epsilon}, \tag{6.23}$$

where ω is the complex mode frequency. DeLucia then writes[154]

$$a_e = 1.31, \tag{6.24}$$

$$a_i = 9.42 \times 10^{-3}. \tag{6.25}$$

These coefficients are chosen such that they reproduce the collisional scalings obtained from the more accurate Lorentz model. The next step is to construct an operator that is valid outside this limit and bridges the regime of low collisionality and high collisionality (relative to the mode frequency). The result is

$$\nu_e = \epsilon \frac{\nu_{ei}}{\hat{v}_e^3} \frac{Z_i + H(\hat{v}_e)}{|1 - 2\epsilon - \lambda|^2} \frac{0.111\delta + 1.31}{11.79\delta + 1}, \tag{6.26}$$

$$\nu_i = \epsilon \frac{\nu_{ii}}{\hat{v}_i^3} \frac{H(\hat{v}_i)}{|1 - 2\epsilon - \lambda|^2} \frac{0.111\delta + 1.31}{11.79\delta + 1}, \tag{6.27}$$

where δ will be defined momentarily. The numerical factors are constructed such that

$$\lim_{\delta \to 0} \frac{0.111\delta + 1.31}{11.79\delta + 1} \approx a_e = 1.31, \tag{6.28}$$

$$\lim_{\delta \to \infty} \frac{0.111\delta + 1.31}{11.79\delta + 1} \approx a_i = 9.42 \times 10^{-3}. \tag{6.29}$$

Thus, the purpose of the δ dependent ratio is so that when the electron and ion collision frequencies have similar limiting behavior for arbitrary frequency ω while still independently abiding by the limiting behavior found when enforcing the ordering in Eq. (6.23). We thus require the numerical

factor δ to depend on the collisional frequency and mode frequency in such a way that

$$\lim_{|\omega|/\nu_{ss'}\to 0} \delta = 0, \tag{6.30}$$

$$\lim_{|\omega|/\nu_{ss'}\to \infty} \delta^{-1} = 0. \tag{6.31}$$

The specific choice of how to construct δ beyond the above constraints is arbitrary and cannot be obtained from analytical analysis alone. It is necessary to make reference to direct numerical simulations using more exact operators and perform a comparison to define δ. The incarnation of this operator was applied to codes used by Rewoldt[155, 157] and then modified in Ref. 141 in response to comparisons with the more exact Lorentz collision operator.

We are now in a position to present the collision operator used in QuaLiKiz. We use the above formalism but make further simplifying assumptions that are valid when considering TEMs. First, we neglect ion-ion collisions completely since they play little role for TEMs. Electron-electron collisions are also ignored as they provide only a small correction to the collision operator since $0 \leq H(\hat{v}_e) \leq 1$. Finally, this collision operator is only used for trapped particles, meaning that particle number, momentum, and energy are not conserved. Although an artificial collision term could in principle be added to passing particles to ensure conservation properties, it has been shown that these terms are negligible corrections in the electrostatic limit.[157] Since QuaLiKiz is an electrostatic code, these conservation properties can be safely ignored. We then write for electrons

$$\left(\frac{\partial f_e}{\partial t}\right)_{\text{coll}} = \begin{cases} -\nu_e\left(\delta f_e - \dfrac{e\phi}{T_e} f_{0e}\right) & \text{if trapped,} \\ 0 & \text{if passing,} \end{cases} \tag{6.32}$$

where ϕ is the perturbed electrostatic field.[140] Meanwhile, because we have no collision operator for ions, we write

$$\left(\frac{\partial f_i}{\partial t}\right)_{\text{coll}} = 0. \tag{6.33}$$

The collision frequency serves to drive the δf_e to $\frac{e\phi}{T_e}$ which corresponds to the electron adiabatic response created by the electrostatic perturbation. We consider two functional forms of δ. The first

one is taken from Ref. 141 and is defined as

$$\delta_K = \left(\frac{|\omega|\epsilon}{37.2\,\nu_{ei} Z_{\text{eff}}} \right)^{1/3}, \tag{6.34}$$

whereas the new one implemented in QuaLiKiz through detailed comparisons with GENE is defined as

$$\delta_Q = 12.0 \left(\frac{|\omega|\epsilon}{\nu_{ei} Z_{\text{eff}}} \right)^{3/2}. \tag{6.35}$$

A detailed comparison of these two operators will be made in Sec. 6.4. We also note that the collision operator as currently implemented in QuaLiKiz uses a slightly different definition for the electron-ion collision frequency. This will be rectified in future implementations. The definition QuaLiKiz uses is

$$\nu_{ei,Q} = \frac{4}{3\sqrt{\pi}} \frac{\nu_{ei}}{,} \tag{6.36}$$

which is based on energy transfer times in collisions as discussed in Sec. 6.3.

6.3 Effective trapped electron fraction

A key parameter in the characterization of TEMs is the trapped particle fraction f_t. At a given poloidal angle θ, the trapped fraction defined as the proportion of particles in velocity space that are trapped and is given by

$$f_t(\theta) = \frac{\int_{\text{trapped}} \mathrm{d}^3 v\, f(\mathbf{v})}{\int \mathrm{d}^3 v\, f(\mathbf{v})} = \frac{1}{n} \int_{\text{trapped}} \mathrm{d}^3 v\, f(\mathbf{v}). \tag{6.37}$$

The boundary in velocity space between trapped particles and passing particles can be characterized by the pitch angle. Since a curve of constant pitch angle forms a cone in velocity space, for an isotropic velocity distribution the trapped fraction can be calculated by simply taking the ratio of a spherical cone's volume to a sphere's volume. The curve defining the trapped-passing boundary is given by

$$v_{\parallel}^2 = v_{\perp}^2 \frac{B_{\text{max}} - B}{B}, \tag{6.38}$$

where $v_\parallel$ is the velocity parallel to the magnetic field, $v_\perp$ is the velocity perpendicular to the magnetic field and related to the magnetic moment $\mu = \left(mv_\perp^2\right)/(2B)$, and $B_{\max}$ is the maximum magnetic field strength on the flux surface. The poloidal dependence on the trapped-passing boundary is evident from the above equation. For a small inverse aspect ratio, this can be written as

$$v_\parallel^2 \approx v_\perp^2 \epsilon(1+\cos(\theta)). \tag{6.39}$$

This is equivalent to the condition that

$$\lambda = 1 - 2\epsilon, \tag{6.40}$$

as discussed in Sec. 6.2. However, the poloidal dependence of the trapped-passing boundary is not obvious when considering the pitch angle parameter unless one also keeps in mind that

$$1 - 2\epsilon < \lambda \leq 1 - \epsilon(1-\cos(\theta)), \tag{6.41}$$

$$1 - 2\epsilon < \lambda \leq 0. \tag{6.42}$$

For an isotropic distribution in the small inverse aspect ratio limit, we then obtain that the trapped particle fraction is

$$f_t(\theta) = \sqrt{\epsilon(1+\cos(\theta))}. \tag{6.43}$$

However, we are typically interested in a simulation of the whole flux surface, not at just a single position. By taking advantage of the fact that the density of particles is approximately a flux function, we can compute the flux surface average of the trapped particle fraction to obtain

$$\langle f_t \rangle = \frac{1}{4\pi^2}\int \mathrm{d}S\, f_t(\theta) = \frac{1}{2\pi}\int_0^{2\pi} \mathrm{d}\theta\, (1+\epsilon\cos(\theta)) f_t(\theta) \approx \frac{1}{2\pi}\int_0^{2\pi} \mathrm{d}\theta\, f_t(\theta) = \frac{2}{\pi}\sqrt{2\epsilon}. \tag{6.44}$$

The trapped fraction drives both CTEM and DTEM instabilities. The specific effect collisions have on the instability can vary between different regimes; in some cases, especially those with particularly large density gradients,[79, 158] collisions can destabilize the TEM.[145] In other cases, collisions instead stabilize the mode.[140, 159, 160] It is important to keep in mind that for extremely high collisionality, one cannot adequately speak of trapped electrons due to the lack of any characteristic

bounce motion.[146] We note that earlier studies often made use of Krook collision operators with no velocity dependence for analytical simplicity, while modern supercomputers allow for the use of more sophisticated collision operators such as the Lorentz or Landau-Boltzmann operator. For the simulations conducted with typical tokamak core parameters and more realistic collision operators, the instability generally stabilizes with increasing collisionality. We introduce the dimensionless quantity ν^* to characterize the collisional regime and define it as

$$\nu^* = \frac{4}{3\sqrt{\pi}} \frac{\nu_{ei}}{\omega_{b0}\epsilon} \tag{6.45}$$

The factor of ϵ^{-1} takes into account the effective collisional frequency relevant for trapped electrons in velocity space as discussed in Sec. 6.2. Meanwhile, the numerical prefactor $4/(3\sqrt{\pi})$ is included by convention, since the characteristic collision time[8] associated with energy transfer between electrons and ions is

$$\tau_e = 3\,(2\pi)^{3/2} \frac{\epsilon_0^2 m_e^{1/2} T_e^{3/2}}{n_e e^2 \lambda_e} = \frac{3\sqrt{\pi}}{4} \nu_{ei}. \tag{6.46}$$

One must mind the differing definitions of the characteristic collision frequencies used in the literature to ensure the right numerical prefactors are used. Meanwhile, the term ω_0 is the characteristic electron bounce frequency[120] and defined to be

$$\omega_{b0} = \frac{\sqrt{T_e/m_e}\sqrt{\epsilon}}{qR_0}, \tag{6.47}$$

where q is the safety factor. Small values of ν^* corresponds to the scenario where trapped electrons undergo many bounce motions before undergoing a significant collision, whereas large values of ν^* imply that the trapped electrons undergo many collisions before completing a single bounce motion. However, this characterization is only valid for deeply trapped thermal electrons. For any given distribution of electrons, there will be a population of low energy trapped electrons that undergo many collisions before completing a bounce motion and a population of high energy trapped electrons that undergo many bounce motions before undergoing a collision. We therefore consider the velocity dependent collisionality parameter $\hat{\nu}$ defined as

$$\hat{\nu}(\mathbf{v}) = \frac{Z_{\text{eff}}\nu_{ei}}{\omega_b \epsilon} \frac{1}{\hat{v}_e^3}. \tag{6.48}$$

We have included $\hat{v}_e^{-3}$ to take into account the velocity dependence of the collisional frequency. Meanwhile, ω_b corresponds to the velocity dependent bounce frequency, defined for small inverse aspect ratio as

$$\omega_b = \frac{\sqrt{E/m_e}\sqrt{\epsilon}}{qR_0}\frac{\pi}{2K(\kappa)} = \omega_{b0}\hat{v}_e\frac{\pi}{2K(\kappa)}. \tag{6.49}$$

Here, K is the complete elliptic integral of the first kind and we define the trapping parameter κ such that

$$\lambda = 1 - 2\epsilon\kappa^2. \tag{6.50}$$

Therefore, for trapped particles, we have

$$|\sin(\theta/2)| \leq \kappa \leq 1, \tag{6.51}$$

and $\kappa = \sin(\theta_b/2)$ where θ_b is the bounce angle. Since all of our simulations have sufficiently small ϵ, this formula is accurate for our purposes.[120] Thus, while the bounce frequency is largely dependent on the velocity, it is also dependent on the pitch angle; particles that are close to the trapped-passing boundary have lower bounce frequency and thus correspond to larger values of $\hat{\nu}$ all else being equal. Intuitively, this corresponds to marginally trapped particles being more easily detrapped. The full expression for $\hat{\nu}$ is then

$$\hat{\nu} = \frac{\nu_{ei}}{\omega_{b0}\epsilon}\frac{2K(\kappa)}{\pi\hat{v}_e^4} = \nu^*\frac{2K(\kappa)}{\pi\hat{v}_e^4}. \tag{6.52}$$

We now use the notion of the trapped particle fraction as inspiration to define the marginally trapped fraction of particles. We dub particles with low values of $\hat{\nu}$ to be marginally trapped as defined by the condition

$$\hat{\nu}a_c \geq 1, \tag{6.53}$$

where a_c is a constant that is $\sim O(1)$. Equivalently, we can write this as

$$\hat{v}_e \leq \left(a_c\nu^*\frac{2K(\kappa)}{\pi}\right)^{1/4}. \tag{6.54}$$

We then define the marginal trapped fraction to be the fraction of total particles that meet the above condition, leading to

$$f_m = \frac{\int_{\text{marginal}} \mathrm{d}^3v\, f_{0e}}{\int \mathrm{d}^3v\, f_{0e}}, \tag{6.55}$$

where f_{0e} is a Maxwellian given by

$$f_{0e} = \frac{n_e}{\left(\sqrt{\pi} v_{\mathrm{th,e}}\right)^3} e^{-v^2/v_{\mathrm{th,e}}^2} = \frac{n_e}{\left(\sqrt{\pi} v_{\mathrm{th,e}}\right)^3} e^{-\hat{v}_e^2}. \tag{6.56}$$

Essentially, we integrate over the speed v up until the marginal condition is met and then integrate over κ. To lowest-order in ϵ, the integral simplifies to

$$f_m = \int_{|\sin(\theta/2)|}^{1} \frac{\mathrm{d}\kappa \sqrt{2\epsilon}\kappa}{\sqrt{\kappa^2 - \sin^2(\theta/2)}} F\left(a_c \nu^* \frac{2K(\kappa)}{\pi}\right), \tag{6.57}$$

where the function F is defined as

$$F(x) = \mathrm{erf}(x^{1/4}) - \frac{2}{\sqrt{\pi}} x^{1/4} e^{-x^{1/2}}. \tag{6.58}$$

The constant a_c therefore sets the boundary at which we consider particles to be marginally trapped. We note that

$$\lim_{a_c \to 0} f_m = f_t, \tag{6.59}$$

$$\lim_{a_c \to \infty} f_m = 0. \tag{6.60}$$

We then define the effective trapped electron fraction that contributes to the trapped electron drive to be

$$f_t^* = f_t - f_m. \tag{6.61}$$

We then take the flux surface average of f_m to remove the poloidal dependence, leading to

$$\begin{aligned} \langle f_m \rangle &\approx \frac{1}{2\pi} \int_0^{2\pi} \mathrm{d}\theta \int_{|\sin(\theta/2)|}^{1} \frac{\mathrm{d}\kappa \sqrt{2\epsilon}\kappa}{\sqrt{\kappa^2 - \sin^2(\theta/2)}} F\left(a_c \nu^* \frac{2K(\kappa)}{\pi}\right), \\ &= \frac{2\sqrt{2\epsilon}}{\pi} \int_0^1 \mathrm{d}\kappa\, K(\kappa)\kappa F\left(a_c \nu^* \frac{2K(\kappa)}{\pi}\right), \end{aligned} \tag{6.62}$$

where the simplified expression is obtained by changing the order of integration. Likewise, the flux surface averaged effective trapped electron fraction is

$$\left\langle f_t^* \right\rangle = \langle f_t \rangle - \langle f_m \rangle = \langle f_t \rangle \left(1 - \int_0^1 \mathrm{d}\kappa\, K(\kappa)\kappa F\left(a_c \nu^* \frac{2K(\kappa)}{\pi}\right)\right). \tag{6.63}$$

In the regime where collisions contribute to stabilization of DTEMs, we hypothesize that the effective trapped electron fraction drives DTEM instabilities in a way that is analogous to the trapped electron fraction drive in CTEMs. For simplicity, we fix other important parameters such as the normalized temperature and density gradients and consider the growth rate γ on a case-by-case basis while allowing ϵ and ν^* to vary. For the purpose of this work, we vary ν_{ei} for any given case by scanning over the reference temperature of the simulation. In general, the growth rate would of course depend on both ϵ and ν^* in a non-trivial way. The growth rate for CTEMs can then be written as

$$\gamma = \gamma(\langle f_t \rangle). \tag{6.64}$$

For DTEMs, we hypothesize that the growth rate can instead be written as

$$\gamma = \gamma\left(\left\langle f_t^* \right\rangle\right). \tag{6.65}$$

That is, by holding everything else fixed, the collisionality and ϵ dependence can be summarized by the effective trapped electron fraction. Intuitively, we claim collisions stabilize the mode via the detrapping effect where electrons that are close to the trapped-passing boundary or of particularly low energy are prone to detrapping. The dimensionless quantity a_c determines the exact strength of this detrapping effect. We therefore hypothesize that in suitable cases, the collisionality and ϵ dependence can be reduced to a 1-parameter model where the parameter a_c is determined by the parameters of the case (e.g. the temperature and density gradients). Equivalently, we can determine the effective inverse aspect ratio ϵ^* by calculating

$$\epsilon^* = \left(\frac{\pi}{2\sqrt{2}} \left\langle f_t^* \right\rangle\right)^2. \tag{6.66}$$

To test the efficacy of this model, we conduct linear gyrokinetic simulations based off of five parameter sets using GENE. The parameter sets are summarized in Table 6.1. We first use two basic cases: the General Atomics (GA) Standard Case[161] and a Tungsten Steady-state Tokamak (WEST) case based on a long L-mode pulse.[162] We also use three additional experimentally motivated cases taken from JETTO runs based on Joint European Torus (JET) profiles where DTEMs play

Case	R/a	Z_{eff}	R/L_{T_e}	R/L_{T_i}	R/L_n	q	s	τ
GA Standard	3	1	9.0	9.0	3.0	2.0	1.0	1
WEST	5	2.8	15.0	9.0	5.5	1.7	0.9	1/2
JETTO Run 73342	3	1.8	9.7	8.1	2.4	2.4	2.0	1
JETTO Run 95272	3	1	10.2	10.2	3.5	2.0	2.1	1
JETTO Hybrid H-mode	3	1.7	11.4	10.0	3.0	2.2	1.8	1

Table 6.1: Summary of cases being simulated.

an important role in turbulent transport.[148, 163] In the table, R/a is the aspect ratio of the machine where a is the minor radius of the machine while R is the major radius. We define also define the parameters

$$\tau = \frac{T_i}{T_e}, \tag{6.67}$$

$$L_{T_s} = -\frac{1}{T_s}\frac{dT_s}{dr}, \tag{6.68}$$

$$L_n = -\frac{1}{n}\frac{dn}{dr}. \tag{6.69}$$

For simplicity, we include deuterium as the ion species with charge $Z_i = 1$ and nucleon number $A_i = 2$. We include the effects of multiple ion species via Z_{eff}. Quasineutrality guarantees then that $L_{n_e} = L_{n_i} = L_n$. The simulations also assume a circular equilibrium defined by the safety factor q and the magnetic shear s. For JETTO Run 73342 and JETTO Hybrid H-mode parameters we use the $s - \alpha$ equilibrium model. For JETTO Run 73342 parameters, we take $\alpha = 0.80$, while for JETTO Hybrid H-mode parameters $\alpha = 0.75$. In all these linear runs, we take the electrostatic limit and thus neglect electromagnetic effects. For all cases, we use the Landau-Boltzmann collision operator.

For each case, we perform a scan over $k_\theta \rho_s$, where k_θ is the poloidal component of the wavenumber of the mode and $\rho_s = \sqrt{T_s}/\Omega_s$, where Ω_s is the reference cyclotron frequency. Note

that s here refers to the primary ion species; since we only have one ion species, $\rho_s = \rho_i$. For each case, the interval is $0.2 \leq= k_\theta \rho_i \leq 0.5$ with increment 0.1. We also scan over ϵ for each case, and for each value of ϵ we scan over ν^* by varying the reference temperature. We perform convergence tests for each individual simulation by varying the resolution of the simulation until the growth rate has sufficiently converged. For the simulations where the TEM is dominant, we use initial value simulations to determine the growth rate. For the runs where the TEM is subdominant to an ITG mode, we use the eigenvalue solver to solve for the TEM growth rate. We use the sign of the real frequency as well as the behavior of the mode with respect to collisionality to determine whether it is a TEM or not for our purposes. It is important, however, to keep in mind that instabilities are not always easily separable from each other, so some caution must be taken when labeling a mode as TEM or ITG;[113] as a result, we shall term a mode ITG-dominated if the sign of the real mode frequency aligns with the ion drift direction and TEM-dominated if the sign of the real mode frequency is associated with the electron drift direction. This is most easily seen in the WEST case where the real frequency of the dominant mode changes with collisionality whereas the dominant mode has real frequency firmly within the TEM regime. For each mode we obtain the frequency $\omega = \omega_r + i\gamma$, where ω_r is the real frequency and γ is the growth rate.

First, we plot the growth rates for all five cases as a function of $k_\theta \rho_s$ as well as ϵ in Figs. 6.1–6.5. The drive created by the trapped electron fraction is clearly evident when comparing the growth rate spectrum across over different values of ϵ. Next, we plot the growth rate as a function of collisionality for $k_\theta \rho_s = 0.3$ in Figs 6.6–6.10. It can be seen that collisions stabilize the mode for moderately high values of ν^* and that, with exception of a small number of cases, the growth rate decreases monotonically with the collisionality. This is in congruence with previously acquired results for typical tokamak core parameters.[141, 160] In general, however, the instability's dependence on collisionality is non-trivial for all of these cases. To test the model, we scan over different values of a_c for any given case, where a_c does not vary within a case for different values of ϵ, ν^*, or $k_\theta \rho_s$. We then obtain a best fit such that the growth rate dependence on ϵ^* is nearly independent of ϵ for the collisional cases and matches the collisionless growth rate. Figs. 6.11–6.15 show the result for

Case	a_c
GA Standard	6.5
WEST	1.2
JETTO Run 73342	5.0
JETTO Run 95272	8.1
JETTO Hybrid H-mode Case	3.9

Table 6.2: Value of a_c for each simulated case.

$k_\theta \rho_s = 0.3$. The only significant deviations occur for the GA and WEST based cases at fairly high values of ϵ as well as when the growth rate saturates with increasing collisionality. This saturation can be clearly seen in the JETTO Run 95272 case. Otherwise, the deviation from the collisionless calculation is less than 5%. The values for a_c determined are shown in Table 6.2. As expected, we see that $a_c \sim O(1)$ for all cases.

Although we have successfully characterized the TEM growth rates with this approach, there are a few caveats. While $a_c \sim O(1)$ for all cases, there is still a wide spread in the specific values with no clear pattern. Thus, any implementation of this model as a reduced version of a collision operator would be ad-hoc without deeper knowledge as to what determines the specific value of a_c. Furthermore, we only analyzed the growth rates for DTEMs. In general, the quasilinear flux ratios and real frequencies do not necessarily corresponds to this model so neatly, thus limiting its effectiveness. We also do not expect this model to accurately describe ITG or ETG modes; a proper collisional model must be able to describe the effect of collisions on those and other instabilities adequately. To test, a brief implementation of this model was attempted in QuaLiKiz to fix the aforementioned issue with core density peaking. We omit the specific analysis for brevity, as the implementation ultimately did not reproduce the requisite density peaking.

6.4 Improvements to QuaLiKiz's collisional operator

Our next task is to improve the collisional operator in QuaLiKiz. The strategy is to change the definition of δ such that the TEM collisionality dependence in QuaLiKiz matches the aforementioned GENE simulations; we use the same exact simulations done in Sec. 6.3 to perform the QuaLiKiz-GENE comparisons. To appropriately change δ, we parameterize it such that

$$\delta = a_\delta \left(\frac{|\omega|\epsilon}{\nu_{ei,Q} Z_{\text{eff}}} \right)^{b_\delta}, \tag{6.70}$$

where a_δ and b_δ are tunable constants. Since our goal is to improve the treatment of highly collisional DTEMs in QuaLiKiz, we must ensure that the behavior for DTEMs is preserved for low collisionality as well. From this parametrization we see that the old definition of the Krook operator formulated in Ref. 141 uses

$$a_{\delta,K} = 0.30, \tag{6.71}$$

$$b_{\delta,K} = \frac{1}{3}, \tag{6.72}$$

whereas the new definition of the Krook operator uses

$$a_{\delta,Q} = 12.0, \tag{6.73}$$

$$b_{\delta,Q} = \frac{3}{2}. \tag{6.74}$$

Notably, the definition of these parameters differ as well in the original formulation detailed in Ref. 154; these free parameters were tuned to match the Lorentz operator used in Ref. 141 to better predict the growth rate for TEMs. In arriving at the new tuning, we scan over values of a_δ and b_δ and fit the resulting collisionality dependence of the TEM growth rates to linear GENE simulations. Essentially, we use the GENE simulations as a reference to compare the old and new version of the Krook operator used in QuaLiKiz. Because the values of a_δ and b_δ cannot be derived analytically, we expect their optimal values to depend on the specific model using the Krook operator as every model will have different underlying assumptions.

As a starting reference, we compare the calculated CTEM growth rates between QuaLiKiz and GENE. Figures for $k_\theta \rho_s$ are shown in Figs. 6.16–6.20. We see here that even in the collisionless case, there are some discrepancies between the growth rates computed in QuaLiKiz and GENE; this is to be expected since the precise growth rate is sensitive to the input parameters even when confined to similar models. The deviation tends to grow in both the limit of large ϵ and the limit of small ϵ. Moreover, the minimum value of ϵ that destabilizes the TEM is slightly different between GENE and QuaLiKiz simulations. For realistic values of ϵ relevant to experimental regimes, however, the agreement is satisfactory given that QuaLiKiz is a greatly reduced model as shown in Chapter 5. In particular, QuaLiKiz assumes that the trapped particles are deeply trapped when calculating the trapped part of the dispersion relation. Moreover, the eigenfunctions used by QuaLiKiz make use of a Gaussian ansatz and are calculated in the fluid limit; it is known that this approximation is rather crude for TEMs.[103] To take into account these differences when comparing DTEM growth rates, we take this discrepancy into account by computing the relative collisional damping in GENE and QuaLiKiz separately; our goal is to match the collisionality dependence using the collisionless growth rate as a given. Thus we compute γ_{ref} to be the collisionless growth rate for a given case and value of ϵ for GENE and QuaLiKiz separately.

Taking inspiration from Ref. 141, we scanned over different values for the free, underivable parameters $a_{\delta,Q}$ and $b_{\delta,Q}$ where each parameter was initially varied separately; for $b_{\delta,Q}$, we varied the exponent slightly over rational numbers between $1/4$ and 2. Meanwhile, $a_{\delta,Q}$ was varied over two orders of magnitude. After converging on a trial set of values, we scanned over a small region in parameter space to determine the final tuning. The final values we acquire are $a_{\delta,Q} = 12.0$, $b_{\delta,Q} = 3/2$. We plot results for $k_\theta \rho_s$ and nominal values of ϵ in Figs. 6.21–6.25. We see marked improvement for all DTEM growth rates and identify the probable culprit behind the issues in integrated modeling. Essentially, the previous version of the collision operator produced damping that was too strong. We confirm this by computing the complete particle, ion heat, and electron heat fluxes in QuaLiKiz over the range $0.1 \leq k_\theta \rho_s \leq 2.0$ for the three JETTO based cases (due to quasineutrality and the lack of any bulk rotation of the plasma, the particle flux is ambipolar). We

can see in Figs. 6.26–6.34 that the important properties of the flux structure are shifted rightwards in collisionality with the new Krook operator, indicating that the effective impact of collisions in the new operator is reduced. We can see that the outward particle flux at the nominal value of ν^* for these simulations is reduced; an artificially large outward particle flux would lead to a less peaked density profile in the core. We note that the net impact on the JETTO Hybrid H-mode case is muted; it is evident from Fig. 6.25 that the collisionality dependence of the old Krook operator was already quite close to that of GENE. Indeed, it is important that we do not ruin the collision operator in the cases where collisionality dependence is correct. Since QuaLiKiz's collision operator functioned quite well in the low-collisionality limit, a crude approach such as artificially reducing ν^* by a factor of 10 would be inappropriate.

Finally, we implement the new collision operator by by running JETTO-QuaLiKiz simulations for H-mode and L-mode ν^* collisionality scans reported in Ref. 148 as shown in Figs. 6.35–6.40, as well as two high-collisionality H-modes (Figs. 6.41, 6.42), a very high-collisionality Ohmic L-mode (Fig. 6.43), and a mid-collisionality heated L-mode (Fig.6.44). We see that the correct behavior is preserved in low-collisionality cases. We also observe definitive improvement in the density profile predictions for mid- to high-collisionality cases L-mode cases without much change in the temperature profile prediction. Some particularly poor cases are shown as well which exhibit noticeable hollowing in the density profile between the core and the edge region; these cases are associated with the highest collisionality regimes among all the discharges studied. While the density profiles do not exhibit the correct behavior with the new change, there is still a net positive improvement in these cases. For completeness, we also include a comparison between an even older version of the Krook operator in Fig. 6.44. In this case, the red curve indicates the version of QuaLiKiz that was based on the old Kotschenreuther version of the Krook operator but was implemented incorrectly. Essentially, the pitch angle dependence of the old Krook operator was coded incorrectly in QuaLiKiz such that the singularity in the Krook operator was not located at the trapped-passing boundary in velocity space, but some other region of velocity space. The bug fix alone resulted in marked improvement in this particular case.

For deeper insight as to why the new Krook operator improves the the density peaking, we compute the instability spectrum for a high-collisionality L-mode case and plot the results in Fig. 6.45. We see here that for $k_\theta \rho_s > 0.2$ the mode switches to a proper TEM-dominated regime for the new Krook operator, while the ITG mode is dominant for low $k_\theta \rho s$. In the old Krook operator, the TEM never becomes dominant for this example. It is known that the interplay between the two modes in the mixed ITG-TEM regime is important for density peaking,[164] further confirming our suspicions that the improper treatment of DTEMs in QuaLiKiz is responsible for a large part in the incorrect density profiles.

6.5 Chapter summary

In this work, we constructed a collisionality model with the aid of GENE simulations using the notion of an effective trapped electron fraction. The resulting model was successful in characterizing the growth rate spectrum for DTEMs by capturing the combined ϵ and ν^* dependence. Further work can be done to extend the applicability of this model by considering more complicated geometries. Moreover, one could also extend the parameter range by including gradient or geometrical parameter scans to gain further insight as to how the dimensionless number a_c depends on the input parameters.

In addition, we successfully improved the collisional model in QuaLiKiz by tuning the dimensionless parameters of the Krook-like operator to GENE simulations. The result was a definitive improvement in moderately collisional L-mode cases while also preserving the correct treatment for low collisionality. We note further improvements can be made to QuaLiKiz given that $\nu^* > 1$ cases still exhibit noticeable density profile hollowing in between the core and the edge. For the Ohmic high-collisionality case, no rotation was included in the simulation, but the impact of intrinsic rotation may have a disproportionate impact on the density peaking, as the presence of rotations tends to quench low $k_\theta \rho s$ modes leading to reduced outward radial convection. Thus, the interplay between the newly improved collision operator and intrinsic rotations would be a fruitful topic of further study.

Appendix 6.A Figures: GENE simulations

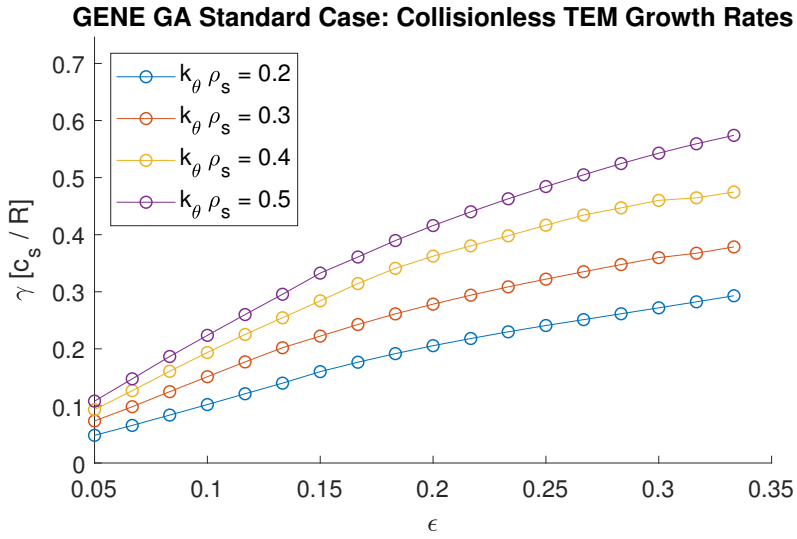

Figure 6.1: Collisionless TEM growth rates calculated by GENE for different values of $k_\theta \rho_s$ plotted against ϵ using GA Standard parameters. Note that the growth rate increases monotonically with ϵ.

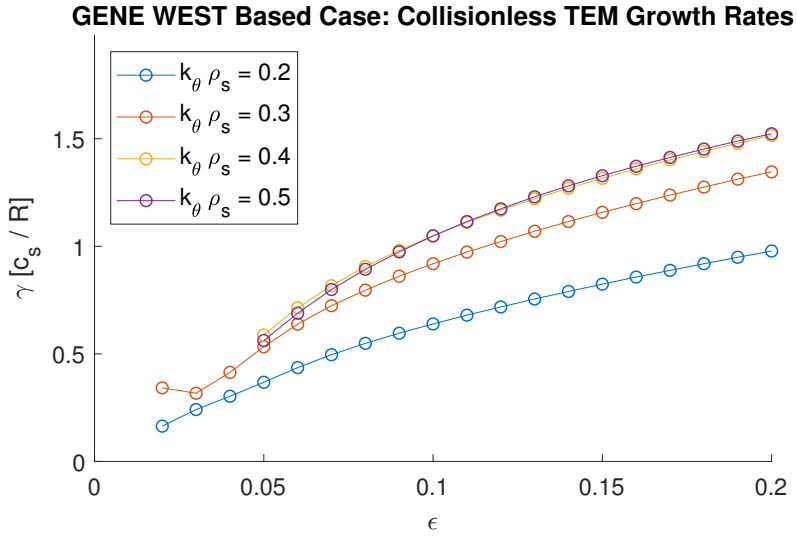

Figure 6.2: Collisionless TEM growth rates calculated by GENE for different values of $k_\theta \rho_s$ plotted against ϵ using WEST parameters. Note that the growth rate increases monotonically with ϵ.

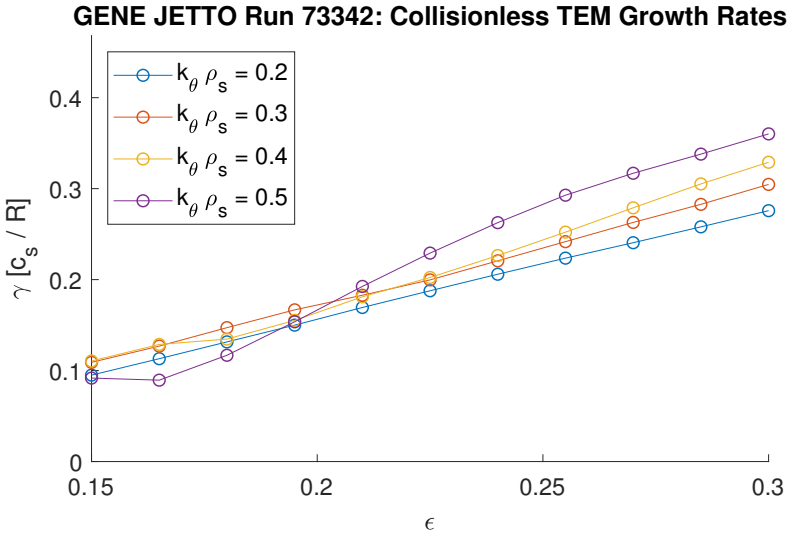

Figure 6.3: Collisionless TEM growth rates calculated by GENE for different values of $k_\theta \rho_s$ plotted against ϵ using JETTO Run 73342 parameters. Note that the growth rate increases monotonically with ϵ.

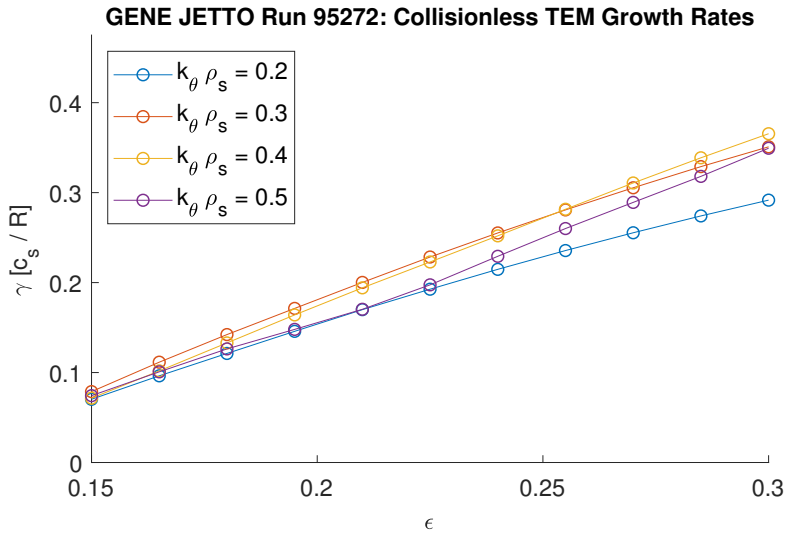

Figure 6.4: Collisionless TEM growth rates calculated by GENE for different values of $k_\theta \rho_s$ plotted against ϵ using JETTO Run 95272 parameters. Note that the growth rate increases monotonically with ϵ.

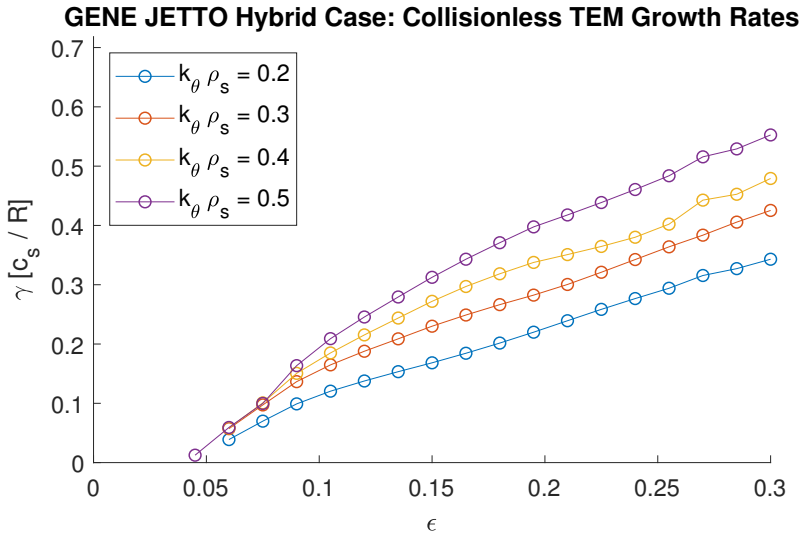

Figure 6.5: Collisionless TEM growth rates calculated by GENE for different values of $k_\theta \rho_s$ plotted against ϵ using JETTO Hybrid H-mode parameters. Note that the growth rate increases monotonically with ϵ.

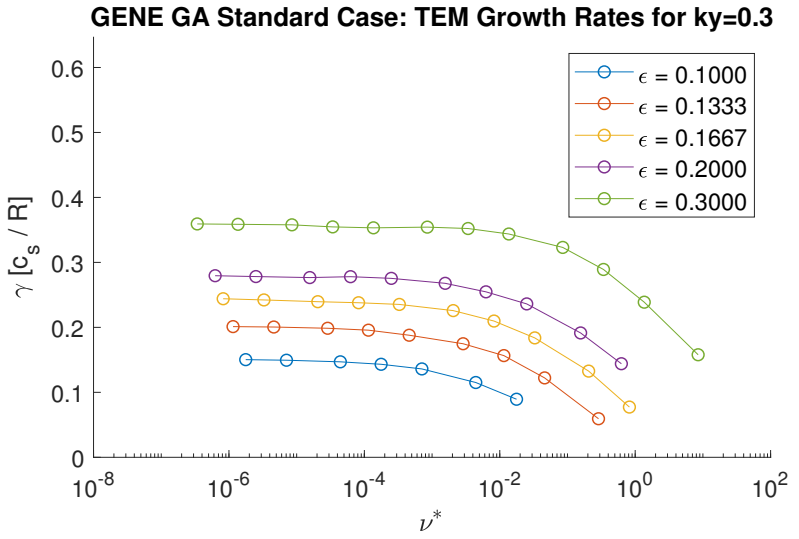

Figure 6.6: Collisional TEM growth rates calculated by GENE for different values of ϵ plotted against ν^* using GA Standard parameters where $k_\theta \rho_s = 0.3$. Note that the growth rate decreases nearly monotonically with ν^*.

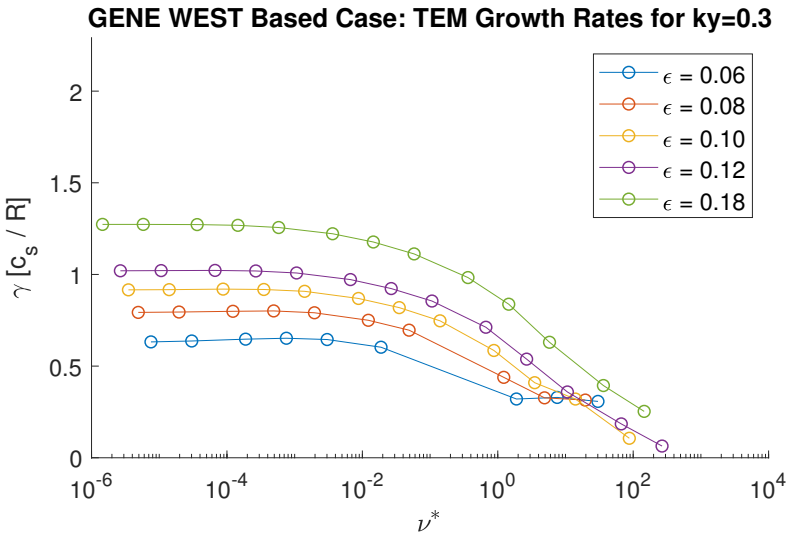

Figure 6.7: Collisional TEM growth rates calculated by GENE for different values of ϵ plotted against ν^* using WEST parameters where $k_\theta \rho_s = 0.3$. Note that the growth rate decreases nearly monotonically with ν^*.

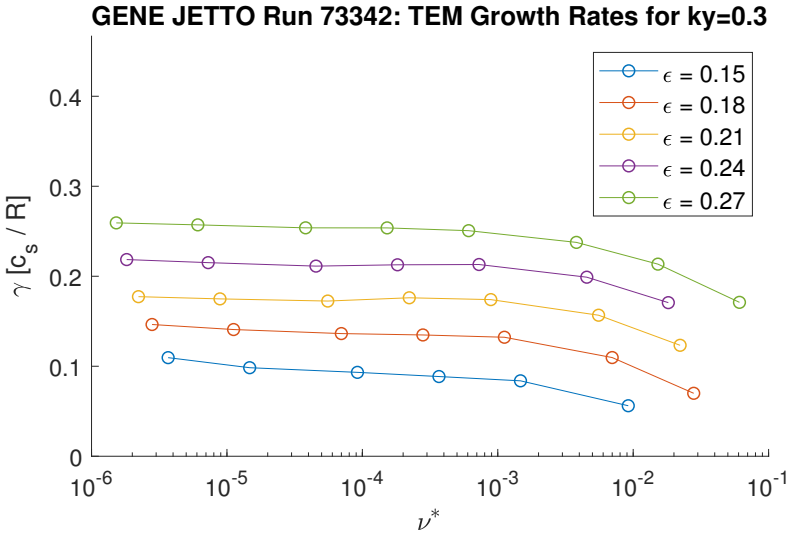

Figure 6.8: Collisional TEM growth rates calculated by GENE for different values of ϵ plotted against ν^* using JETTO Run 73342 parameters where $k_\theta \rho_s = 0.3$. Note that the growth rate decreases nearly monotonically with ν^*.

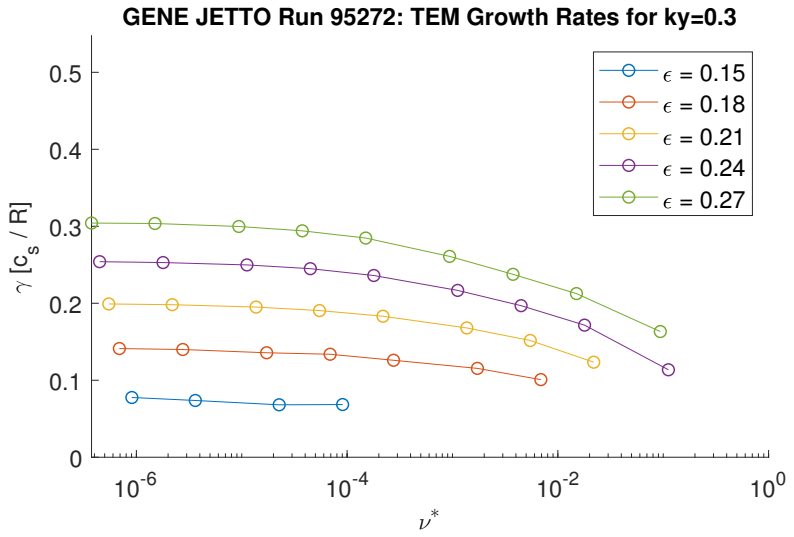

Figure 6.9: Collisional TEM growth rates calculated by GENE for different values of ϵ plotted against ν^* using JETTO Run 95272 parameters where $k_\theta \rho_s = 0.3$. Note that the growth rate decreases nearly monotonically with ν^*.

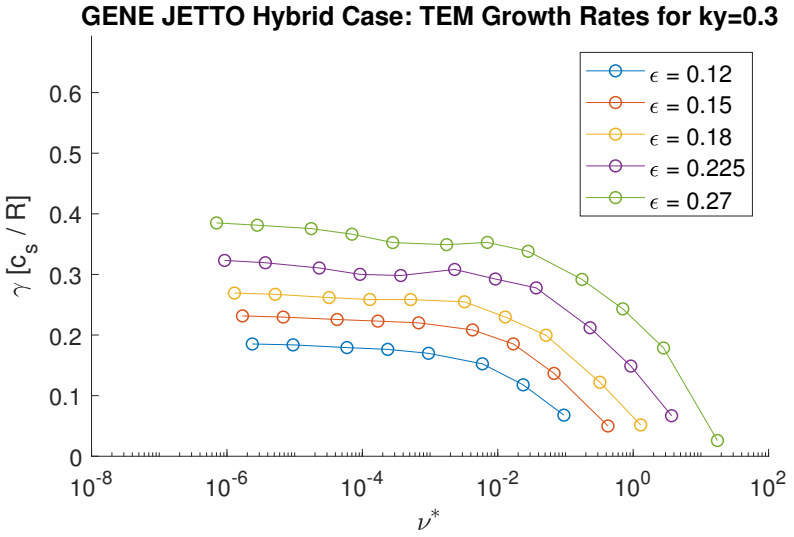

Figure 6.10: Collisional TEM growth rates calculated by GENE for different values of ϵ plotted against ν^* using JETTO Hybrid H-mode parameters where $k_\theta \rho_s = 0.3$. Note that the growth rate decreases nearly monotonically with ν^*.

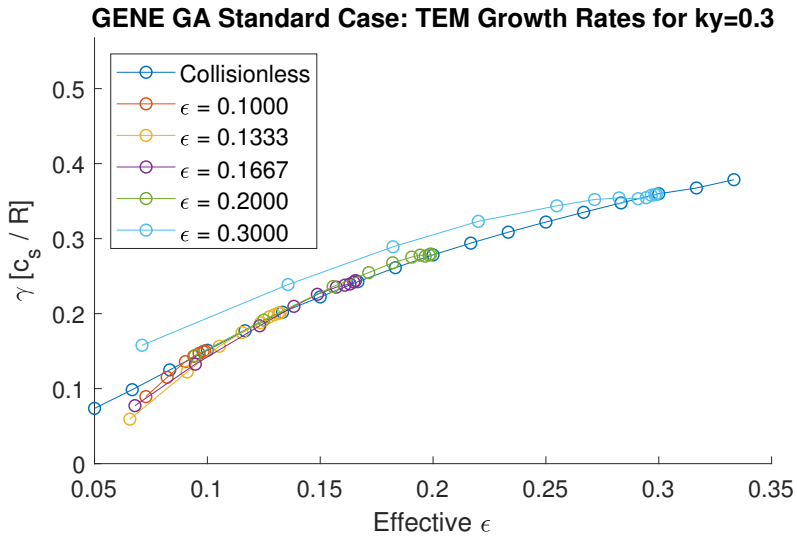

Figure 6.11: TEM growth rates calculated by GENE for different values of nominal ϵ plotted against effective ϵ^* (via the effective trapped fraction model) using GA Standard parameters where $k_\theta \rho_s = 0.3$. Note the close agreement.

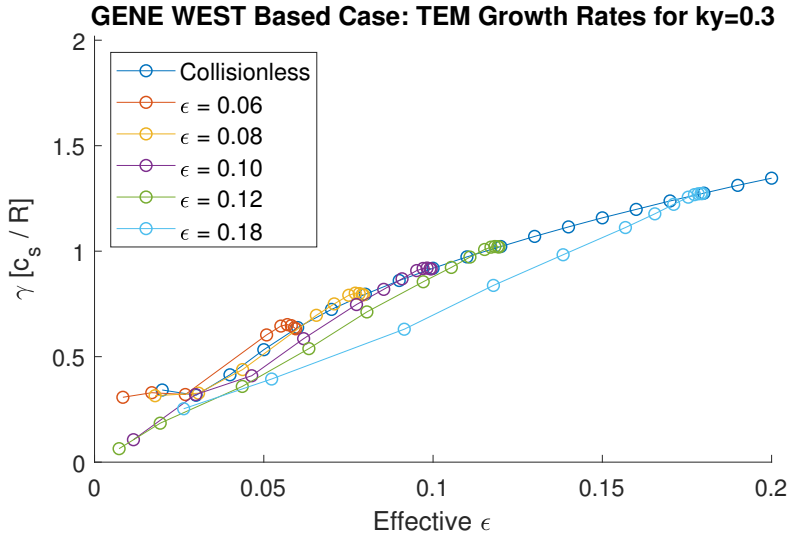

Figure 6.12: TEM growth rates calculated by GENE for different values of nominal ϵ plotted against effective ϵ^* (via the effective trapped fraction model) using WEST parameters where $k_\theta \rho_s = 0.3$. Note the close agreement.

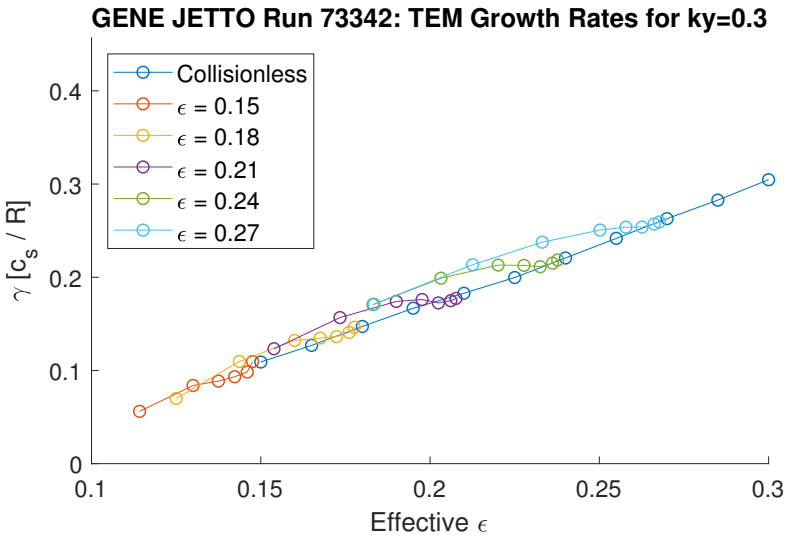

Figure 6.13: TEM growth rates calculated by GENE for different values of nominal ϵ plotted against effective ϵ^* (via the effective trapped fraction model) using JETTO Run 73342 parameters where $k_\theta \rho_s = 0.3$. Note the close agreement.

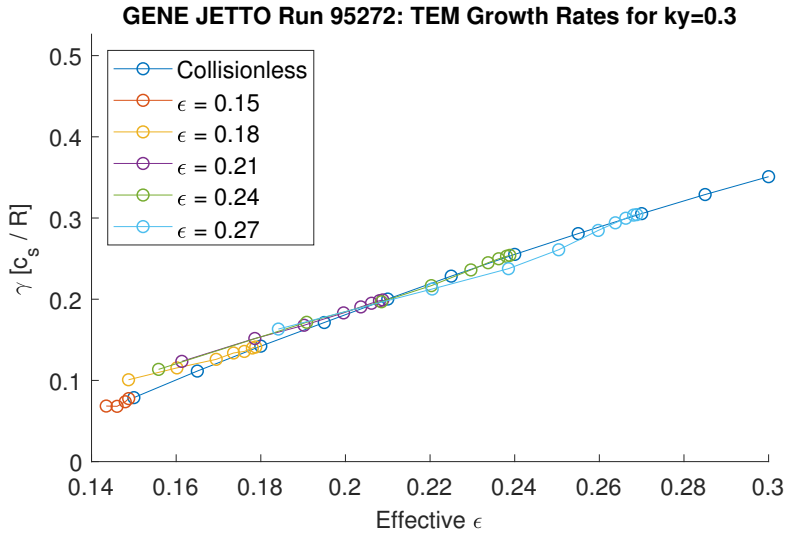

Figure 6.14: TEM growth rates calculated by GENE for different values of nominal ϵ plotted against effective ϵ^* (via the effective trapped fraction model) using JETTO Run 95272 parameters where $k_\theta \rho_s = 0.3$. Note the close agreement.

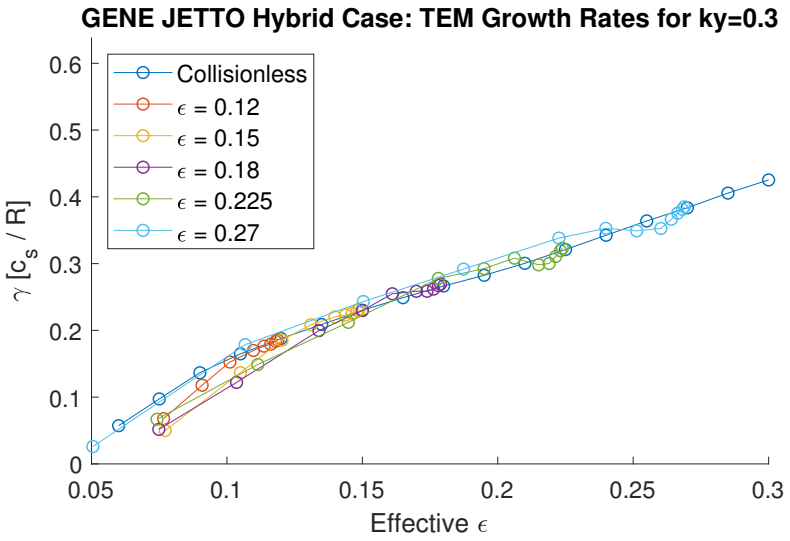

Figure 6.15: TEM growth rates calculated by GENE for different values of nominal ϵ plotted against effective ϵ^* (via the effective trapped fraction model) using JETTO Hybrid H-mode parameters where $k_\theta \rho_s = 0.3$. Note the close agreement.

Appendix 6.B Figures: QuaLiKiz-GENE comparisons

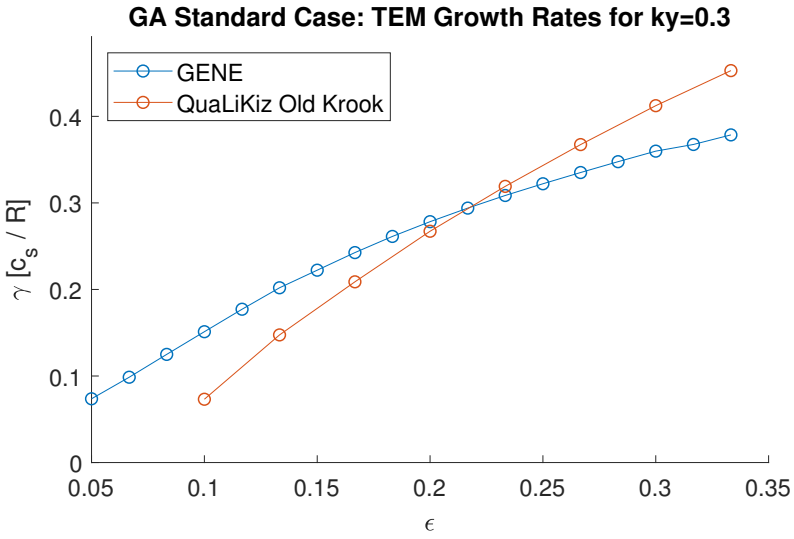

Figure 6.16: Collisionless TEM growth rates calculated by GENE and QuaLiKiz using GA Standard parameters plotted against ϵ, where $k_\theta \rho_s = 0.3$. Since this is calculated with no collisions, both Old Krook and New Krook in QuaLiKiz would agree perfectly.

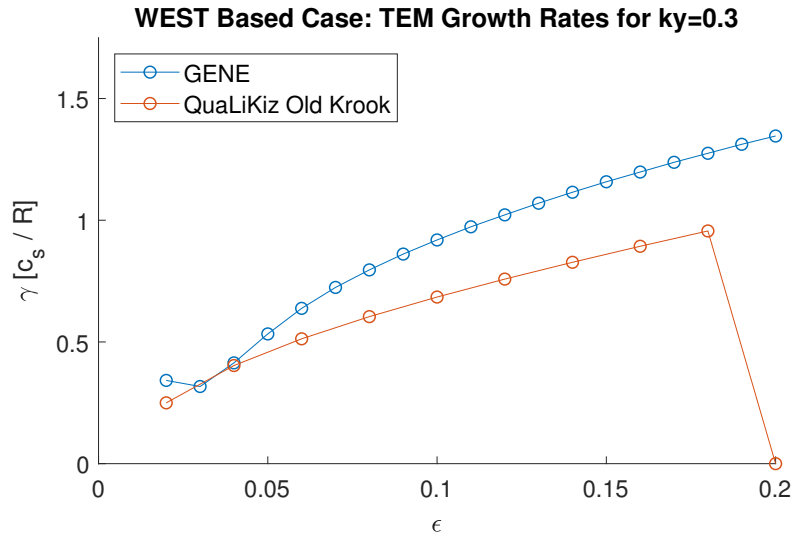

Figure 6.17: Collisionless TEM growth rates calculated by GENE and QuaLiKiz using WEST parameters plotted against ϵ, where $k_\theta \rho_s = 0.3$. Since this is calculated with no collisions, both Old Krook and New Krook in QuaLiKiz would agree perfectly.

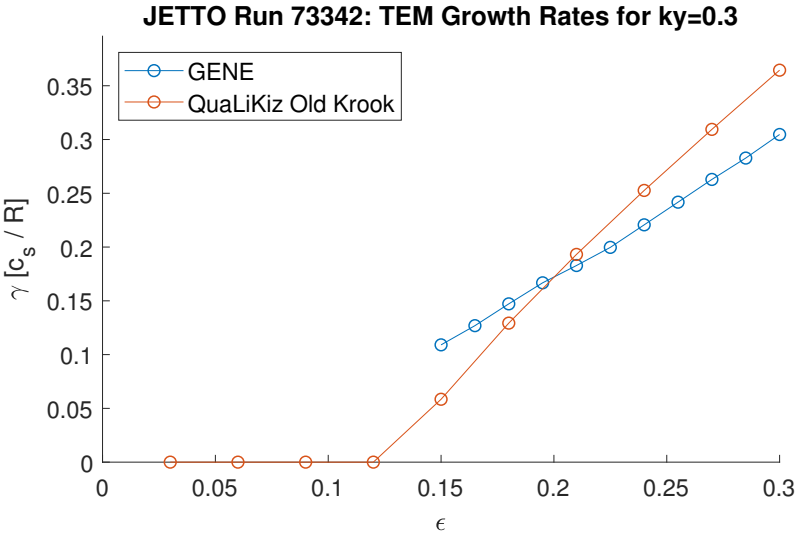

Figure 6.18: Collisionless TEM growth rates calculated by GENE and QuaLiKiz using JETTO Run 73342 parameters plotted against ϵ, where $k_\theta \rho_s = 0.3$. Since this is calculated with no collisions, both Old Krook and New Krook in QuaLiKiz would agree perfectly.

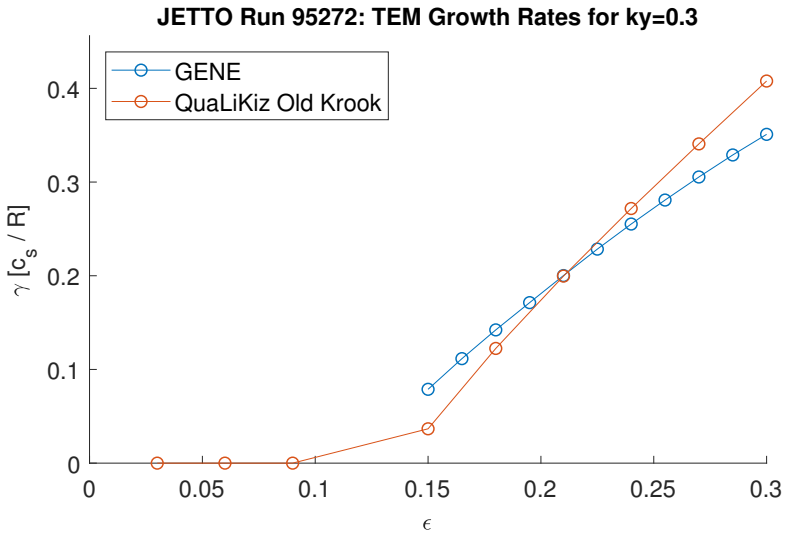

Figure 6.19: Collisionless TEM growth rates calculated by GENE and QuaLiKiz using JETTO Run 95272 parameters plotted against ϵ, where $k_\theta \rho_s = 0.3$. Since this is calculated with no collisions, both Old Krook and New Krook in QuaLiKiz would agree perfectly.

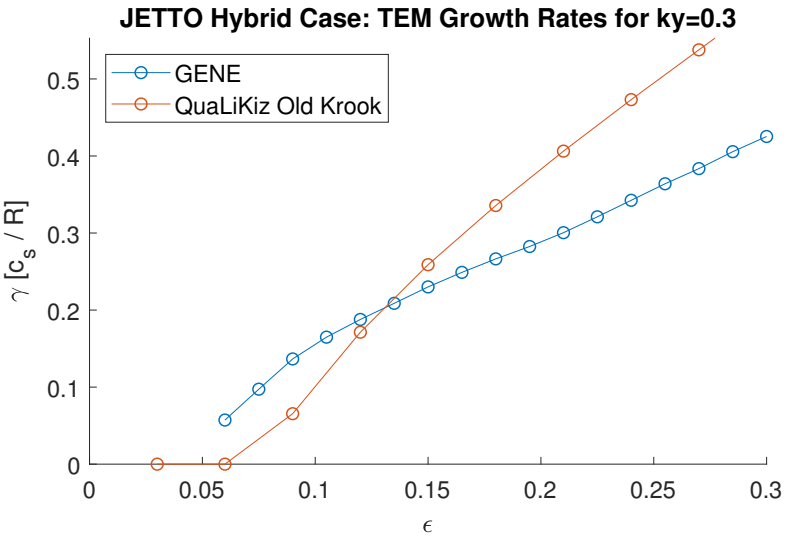

Figure 6.20: Collisionless TEM growth rates calculated by GENE and QuaLiKiz using JETTO Hybrid H-mode parameters plotted against ϵ, where $k_\theta \rho_s = 0.3$. Since this is calculated with no collisions, both Old Krook and New Krook in QuaLiKiz would agree perfectly.

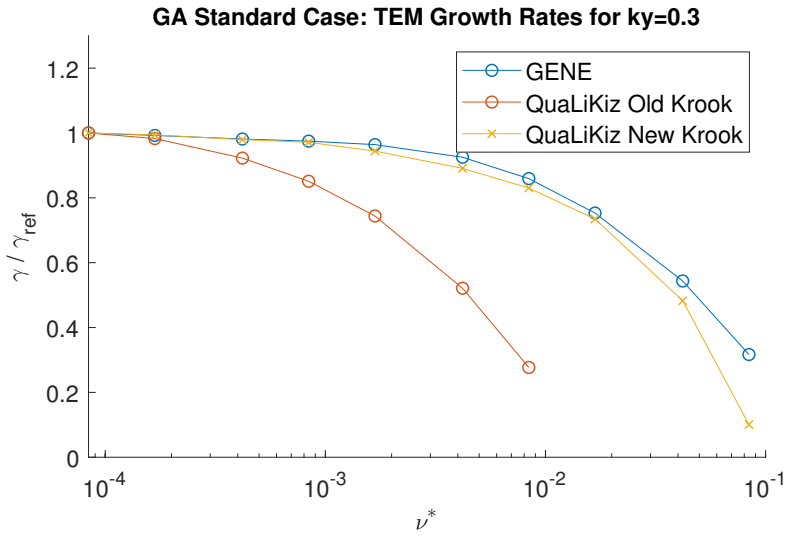

Figure 6.21: Collisional TEM growth rates calculated by GENE and QuaLiKiz (relative to their reference growth rates). Here, we use GA Standard parameters where $k_\theta \rho_s = 0.3$ and plot against ν^* for $\epsilon = 0.1667$. Note the significantly improved agreement between GENE and New Krook implemented in QuaLiKiz.

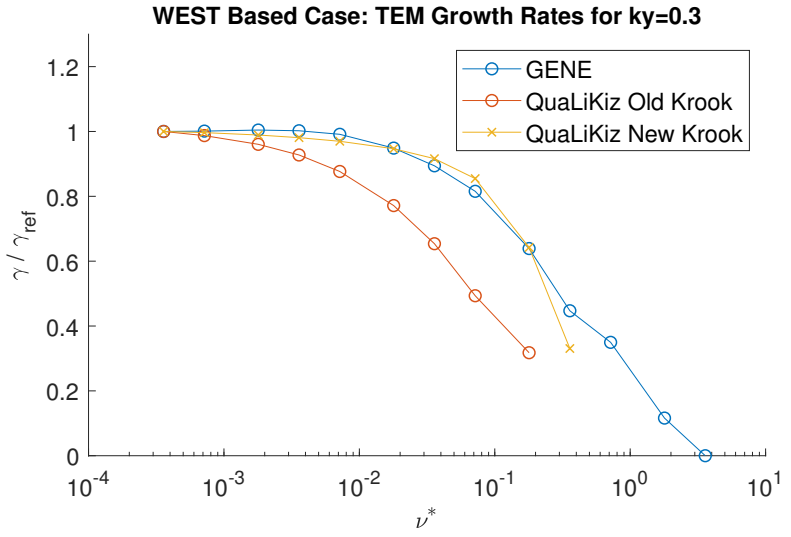

Figure 6.22: Collisional TEM growth rates calculated by GENE and QuaLiKiz (relative to their reference growth rates). Here, we use WEST parameters where $k_\theta \rho_s = 0.3$ and plot against ν^* for $\epsilon = 0.10$. Note the significantly improved agreement between GENE and New Krook implemented in QuaLiKiz.

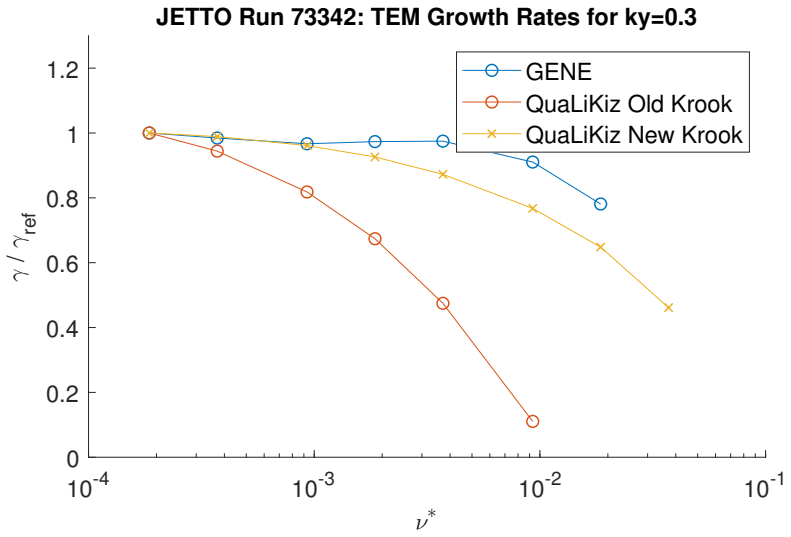

Figure 6.23: Collisional TEM growth rates calculated by GENE and QuaLiKiz (relative to their reference growth rates). Here, we use JETTO Run 73342 parameters where $k_\theta \rho_s = 0.3$ and plot against ν^* for $\epsilon = 0.24$. Note the significantly improved agreement between GENE and New Krook implemented in QuaLiKiz.

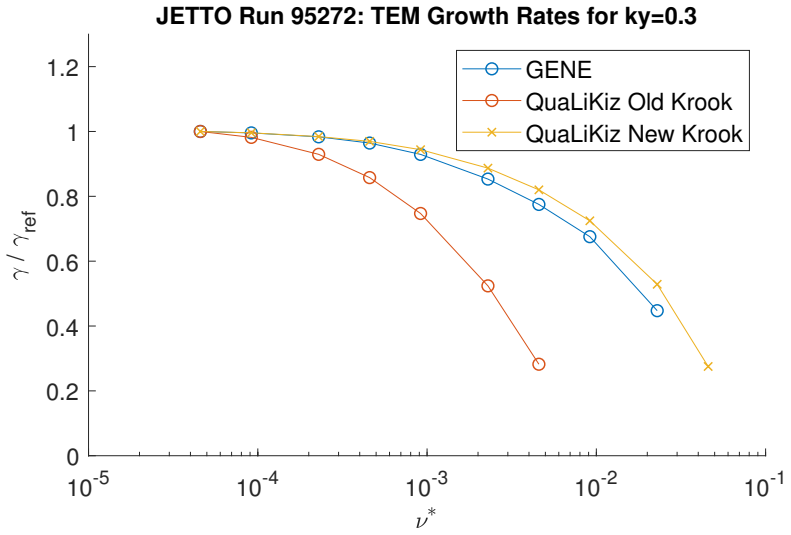

Figure 6.24: Collisional TEM growth rates calculated by GENE and QuaLiKiz (relative to their reference growth rates). Here, we use JETTO Run 95272 parameters where $k_\theta \rho_s = 0.3$ and plot against ν^* for $\epsilon = 0.24$. Note the significantly improved agreement between GENE and New Krook implemented in QuaLiKiz.

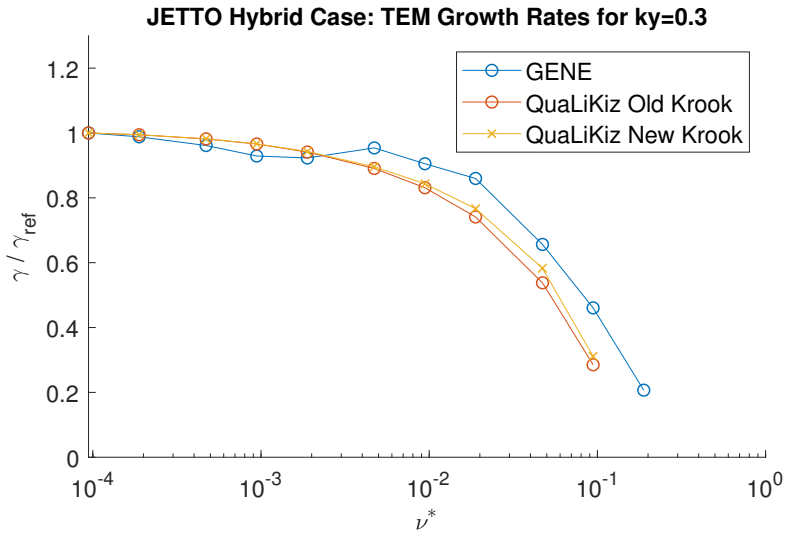

Figure 6.25: Collisional TEM growth rates calculated by GENE and QuaLiKiz (relative to their reference growth rates). Here, we use JETTO Hybrid H-mode parameters where $k_\theta \rho_s = 0.3$ and plot against ν^* for $\epsilon = 0.225$. Note the significantly improved agreement between GENE and New Krook implemented in QuaLiKiz.

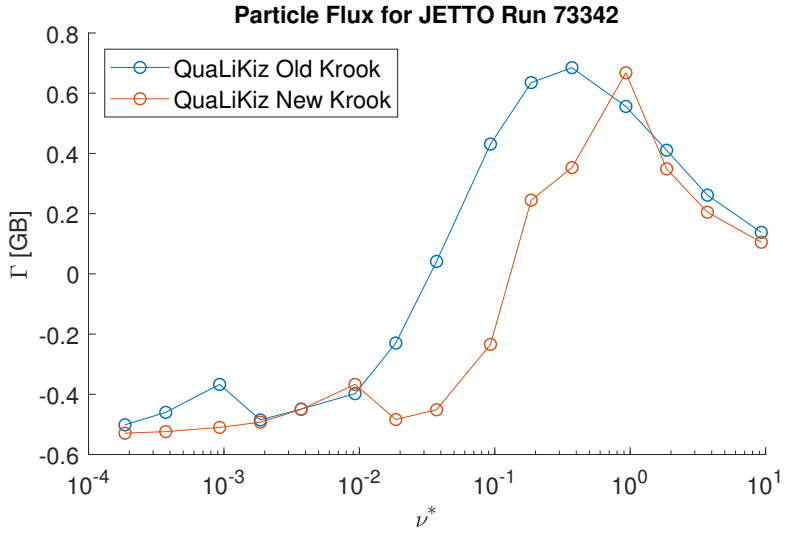

Figure 6.26: Total integrated particle flux calculated in QuaLiKiz for JETTO Run 73342 parameters plotted against ν^* where $\epsilon = 0.24$. Note that nominal $\nu^* = 0.50$.

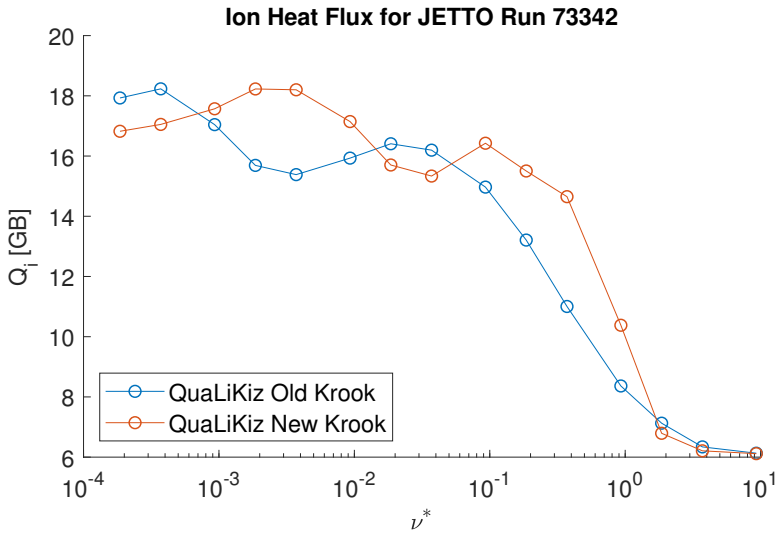

Figure 6.27: Total integrated ion heat flux calculated in QuaLiKiz for JETTO Run 73342 parameters plotted against ν^* where $\epsilon = 0.24$. Note that nominal $\nu^* = 0.50$.

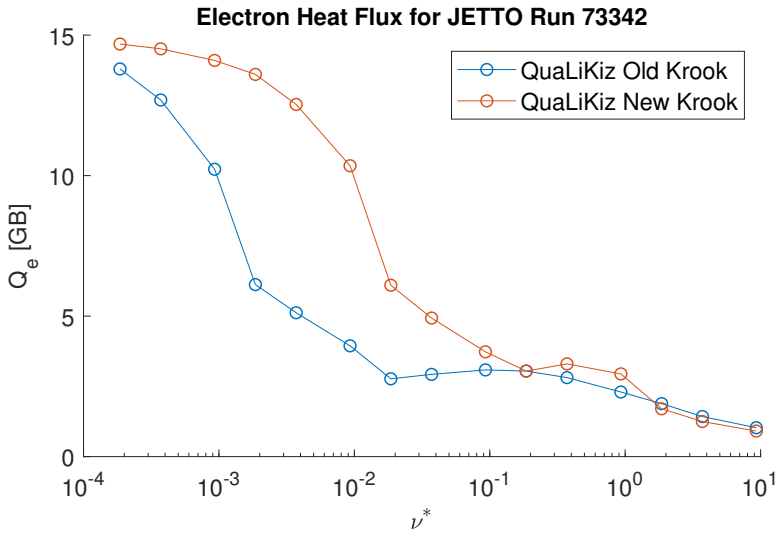

Figure 6.28: Total integrated electron heat flux calculated in QuaLiKiz for JETTO Run 73342 parameters plotted against ν^* where $\epsilon = 0.24$. Note that nominal $\nu^* = 0.50$.

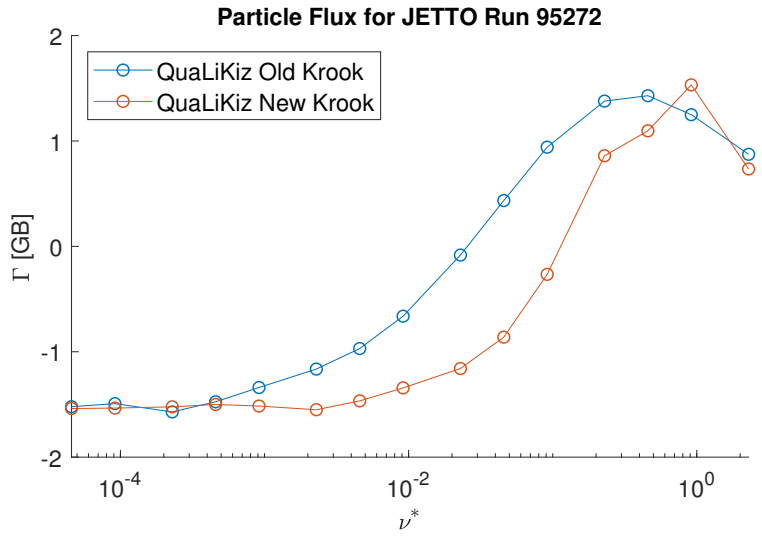

Figure 6.29: Total integrated particle flux calculated in QuaLiKiz for JETTO Run 95272 parameters plotted against ν^* where $\epsilon = 0.24$. Note that nominal $\nu^* = 0.50$.

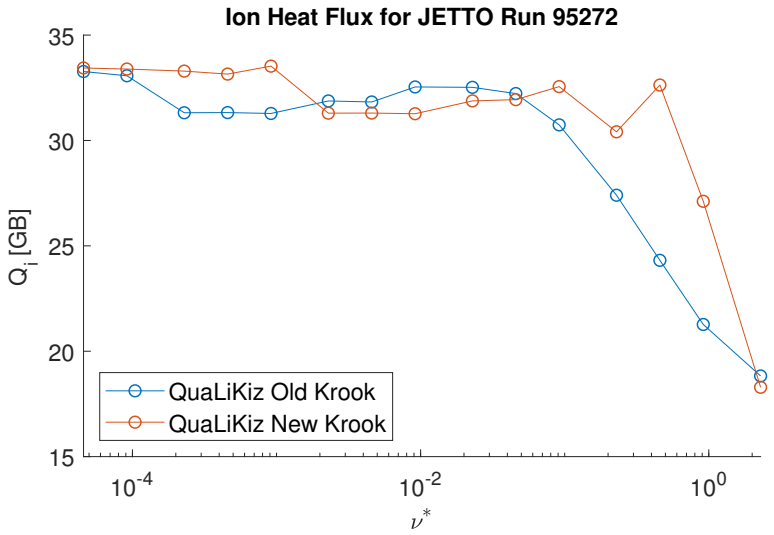

Figure 6.30: Total integrated ion heat flux calculated in QuaLiKiz for JETTO Run 95272 parameters plotted against ν^* where $\epsilon = 0.24$. Note that nominal $\nu^* = 0.50$.

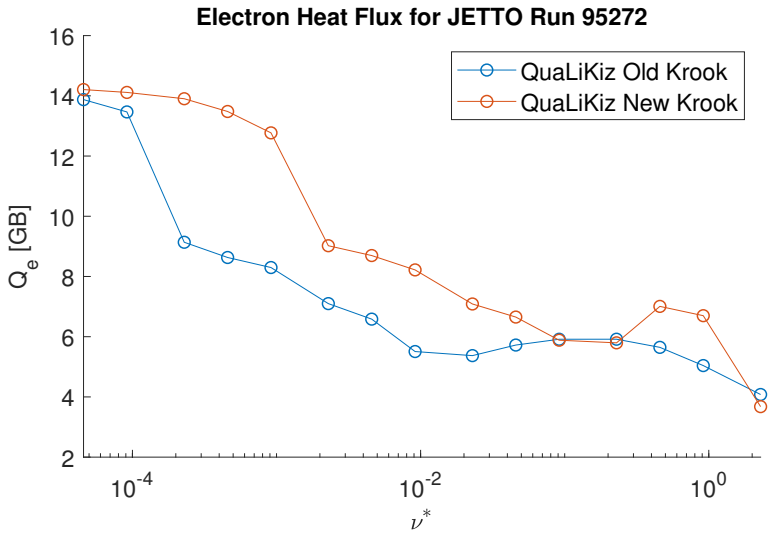

Figure 6.31: Total integrated electron energy flux calculated in QuaLiKiz for JETTO Run 95272 parameters plotted against ν^* where $\epsilon = 0.24$. Note that nominal $\nu^* = 0.50$.

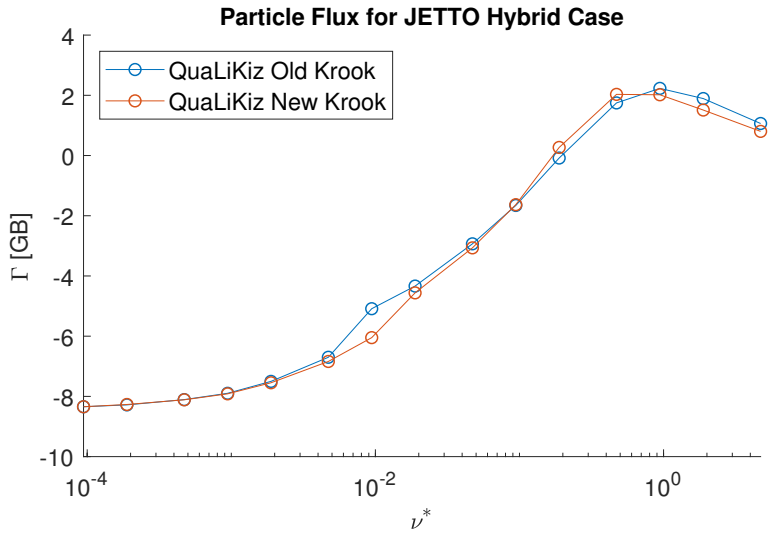

Figure 6.32: Total integrated particle flux calculated in QuaLiKiz for JETTO Hybrid H-mode parameters plotted against ν^* where $\epsilon = 0.225$. Note that there is very little change.

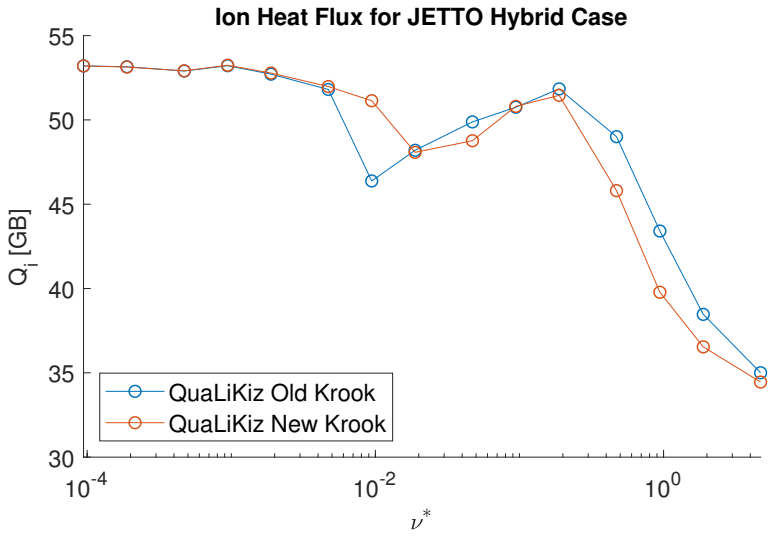

Figure 6.33: Total integrated ion heat flux calculated in QuaLiKiz for JETTO Hybrid H-mode parameters plotted against ν^* where $\epsilon = 0.225$. Note that there is very little change.

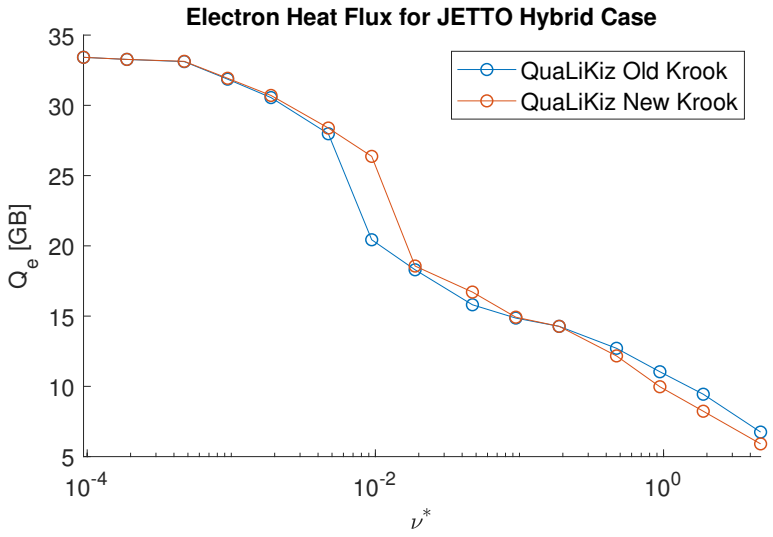

Figure 6.34: Total integrated electron heat flux calculated in QuaLiKiz for JETTO Hybrid H-mode parameters plotted against ν^* where $\epsilon = 0.225$. Note that there is very little change.

Appendix 6.C Figures: Integrated modeling results

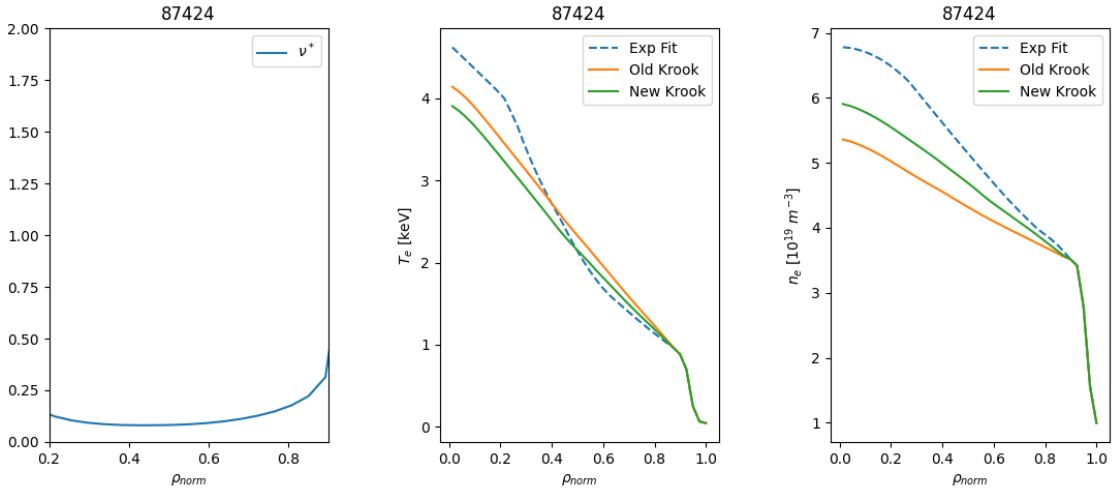

Figure 6.35: Integrated modeling of JET H-mode as part of collisionality scan in Ref. 148. Note the improvement in density peaking.

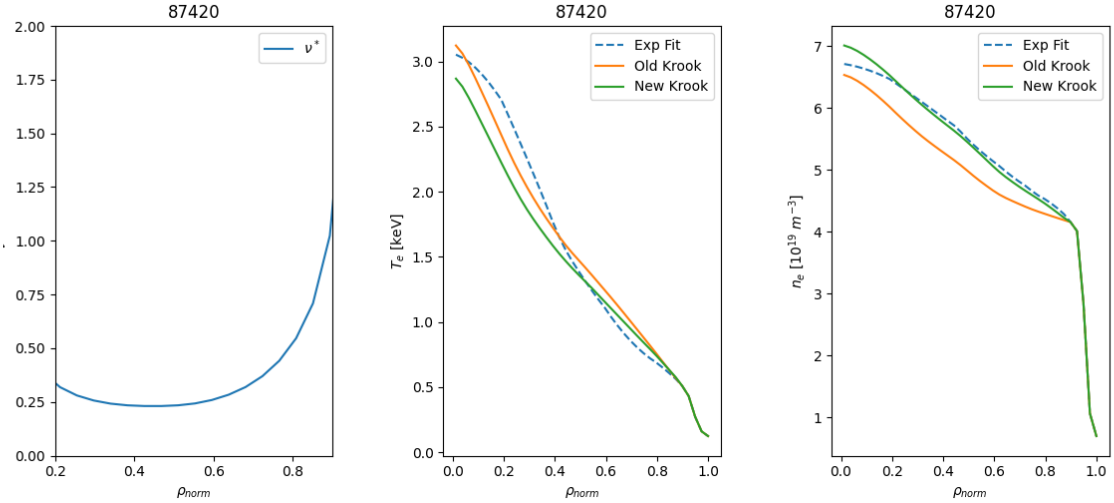

Figure 6.36: Integrated modeling of JET H-mode as part of collisionality scan in Ref. 148. Note the improvement in density peaking.

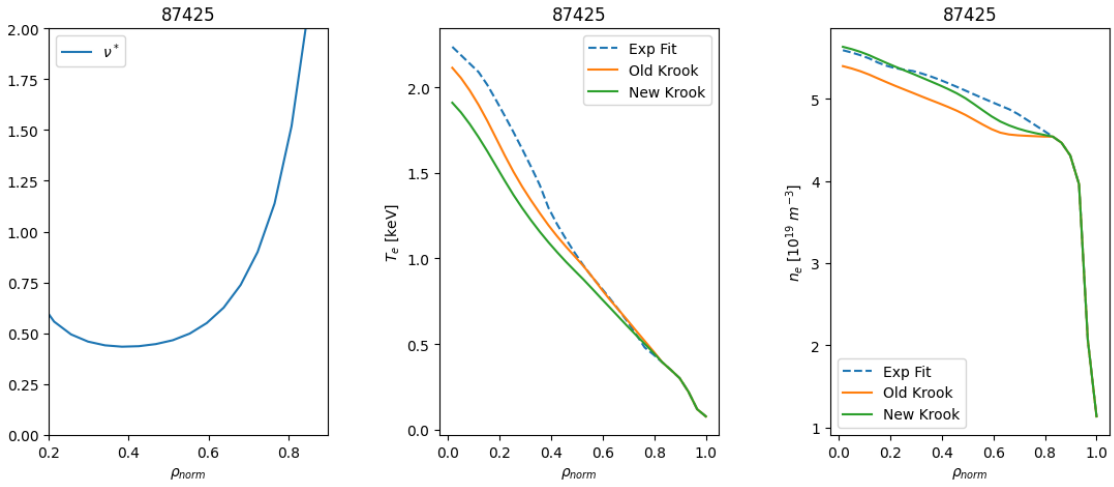

Figure 6.37: Integrated modeling of JET H-mode as part of collisionality scan in Ref. 148. Note the improvement in density peaking.

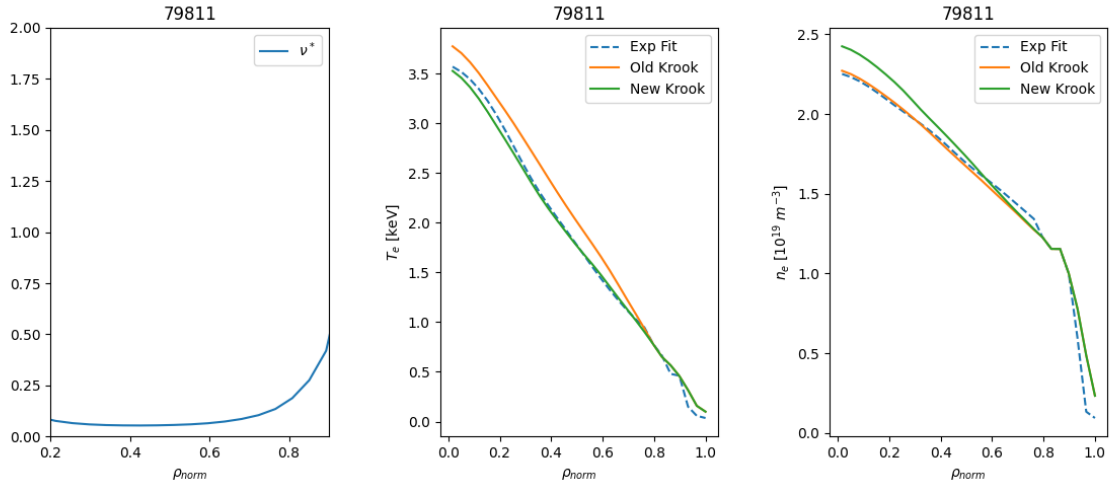

Figure 6.38: Integrated modeling of JET L-mode as part of collisionality scan in Ref. 148. Note that agreement is retained.

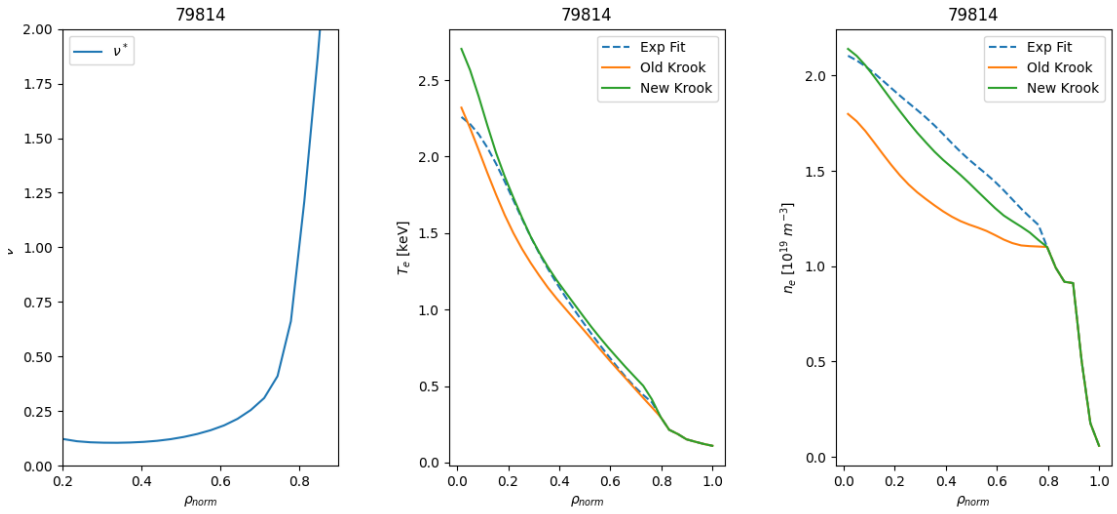

Figure 6.39: Integrated modeling of JET L-mode as part of collisionality scan in Ref. 148. Note the improvement in density peaking.

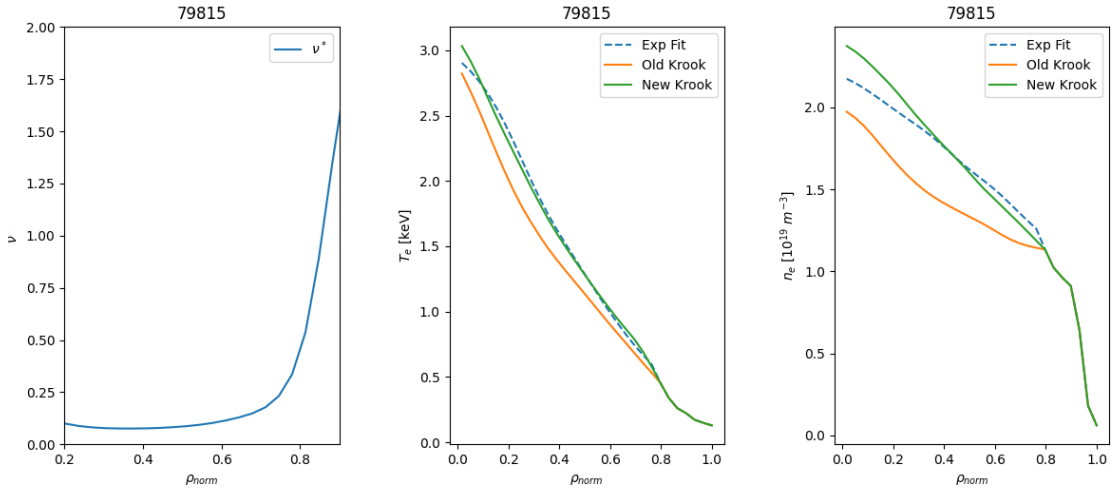

Figure 6.40: Integrated modeling of JET L-mode as part of collisionality scan in Ref. 148. Note the improvement in density peaking.

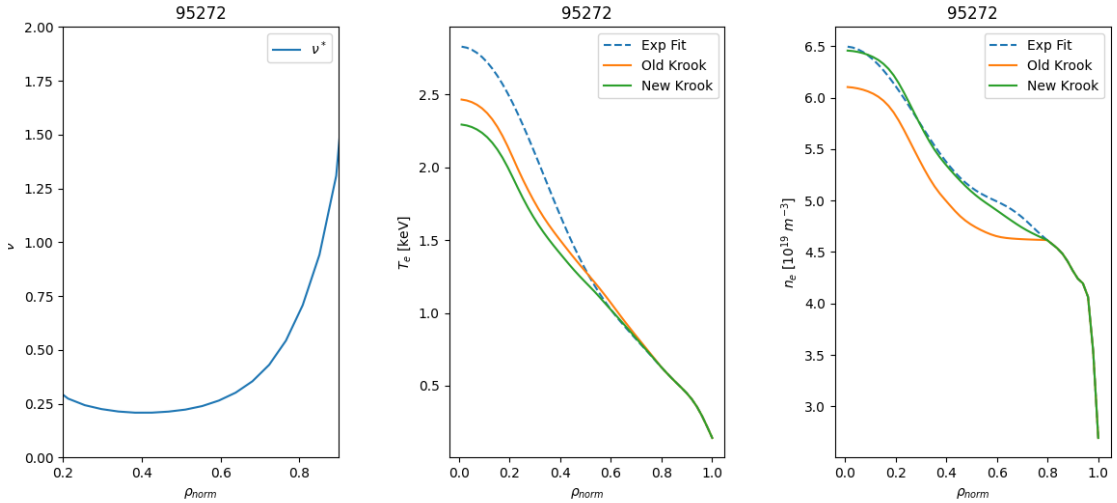

Figure 6.41: High collisionality H-mode. Note the improvement in density peaking.

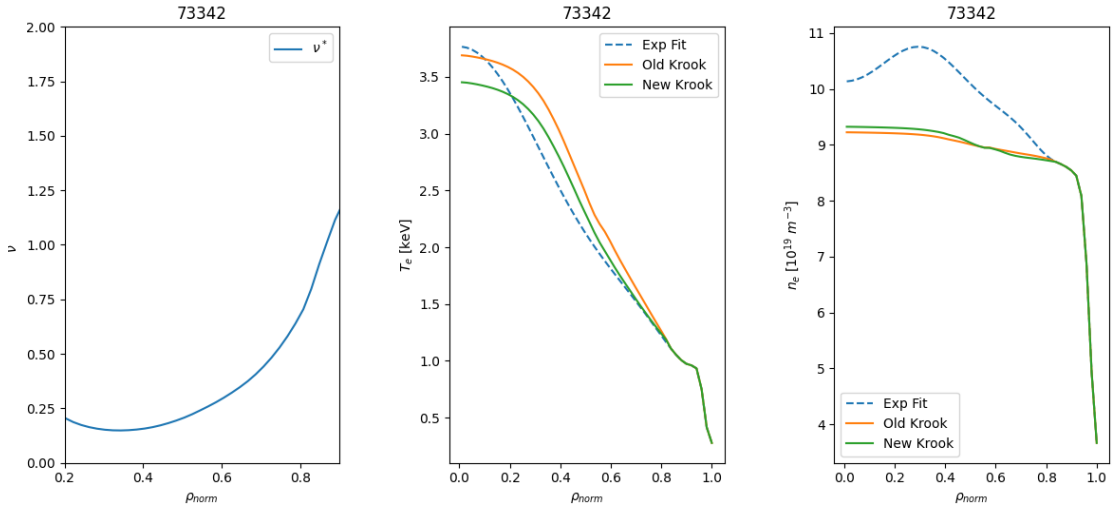

Figure 6.42: Integrated modeling of high-collisionality H-mode. Note that there is not much improvement.

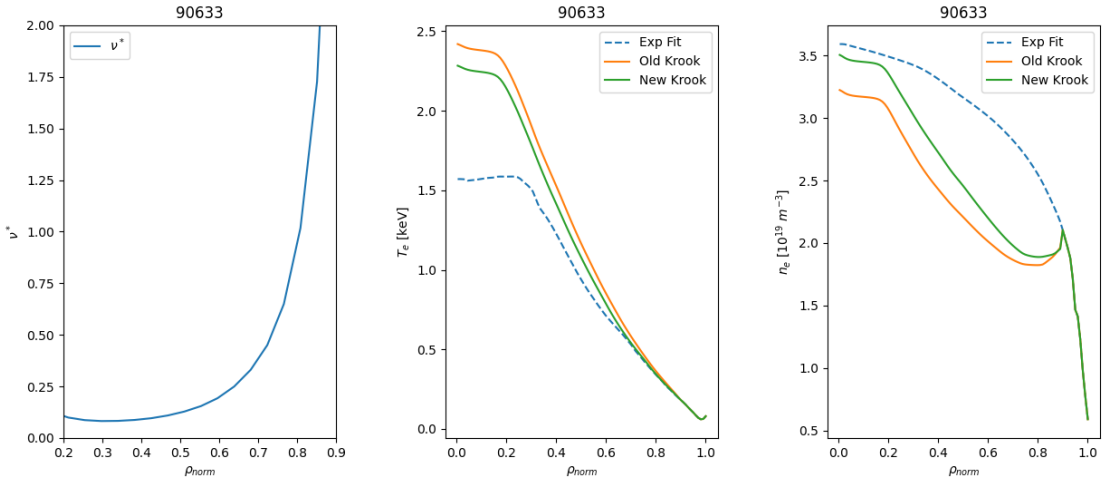

Figure 6.43: Integrated modeling of high-collisionality Ohmic L-mode. Note that, despite slight improvement, there is significant density hollowing.

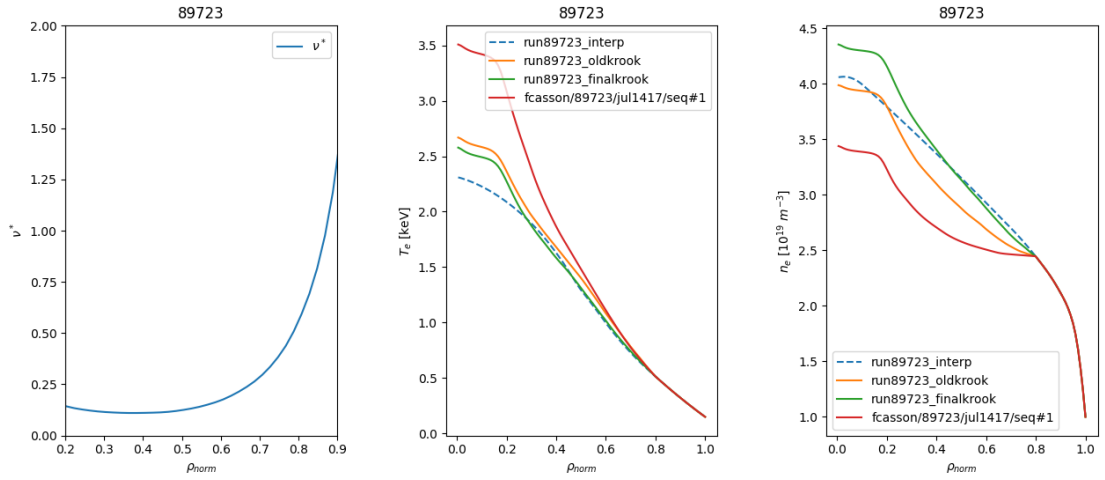

Figure 6.44: Integrated modeling of medium-collisionality heated L-mode. Note the slight improvement between Old Krook and New Krook as well as the significant improvement between Old Krook and the incorrect implementation of the collision operator (red).

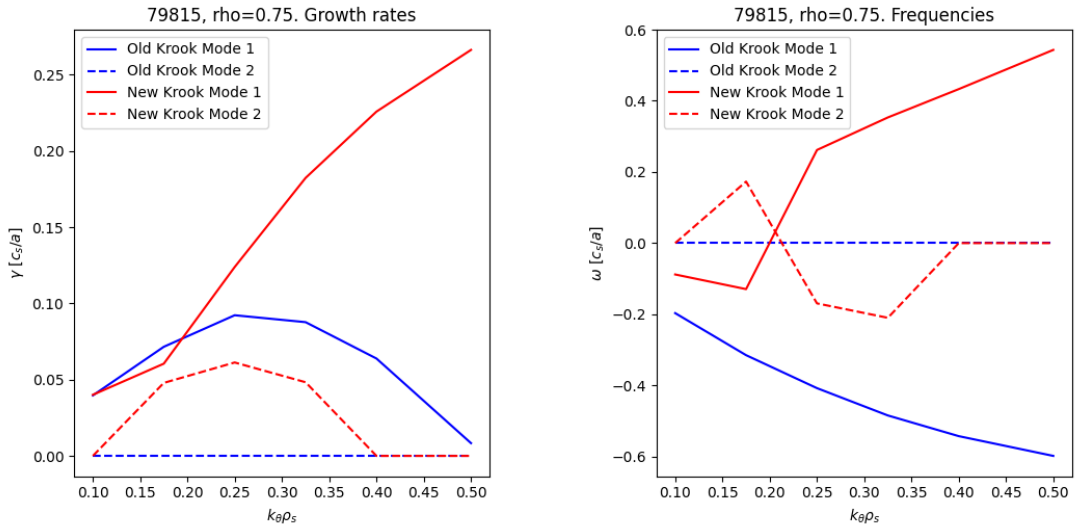

Figure 6.45: Instability spectrum plotted against $k_\theta\rho_s$ for JET L-mode at $\rho_{\text{norm}} = 0.75$. Note that with New Krook we retain the correct TEM instability, whereas for Old Krook the TEM is stable.

CHAPTER 7

Conclusions

7.1 Summary

Kinetic physics and microturbulence simulations are essential to understanding and accurately simulating turbulent transport in tokamak plasmas. Because it is intractable to always couple nonlinear gyrokinetic kinetic models to fluid transport codes, it is necessary to develop reduced models that can quickly extract the relevant microturbulent physics while retaining a high enough accuracy. The quasilinear approximation is an extremely powerful method of model reduction that requires a developed understanding of adiabatic invariance and the action-angle formalism. This alone, however, is not enough in an integrated modeling context; further reductions and approximations are necessary to reduce the model.

In this dissertation, we investigated the theory of adiabatic invariance in tokamak plasmas, an essential component of modern quasilinear theory. First, we quantified the degree to which magnetic moment invariance is broken in a wide variety of electromagnetic fields. We then catalogued the conditions necessary to preserve magnetic moment invariance. Not only does this investigation resolve on quantitative footing when gyrokinetics can break down, by examining specific cases it also serves to better understand the theory of adiabatic invariance in its own right.

To continue this theoretical investigation, we then analyzed bounce-transit motion in concentric circular axisymmetric magnetic fields. We discovered the small inverse aspect ratio approximation usually used to analyze guiding center motion in this specific geometry is unnecessary. We then systematically derived new, more exact equations that summarize bounce-transit motion and the

toroidal drift motion that incorporate a nonzero, finite inverse aspect ratio. This then allowed us to rigorously determine the validity of the small inverse aspect ratio approximation. We found that the approximation is quite accurate for conventional tokamaks with large aspect ratios and positive magnetic shear. Tokamak geometries which exhibit large values of the inverse aspect ratio, such as spherical tokamaks, result in a breakdown of the approximated formulas even without considering the effects of more realistic geometries. The investigations into gyromotion and bounce-transit guiding center motion together fill an important gap in the literature; not only do they validate approximations taken for granted in modern studies, but they also illustrate detailed, fundamental analysis of single charged particle motion in magnetic fields.

With a detailed understanding of adiabatic invariance and guiding center particle motion in hand, we then gave a complete and extensive derivation of the quasilinear code QuaLiKiz. Although the code itself is well validated and widely used for simulating turbulent transport in the tokamak core, the underlying physics of the code was only partially illustrated in the various publications and dissertations regarding QuaLiKiz throughout the years. This work illustrates how each approximation enters into the derivation of QuaLiKiz. This is instrumental in understanding both the differences between QuaLiKiz and other gyrokinetic models as well as improving QuaLiKiz in the future. This detailed analytical work is also necessary to resolve any misconceptions about the physics of QuaLiKiz as well as correct any errors within the code base (such as the collision operator). Furthermore, this work in tandem with the previously discussed analytical work can help future theoreticians understand how to construct a quasilinear model from first principles. In addition to this work, we also implemented the Genz and Malik algorithm for numeric integrations. This new implementation led to a moderate speedup in QuaLiKiz; moreover, QuaLiKiz is now fully open source as of version 2.8.0.

Finally, we conducted numerical simulations of the linear trapped electron mode (TEM) for various tokamak core parameters. TEM turbulence is responsible for much of anomalous transport; in particular, it was found that the QuaLiKiz treatment of the collisional or dissipative TEM (DTEM) led to incorrect density profiles in the tokamak core for highly collisional regimes. It is also evident

that modern, systematic kinetic simulations of DTEMs in the tokamak core is quite lacking; many studies that attempt to characterize DTEMs predate modern gyrokinetic simulations. We used the gyrokinetic code GENE to perform a systematic study of linear DTEMs. We then used these simulations to construct a reduced model that successfully characterizes DTEM growth rates based on the notion of the effective trapped fraction. With these simulations in hand, we then performed a detailed comparison between GENE and QuaLiKiz DTEM calculations with the goal of improving QuaLiKiz's collision operator. The subsequent retuning of the Krook-like operator in QuaLiKiz based on these simulations led to substantial improvement in density profile predictions of high-collisionality JETTO runs; many of the predicted density profiles now exhibit correct density peaking in the core. This improvement will allow QuaLiKiz to successfully characterize a wider parameter space of tokamak core parameter regimes while retaining its greatest strength of computational speed.

7.2 Outlook

The analytical studies conducted in this dissertation mainly consider fundamental cases. We anticipate that the analyses used in this work can in principle be extended for more complicated electromagnetic cases. For instance, one could investigate magnetic moment invariance where the different fundamental electromagnetic field scenarios are combined to determine whether their interaction leads to conservation breaking of the magnetic moment that is quantitatively more complex. In the case of bounce-transit motion, attempts could be made to incorporate more realistic magnetic field geometry characteristics into the analysis as perturbations. When incorporating a small Shafronov shift or elongation, for instance, the bounce-transit motion is often analyzed such that the circular geometry is the dominating effect. One could conduct an investigation where the more exact formulas for circular geometry are used to determine if there is any interplay between more complicated geometrical features and finite inverse aspect ratio effects.

The complete QuaLiKiz derivation will prove to be essential for extending the physics of

QuaLiKiz. It is clear that the effect of more general magnetic geometries would in principle affect the derivation in the bounce-transit motion as well as the toroidal drift motion. However, we have seen that approximations to the geometry more strongly affect the toroidal drift motion than the bounce-transit motion. Moreover, the inclusion of the Shafranov shift is already slightly inconsistent as we consider it for the toroidal drift motion, not for the bounce-transit motion. This suggests an avenue to including effects such as elongation and triangularity where we only include them for the toroidal drift motion as a rough approximation. Meanwhile, it is now evident that the inclusion of electromagnetic effects would propagate through the entirety derivation; a brief sketch of the complexities of such effects were given in the theoretical framework of this dissertation. It is also now clear that there exists a strong assumption in the passing part of the dispersion relation regarding the integration over the pitch angle parameter; it would be fruitful to investigate the impact of this approximation and determine whether it could be improved.

With the newly improved version of the Krook-like operator in QuaLiKiz, we can now more reliably predict turbulent transport for collisional regimes. The retuning, however, does not improve all cases uniformly. The interplay between collisions and rotations, for instance, must be investigated further to better understand which parameter regimes are improved and which remain difficult for QuaLiKiz. Furthermore, the theoretical analysis of the Krook-like operator implemented in QuaLiKiz can allow for refinements such as the inclusion electron-electron collisions and better conservation properties.

Finally, the effective trapped fraction model suggests several avenues of further study. The effects of non-circular geometries could be incorporated by considering a more accurate assessment of trapped electron motion. More importantly, the model as constructed completely neglects the role of passing electrons; improvements to the model could be made by incorporating potential destabilizing influences of marginally passing electrons that diffuse into the trapped part of velocity space. In addition, there remains the question of how to correlate the dimensionless fitting parameter of the model to the scenario being investigated; this would require further simulations of DTEMs in a wider area of parameter space. Finally, the effective trapped fraction model presented is not

adequate in describing more complicated features of linear DTEMs such as the real part of the mode frequency or the quasilinear flux ratios, thereby preventing it from being used to reliably characterize collisions in a reduced model. An extension of the model that could successfully characterize these quantities would make it more immediately applicable.

REFERENCES

[1] International Energy Agency (IEA). *Key World Energy Statistics 2020*. https://www.iea.org/reports/key-world-energy-statistics-2020 (Paris, 2020).

[2] U.S. Energy Information Administration (EIA). *International Energy Outlook 2013*. https://www.eia.gov/outlooks/archive/ieo13/ (Washington, D.C., 2013).

[3] International Energy Agency (IEA). *World Energy Balances: Overview*. https://www.iea.org/reports/world-energy-balances-overview (Paris, 2020).

[4] U.S. Energy Information Administration (EIA). *Average U.S. construction costs for solar and wind generation continue to fall*. https://www.eia.gov/todayinenergy/detail.php?id=45136 (Washington D.C., 2020).

[5] L. Eyraud, A. Wane, C. Zhang, and B. Clements. IMF Working Paper No. 11/296 (2011).

[6] D. Conway, C. Dalin, W. A. Landman, and T. J. Osborn. Nature Energy **2**, 946 (2017).

[7] S. Tongsopit, N. Kittner, Y. Chang, A. Aksornkij, and W. Wangjiraniran. Energy Policy **90**, 60 (2016).

[8] J. Wesson. *Tokamaks* (Oxford University Press, Oxford, 2012).

[9] C. E. Rolfs and W. S. Rodney. *Cauldrons in the Cosmos: Nuclear Astrophysics* (Univ. of Chicago Press, Chicago, 1998).

[10] U.S. Geological Survey. *Mineral Commodity Summaries*. https://doi.org/10.3133/mcs2020 (Washington, D.C., 2020).

[11] Y. Lechón, H. Cabal, R. Sáez, B. Hallberg, K. Aquilonius, T. Schneider, S. Lepicard, D. Ward, T. Hamacher, and R. Korhonen. Fusion Engineering and Design **69**, 683 (2003).

[12] R. Kembleton. In T. M. Letcher, ed., *Future Energy (Third Edition)*, pages 543 – 560 (Elsevier, 2020).

[13] Nuclear Energy Study Group. *Nuclear power and proliferation resistance: Securing benefits, limiting risk*. https://www.aps.org/policy/reports/popa-reports/proliferation-resistance/index.cfm (2005).

[14] A. Glaser and R. Goldston. Nuclear Fusion **52**, 043004 (2012).

[15] Paris Agreement. *Report of the Conference of the Parties to the United Nations Framework Convention on Climate Change*. https://treaties.un.org/pages/ViewDetails.aspx?src=TREATY&mtdsg_no=XXVII-7-d&chapter=27&clang=_en (21st Session, Paris, 2015).

[16] ITER. https://www.iter.org/ (2020).

[17] W. M. Stacey. *Fusion Plasma Physics* (Wiley-VCH, Weinheim, 2012).

[18] J. D. Lawson. Proceedings of the Physical Society. Section B **70**, 6 (1957).

[19] N. J. Peacock, D. C. Robinson, M. J. Forrest, P. D. Wilcock, and V. V. Sannikov. Nature **224**, 488 (1969).

[20] S. Hirshman and D. Sigmar. Nuclear Fusion **21**, 1079 (1981).

[21] J. A. Bittencourt. *Fundamentals of Plasma Physics* (Springer, New York, 2007).

[22] Y. Sarazin. *Turbulence and Transport* (Commissariat à l'Energie Atomique, Saint-Paul-Lez-Durance, France, 2013).

[23] W. Horton. Reviews of Modern Physics **71**, 735 (1999).

[24] J. Citrin, C. Bourdelle, F. J. Casson, C. Angioni, N. Bonanomi, Y. Camenen, X. Garbet, L. Garzotti, T. Görler, O. Gürcan, et al. Plasma Physics and Controlled Fusion **59**, 124005 (2017).

[25] R. J. Goldston and P. H. Rutherford. *Introduction to Plasma Physics* (IOP Publishing, London, 1995).

[26] M. Kruskal. In *Rendiconti del Terzo Congresso Internazionale sui Fenomeni D'Ionizzazione nei Gas tenuto a Venezia* (Societa Italiana di Fisica, Milan, Italy, 1957).

[27] R. G. Littlejohn. The Physics of Fluids **24**, 1730 (1981).

[28] R. G. Littlejohn. Journal of Plasma Physics **29**, 111–125 (1983).

[29] W. D. D'haeseleer, W. N. G. Hitchon, J. D. Callen, and J. L. Shohet. *Flux Coordinates and Magnetic Field Structure* (Springer, Berlin, 1991).

[30] R. B. White. *The Theory of Toroidally Confined Plasmas* (Imperial College Press, London, 2014).

[31] P. Helander and D. J. Sigmar. *Collisional Transport in Magnetized Plasmas* (Cambridge University Press, Cambridge, 2005).

[32] H. Goldstein, C. Poole, and J. Safko. *Classical Mechanics* (Addison-Wesley, San Francisco, 2001).

[33] C. G. Wells and S. T. C. Siklos. European Journal of Physics **28**, 105 (2006).

[34] V. I. Arnold. *Mathematical Methods of Classical Mechanics* (Springer-Verlag, New York, 1989).

[35] V. I. Arnol'd. Russian Mathematical Surveys **18**, 9 (1963).

[36] T. G. Northrop. *The Adiabatic Motion of Charged Particles* (Interscience Publishers, New York, 1963).

[37] D. R. Nicholson. *Introduction to Plasma Theory* (Wiley, New York, 1983).

[38] P. H. Rutherford and E. A. Frieman. The Physics of Fluids **11**, 569 (1968).

[39] A. J. Brizard and T. S. Hahm. Reviews of Modern Physics **79**, 421 (2007).

[40] S. M. Mahajan and C. Y. Chen. The Physics of Fluids **28**, 3538 (1985).

[41] X. Garbet, Y. Idomura, L. Villard, and T. Watanabe. Nuclear Fusion **50**, 043002 (2010).

[42] M. Kikuchi, K. Lackner, and M. Q. Tran. *Fusion Physics* (International Atomic Energy Agency, Vienna, 2012).

[43] W. Wan, Y. Chen, and S. E. Parker. Physics of Plasmas **12**, 012311 (2005).

[44] B. N. Rogers, S. Kobayashi, P. Ricci, W. Dorland, J. Drake, and T. Tatsuno. Physics of Plasmas **14**, 092110 (2007).

[45] X. Y. Wang, Y. Lin, L. Chen, and Z. Lin. Physics of Plasmas **15**, 072103 (2008).

[46] M. J. Pueschel, F. Jenko, D. Told, and J. Büchner. Physics of Plasmas **18**, 112102 (2011).

[47] M. J. Pueschel, D. Told, P. W. Terry, F. Jenko, E. G. Zweibel, V. Zhdankin, and H. Lesch. The Astrophysical Journal Supplement Series **213**, 30 (2014).

[48] G. G. Howes, W. Dorland, S. C. Cowley, G. W. Hammett, E. Quataert, A. A. Schekochihin, and T. Tatsuno. Physical Review Letters **100**, 065004 (2008).

[49] G. G. Howes, J. M. TenBarge, W. Dorland, E. Quataert, A. A. Schekochihin, R. Numata, and T. Tatsuno. Physical Review Letters **107**, 035004 (2011).

[50] D. Told, F. Jenko, J. M. TenBarge, G. G. Howes, and G. W. Hammett. Physical Review Letters **115**, 025003 (2015).

[51] A. B. Navarro, B. Teaca, D. Told, D. Groselj, P. Crandall, and F. Jenko. Physical Review Letters **117**, 245101 (2016).

[52] D. Told, J. Cookmeyer, F. Muller, P. Astfalk, and F. Jenko. New Journal of Physics **18**, 065011 (2016).

[53] H. Qin and R. C. Davidson. Physical Review Letters **96**, 085003 (2006).

[54] N. Tronko, A. Bottino, and E. Sonnendrücker. Physics of Plasmas **23**, 082505 (2016).

[55] D. O. Gough. Astronomische Nachrichten **328**, 273 (2007).

[56] R. M. Kulsrud. Phys. Rev. **106**, 205 (1957).

[57] A. Baños. Journal of Plasma Physics **1**, 305–316 (1967).

[58] J. B. Taylor. Physics of Fluids **10**, 1357 (1967).

[59] A. J. Brizard. Physics of Plasmas **24**, 042115 (2017).

[60] P. F. Byrd and M. D. Friedman. *Handbook of Elliptic Integrals for Engineers and Scientists* (Springer, Berlin, 1971).

[61] M. Abramowitz and I. A. Stegun. *Handbook of Mathematical Functions with Formulas, Graphs, and Mathematical Tables*. No. 55 in NBS Applied Mathematics Series (National Bureau of Standards, Washington, D.C., 1964).

[62] G. Labahn and M. Mutrie. *Reduction of Elliptic Integrals to Legendre Normal Form. Tech. rep.*, Department of Computer Science, University of Waterloo, Waterloo, Ontario (1997).

[63] H. Weitzner. The Physics of Fluids **24**, 2280 (1981).

[64] J. R. Johnson and C. Z. Cheng. Geophysical Research Letters **28**, 4421 (2001).

[65] J. A. Krommes. Physics of Plasmas **20**, 124501 (2013).

[66] N. Tronko, A. Bottino, T. Görler, E. Sonnendrücker, D. Told, and L. Villard. Physics of Plasmas **24**, 056115 (2017).

[67] A. J. Brizard. Physics of Plasmas **20**, 092309 (2013).

[68] N. Tronko and A. J. Brizard. Physics of Plasmas **22**, 112507 (2015).

[69] J. A. Rome and Y.-K. M. Peng. Nuclear Fusion **19**, 1293 (1979).

[70] M. A. Beer and G. W. Hammett. Physics of Plasmas **3**, 4018 (1996).

[71] F. L. Hinton and R. D. Hazeltine. Reviews of Modern Physics **48**, 239 (1976).

[72] G. M. Staebler, J. E. Kinsey, and R. E. Waltz. Physics of Plasmas **12**, 102508 (2005).

[73] G. Depret, X. Garbet, P. Bertrand, and A. Ghizzo. Plasma Physics and Controlled Fusion **42**, 949 (2000).

[74] L. Wang and T. S. Hahm. Physics of Plasmas **16**, 062309 (2009).

[75] A. J. Brizard. Physics of Plasmas **7**, 3238 (2000).

[76] J. Decker, Y. Peysson, A. J. Brizard, and F.-X. Duthoit. Physics of Plasmas **17**, 112513 (2010).

[77] B. B. Kadomtsev and O. P. Pogutse. Soviet Physics Journal of Experimental and Theoretical Physics **24**, 1172 (1967).

[78] J. W. Connor, R. J. Hastie, and T. J. Martin. Nuclear Fusion **23**, 1702 (1983).

[79] J. W. Connor, R. J. Hastie, and P. Helander. Plasma Physics and Controlled Fusion **48**, 885 (2006).

[80] R. J. Hastie and K. W. Hesketh. Nuclear Fusion **21**, 651 (1981).

[81] F. Zonca, P. Buratti, A. Cardinali, L. Chen, J.-Q. Dong, Y.-X. Long, A. Milovanov, F. Romanelli, P. Smeulders, L. Wang, et al. Nuclear Fusion **47**, 1588 (2007).

[82] J. P. Graves. Plasma Physics and Controlled Fusion **55**, 074009 (2013).

[83] F. L. Hinton and M. N. Rosenbluth. Plasma Physics and Controlled Fusion **41**, A653 (1999).

[84] Y. Xiao and P. J. Catto. Physics of Plasmas **13**, 102311 (2006).

[85] F.-X. Duthoit, A. J. Brizard, and T. S. Hahm. Physics of Plasmas **21**, 122510 (2014).

[86] A. J. Brizard. Physics of Plasmas **18**, 022508 (2011).

[87] R. B. White. *The Theory of Toroidally Confined Plasmas* (Imperial College Press, London, 2006).

[88] *NIST Digital Library of Mathematical Functions*. `http://dlmf.nist.gov/` Release 1.0.26 of 2020-03-15. F. W. J. Olver and A. B. Olde Daalhuis, D. W. Lozier, B. I. Schneider, R. F Boisvert, C. W. Clark, B. R. Miller, B. V. Saunders, H. S. Cohl, and M. A. McClain, eds.

[89] T. O'Neil. The Physics of Fluids **8**, 2255 (1965).

[90] D. A. Gates, J. Ahn, J. Allain, R. Andre, R. Bastasz, M. Bell, R. Bell, E. Belova, J. Berkery, R. Betti, et al. Nuclear Fusion **49**, 104016 (2009).

[91] B. Lloyd, J.-W. Ahn, R. J. Akers, L. C. Appel, D. Applegate, K. B. Axon, Y. Baranov, C. Brickley, C. Bunting, R. J. Buttery, et al. Plasma Physics and Controlled Fusion **46**, B477 (2004).

[92] X. Lapillonne, S. Brunner, T. Dannert, S. Jolliet, A. Marinoni, L. Villard, T. Görler, F. Jenko, and F. Merz. Physics of Plasmas **16**, 032308 (2009).

[93] V. D. Shafranov. Journal of Nuclear Energy. Part C, Plasma Physics, Accelerators, Thermonuclear Research **5**, 251 (1963).

[94] M. Kruskal. Journal of Mathematical Physics **3**, 806 (1962).

[95] A. Baños. Journal of Plasma Physics **1**, 305–316 (1967).

[96] J. R. Cary and A. J. Brizard. Reviews of Modern Physics **81**, 693 (2009).

[97] C. D. Stephens, R. W. Brzozowski III, and F. Jenko. Physics of Plasmas **24**, 102517 (2017).

[98] N. Howard, C. Holland, A. White, M. Greenwald, and J. Candy. Nuclear Fusion **56**, 014004 (2016).

[99] C. Bourdelle. *Analyse de stabilité de plasmas de tokamak*. PhD thesis, Université Joseph Fourier-Grenoble I, France (2000).

[100] C. Bourdelle, X. Garbet, G. Hoang, J. Ongena, and R. Budny. Nuclear Fusion **42**, 892 (2002).

[101] C. Bourdelle, X. Garbet, F. Imbeaux, A. Casati, N. Dubuit, R. Guirlet, and T. Parisot. Physics of Plasmas **14**, 112501 (2007).

[102] X. Garbet, L. Laurent, F. Mourgues, J. Roubin, and A. Samain. Journal of Computational Physics **87**, 249 (1990).

[103] P. Cottier, C. Bourdelle, Y. Camenen, . D. Gürcan, F. J. Casson, X. Garbet, P. Hennequin, and T. Tala. Plasma Physics and Controlled Fusion **56**, 015011 (2014).

[104] F. Jenko and A. Kendl. New Journal of Physics **4**, 35 (2002).

[105] P. Xanthopoulos and F. Jenko. Physics of Plasmas **14**, 042501 (2007).

[106] H. E. Mynick, N. Pomphrey, and P. Xanthopoulos. Physical Review Letters **105**, 095004 (2010).

[107] M. Nunami, T.-H. Watanabe, and H. Sugama. Plasma and Fusion Research **5**, 016 (2010).

[108] J. A. Baumgaertel, E. A. Belli, W. Dorland, W. Guttenfelder, G. W. Hammett, D. R. Mikkelsen, G. Rewoldt, W. M. Tang, and P. Xanthopoulos. Physics of Plasmas **18**, 122301 (2011).

[109] T. Dannert and F. Jenko. Physics of Plasmas **12**, 072309 (2005).

[110] F. Jenko, T. Dannert, and C. Angioni. Plasma Physics and Controlled Fusion **47**, B195 (2005).

[111] F. Merz and F. Jenko. Physical Review Letters **100**, 035005 (2008).

[112] T. Görler and F. Jenko. Physics of Plasmas **15**, 102508 (2008).

[113] F. Merz and F. Jenko. Nuclear Fusion **50**, 054005 (2010).

[114] J. Citrin, C. Bourdelle, P. Cottier, D. F. Escande, O. D. Gürcan, D. R. Hatch, G. M. D. Hogeweij, F. Jenko, and M. J. Pueschel. Physics of Plasmas **19**, 062305 (2012).

[115] C. Bourdelle. *Turbulent Transport in Tokamak Plasmas: briding theory and experiment*. Habilitation thesis, Université de Provence, Aix-Marseille I, France (2015).

[116] C. Bourdelle, J. Citrin, B. Baiocchi, A. Casati, P. Cottier, X. Garbet, and F. I. and. Plasma Physics and Controlled Fusion **58**, 014036 (2016).

[117] A. Genz and A. Malik. Journal of Computational and Applied Mathematics **6**, 295 (1980).

[118] A. N. Kaufman. The Physics of Fluids **15**, 1063 (1972).

[119] X. Garbet. *Instabilities, turbulence and transport in a magnetized plasma*. Habilitation thesis, Université de Provence, Aix-Marseille I, France (2001).

[120] C. D. Stephens, X. Garbet, and F. Jenko. Physics of Plasmas **27**, 052504 (2020).

[121] X. Garbet, D. Esteve, Y. Sarazin, J. Abiteboul, C. Bourdelle, G. Dif-Pradalier, P. Ghendrih, V. Grandgirard, G. Latu, and A. Smolyakov. Physics of Plasmas **20**, 072502 (2013).

[122] A. Samain. Nuclear Fusion **10**, 325 (1970).

[123] C. Nguyen, X. Garbet, and A. I. Smolyakov. Physics of Plasmas **15**, 112502 (2008).

[124] C. Johnson. *Numerical Solution of Partial Differential Equations by the Finite Element Method* (Cambridge University Press, Cambridge, 1991).

[125] J. W. Connor, R. J. Hastie, and J. B. Taylor. Proceedings of the Royal Society A **365**, 1 (1979).

[126] J. Candy. Plasma Physics and Controlled Fusion **51**, 105009 (2009).

[127] H. Biglari and L. Chen. The Physics of Fluids **29**, 2960 (1986).

[128] R. Kubo. Journal of Mathematical Physics **4**, 174 (1963).

[129] J. A. Krommes. Physics Reports **360**, 1 (2002).

[130] Y. Lin, J. E. Rice, S. J. Wukitch, M. J. Greenwald, A. E. Hubbard, A. Ince-Cushman, L. Lin, M. Porkolab, M. L. Reinke, and N. Tsujii. Physical Review Letters **101**, 235002 (2008).

[131] A. Casati, C. Bourdelle, X. Garbet, F. Imbeaux, J. Candy, F. Clairet, G. Dif-Pradalier, G. Falchetto, T. Gerbaud, V. Grandgirard, et al. Nuclear Fusion **49**, 085012 (2009).

[132] J. E. Kinsey, G. M. Staebler, and R. E. Waltz. Physics of Plasmas **15**, 055908 (2008).

[133] W. Horton. In A. A. Galeev and R. N. Sudan, eds., *Handbook of Plasma Physics, Basic Plasma Physics, Volume II* (Elsevier, New York, 1984).

[134] F. Jenko, W. Dorland, M. Kotschenreuther, and B. N. Rogers. Physics of Plasmas **7**, 1904 (2000).

[135] B. Davies. Journal of Computational Physics **66**, 36 (1986).

[136] M. Guasti. International Journal of Mathematical Education in Science and Technology **23**, 895 (1992).

[137] S. G. Johnson. *Cubature*. http://ab-initio.mit.edu/wiki/index.php/Cubature_Multi-dimensional_integration) (2017).

[138] Ö. D. Gürcan. Journal of Computational Physics **269**, 156 (2014).

[139] O. Linder. *Comparison of Tokamak Linear Microstability Calculations between the Gyrokinetic Codes QuaLiKiz and GENE*. Intership report, Eindhoven University of Technology (2016).

[140] M. Romanelli, G. Regnoli, and C. Bourdelle. Physics of Plasmas **14**, 082305 (2007).

[141] M. Kotschenreuther, G. Rewoldt, and W. Tang. Computer Physics Communications **88**, 128 (1995).

[142] P. C. Liewer, J. M. McChesney, S. J. Zweben, and R. W. Gould. The Physics of Fluids **29**, 309 (1986).

[143] B. B. Kadomtsev and O. P. Pogutse. In M. A. Leontovich, ed., *Reviews of Plasma Physics: Volume 5*, pages 249–400 (Springer US, Boston, 1995).

[144] G. T. Hoang, C. Bourdelle, B. Pégourié, B. Schunke, J. F. Artaud, J. Bucalossi, F. Clairet, C. Fenzi-Bonizec, X. Garbet, C. Gil, et al. Physical Review Letters **90**, 155002 (2003).

[145] B. B. Kadomtsev and O. P. Pogutse. Soviet Physics Journal of Experimental and Theoretical Physics **31**, 898 (1970).

[146] B. B. Kadomtsev and O. P. Pogutse. Nuclear Fusion **11**, 67 (1971).

[147] M. Romanelli, G. Corrigan, V. Parail, S. Wiesen, R. Ambrosino, P. da Silva Aresta Belo, L. Garzotti, D. Harting, F. Köchl, T. Koskela, et al. Plasma and Fusion Research **9**, 3403023 (2014).

[148] T. Tala, H. Nordman, A. Salmi, C. Bourdelle, J. Citrin, A. Czarnecka, F. Eriksson, E. Fransson, C. Giroud, J. Hillesheim, et al. Nuclear Fusion **59**, 126030 (2019).

[149] R. Hazeltine and F. Waelbroeck. *The Framework of Plasma Physics* (CRC Press, Boca Rotan, 2004).

[150] A. S. Richardson. *The NRL Plasma Formulary* (2019).

[151] P. Crandall. *Collisional and Electromagnetic Physics in Gyrokinetic Models*. PhD thesis, University of California, Los Angeles (2019).

[152] S. P. Hirshman and D. J. Sigmar. The Physics of Fluids **19**, 1532 (1976).

[153] P. L. Bhatnagar, E. P. Gross, and M. Krook. Physical Review **94**, 511 (1954).

[154] J. DeLucia and G. Rewoldt. *Improved Krook Model Collision Operator for Trapped-Particle Mode Calculation*. *Tech. rep.*, Plasma Physics Laboratory, Princeton University (1981).

[155] G. Rewoldt, W. M. Tang, and R. J. Hastie. The Physics of Fluids **30**, 807 (1987).

[156] M. Rosenbluth, D. Ross, and D. Kostomarov. Nuclear Fusion **12**, 3 (1972).

[157] G. Rewoldt, W. M. Tang, and R. J. Hastie. The Physics of Fluids **29**, 2893 (1986).

[158] C. Zhao, T. Zhang, and Y. Xiao. Physics of Plasmas **24**, 052509 (2017).

[159] F. Y. Gang, P. H. Diamond, and M. N. Rosenbluth. Physics of Fluids B: Plasma Physics **3**, 68 (1991).

[160] P. Manas, Y. Camenen, S. Benkadda, W. A. Hornsby, and A. G. Peeters. Physics of Plasmas **22**, 062302 (2015).

[161] R. E. Waltz, G. M. Staebler, W. Dorland, G. W. Hammett, M. Kotschenreuther, and J. A. Konings. Physics of Plasmas **4**, 2482 (1997).

[162] X. Yang, P. Manas, C. Bourdelle, J. F. Artaud, R. Sabot, Y. Camenen, J. Citrin, F. Clairet, C. Desgranges, P. Devynck, et al. Nuclear Fusion **60**, 086012 (2020).

[163] M. Keilhacker, A. Gibson, C. Gormezano, and P. H. Rebut. Nuclear Fusion **41**, 1925 (2001).

[164] E. Fable, C. Angioni, and O. Sauter. Plasma Physics and Controlled Fusion **52**, 015007 (2010).